Kinetic Modeling and Automated Optimization in Microreactor Systems

by

Jason Stuart Moore

B.S. Chemical and Biomolecular Engineering, Georgia Institute of Technology, 2007
M.S. Chemical Engineering Practice, Massachusetts Institute of Technology, 2009

Submitted to the Department of Chemical Engineering
in partial fulfillment of the requirements for the degree of

Doctor of Philosophy in Chemical Engineering
at the
MASSACHUSETTS INSTITUTE OF TECHNOLOGY

February 2013

Author _____
Department of Chemical Engineering
September 24, 2012

Certified by _____
Klavs F. Jensen
Warren K. Lewis Professor of Chemical Engineering
Professor of Materials Science and Engineering
Thesis Supervisor

Accepted by _____
Patrick S. Doyle
Chairman, Committee for Graduate Student

Kinetic Modeling and Automated Optimization in Microreactor Systems

by
Jason Stuart Moore

Submitted to the Department of Chemical Engineering on September 24, 2012
in partial fulfillment of the requirements for the degree of
Doctor of Philosophy in Chemical Engineering

ABSTRACT

The optimization, kinetic investigation, or scale-up of a reaction often requires significant time and materials. Silicon microreactor systems have been shown advantageous for studying chemical reactions due to their small volume, rapid mixing, tight temperature control, large range of operating conditions, and increased safety. The primary goal of this thesis is to expand the capabilities of automated microreactor systems to increase their scope and efficiency.

An automated optimization platform is built utilizing continuous inline IR analysis at the reactor exit, and a Paal-Knorr reaction is chosen as the first example chemistry. This reaction, where both the first and second reaction steps affect the overall rate, leads to a more complex conversion profile. A steepest descent algorithm is first used to optimize conversion and production rates. The steepest descent algorithm tends to move slowly up the production rate ridge, significantly reducing efficiency. This issue is overcome by using a Fletcher-Reeves conjugate gradient method, which finds the constrained optimum in much fewer experiments. The conjugate gradient algorithm is then further improved upon by incorporating a hybrid Armijo line search and bisection contraction method. However, the conversion is only about 40% at the maximum in production rate. A further optimization is performed using a quadratic loss function to penalize conversions of less than 85%. This optimization of production rate led to an optimum at higher residence time, where a conversion of 81% is achieved.

In the conventional view of reaction analysis, batch reactions are thought to be significantly more efficient in generating time-course reaction data than flow reactions, which are generally limited to steady-state studies. By taking advantage of the low dispersion in microreactors, successive fluid elements of the reactor may be treated as separate batch reactors. By continuously manipulating the reaction flow rate and tracking the total reaction time of each fluid element, time-course data analogous to that conventionally derived from batch reactors are generated and shown to be in agreement with steady-state results.

Palladium-catalyzed carbonylation and CN-coupling reactions are used extensively in laboratory synthesis and industrial processes. The primary reaction studied involves the coupling of bromobenzene and morpholene with the addition of one or two carbonyl groups. The dependence of reaction conversion and selectivity on temperature, CO pressure, and Pd concentration are investigated using GC and IR analysis. A temperature ramp method is employed to rapidly investigate temperature effects on reaction rate and selectivity. The

experiments reveal a change in the rate determining step at approximately 120 °C and corresponded well with GC data taken at several setpoints. In addition, the activation energy of the lower temperature regime as determined by this IR analysis is found to be very similar to that found by GC analysis, the experiments for which took significantly longer both to perform and analyze. Furthermore, the data collected from these experiments are used to fit a kinetic model.

Multicomponent reactions (MCRs) are important to drug discovery by affording complex products in only a single step. By linking two of these MCRs, a Petasis boronic acid-Mannich reaction and an Ugi reaction, six different components could be incorporated in a relatively short time. The kinetics of each reaction are investigated with online UPLC analysis, allowing for quantification of a number of reaction components, including monitoring the formation of side products that were unknown prior to experimentation.

A simple microcalorimeter is built using thermoelectric elements and a silicon microreactor to experimentally determine the heats of reaction during flow to allow for understanding the heat transfer needs for scale up. The result from the nitration of benzene, which has a heat of reaction of -117 kJ/mol, is -118.6 ± 2.4 kJ/mol. The experimentally determined values are close to the known values; however, there is significant noise in the output during the reaction due to the two-phase nature of the reaction. The Paal-Knorr reaction is further investigated to determine the limits of sensitivity of the microcalorimetry system. A continuous concentration ramp experiment is performed with online IR analysis, enabling the thermoelectric output to be adjusted for reaction rate to determine the sensitivity to the heat of reaction. Below approximately 2 M, the sensitivity decreases rapidly, largely due to noise in the temperature control and concentration. To attempt to correct for the former, a calorimetry system with larger thermal mass is constructed and shown to decrease the sensitivity limit to 1 M, corresponding to a heat flow of approximately 0.05 W.

Thesis Supervisor:	Klavs F. Jensen
Title:	Department Head, Chemical Engineering
	Warren K. Lewis Professor of Chemical Engineering
	Professor of Materials Science and Engineering

Dedicated in Loving Memory of

Virginia "Ginger" Anne

ACKNOWLEDGEMENTS

Having never read beyond the first paragraph of Dickens's *A Tale of Two Cities*, I can't say for certain if the "superlative degree" is meant to be the Ph.D. and the two cities Boston and Cambridge. But now that I'm about to leave the Great White North, where I feel that Winter is Coming in September and you can never be too careful about polar bears in February, I have the opportunity reflect on the past five years before I move to the Land of the Long Summer.

Firstly, I must thank my advisor, Klavs Jensen. None of this work would have been possible without him. I greatly appreciate his support, his impressive breadth of knowledge, and the freedom he gave me to shape my research. I would also like to thank my committee members, William Green and Timothy Jamison, for their feedback in the many discussions through the years. Additionally, I would like to thank Bill for allowing me to TA 10.34 for him. It was a great learning experience.

I'm very grateful to my collaborators over the course of this thesis, especially to Chris Smith for his extensive work on the carbonylation project and for assisting Norbert Heublein and me on the Petasis/Ugi work. I owe a significant portion of this thesis to their efforts. Chris also added several amusing Britishisms to my vocabulary, most of which aren't really appropriate to mention here specifically. Many thanks also to Stephen Born for his practical chemistry knowledge and amusing discussions, especially for convincing me that making rocket fuel to test my microcalorimeter was a bit much. Thanks to Jonathan McMullen for pioneering the work on automation in our lab and to Nick and Lei Gu for all the reactors. I'm very thankful for all the lab members who made the lab a much more enjoyable place to work: Vicki for staring in my favorite day-time sitcom, The Jon and Vicki Show, and for the many conversations on life, the universe, and everything; Brandon for having red hair (I told you I'd do it); Kevin for knowing what the Campanile is really about; and Patrick for putting up with living with me for five years. I'll miss you all.

I would also like to thank the many members of the department whose efforts have been instrumental in keeping everything running smoothly. Thank you Alina Haverty, Suzanne Maguire, Joel Dashnaw, and Steve Wetzel. Thanks also to the Practice School, especially Claude Lupis, William Dalzell, and Beth Tuths. It was a great, once in a lifetime experience.

I couldn't have done all this without the support of my many friends and family. Thanks to my parents for their love. Thanks to the many friends I've made in Cambridge who made it so much more fun. Thanks to Lisa, Adam, Mary, Dan, Matt, Eric, and Veronica for all that they have taught me about life and for all the good times. Thanks to Jason and Dave for giving me an amazing place to relax. Thanks also to all of my Georgia Tech friends who've kept in touch and know how to throw the best parties. Thanks to Colin, a paragon of friendship. Thanks to Mike for putting together the best vacations ever and for always having an open couch. Thanks to Kyle, Sean, and Kevin for all the board games and always getting my jokes.

I gratefully acknowledge the funding for this thesis research from Novartis and the Novartis-MIT Center for Continuous Manifacturing. I also thank Mettler Toledo for early access to their ReactIR microflow cell and technical assistance.

TABLE OF CONTENTS

LIST OF FIGURES

LIST OF TABLES

LIST OF SCHEMES

1 MOTIVATION, BACKGROUND, AND GOALS

1.1 MOTIVATION

1.1.1 WHY MICROREACTORS?

Microreactors offer a variety of advantages over more traditional macro-scale systems. In microsystems, channel widths are typically on the order of hundreds of micrometers. At such length scales, flow is nearly always laminar requiring mixing to occur by diffusion, as convective mixing is significantly reduced as compared to turbulent flow. However, the reduced dimensions also allow diffusion to rapidly transform large concentration gradients into a homogeneous system. This rapid mixing can greatly increase reaction rates where under more standard conditions the rate is limited by diffusion rather than kinetics.[1] Indeed, numerous examples can be found where reactions that require 24 hours in batch can be performed in microsystems in 20 minutes.2

Channel size also plays an important role in temperature control. In a microreactor, the large wall surface-area-to-volume ratio allows for improved heat transfer.3 This effect is enhanced not only by size but also by composition. In particular, silicon microreactors have high thermal conductivity (Si: 157 W/(m·K); stainless steel: 16 W/(m·K); glass: 1.1 W/(m·K))4·5, allowing for more accurate and rapid temperature control1 as well as reduced internal temperature gradients making isothermal operation possible in contrast to larger systems, which often cannot efficiently remove heat, leading to internal hot spots.[6] Further, during the production of silicon microreactors, a thin silicon dioxide layer can be grown on the surface to provide a surface that is chemically inert under most conditions. The silicon itself is also transparent to most infrared radiation, a property that is retained with thin SiO_2 layers.7

Additionally, mixing can be further enhanced by addition of a second, immiscible phase due to Taylor recirculation, as is shown in Figure 1.1.8 Furthermore, as illustrated in Figure 1.2, the segmented flow prevents axial dispersion,[9] which can have significant effects at short residence times.[10] In the ideal case of complete separation of the liquid segments, they can be interpreted as individual well-mixed batch reactors.

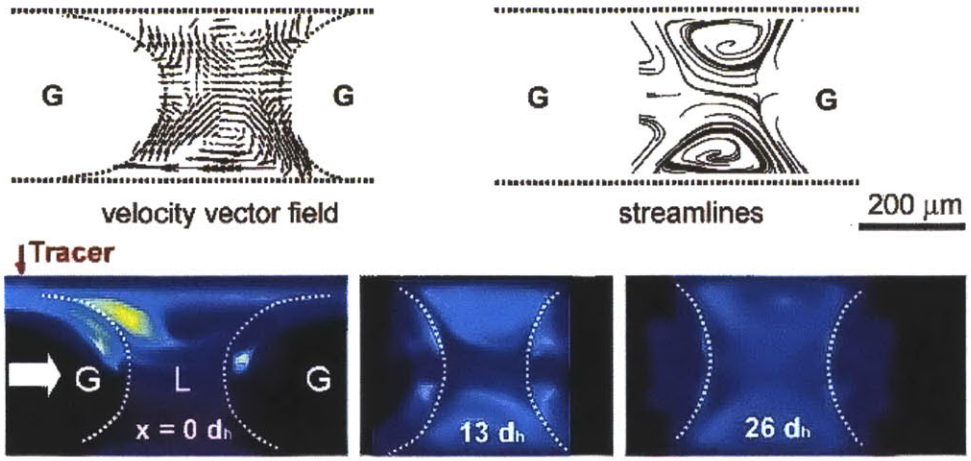

Figure 1.1. Mixing and fluid flow within the liquid phase of gas-liquid slug flow.[8]

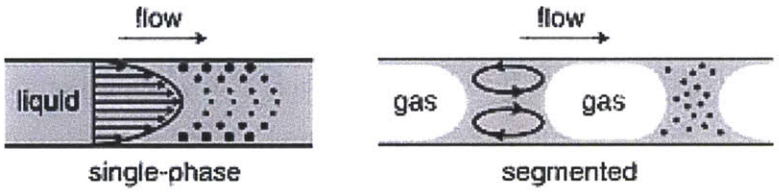

Figure 1.2. Reduced dispersion of the liquid phase by segmentation with a gas phase.[9]

Silicon microreactors have been shown to be highly versatile. A number of flow systems have been used, such as gas-liquid,[11] liquid-liquid,[12] and gas-liquid-solid[13] reactions, which are often used in conjunction with other unit operations, such as separators and extractors. Furthermore, silicon microreactors have been shown to be able to operate at high temperatures and pressures.[14] In addition, the small volumes of microreactors allow dangerous chemistries to be conducted more safely. For example, fluorination and chlorination of aromatics, nitration to form highly energetic compounds, and reactions carried out in the explosive regime can all be safely conducted in microreactors.2

1.1.2 Advantages of Continuous Chemistry

Throughout the chemical industry, the emphasis on continuous processes continues to grow due to increased process safety, reduced costs, and higher product quality[15] as well as reduced environmental impact.[16] Significant interest in changing from the batch to the continuous paradigm currently exists in the area of pharmaceuticals, which in part due to a stricter level of regulatory requirements has lagged behind much of the industry. However, the FDA has recently created an initiative promoting the use of inline process analytical technology

"facilitating continuous processing to improve efficiency and manage variability" and to increase "process understanding" and automation to aid in drug screening and scale-up.[17]

As each stage of clinical trials and the final market production requires larger quantities of drug to be made, the ability to scale-up efficiently becomes important to whether a product can move forward. Batch processes are not easily scaled up; for example, a stirred reactor can be scaled up based upon constant impeller power input per unit volume, impeller rotation frequency, or impeller tip speed, all of which generally lead to significantly different power requirements and mixing conditions. Moreover, as there is a finite time before patents expire, the speed at which scale-up steps can be carried out translates directly into additional time on the market before generics significantly reduce market share.[18]

The use of microreactors further increases product quality because they lack the thermal and concentration gradients found in larger-scale systems, allowing more exact control of process conditions for optimal yield. Additionally, due to the increasing cost and decreasing efficiency in research into new pharmaceutical products, ways to reduce the cost of drug development and manufacture are becoming increasingly important. Microreactors may be key to solving these issues because they are not scaled up in the traditional way, but instead are scaled out by increasing the number of identical microreactors and eliminating the need to develop process conditions at another scale.[18]

However, microreactor scale out will not ultimately prove to be the best solution in every case. As the fluid volumetric flow rates required rise, so too do the number of microreactors, eventually reaching levels where it would be more economically feasible to use a more traditional continuous system. In such cases, efficient scale up again becomes important. Knowing the kinetics and thermodynamics of the reaction would allow simulations to be performed to determine the optimal operating conditions under the effects of increased mass transfer limitations.6

Further cost savings can be realized by increasing automation in the processes of drug development using microreactors. Automating the optimization of syntheses, especially those that are multi-step or those containing several unit operations, would significantly reduce the

labor, time, and materials required.[7] Additionally, automation can be applied to the kinetic studies as well as screening experiments to reap greater savings.

1.2 BACKGROUND

1.2.1 UNIT OPERATIONS IN MICROSYSTEMS

Microreactors must often be combined with separation for multi-step synthesis (Figure 1.3). Separations devices have been designed to separate two fluid phases in slug flow for both gas-liquid and liquid-liquid systems. This is accomplished by taking advantage of the surface tension that becomes significant at the microscale (i.e., the Bond number and capillary number are $\ll 1$), surpassing gravitational and viscous effects that typically dominate at the macroscale. One such separator uses 20 μm wide capillaries etched into the side of a channel on the silicon chip to selectively remove liquid from gas-liquid flow due to the selective wetting of the capillaries by the liquid phase when the pressure difference across the capillary opening is smaller than the capillary pressure.[19] For liquid-liquid systems, interfacial forces are typically lower, requiring smaller channels for higher capillary forces. Such separations have been achieved with a thin porous fluoropolymer membrane with pore diameters of approximately 0.1 to 1 μm, which selectively wets non-aqueous solvents when the pressure difference does not surpass the capillary pressure.[20] Examples of both types of separators are shown below in Figure 1.4.

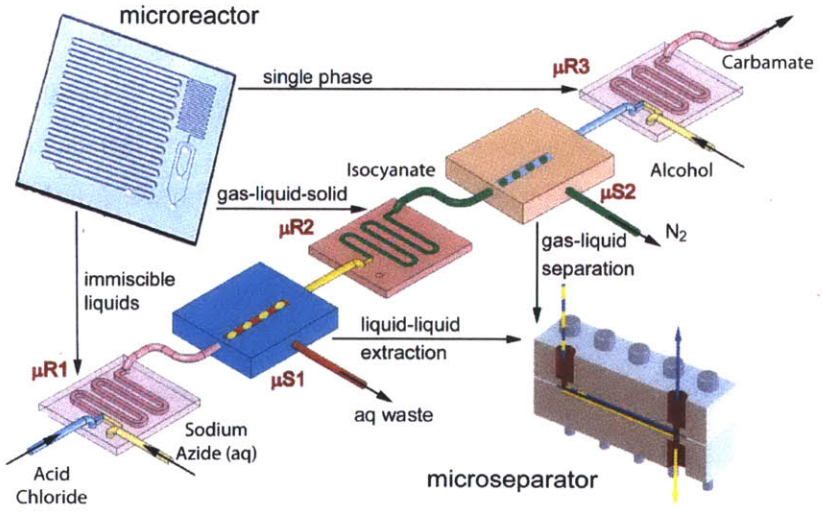

Figure 1.3. Synthesis of carbamate involving multiple micro unit operations.[21]

a) 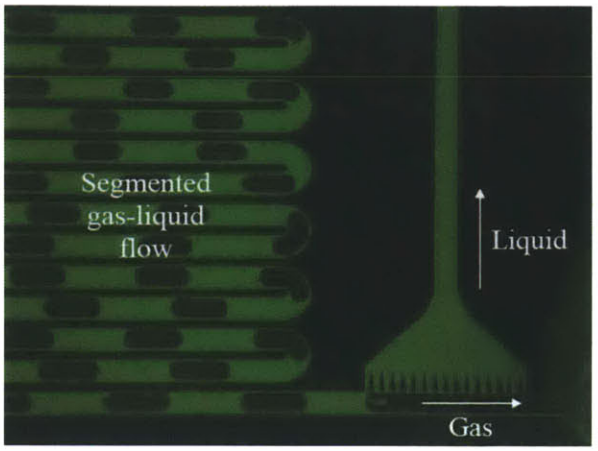

b) 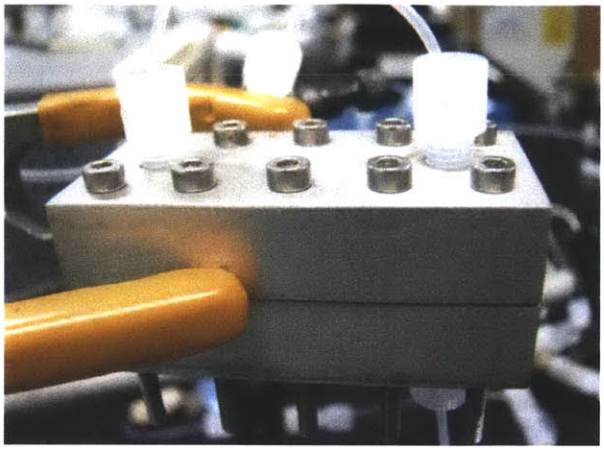

Figure 1.4. a) Gas-liquid separator in silicon.[19] b) Liquid-liquid separator in stainless steel.

Additional types of operations that make use of these separation devices are extraction and distillation. Slug flow has been used to perform extractions,[22] which has a variety of possible uses, such as removing the reaction product from a reaction stream so that unused reactants and catalyst can be recycled.[23] Distillation is another separation technique frequently used at the macroscale. This process requires boiling a liquid phase, which can be difficult in a microreactor due to a lack of nucleation sites leading to superheating rather than boiling. This challenge has recently been overcome by using an inert gas in slug flow with the liquid mixture to be separated.[24, 25]

1.2.2 Optimization Techniques

A great diversity exists in the field of optimization. A number of optimization techniques have been based upon an algorithm that begins at a specified initial condition and then steps generally along a trajectory designed to climb toward a single optimum. Other techniques are based around global search algorithms, either dividing the parameter space into a number of branches and then further subdivides them as the optimization progresses or using concepts found in nature to incorporate elements of structured randomness.

1.2.2.1 Local Optimizations

The stepping trajectory based algorithms, such as simplex and steepest descent methods, are designed as more directed searches than the other types of methods. The simplex method in n dimensions is based around an $n + 1$ vertex hyper-triangle where experiments are performed at each vertex and then the value of an objective function at each point is calculated. Whichever

vertex has the worst value of the function is discarded and that point is reflected through the hyper-triangle as the next set of conditions to be tested. This process is repeated as the algorithm moves uphill in the objective function. Once the simplex reaches a point where reflection of each vertex results in a poorer resulting function value, the algorithm then contracts either by moving inward from one vertex or by keeping only the best point and then moving all other vertices inward.[26, 27]

Gradient-based methods, such as the steepest descent method, begin from an initial guess and move a distance along the gradient of the objective function to the next set of conditions. Unlike the simplex method where the step size is initially set and remains unchanged until the area of the optimum is reached, the steepest descent method may vary the step size for each step.[28] However, the steepest descent method often results in inefficient zig-zag trajectories in narrow valleys or hills, requiring more advanced methods like conjugate gradient to determine search directions.[27]

1.2.2.2 Global Optimizations

The SNOBFIT (Stable Noisy Optimization by Branch and Fit) algorithm by Huyer and Neumaier is one example of an algorithm that attempts to find the global maximum by partitioning the parameter space into several local searches. The algorithm first attempts to increase the chance of finding a global optimum by creating a space-filling set of initial points where the objective function will be evaluated. The algorithm then creates local quadratic models around each point using a set of the points nearest neighbors. The minimum of each model is calculated, and if the objective function has not already been evaluated at these points, a set number of the best points are added to the next list of points to be calculated. If the number of points to be evaluated in the next step is lower than a set number of points, additional random data points in unexplored areas are added. The major advantage of this algorithm is that, unlike the algorithms in the previous section, SNOBFIT is not a greedy algorithm. Thus, it will not become trapped in a local optimum that is not the global optimum. However, while this algorithm is able to span the entire parameter space and find a global optimum, such convergence is only guaranteed as the number function evaluations becomes large.[29]

One example of nature-mimicking optimizations is the mimetic algorithm, which incorporates aspects of more traditional trajectory based hill-climbing with a genetic algorithm.

The genetic algorithm creates an initial random population of conditions and codes each into an array, which serves as a chromosome analog. Once the value of the objective function is evaluated at each condition, each is given a fitness score. Higher scores increase the likelihood that the corresponding chromosome will be included in a list from which the next generation will be created, which is done by mimicking the crossing-over and mutation steps of meiosis. A variety of modifications can be made to this algorithm, such as using more than two parents per offspring and including a so-called incest prevention algorithm, which checks the Hamming distance to make sure that two parents that are much more closely related than the rest of the population cannot breed to prevent premature convergence. Once the genetic algorithm has narrowed in on the area containing the optimum, another optimization technique, such as steepest descent, is used to fine-tune the optimum.[30]

A more probabilistic algorithm is simulated annealing, which is designed around principles of statistical mechanics and mimics the movement of atoms at a certain temperature. After a random starting position, each subsequent step is generated by a random displacement. The objective function is modeled as an energy surface. If the resulting objective function is more favorable, the step is accepted; however, if the objective function is less favorable, the step may still be accepted with a probability proportional to the negative exponent of the function change over an effective temperature. Initially, the temperature is set high enough that the optimization is able to move between local optima, but as the optimization proceeds, this temperature is lowered, which causes the optimization to become trapped in one optimum.[31] Similar to this cooling down process, the mutation rate of the genetic algorithm can be set initially high and made to decrease with each generation.[32] The major downside of both of these algorithms is that they generally require a large number of evaluations of the objective function, making them untenable for experimental optimization if the experiments cannot be done on the order of seconds.

1.2.3 Previous Work in Automated Optimization

Previously work on automated optimization in the Jensen group was performed by Jonathan McMullen. Several automated microreactor systems were developed to integrate online reaction analysis with feedback control for: 1) rapid reaction screening to develop libraries,[33] 2) single-trajectory local optimization by simplex and steepest descent methods and global

optimization by the SNOBFIT method,[34] 3) kinetic model discrimination and parameter fitting,[35] 4) rapid reaction modeling and scale-up,[36] and 5) automated system flushing and acoustic irradiation for dealing with reactor clogging due to solids buildup.[37]

1.3 Thesis Goals

The primary aim of this thesis is to expand the capabilities of automated microreactor systems to increase their scope and efficiency. This was demonstrated by changing control and measurement techniques around the same basic system to achieve new reaction understanding. This aim is then further divided as follows:

1. To incorporate additional and more sophisticated online measurement techniques to broaden the range of applicable chemistries and enable continuous process monitoring.

2. To expand upon existing automated optimization algorithms to allow for application to more complex flow systems.

3. To investigate the kinetics of reaction processes involving multiple steps.

1.4 Thesis Outline

An automated multi-trajectory optimization platform with continuous online infrared (IR) monitoring is presented in Chapter 2. The production rate of a Paal-Knorr reaction is maximized within a constrained temperature and residence time design space. The automated platform utilizes a microreactor system to carry out optimizations with low material requirements and implements a micro IR flow cell for continuous online monitoring of reaction conversion. The approach to steady state at each set of reaction conditions is assessed continuously before the objective function is evaluated and reactor conditions move to the next setpoint. Several optimization algorithms are tested for their performance on a complex objective terrain (Figure 1.5). Each function comes to agreement on the optimal conditions but requires a significantly different number of experiments to reach the final conditions. Additionally, multiple objective functions are compared to analyze the tradeoff between production rate and conversion.

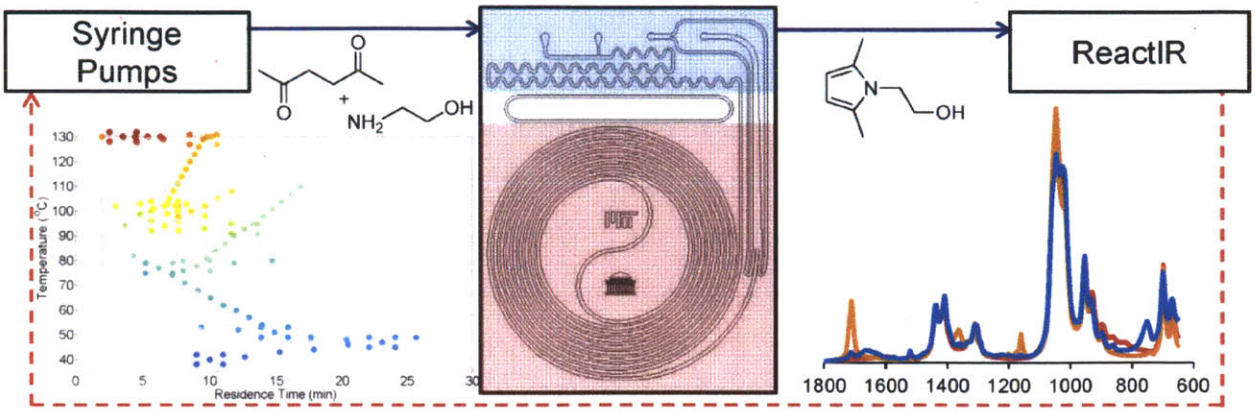

Figure 1.5. Chapter **2** summary figure demonstrating IR-based feedback control and the results of one such optimization.

In the conventional view of reaction analysis, batch reactions are thought to be significantly more efficient in generating time-course reaction data than flow reactions, which are generally limited to steady-state studies. By taking advantage of silicon microreactors under conditions of low dispersion with inline IR analysis, successive fluid elements of the reactor may be treated as separate batch reactors. In Chapter 3, by continuously manipulating the flow rate and temperature of a Paal-Knorr reaction while tracking the total reaction time of each fluid element, reaction conversion was shown to correspond accurately to steady-state results (Figure 1.6). This approach required significantly less time and materials, allowing for the rapid generation of a kinetic model.

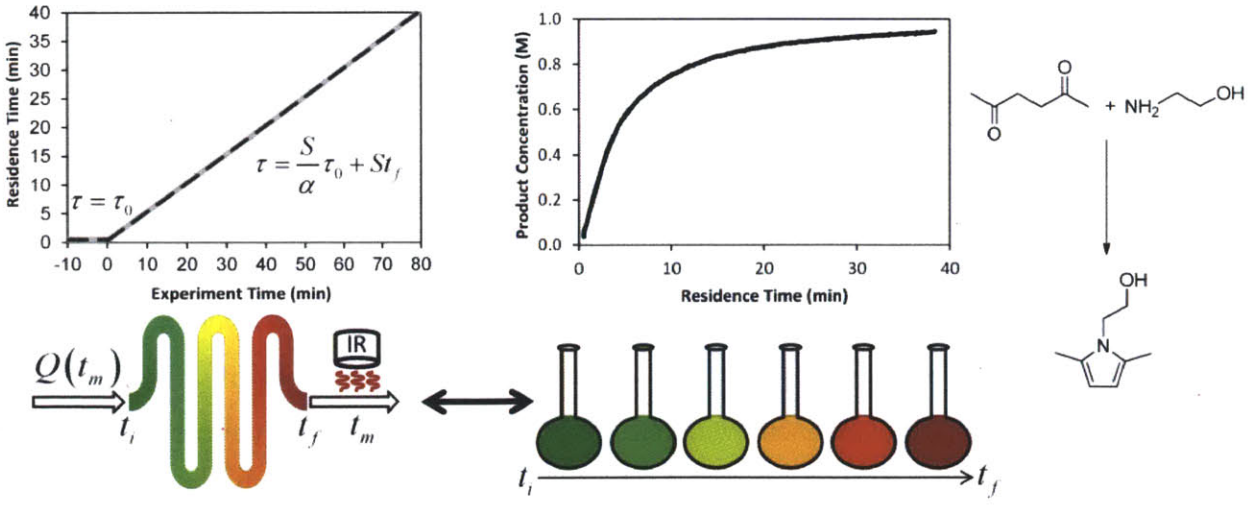

Figure 1.6. Chapter 3 summary figure demonstrating the product profile from a continuous residence time ramp and the relationship between a low-dispersion flow reactor and a well-mixed batch reactor. Color represents extent of conversion from low (green) to high (red).

In Chapter 4, temperature, pressure, gas stoichiometry, and residence time were varied to control the yield and product distribution of the palladium-catalyzed aminocarbonylation of aromatic iodides, bromides, and chlorides in both a silicon microreactor and a packed-bed tubular reactor, although the choice of reactor was observed to have a significant influence on the reaction. Automation of the system setpoints and product sampling enabled facile and repeatable reaction analysis with minimal operator supervision. It was observed that the reaction was divided into two temperature regimes. This effect was kinetically investigated through focus on the aminocarbonylation of aryl bromide. To this end, an automated system was used to screen steady-state conditions for offline analysis by gas chromatography to fit a reaction rate model. Additionally, a transient temperature ramp method utilizing online infrared analysis was used, leading to more rapid determination of the reaction activation energy of the lower temperature regimes (Figure 1.7). The entire reaction spanning both regimes was modeled in good agreement with the experimental data.

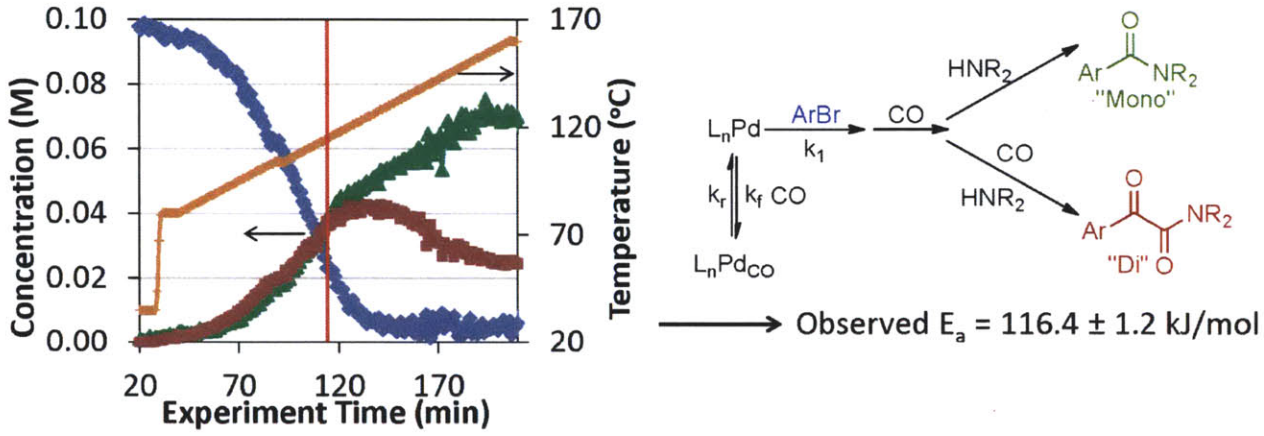

Figure 1.7. Chapter **4** summary figure showing conversion, selectivity, and kinetics results from a continuous temperature ramp experiment.

Chapter 5 presents an experimental study on a Petasis-Ugi tandem reaction conducted in a continuous flow microreactor system. Although the two individual reactions were discovered decades ago, their exact mechanisms are still in dispute. A reason for this lack of knowledge is that both reactions are multicomponent reactions, involving three reagents in the case of the Petasis reaction and four in the Ugi reaction. Multicomponent reactions typically proceed by following a specific pathway of bimolecular reactions and intramolecular rearrangements resulting in a variety of unstable intermediates that cannot be isolated. One goal of this study was

to validate proposed mechanisms of the individual reactions by a kinetic interpretation of experimental data.

Besides the study of individual Petasis and Ugi reactions, the conducted experiments implemented and examined a Petasi-Ugi tandem reaction. By employing the product of a suitable Petasis reaction as reagent in a successive Ugi reaction without any intermediate purification, it was effectively possible to accomplish a six-component reaction. Such a chemical reaction assembling six different compounds in a uniquely ordered manner to one specific molecule is a valuable tool for applications like screening for biological activity.

In the course of the presented study, the examined chemical reactions were transferred from conduction in traditional batch reactors to an automated continuous flow microreactor setup, where kinetic analyses were performed (Figure 1.8). The employed microreactors enabled measurements at stationary and precisely controlled conditions, while the small consumption of chemicals led to increased safety, reduced costs, and a lower environmental impact compared to the conduction of similar experiments in batch reactors.

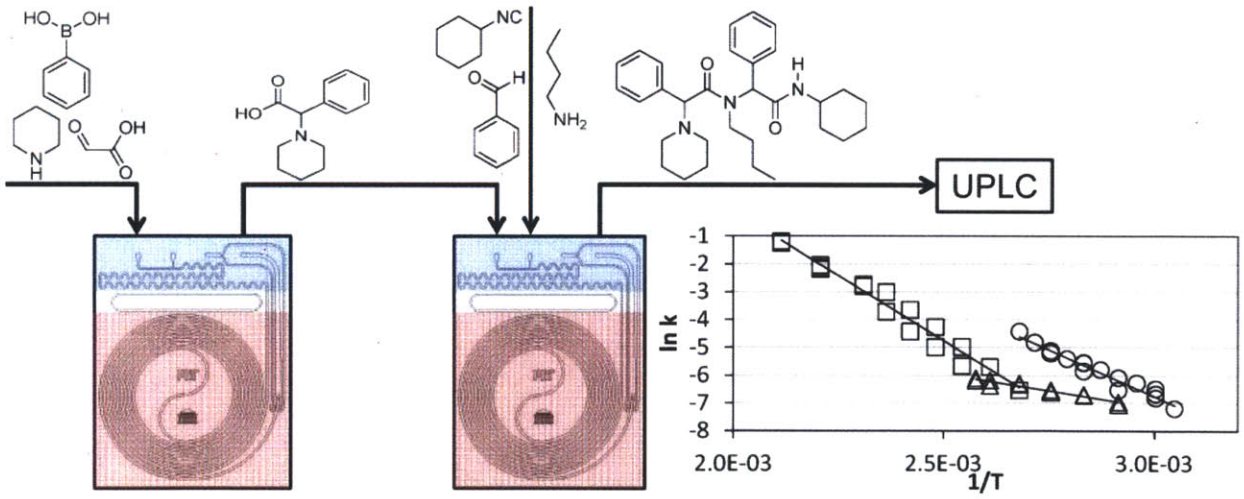

Figure 1.8. Chapter **5** summary figure showing Petasis and Ugi reactions in series with the resulting Arrhenius plot from online UPLC analysis.

Silicon microreactors have proven well suited to highly exothermic reactions due to their high thermal conductivity. Chapter 6 presents a simple flow microcalorimeter using thermoelectric elements and a silicon microreactor to measure heats of reaction that would be necessary to determine the heat transfer needs for scale up. The two-phase nitration of benzene

was initially studied, and the measured heat of reaction of -118.6 ± 2.4 kJ/mol agreed with the literature value of -117 kJ/mol. A single-phase Paal-Knorr reaction was then studied with inline IR analysis. The lower limit of heat flux at which the microcalorimeter was sensitive was determined *via* a continuous concentration ramp experiment. A second-generation calorimeter was then built, which significantly improved the stability and sensitivity (Figure 1.9).

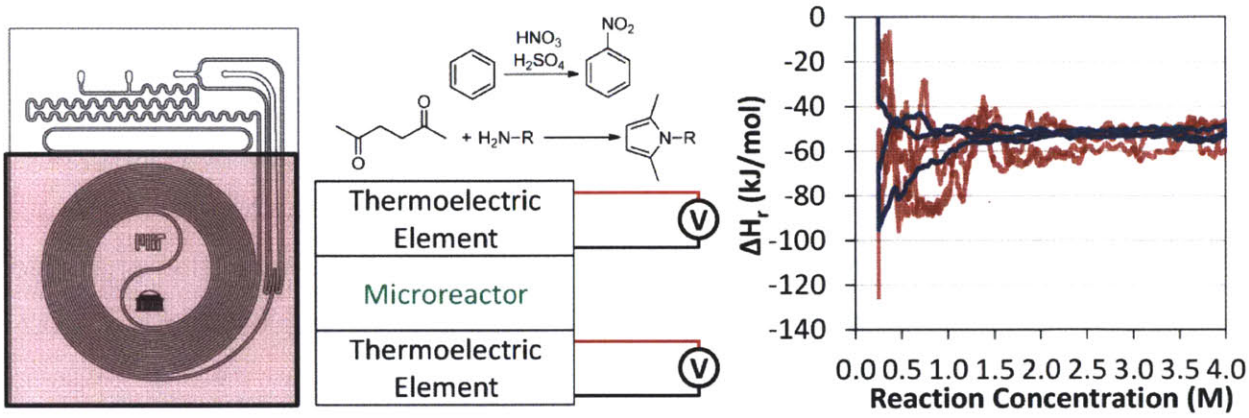

Figure 1.9. Chapter **6** summary figure showing the thermoelectric elements sandwiched around the microreactor and the sensitivity difference between the first- (red) and second-generation (dark blue) calorimeters.

Chapter 7 summarizes the impact of this thesis and describes possible future research areas and applications.

2 AUTOMATED MULTI-TRAJECTORY METHOD FOR REACTION OPTIMIZATION IN A MICROFLUIDIC SYSTEM USING ONLINE IR ANALYSIS

2.1 INTRODUCTION

The optimization of a reaction process is often expensive, requiring significant investments in time and material.[7, 38] Microreactor systems carry out these optimizations at reduced costs, due to low material requirements and waste generation.[16, 39] Additionally, the reduced channel widths allow for reactions that would be mass transfer limited at larger scales to be kinetically controlled,[40, 41] and this enhanced reaction rate often produces significantly higher reaction yields.2 The use of silicon devices also enhances heat transfer, allowing for tight control of reaction temperature and reducing internal temperature gradients that occur in energetic reactions at larger scales.1, 3, 42 Furthermore, these devices can be operated at high temperature and pressure, allowing access to reaction conditions not achievable in batch.[14, 43] These advantages enable a more intrinsic understanding of the reaction under investigation and have found application in a number of industries.6, 44, 45 Moreover, the known fluid-flow characteristics combined with controlled mass and heat transfer effects enable scaling of the optimum conditions to larger production systems.[36, 46] Lastly, as these flow experiments are performed sequentially, they can progress towards the optimal conditions using information from previous experiments, so that fewer unnecessary and unproductive experiments are performed that do not show improvement over the current conditions.

In an effort to utilize the advantages of the micro-scale, our group has recently described a microreactor system to perform single-trajectory automated optimization of reactions in a multi-variable design space.[34, 36] This optimization platform assessed each reaction once by analyzing a reaction sample by HPLC after a fixed number of residence times. In the trajectory method used, the algorithm was designed to move from an initial condition along a single path toward the optimum. Intelligently updating reaction conditions based on inline analytical techniques has been shown to significantly improve optimization performance.[47] However, in more complex reaction schemes, the terrain of the objective function will not point so directly to

the optimal conditions. Herein is described an expanded multi-trajectory optimization system, allowing for the optimization of such a complex reaction system. This analysis takes into account the changing behavior of the objective function by re-analyzing the objective terrain and changing the search direction during the optimization.

This work focuses on the overall approach used to conduct reaction optimizations, regardless of the reaction or the actual objective function. Thus, it would be possible to interchange objectives or even reactions using the same methodology. A well-known method that is often used to accomplish this is design of experiments (DoE); however, this approach assumes that the objective function can be well modeled over its entirety by a low-order function. Here, no such assumption is necessary, and this approach is intended to be extendable to more complex systems where design of experiments would fail to adequately capture the nature of the objective function.

Most previous studies have monitored performance only intermittently and at a single wavelength. In this example, the reaction progression was analyzed quantitatively *via* online ATR-FTIR using Mettler Toledo's ReactIR micro flow cell, which has a 51-uL flow cell equipped with a multi-pass diamond window to allow for continuous monitoring of the mid-IR range.[48] This analytical technique has previously been used in characterizing system dispersion and chromatographic effects, reaction screening, and monitoring reactor failures, though none of the data was used to quantitatively assess reaction progress, much less investigate reaction kinetics.[49, 50] Additionally, use of online IR measurements in process optimization has typically been done by testing a few settings of process variables, changing one at a time, and observing the relative size of the desired peak, without quantitative analysis or investigation of parameter interactions.[51]

The IR micro flow cell enables monitoring of the reaction's approach to steady state, ensuring that steady-state data is used for analysis. Thus, the next set of reaction conditions can begin as soon as the previous steady state had been reached and assessed, rather than waiting a fixed number of residence times and assuming that steady state has occurred, as has been done previously.[34] Moreover, this analysis can be performed directly inline at reaction concentrations by using the entire reactor effluent, rather than requiring significant dilution of only a small reaction sample, as with HPLC sampling, enabling better characterization of system fluctuations

and non-destructive analysis between unit operations. It would also be possible to monitor the reaction with online IR in the presence of unknown reaction species (intermediates or byproducts); however, as with any measurement technique, each reaction species would have to be isolated and calibrated to be certain of quantitative analysis. In addition, the impact of unknown species is dependent on the spectrum analysis technique used. For calibration to a peak height, other species are less likely to have adverse effect unless they contain an overlapping peak. Conversely, if a chemometric principle component analysis is used, any significant uncalibrated impurity can result in altering the spectrum decomposition, preventing quantification. For these reactions, inline analysis would have to be done with other methods such as HPLC, as has been demonstrated previously.[34]

A Paal-Knorr reaction of 2,5-hexanedione (**1**) and ethanolamine (**2**) in dimethyl sulfoxide (DMSO) (Scheme 2.1), where both the first and second reaction steps affect the overall rate, leads to a more complex conversion profile, although the exact structure of the reaction intermediate is still under some debate.[52, 53] At short reaction times the initial second-order step significantly affects the overall rate of product formation, which leads to a tapered plateau in the reaction production rate. The Paal-Knorr reaction is widely used to form pyrrole rings in synthetic[54, 55] and biological molecules.[56, 57] Beyond the mechanism (Scheme 2.2), the Paal-Knorr reaction has been studied to create libraries [58] and was recently the subject of an optimization and scale-up study.[59] However, more standard one-at-a-time and DoE methods were used to optimize conversion, which were then analyzed *via* offline GC analysis after quench and dilution.

While it is possible to determine conversion based on the advanced chemometric analysis of the IR spectrum, reaction conversion of the Paal-Knorr reaction could be monitored simply by calibration to a single peak height normalized to a single point baseline. Figure 2.1 shows the IR spectrum of the main reaction species, enumerating the main peaks that could be easily followed to assess reaction conversion by monitoring hexanedione consumption and product formation.

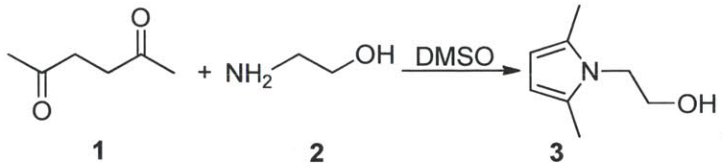

Scheme 2.1. Paal-Knorr reaction.[60, 61]

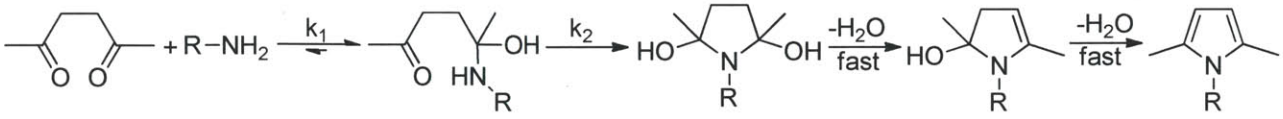

Scheme 2.2. Paal-Knorr reaction mechanism.[53, 56, 62]

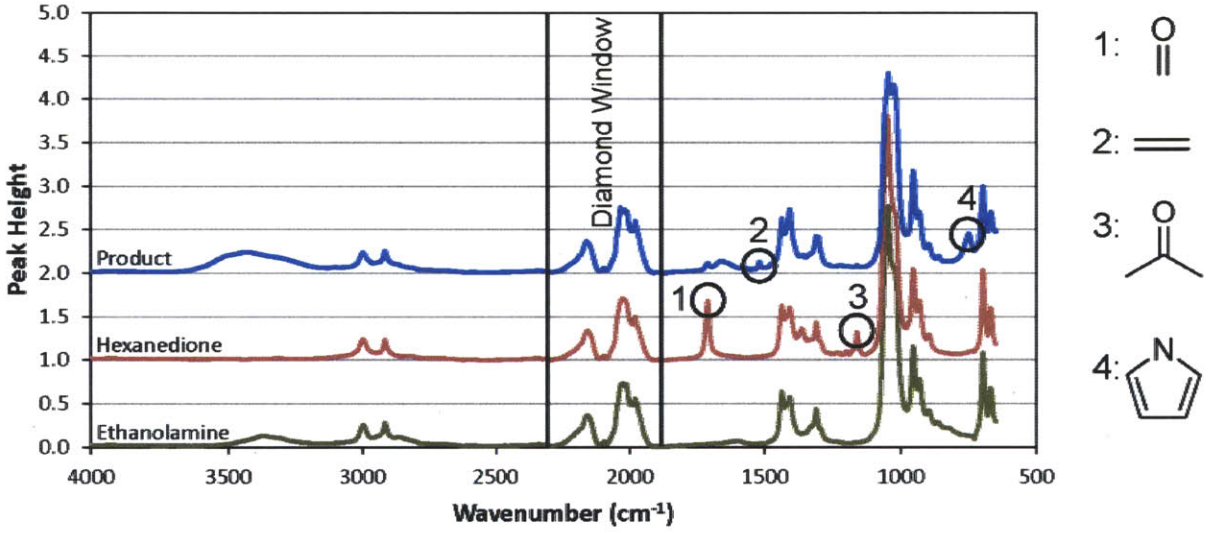

Figure 2.1. IR spectrum of the Paal-Knorr reaction species and their corresponding moiety in DMSO after solvent subtraction.

Other works have investigated the use of various online analysis techniques to continuously analyze the components of flow systems. For example, Mechtilde, Eduard, and Andreas have shown that they can use an external Raman probe to scan different residence times down the reactor length. While feedback and optimization are mentioned as possible applications of this technique, no details or results from such are given[63]. The Kazarian group has demonstrated the ability to generate 8 fps IR movies of the entire flow path, which has the potential to be a powerful tool. However, at present this approach still has significant challenges that must be overcome. The small size of the array, approximately a few millimeters on a side, limits the residence times that can be monitored. Also, the use of paraffin walls limits applicable

chemistries and temperature range. Furthermore, having the IR detector as the reactor base prevents the decoupling of reactor and measuring temperatures, requiring that calibrations be a function of not only concentration but also temperature.[64]

Herein is presented a microreaction platform, which is used to compare the performance of several automated optimization algorithms to optimize multiple objective functions related to the Paal-Knorr reaction. This setup and these methods aim to target issues of high cost and difficulty typically involved in finding optimal conditions in a complex reaction system.

2.2 EXPERIMENTAL SECTION

The microfluidic system used is shown schematically in Figure 2.2, including a schematic of the silicon microreactor. Flow was achieved with two Harvard syringe pumps (PHD 2000), which were controlled via daisy-chained RS-232 communications to a Dell (Optiplex 960) computer. These syringe pumps were connected to a silicon microreactor with a 232-μL reaction zone and a cooled inlet/outlet zone, which allows the reactant streams to fully mix before reaction occurs and thermally quenches the reaction.[65, 66] In addition, due to the high heat transfer coefficient of silicon, the temperature of the reaction zone could be quickly changed between setpoints and the fluid stream rapidly reached the desired temperature in both reaction and quench zones.

The temperature of the reaction zone was controlled with an Omega (CN9311) controller and an Omega (CSS-01235/120V) heating cartridge. This controller was connected through an RS-232 cable to the computer to allow programming the temperature setpoint and reading the measured reactor temperature. The microreactor inlet and outlet region was maintained at room temperature with a recirculating water bath. A Mettler Toledo ReactIR iC 10 outfitted with a DiComp ATR 51-μL flow cell was used for continuous inline monitoring, averaging 167 spectra scans once per minute and saving to an Excel file. The flow cell head was maintained at 35 °C so that spectra were always collected at the same temperature, removing the requirement to account for temperature effects in the IR spectrum. Labview software (version 8.5.1) on the computer communicated with the syringe pumps and temperature controller and read the IR Excel export files to determine reaction conversion based on calibrations to peak heights. Matlab scripts (version 2010b) within Labview ran the optimization algorithms to determine reaction setpoints.

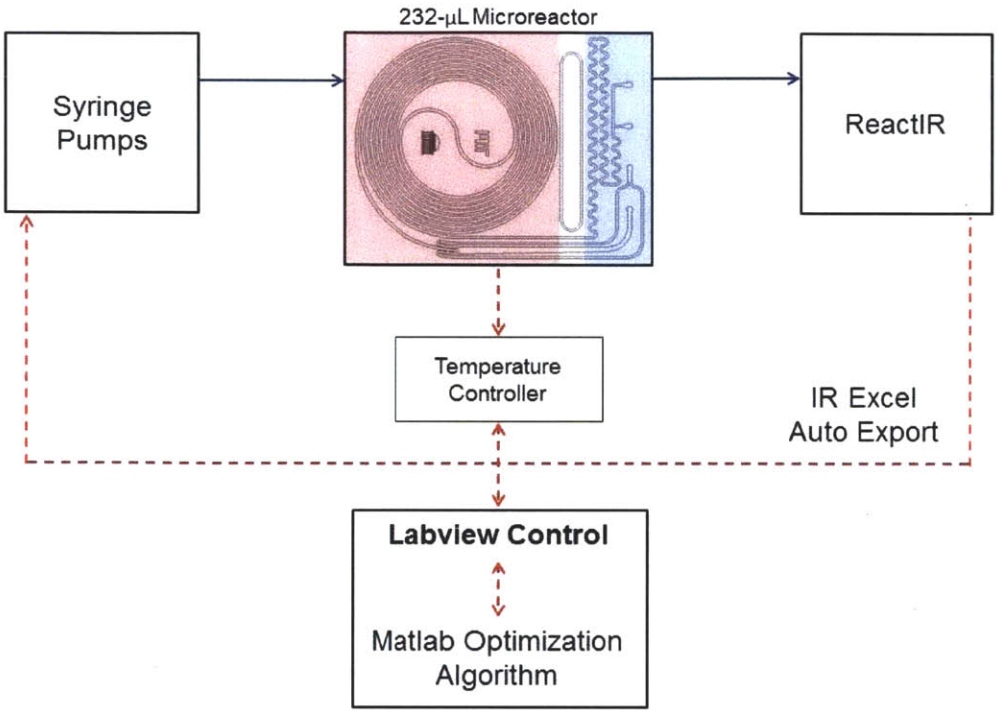

Figure 2.2. Automation system schematic.Solid lines represent fluid flow and dashed lines represent data flow.

2.3 METHOD

Two optimization algorithms, steepest descent and conjugate gradient,[27, 67, 68] were used to vary reaction temperature, T, and residence time, τ, to maximize the objective function, J,

$$\max J = \left(\frac{\text{conversion}}{\text{residence time}}\right) = \left(\frac{X}{\tau}\right) \propto \text{Production Rate} \tag{2.1}$$

which is proportional to the reaction production rate. The search algorithms were carried out by performing a full-factorial DoE around a starting point, then moving along a trajectory in order to maximize the objective function. The process was then repeated, setting the conditions that maximized the objective function as the new starting point. For the steepest descent algorithm, at each new DoE a new search direction is calculated based solely upon that DoE, which allows the search direction to rapidly change between trajectories. However, for conjugate gradient, the new search direction is a weighted sum of the previous search direction and what would be the new steepest descent search direction. This prevents large shifts in the search direction, which makes the conjugate gradient less likely to become trapped by more difficult terrain.[27]

The optimization was performed by first inputting initial conditions, trajectory and DoE step sizes, and constraints on allowable trajectory conditions. The Matlab optimization algorithm was then started. At each setpoint, reactor temperature was deemed to be equilibrated once within 1 °C of setpoint, although the temperature controller generally maintained within 0.2 °C of setpoint. After equilibration, a minimum flush volume was completed to ensure that the previous steady-state reactor effluent had exited the IR flow cell. The IR data was then continuously monitored until the reaction reached steady state, at which point the objective function was calculated. The algorithm performed an initial DoE around the specified starting location and fit a linear response surface to the objective function. From this surface, the gradient was found and the i^{th} search direction, S_i, was calculated by either the steepest descent (Eq. 2.2a-b) or the Fletcher-Reeves conjugate gradient method (Eq. 2.3a-c).[27] The reaction conditions then stepped along this trajectory until the algorithm either terminated or contracted.

$$S_1 = \nabla J(x_1) \tag{2.2a}$$

$$S_{k+1} = \nabla J(x_{k+1}), k \geq 1 \tag{2.2b}$$

$$S_1 = \nabla J(x_1) \tag{2.3a}$$

$$S_{k+1} = \nabla J(x_{k+1}) + \beta_k S_k, k \geq 1 \tag{2.3b}$$

$$\beta_k = \frac{\left\|\nabla J(x_{k+1})\right\|^2}{\left\|\nabla J(x_k)\right\|^2}, k \geq 1 \tag{2.3c}$$

Termination was triggered if one of the following occurred: (a) by reaching an experimental condition at which all constraints were active, i.e. at a corner of the constrained design space, (b) reaching the maximum number of experiments, (c) reaching a constraint that would cause stepping along the constraint boundary to reduce step size below a set minimum, or (d) when the last objective function calculated was less than or equal to 95% of the maximum objective function value found along the trajectory. This last condition was set at 95% rather than 100% to prevent small decreases in the objective function due to experimental error within relatively flat regions from causing termination.

Contraction was triggered if the objective function decreased with the first step beyond the DoE, indicating that the optimum was very near to the initial condition. Once the trajectory optimum was found, this procedure was then repeated beginning at the trajectory optimum unless contraction occurred and the maximum objective function value found was along the trajectory rather than at a DoE corner within the design space.

The step sizes for the DoE were set to ± 2 °C and ± 1 min and the trajectory step size was initially set to 3 units (normalized °C and min). These sizes allowed for capturing local variations, which became especially important in the neighborhood of the objective plateau, while allowing for enough change in experimental conditions to have only a small effect due to experimental variances. However, if the trajectory optimum is far from the initial conditions, having a fixed step size on the trajectories can lead to performing experiments at a large number of setpoints. Thus, an Armijo-type line search[67] was implemented in another optimization run, replacing the previous contraction algorithm. The Armijo algorithm determines the step size, Δx, along the search trajectory by the formula:

$$\Delta x = (-1)^{\beta} \Delta x_{\max} \alpha^{n} \tag{2.4}$$

Here Δx_{max} is the maximum desired step size, set here to 16 units, and α is a number between 0 and 1, set here to 0.5. While moving along the trajectory, n and β are 0 until a step is not accepted, by triggering a termination criterion. Then Armijo contraction is performed around the current trajectory maximum by setting β to 0 or 1, based upon which interval around the maximum should contain the optimum by the bisection or quadratic interpolation methods, and incrementing the value of n by 1 until the step is accepted or the minimum step size is reached, completing termination.

2.4 Results and Discussion

A Paal-Knorr reaction (Scheme 2.1) was used to show the performance of this multi-trajectory automated optimization platform within the constraints 30 °C $\leq T \leq$ 130 °C and 2 min $\leq \tau \leq$ 30 min on the trajectory points and DoE center points. This maximum temperature was set for the reaction due to the use of a polycarbonate reactor cover. As polycarbonate has a glass transition temperature of 150 °C, a maximum temperature limit was set slightly lower. Along the

same lines, a minimum residence time of 2 minutes was set because a faster pumping rate would cause the system pressure drop to exceed the capabilities of the Harvard syringe pumps. As the overall goal was not simply to show what conditions led to maximizing the objective function, but a total methodology for performing the optimization, constraint handling was deemed relevant, since no real parameter space is without limit. However, as it was possible to replace the polycarbonate cap with pyrex, a further optimization was run to investigate higher temperatures where decomposition and vaporization became issues.

Results for the optimization of the objective function (Eq. 2.1) with constant step-size trajectories for the steepest descent and conjugate gradient methods can be seen in Figure 2.3 (a) and (b), respectively. Additionally, results from the combination of the conjugate gradient and the Armijo algorithms can be seen in Figure 2.3 (c). In each figure, values of the objective function are given by the color bar at right, control variable boundaries are denoted by dashed red lines, initial conditions are boxed in black at the bottom left, optimal conditions are boxed in red at the top left, and the initial DoE of each trajectory is numbered. Full tables of conditions, conversion, and objective function values are given in Appendix A, in additional to the model used to provide the plot contours. The initial conditions of 40 °C and 10 minutes residence time can be seen in the box at the lower left in the figures. Both search-direction algorithms initially moved rapidly toward increasing residence time at low temperature. The steepest descent method begins to zig-zag (Figure 2.3 (a)), moving slowly upwards in temperature with large changes in residence time in a low-efficiency manner that is typical of this algorithm type when moving along ridges.[27] This behavior becomes worse in trajectories 4 through 9 as the sides of the ridge in the objective function become steeper, forcing the trajectories to take only a few steps before moving off the plateau and terminating. Only by happening to have a point near the very center of the plateau at a particular temperature would the trajectory point enough toward increasing temperature to end this pattern. Trajectory 5 nearly accomplished this, but the large number of points beyond the optimum indicates that the objective decreased slightly beyond it, but stayed within 95% for several points before terminating. Had this trajectory been slightly more in the positive temperature direction, as in trajectory 10, it would have significantly decreased the total number of experiments.

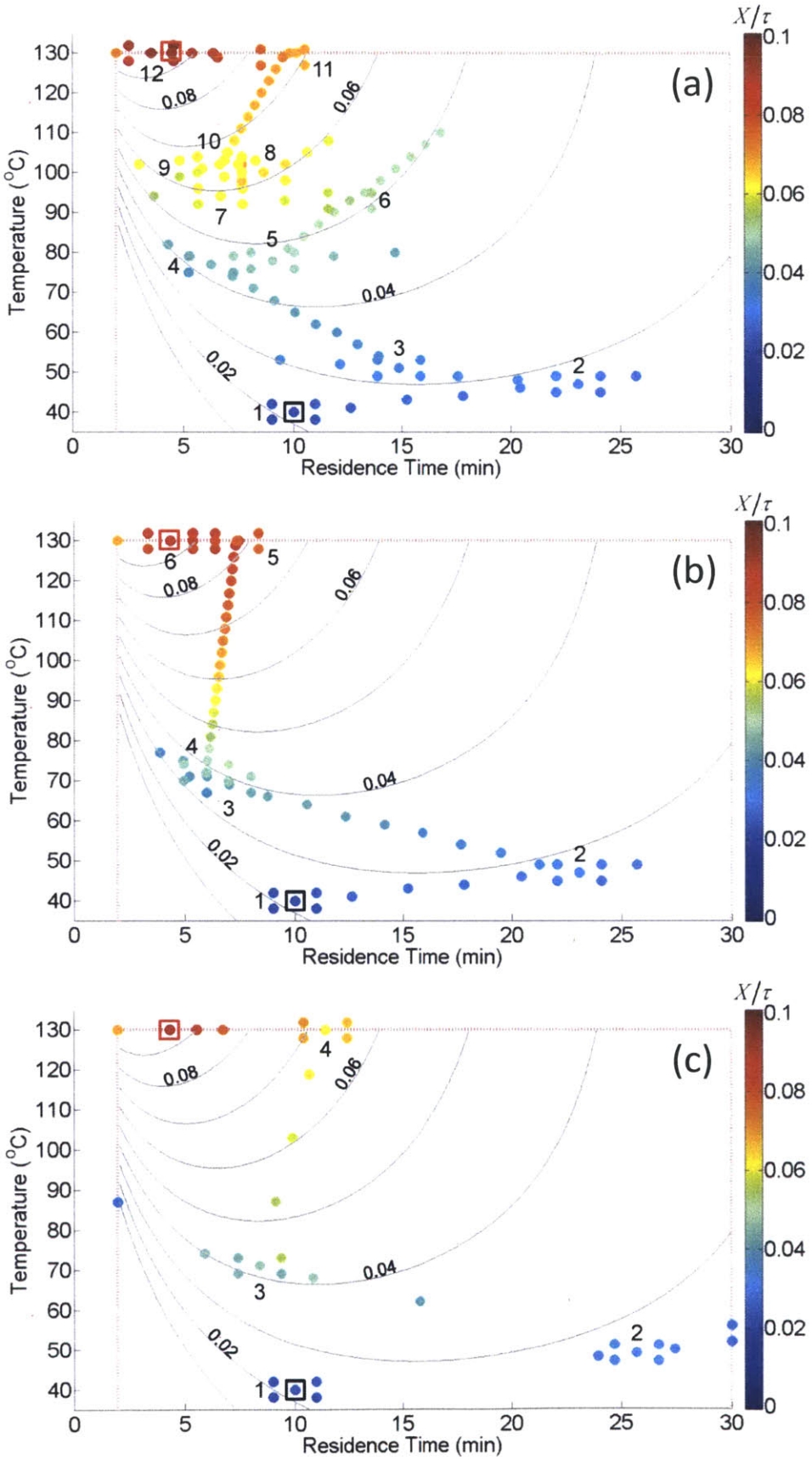

Figure 2.3. Maximization of the production rate of the Paal-Knorr reaction with different optimization strategies. Values of the objective function are given by the color bar at right. Control variable boundaries are denoted by dashed red lines. The initial conditions are boxed in black at the bottom left, and the optimum is boxed in red at the top left. The initial DoE of each trajectory is numbered.

(a) Steepest descent method.

(b) Conjugate gradient method.

(c) Armijo conjugate gradient method.

The conjugate gradient algorithm approaches the optimum much more efficiently because the algorithm cannot double back upon itself the way that steepest descent can. In Figure 2.3 (b), trajectory 2 appears to double back, but compared to Figure 2.3 (a), this behavior is much less pronounced. Trajectory 3 is then very short for the same reason, where the gradient of the DoE points largely towards increasing residence time but the algorithm prevents such a large change in the search direction. Trajectory 4 then continues to adjust the search direction, resulting in a search that bypasses the troubles of steepest descent.

The comparison of Figure 2.3 (b) and (c) reveals that further efficiency gains are realized by the implementation of the Armijo line search, which significantly reduces the number of setpoints necessary along the trajectories. Additionally, the ability of the Armijo algorithm to find a better trajectory optimum ensures that the search directions of the conjugate gradient more correctly points toward the design space optimum, resulting in fewer trajectories.

Ultimately, all three algorithms contracted along the upper temperature boundary and reached approximately the same optimum: $T = 130\ ^{\circ}C$ and $\tau = 4.49$ min for steepest descent, $T = 130\ ^{\circ}C$ and $\tau = 4.36$ min for standard conjugate gradient, and $T = 130\ ^{\circ}C$ and $\tau = 4.36$ min for Armijo conjugate gradient. However, the Armijo conjugate gradient method converged at a significantly faster rate, requiring only 38 experimental setpoints (i.e., individual experiments) in 4 trajectories, while the standard conjugate gradient required 75 setpoints in 6 trajectories, still significantly outpacing the steepest descent, which required 126 setpoints in 12 trajectories.

The performances of the algorithms are summarized in Table 2.1 and Figure 2.4. The points toward the end of the plots are the final optimization along the upper temperature constraint. Because the constraints were on the DoE center and trajectory points but not on the DoE factorial points, some of the points in the last 2 DoE runs for each method were beyond the allowed space. Thus, these points run at higher temperatures show higher conversion and thus higher objective function values than the optimum, but were not valid optimal points.

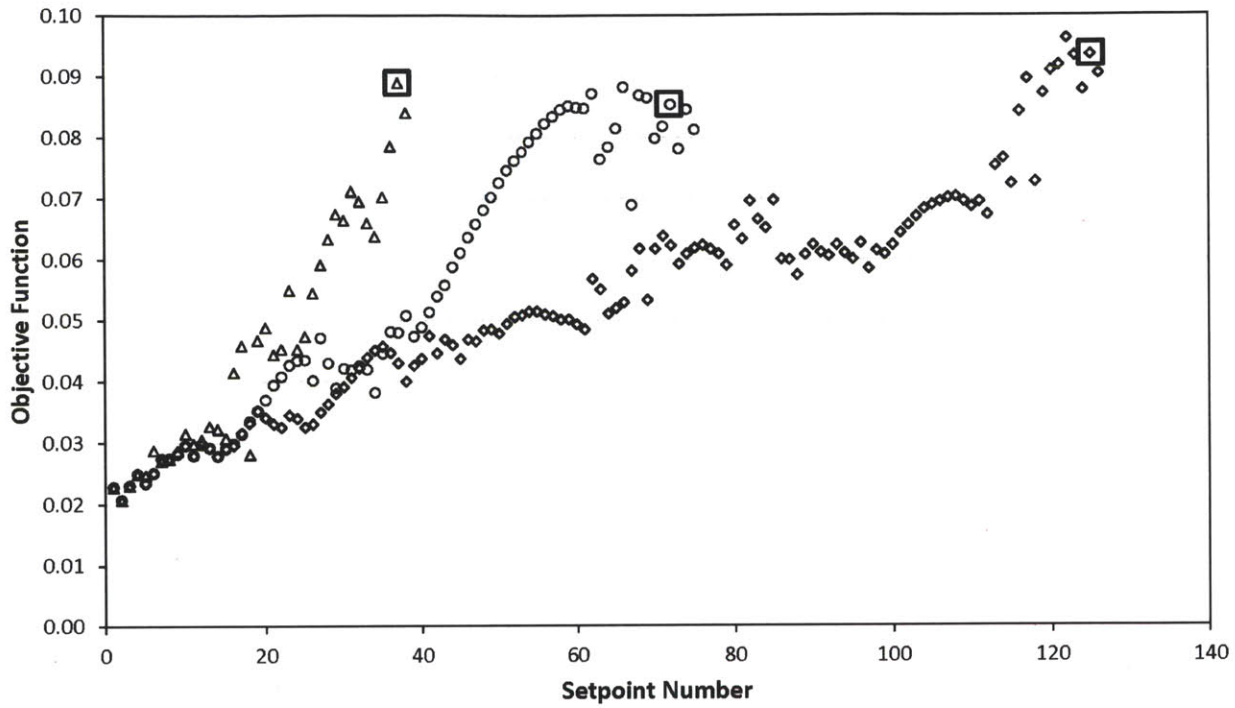

Figure 2.4. Objective function value at each setpoint for steepest descent (◇), conjugate gradient (O), and Armijo conjugate gradient (△).The optimum for each algorithm is boxed.

The above optimizations of production rate resulted, however, in conversions of only approximately 40%. To attempt to find an optimum at a more desirable conversion, another optimization was performed using a new objective function (Eq. 2.5) with a quadratic loss function, a standard method to impose soft inequality constraints, [67] to penalize conversions of less than 85%.

$$\max J_{penalty} = \frac{X}{\tau} - \left(\max\left(0, 0.85 - X^2\right)\right) + 0.85^2 \tag{2.5}$$

Table 2.1. Summary of optimization algorithm performance.

Method	Number of Trajectories	Number of Setpoints	Total Volume (mL)	Optimum				
				T (°C)	τ (min)	X	X/τ	$J_{penalty}$
Steepest Descent	12	126	44.6	130	4.49	0.420	0.094	0.632
Conjugate Gradient	6	75	25.2	130	4.36	0.385	0.088	0.594
Armijo Conjugate Gradient	4	38	13.9	130	4.36	0.387	0.089	0.597
Penalized Armijo Conjugate Gradient	2	17	6.5	130	12.36	0.807	0.065	0.786
				130	30.00	0.935	0.031	0.754
Optimization Above 130 °C	4	48	17.0	212	6.00	0.764	0.127	0.843

This optimization, shown in Figure 2.5 was performed using the Armijo conjugate gradient algorithm with the optimum from the previous optimization as the initial conditions and ran along the upper temperature boundary of 130 °C. While during the process of the optimization a maximum conversion of 94% was found, the maximum of the penalized objective function was found to be 0.786 at T = 130 °C and τ = 12.36 min, where the conversion was 81% and X/τ was 0.065. Therefore, there is a large tradeoff between conversion and production rate. Ultimately, an economic analysis on the full process, including separation costs, would be necessary to determine the desired weighting and limits on the two objectives to use for a final optimization.

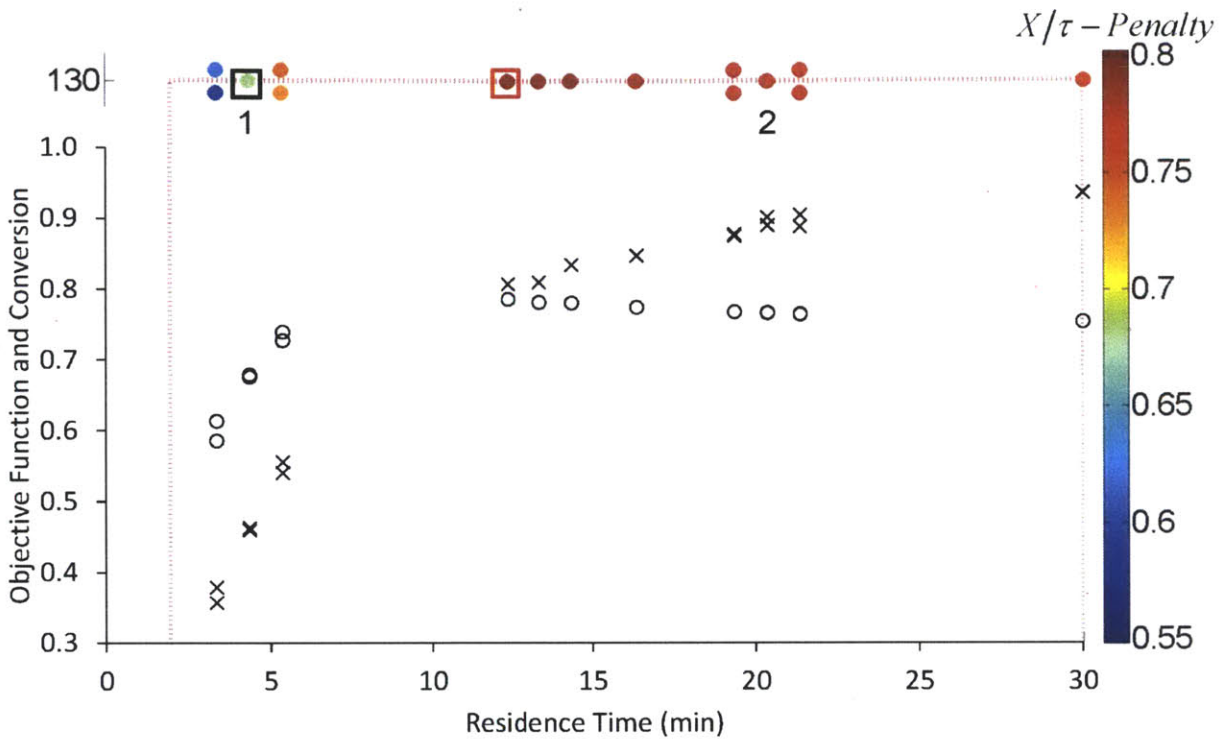

Figure 2.5. Penalized Armijo conjugate gradient method. The conversion (×) and objective function value (O) at each setpoint are shown. Values of the objective function are also given by the color bar at right. Control variable boundaries are denoted by dashed red lines. The initial conditions are boxed in black at the top left, and the optimum is boxed in red at the top center. The initial DoE of each trajectory is numbered.

As the optimizations performed all found an optimum at which the upper temperature constraint was active, a final optimization was run where the maximum allowable temperature was set only by the ability of the controller to heat the reactor. The results of this optimization utilizing the same penalized objective function with the Armijo conjugate gradient method are given in Figure 2.6, which found an optimum at 212 °C and 6.00 minutes residence time with objective value of 0.843, corresponding to a conversion of 76.4%. Here, 4 trajectories are run with a final DoE around the optimum to confirm that the center point of the DoE has an objective value above that found at the corners. The rapid drop in conversion above 212 °C is due to the vaporization of a large portion of the reaction mixture, causing a transition to annular flow with significantly reduced residence time. This is further compounded by the partial breakdown of DMSO into significantly lower boiling components. While additional backpressure would allow for the reaction to reach somewhat higher temperatures before boiling, the increased DMSO decomposition limits the utility of this approach.

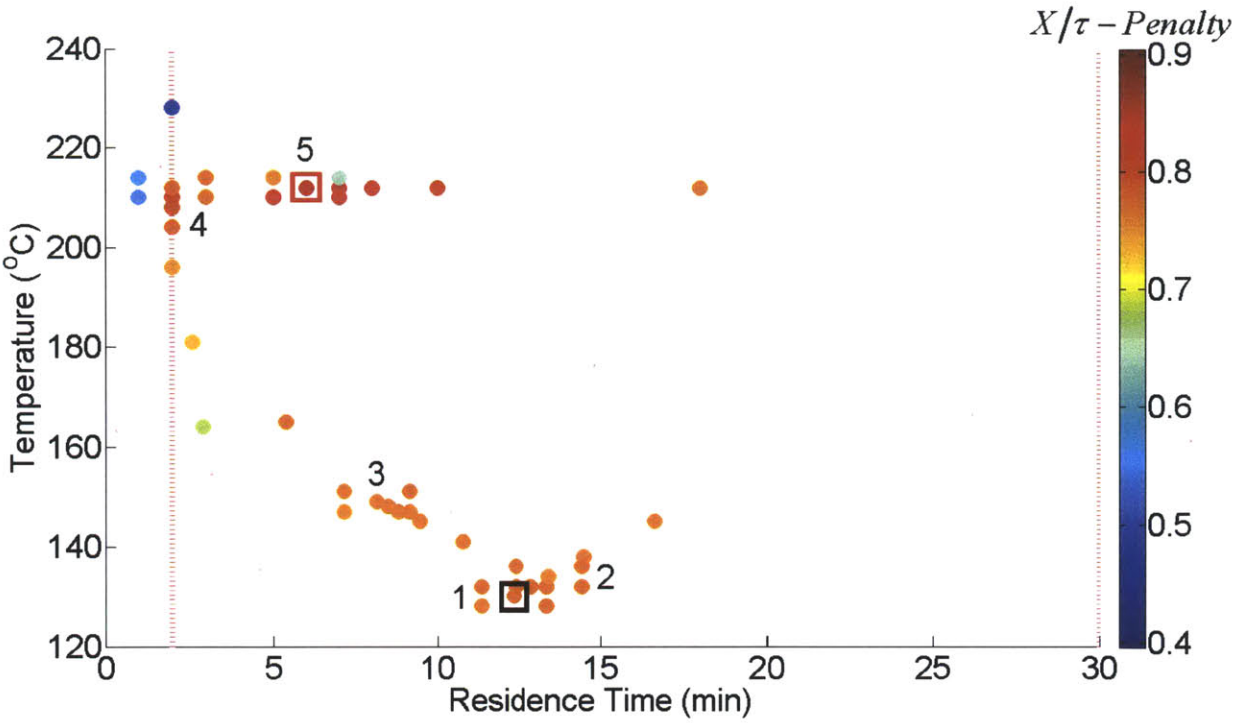

Figure 2.6. Penalized Armijo conjugate gradient method above 130 °C.Values of the objective function are given by the color bar at right. Control variable boundaries are denoted by dashed red lines. The initial conditions are boxed in black at the bottom left, and the optimum is boxed in red at the top left. The initial DoE of each trajectory is numbered.

Reaction stoichiometry was not investigated here, because it would result in a trivial optimization where increasing concentration leads to increased reaction rate, as shown by Nieuwland et al.[59] Comparing these two approaches, their approach contained 58 experiments to model the reaction with a resulting leave-one-out cross-validation value of approximately 70%. Here, the final constrained optimization run required only 38 setpoints to find the optimal production rate and the overall reaction model generated clustered significantly closer to the parity line.

Because this reaction is relatively well understood, it is known from modeling that the objective is convex within the parameter space, so that regardless of initial conditions, the same optimum will be found. The same initial conditions were used for each search technique to aid in the ability to distinguish their performances. However, for more complex systems, multiple initial conditions may be necessary to test if there are multiple local optima. While global optimization techniques do exist, they tend to require significantly more evaluations of the

objective, and therefore experiments, than local search techniques, while still being unable to guarantee that a true global optimum is found.

The above examples demonstrate that the automated system and algorithms can efficiently optimize a range of objectives in a reaction system, including those that offer more complex terrains. The platform is able to perform several sequential experiments with minimal operator intervention. Thus, by intelligently choosing experimental conditions, controlling and monitoring reaction temperature and residence time, and analyzing reactor effluent concentration, not only does the automated microsystem save significant reagents during the optimizations, but also produces significant time savings for the experimenter.

2.5 CONCLUSIONS

An automated microreactor system combined with continuous online IR analysis has enabled evaluation of multi-trajectory optimization strategies for maximizing the production rate of a Paal-Knorr reaction example. The conjugate gradient algorithm was significantly more efficient than the steepest descent method due to the shape of the objective function. Additionally, the incorporation of an Armijo-type line-search algorithm further increased the optimization efficiency. The use of continuous online analysis allowed several measurements of reactor effluent concentrations within a short time, ensuring that each experiment had reached steady state within a set degree of error before moving on to the next set of conditions, allowing for dynamic experiment duration. Thus, each experiment was only as long as necessary, which, paired with a microreaction system, minimized reagent consumption and further increased system efficiency. Similar techniques could be envisioned for the optimization of more complex reaction systems or those with multiple unit operations, which could incorporate continuous inline IR to non-destructively analyze the output of each step. As there were no significant side reactions, selectivity and impurity profile could not be investigated in this study. However, investigating such aims for other reactions would again simply require interchanging the appropriate objective function to take into account the concentration of one or more side products and to penalize for their formation.

3 "BATCH" KINETICS IN FLOW IN A MICROREACTOR SYSTEM USING ONLINE IR ANALYSIS AND CONTINUOUS CONTROL

3.1 INTRODUCTION

The current paradigm for generating kinetic data can be broken down into either sampling steady-state conditions in flow or generating time-course data in batch,[69] which have proven particularly useful in identifying complex kinetic mechanisms.[70] Unfortunately, both of these techniques have significant limitations. While continuous flow experiments, especially in microreactors, have advantages over batch in terms of mixing times,[2, 13] temperature control,[1, 3] materials savings,[7] and the ability to perform sequential experiments without intermediate cleaning steps, batch experiments are seen as better suited to generating kinetic data due to the ability to collect data from many time points in a single experiment.[70] However, with continuous online measurement, it is possible to obtain such time-course data from flow experiments by continuously controlling flow rate in a low-dispersion reactor.[10] This analysis is possible because, under ideal conditions, a batch reactor and a plug-flow reactor have the same kinetics performance equation; *i.e.*, they will have the exact same conversion as a function of conditions and time for any reaction, as time in the batch reactor corresponds to residence time in the plug flow reactor.[69] These reactors are typically treated differently only due to deviations from ideality, such as concentration or temperature gradients or imperfect mixing.

A recent contribution by Mozharov *et al.* presented a method to take advantage of the ideality of microreactors to derive time-course data *via* flow manipulation.[71] In their method, a Knoevenagel condensation in a microreactor was allowed to come to steady state at a low flow rate. Then a step change in flow rate was performed to rapidly flush the contents of the reactor. As this reactor volume exited, the concentration of the product was measured with an inline Raman probe. While this enabled generation of a conversion curve in agreement with steady-state experiments, the exact reaction times during this flow rate step change could not be known because the step change was not actually instantaneous, requiring graphical and empirical estimation of reaction times.

The method developed here involves allowing a microreactor system to come to steady state at short residence time, which significantly reduces the initial waiting period before flow manipulation can begin. Uncertainty in accurate determination of residence time is avoided through a controlled ramp rather than a step change in flow rate. This enables the rate of the change in residence time to be set, allowing control over the trade-off between more experimental data and experiment duration. The efficacy of this new technique was demonstrated using a Paal-Knorr reaction of 2,5-hexanedione (**1**) and ethanolamine (**2**) in dimethyl sulfoxide (DMSO) (Scheme 2.1)[52, 53] in an automated flow platform previously detailed,[72] which used an inline Mettler Toledo ReactIR ATR-FTIR flow cell[48] to continuously monitor the effluent from a silicon microreactor.

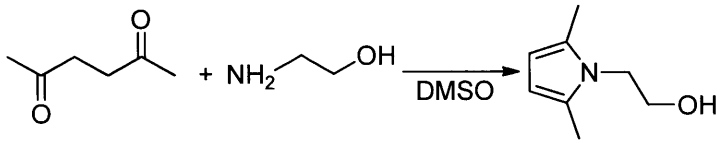

1 2 3

Scheme 3.1. Paal-Knorr reaction.[60, 61]

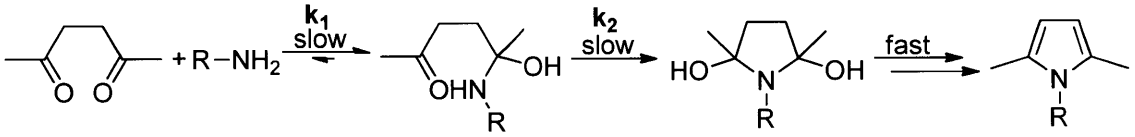

Scheme 3.2. Paal-Knorr reaction mechanism.[53, 56, 62]

3.2 EXPERIMENTAL SECTION

The microfluidic system used in this work is depicted in Figure 3.1, including a schematic of the silicon microreactor. Two Harvard syringe pumps (PHD 2000) were used to control the residence time. The flow rates were updated each second *via* daisy-chained RS-232 communications to a Dell (Optiplex 960) computer. These syringe pumps were connected to a silicon microreactor [65] with a 120-μL reaction zone and a cooled inlet/outlet zone, the temperature of which was maintained at 22 °C with a recirculating VWR chiller (model 1171MD). The cooled section allowed the reactant streams to mix fully before reaction occurred and thermally quenched the reaction. The temperature of the reaction zone was controlled with an Omega (CN9311) controller and an Omega (CSH-102135/120V) heating cartridge. This

controller was connected by an RS-232 cable to the computer to read the measured reactor temperature and program the temperature setpoint. In addition, due to the high heat transfer coefficient of silicon, the temperature of the reaction zone could be quickly changed between setpoints and the fluid stream rapidly reached the desired temperature in both reaction and quench zones. A Mettler Toledo ReactIR iC 10 outfitted with a DiComp ATR 10-μL flow cell was used for continuous inline monitoring, averaging 30 spectrum scans and saving to an Excel file once every 15 seconds. Labview software (version 8.5.1) on the computer communicated with the syringe pumps and temperature controller and read the IR Excel export files to determine reaction conversion based upon calibrations to peak heights. Matlab scripts (version 2010b) within Labview controlled the reaction temperature setpoints and syringe pump flow rates.

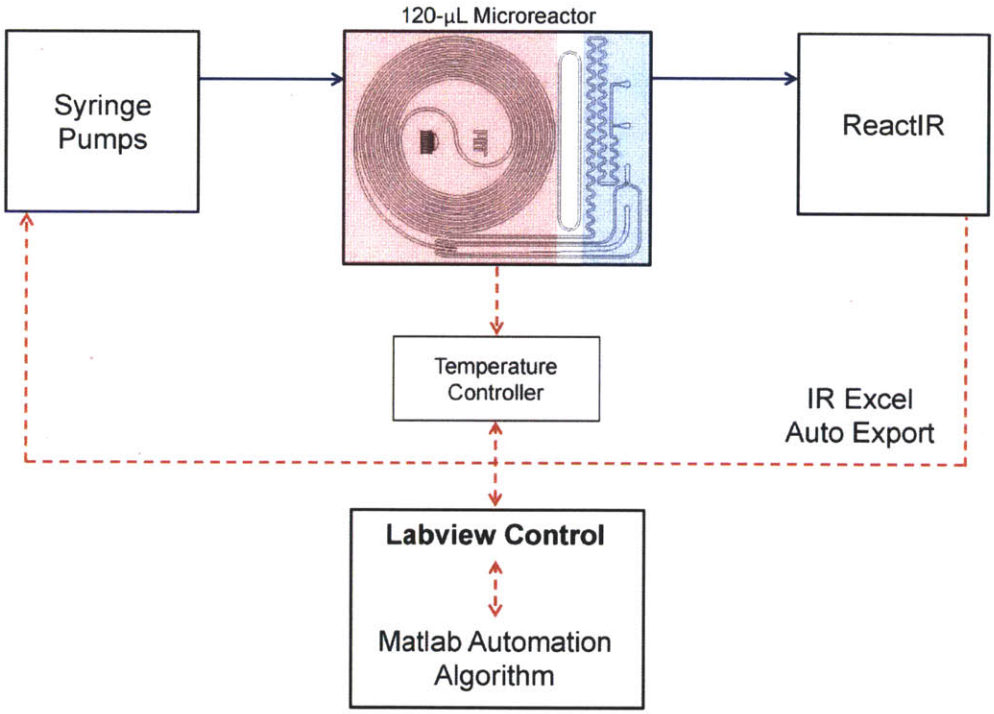

Figure 3.1. Automation system schematic.Solid lines represent fluid flow and dashed lines represent data flow.

3.3 METHOD

Under conditions of low dispersion, which are easily achieved with the narrow widths of microreactor channels,[10] a flow reactor may be treated as a series of batch reactors (Figure 3.2). This treatment allows well-controlled system transients to be used to generate kinetic

information much more rapidly than with traditional flow experiments, as long as the history of each fluid element is known when it exits the reactor.

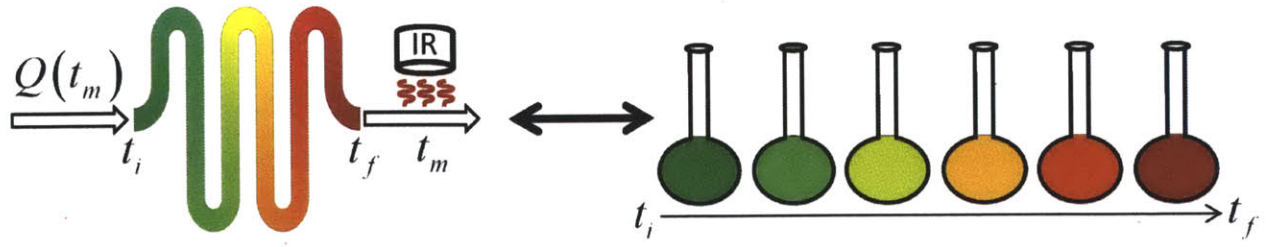

Figure 3.2. Treatment of a low-dispersion flow reactor as a series of well-mixed batch reactors. Color represents extent of conversion from low (green) to high (red).

The method used to generate this time profile is to initially set the flow system of volume V_r at a short residence time, τ_0. After this system has reached steady state, the residence time is gradually increased at a constant rate α times the experiment time, t, by reducing the flow rate, Q, in a controlled manner such that the system instantaneous residence time, τ_{ins}, is always known.

$$\tau_{ins} = \tau_0 + \alpha t = \frac{V_r}{Q(t)} \tag{3.1}$$

Each "pseudo-batch" reactor passes through the reactor in a time τ from initial time, t_i, to final time, t_f, which are unique for each fluid element.

$$\tau = t_f - t_i \tag{3.2}$$

$$V_r = \int_{t_i}^{t_f} Q(t)\,dt = \int_{t_i}^{t_f} \frac{V_r}{\tau_0 + \alpha t}\,dt \tag{3.3}$$

Solving the integral then yields the residence time each fluid element spends in the reactor as a function of when it exits the reactor,

$$\tau = \left(1 - e^{-\alpha}\right)\left(t_f + \frac{\tau_0}{\alpha}\right) \tag{3.4}$$

which can be rewritten as the linear residence time ramp

$$\tau = \frac{S}{\alpha}\tau_0 + St_f \tag{3.5}$$

by defining S as the slope of τ versus t_f:

$$S = \left(1 - e^{-\alpha}\right) \tag{3.6}$$

An example of the resulting residence time profile is given in Figure 3.3, which shows how the residence time is initially at τ_0 until time 0, at which point the residence time approaches the expected behavior from Eq 3.5. The segment of the residence time which does not agree with Eq. 3.5 is due to the single reactor volume as the flow manipulation begins. The residence time profile of this segment can be found by solving

$$V_r = \int_{t_i}^{0} \frac{V_r}{\tau_0} dt + \int_{0}^{t_f} \frac{V_r}{\tau_0 + \alpha t} dt \tag{3.7}$$

Full derivations are provided in Appendix B.

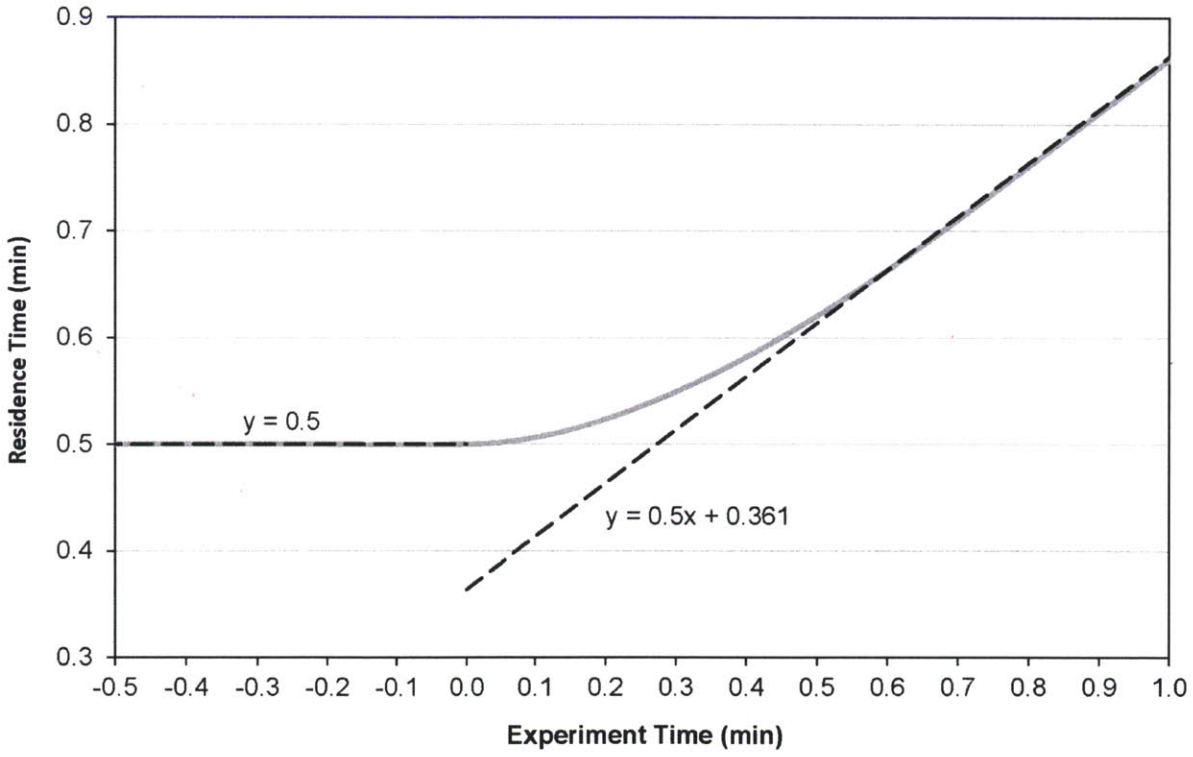

Figure 3.3. Example residence time, τ, vs. experiment time, t_f, with $\tau_0 = 0.5$ min, $S = 0.5$, and $\alpha = 0.693$. The gray line shows the residence time, τ, experienced by a fluid element.

This method results in a predictable and accurate residence time profile. Additionally, the reactor effluent can be measured for a longer period to reduce variability and increase data collection. This approach enables a greater sampling rate of the experimentally collected conversion data (Figure 3.4) with a data density 10-fold higher than previously reported by Mozharov *et al.*,[71] reducing the error of estimated kinetic parameters. Moreover, if a low value of S is used, the data density can be further increased, allowing generation of time-course data that cannot be captured in batch systems due to reaction kinetics that result in complete conversion too quickly for conventional *in situ* analysis techniques. However, this approach would require analysis of more reactor volumes (Figure 3.5).

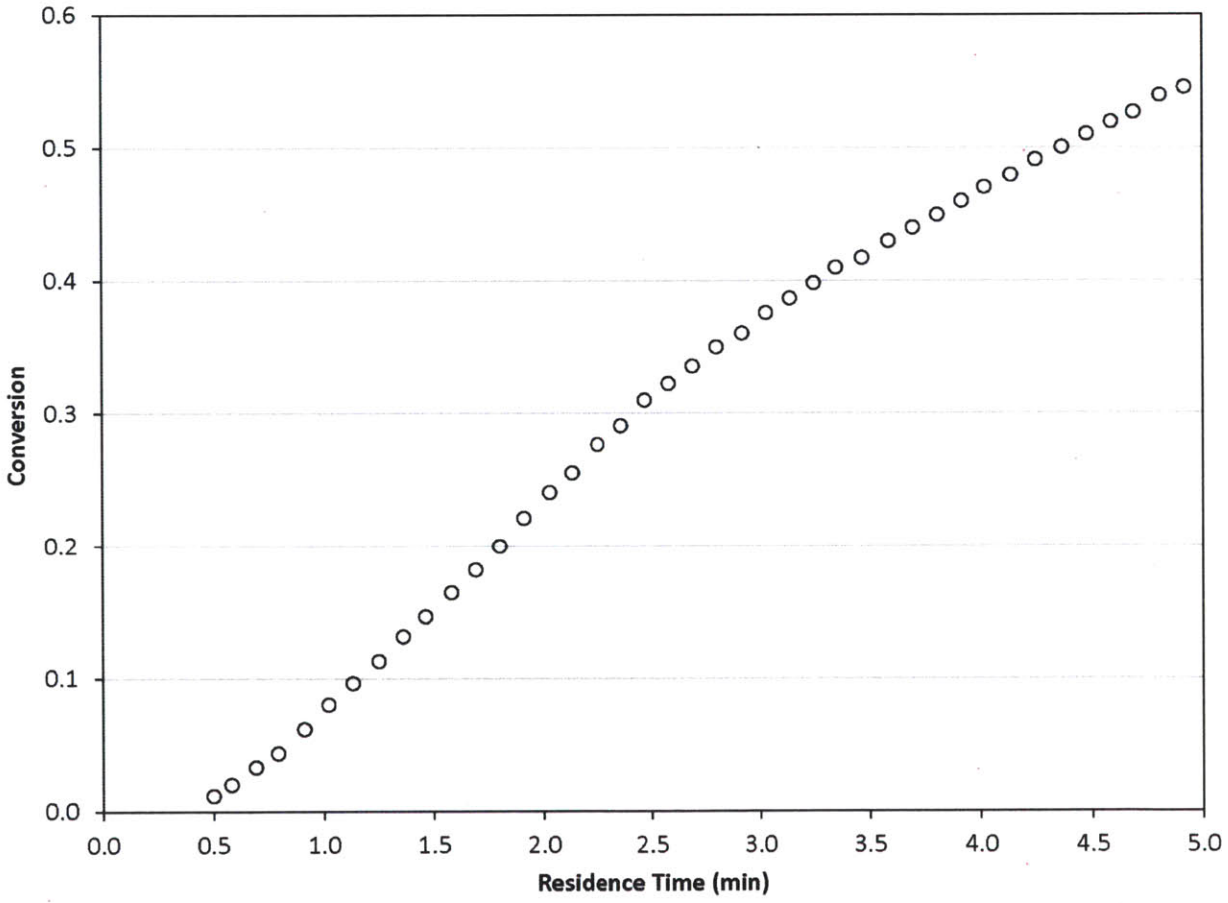

Figure 3.4. Conversion data collected from a residence time ramp experiment with $S = 0.5$ and an IR sample collection frequency of 15 seconds.

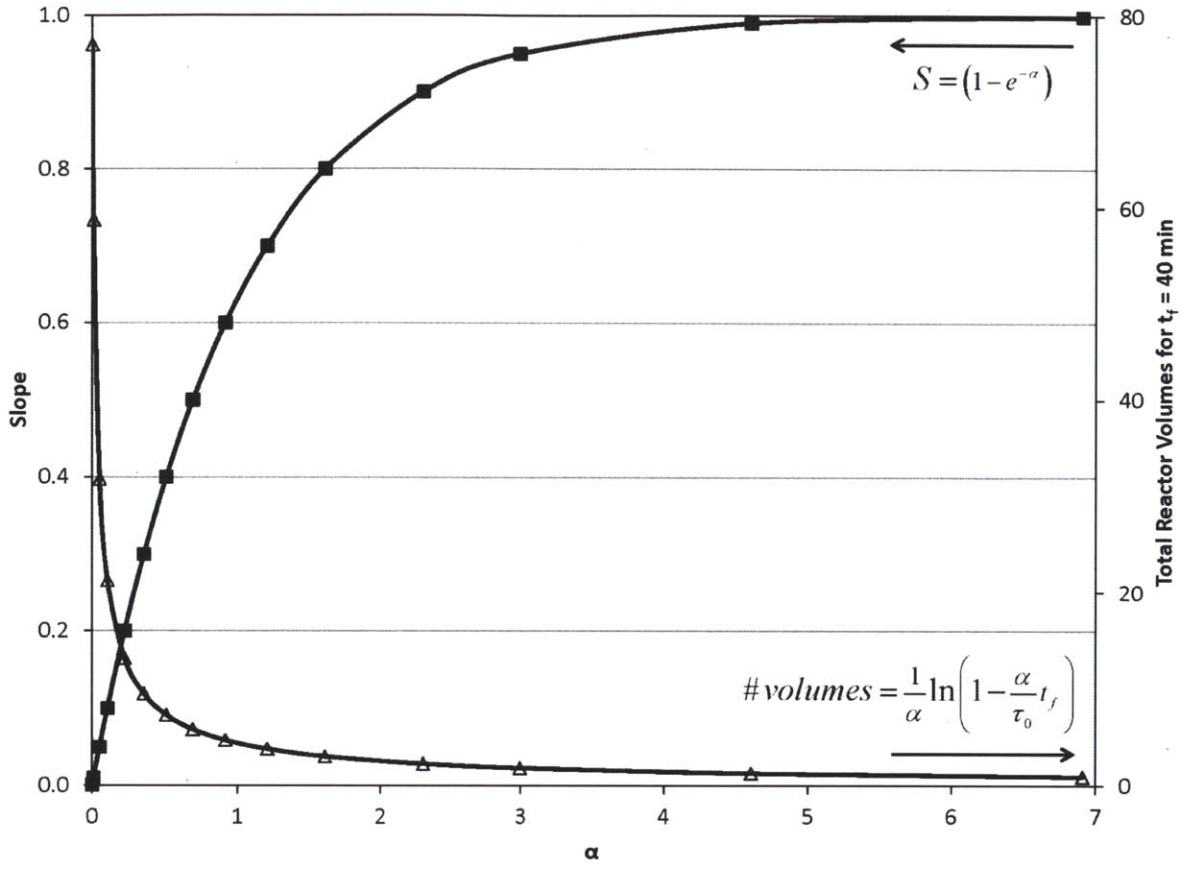

Figure 3.5. S (■) and reactor volumes for t_f = 40 min (△) as a function of α, the rate of change of instantaneous residence time.

3.4 Results and Discussion

3.4.1 Method Validation

This linear residence time ramp method was first tested at 130 °C with several values of S, and the results were compared to data generated by traditional steady state experiments, as shown in Figure 3.6. As the figure shows, while the residence time profile results follow the same trend as the steady state values, there is a slight deviation in the product concentration from the steady states that increases as S approaches 1. However, the model described above assumes that the product concentration is measured exactly at the end of the reaction zone. This is not actually true in the experimental setup – there is a small dead volume between the end of the reaction zone and the inline IR flow cell due to the silicon reactor's thermal quench zone, the

reactor's cooling chuck, and the tubing connecting the reactor to the IR flow cell. The model can be corrected for this dead volume as follows.

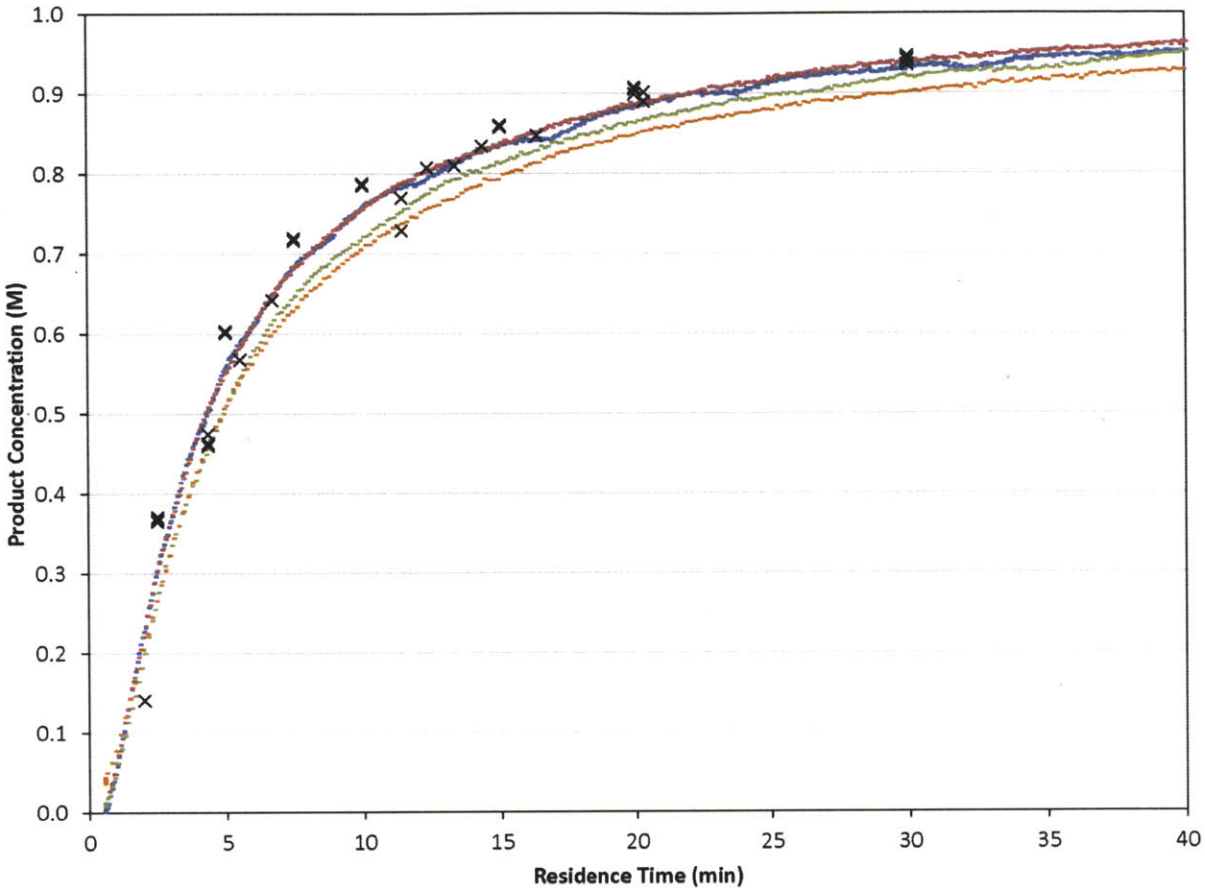

Figure 3.6. Residence time ramp results with $S = 1/4$ (blue), $S = 1/3$ (red), $S = 1/2$ (green), and $S = 2/3$ (orange). Steady states (✕).

Equation 3.3 can be reintegrated for the dead volume, V_d, to determine the time difference between when a fluid element exits the reaction zone and when the concentration is actually measured, t_m.

$$V_d = \int_{t_f}^{t_m} \frac{V_r}{\tau_0 + \alpha t} dt \tag{3.8}$$

Solving for t_m in terms of t_f gives

$$t_m = e^{\frac{V_d}{V_r}\alpha} t_f + \left(e^{\frac{V_d}{V_r}\alpha} - 1 \right) \frac{\tau_0}{\alpha} \tag{3.9}$$

Substituting the relationship between t_f and τ from Eq. 3.5 then yields the residence time profile as a function of t_m:

$$\tau = Se^{-\frac{V_d}{V_r}\alpha}\left(t_m + \frac{\tau_0}{\alpha}\right) \tag{3.10}$$

The residence time profile results from Figure 3.6 can now be plotted as a function of this residence time, as is shown in Figure 3.7. As can be seen, the product concentrations for each residence time profile are now in better agreement, both with each other for different values of S and with the steady state concentration results.

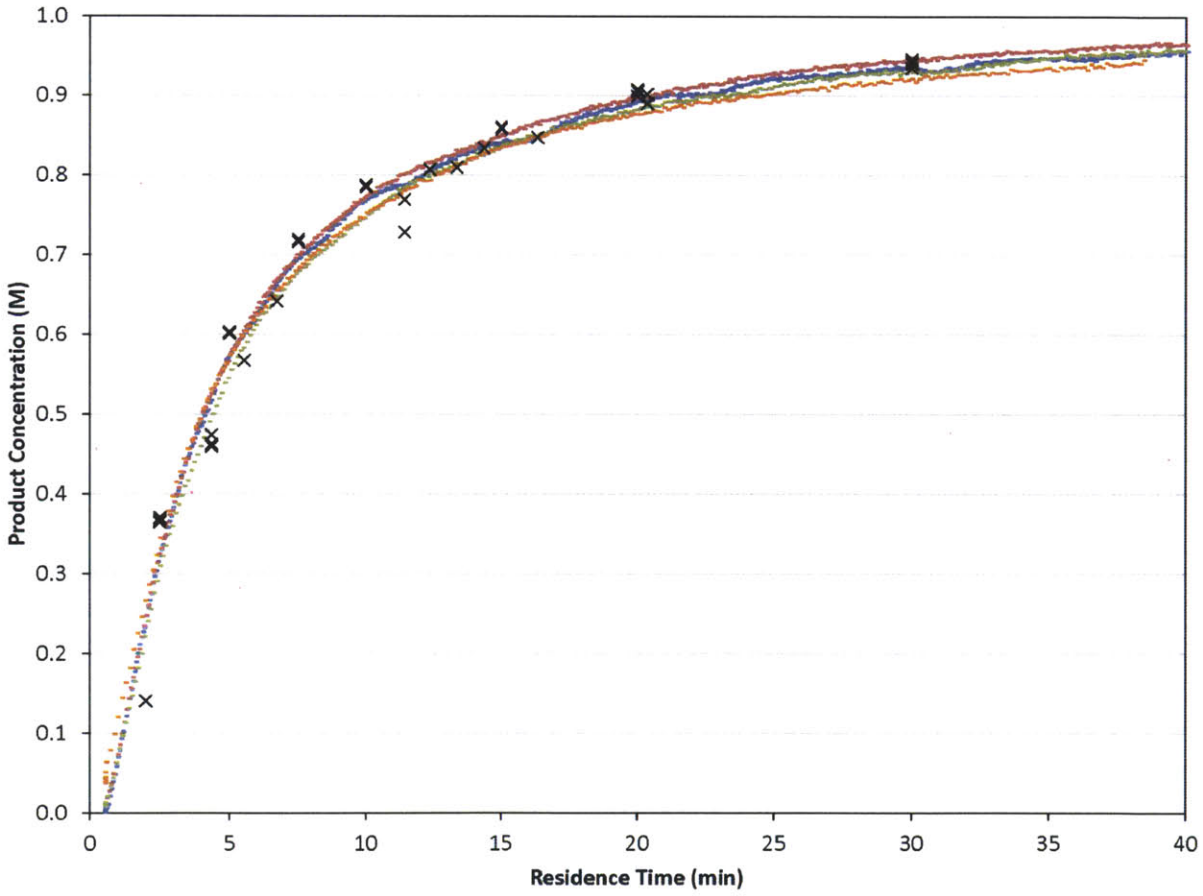

Figure 3.7. Residence time ramp results using corrected residence time with $S = 1/4$ (blue), $S = 1/3$ (red), $S = 1/2$ (green), and $S = 2/3$ (orange). Steady states (×).

3.4.2 *Kinetics Analysis*

With the continuous residence time ramp validated, the method was then used to generate conversion profiles at several temperatures. This data was then used to fit a kinetic model (based upon Scheme 3.2), in which a second-order reaction between the starting materials forms an intermediate that then undergoes first-order conversion, followed by rapid conversion to the product. The reverse reaction in the first step is assumed to be significantly slower, thus having a small effect on the overall reaction rate. The automated platform was used to run the reaction conditions shown in Figure 3.8, in which once the temperature had equilibrated at a setpoint and the residence time had equilibrated at τ_0, the residence time ramp ran for 70 minutes. The temperature setpoint then was changed to the next set of conditions, and the process repeated. The duration was set at 70 minutes by adding 10 minutes to the time that would be necessary for t_f to reach 40 minutes, allowing the residence time ramp to cover nearly the full range of reaction conversions, with additional time for the reactor effluent to reach the IR flow cell.

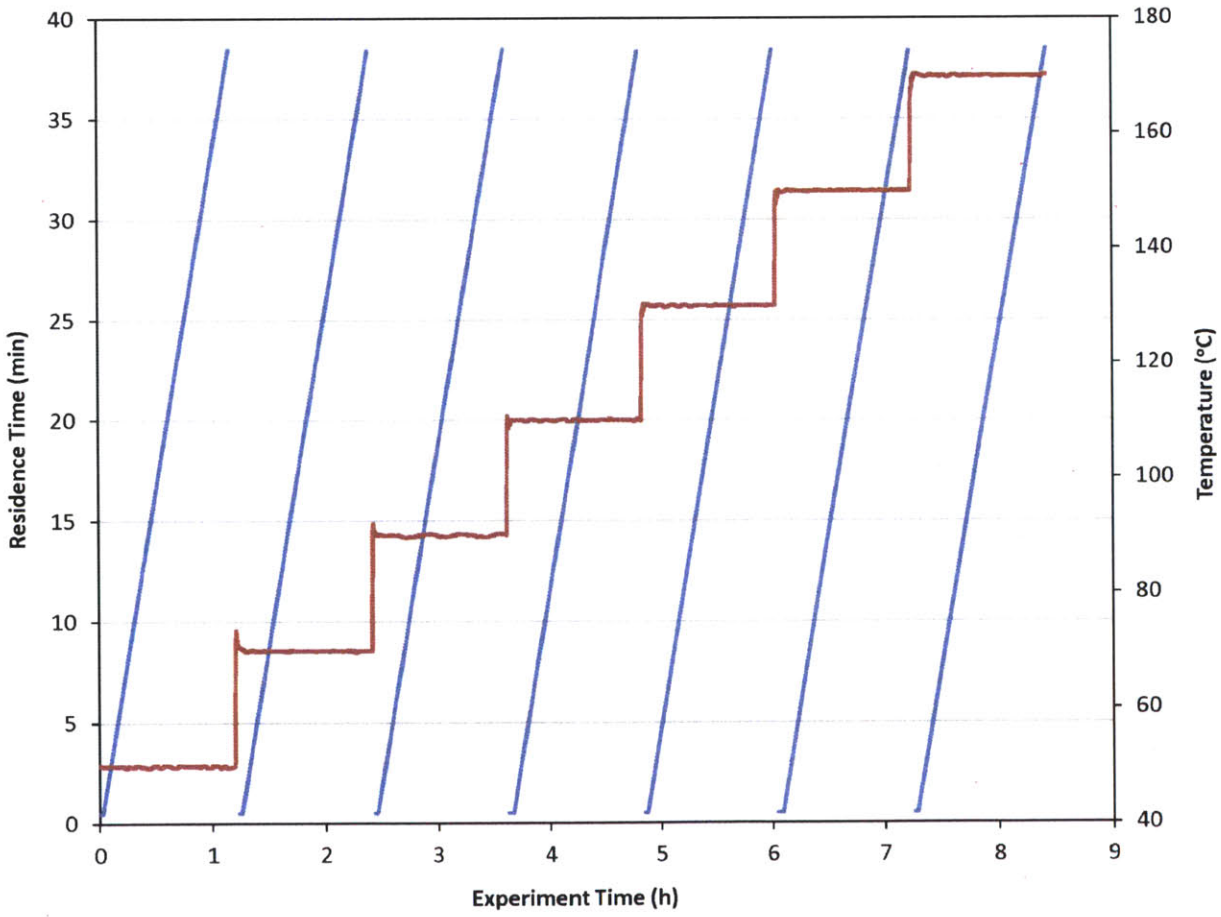

Figure 3.8. Residence time (blue), setpoint temperature (green), and actual temperature (red).

The data generated at 15 second sample intervals during the first experiment are shown in Figure 3.9. These product concentration curves are then assigned to their corresponding temperatures, as illustrated in Figure 3.10. Three experimental repeats were performed, and the two kinetic parameters, k_1 and k_2 in Scheme 3.2, were then fit by least-squares regression in Matlab at each temperature using every 20th data point as a test set. The resulting activation energies are given in Table 3.1, where error bars represent one standard error. (See Figure B.1 for the Arrhenius plot.) Using this model, a parity plot for the three experimental repeats using all reaction data as a validation set is given in Figure 3.11. As shown, the data clusters closely to the parity line.

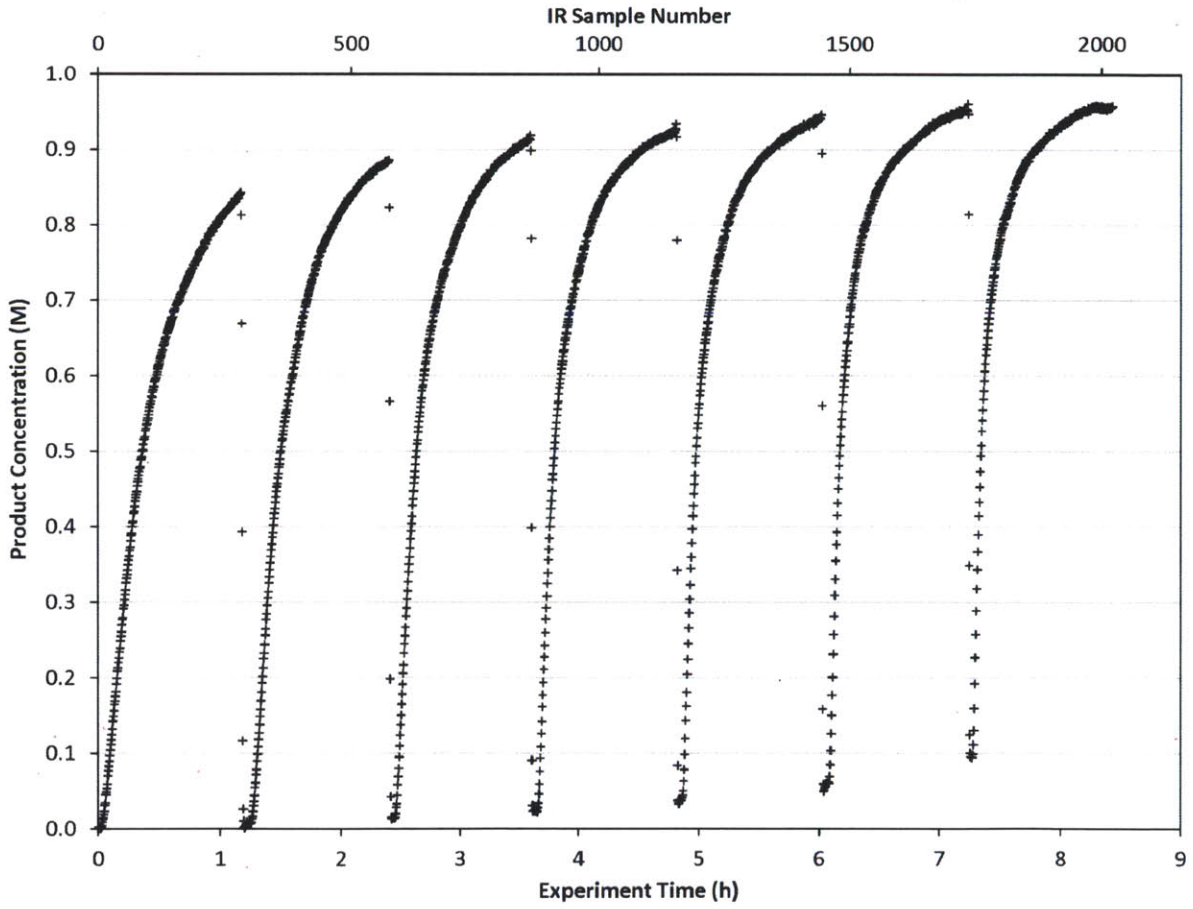

Figure 3.9. Paal-Knorr product concentration found by inline IR analysis at 15 second sample intervals.

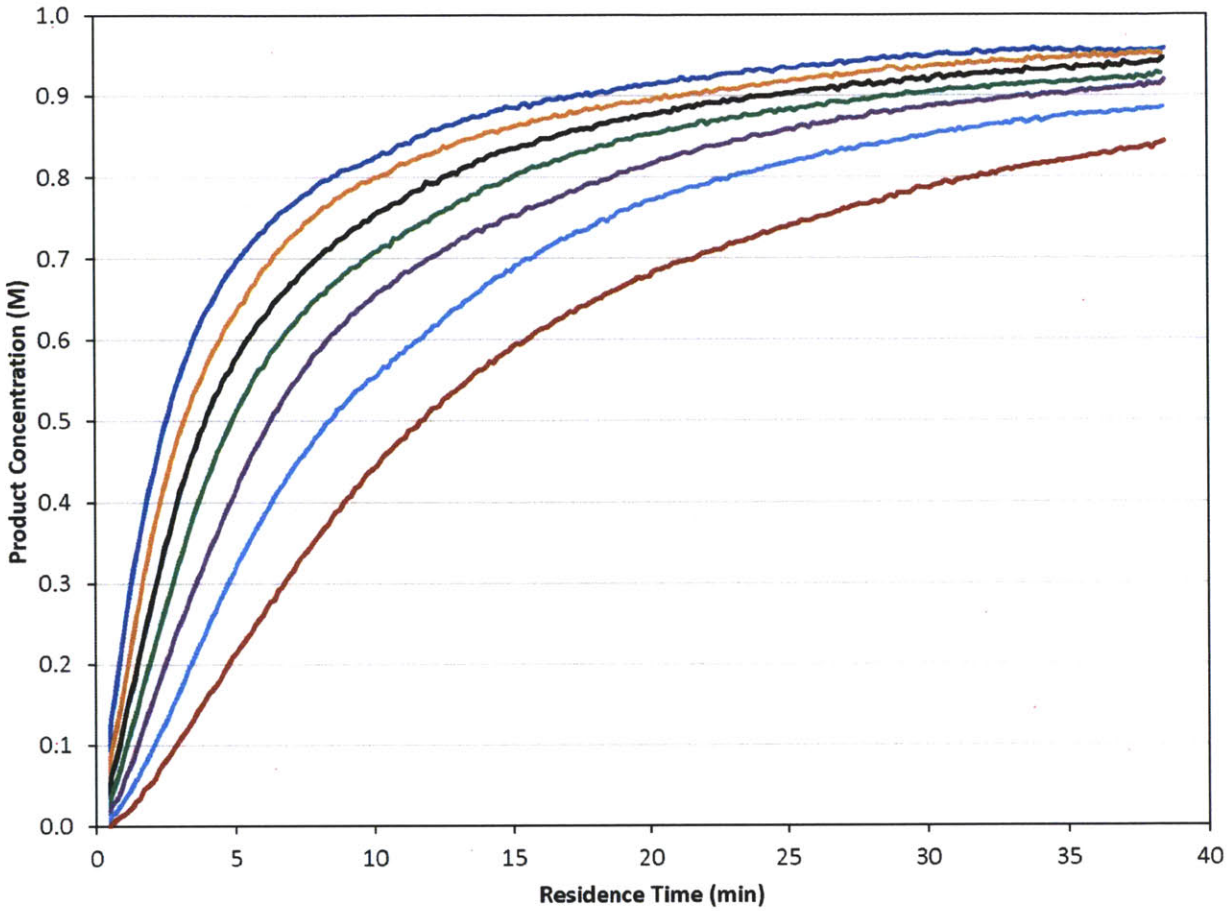

Figure 3.10. Paal-Knorr product concentration as a function of residence time at temperatures (°C) from top to bottom: 170, 150, 130, 110, 90, 70, 50.

Table 3.1. Paal-Knorr activation energies.

Reaction	E_a (kJ/mol)
1	12.2 ± 0.4
2	20.0 ± 0.9

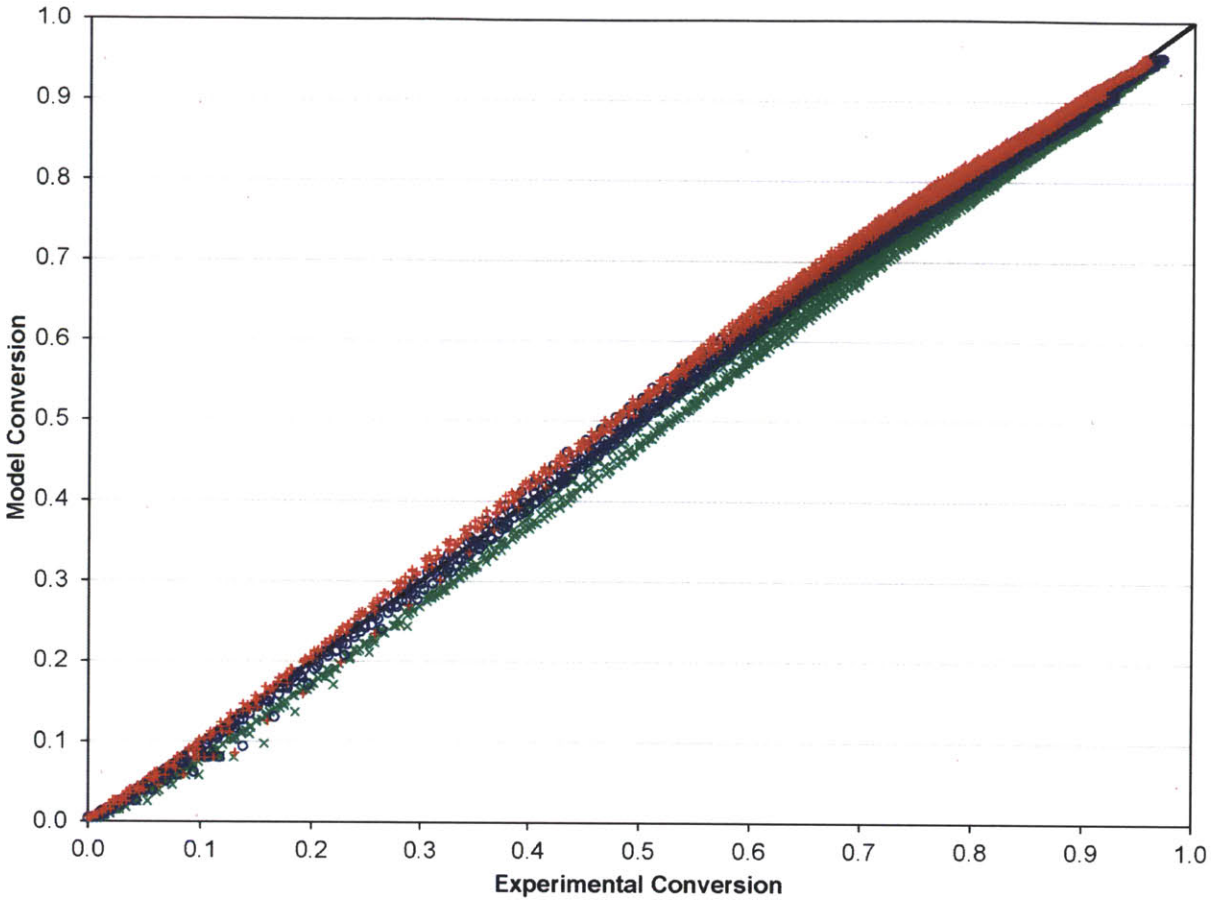

Figure 3.11. Comparison of model and experimental conversion for repeat 1 (×), 2 (○), and 3 (+).

This analysis demonstrates the significantly higher efficiency of this method to generate data for kinetic analysis than traditional steady state techniques. The experiment depicted in Figure 3.8 required approximately 8 hours and 5 mL of each 1 M reactant solution for completion. In contrast, had traditional steady state reactions been performed at each temperature and residence times of 10, 20, 30, and 40 minutes, allowing four residence times for steady state as is typically done,[34] the experiment would have required almost 2 days and 13.5 mL of each reaction solution.

3.5 Conclusions

A method to rapidly generate time-course reaction data from flow reactors has been developed and found to produce data in agreement with traditional steady state flow analysis, showing that there is more overlap between the domains of batch and flow than is generally

assumed. This method was then used in an automated microreactor system, allowing for rapid and tight control of operating conditions, to generate conversion-residence time profiles at several temperatures. The resulting data were used to fit parameters to a kinetic model, which was shown to describe the experimental results well.

4 KINETICS ANALYSIS AND AUTOMATED ONLINE SCREENING OF AMINOCARBONYLATION OF ARYL HALIDES IN FLOW

4.1 INTRODUCTION

The carbonyl group is one of the key building blocks of nature, where it is essential for the construction of proteins, many polymers, and numerous drugs. The ubiquity of these high value products has stimulated a demand for efficient new routes and safe processes to produce this functional group.[73] Palladium-catalyzed carbonylation offers a rapid and modular route for the union of three components (electrophile, CO, and nucleophile) in an atom efficient manner (Scheme 4.1).[74-77] The difficulties in handling toxic and flammable gases like CO within pressure vessels for screening and eventual scale-up have led to the innovative use of alternative CO sources including DMF,[78, 79] aldehydes,[80] and $Mo(CO)_6$.[81, 82] Notwithstanding these advances, the simplicity, cost, and availability of carbon monoxide gas make its continued use inevitable.

To address the control and containment of gases, a number of publications have employed continuous flow technologies due to the intrinsic advantages of the micro-scale, with a small footprint suitable for installation in laboratory fume hoods. Recent advances include *in-situ* generated hydrogen[83-85] and porous membranes[86, 87] for gas delivery, but the most focus has been on slug flow.[85, 88-90]

Herein is reported an automated screening system applicable for gas/liquid reactions in flow. Biphasic systems, especially gas-liquid reactions, are of special interest due to the many variables and difficulties associated with such reactions. In batch systems, expensive and specialized equipment is necessary to cope with the temperatures and pressures required. The use of microreactors in gas-liquid reactions enables facile control over the temperature, pressure, and reaction time.[41] The small size of the reactor permits high temperatures and pressures to be routinely applied,[14, 43] enabling a safe work environment and an expanded reaction space with high reproducibility.

[38] This Matlab driven reaction system automatically collects samples for offline analysis and adjusts reaction conditions, including temperature and reaction time. The system was

effective with both silicon microreactors[65, 66] and packed-bed tubular reactors and successfully used for the carbonylation of aromatic iodides, bromides, and chlorides (Scheme 4.1).

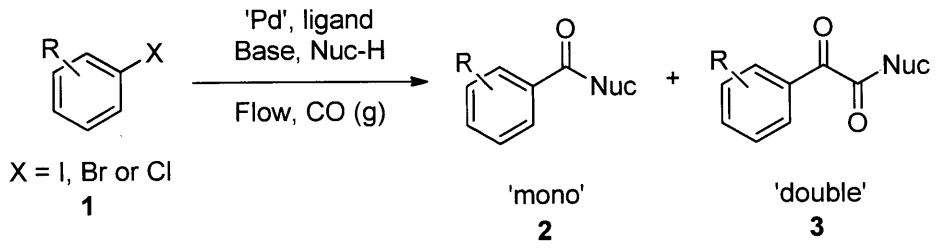

Scheme 4.1. General reaction scheme.

The initial results from these studies were promising in investigating the scope of the carbonylation chemistry, gaining a qualitative understanding of the effects of several parameters on the reaction. Further improvement and more understanding were needed to generate a kinetic model describing the process. This led to focusing on the aminocarbonylation of *p*-bromobenzonitrile with morpholine and the incorporation of inline IR analysis and a continuous temperature ramp to rapidly determine activation energy.

4.2 Experimental Section

4.2.1 System Description

Liquid stream A (aryl halide, base, and internal standard in morpholine) and liquid stream B (catalyst and ligand in toluene) in 8-mL Harvard stainless steel syringes were driven (Harvard Apparatus PhD 2000) and mixed, whereupon they met the gas stream (dispensed using a UNIT mass flow controller) ensuring a 1:1 volumetric liquid-gas ratio (1:1, v:v, l:g) at room temperature for consistency before passing through the reactor.[91] The outflow passed through a six-way valve attached to a 250-μL reagent loop and a Gilson FC 204 fraction collector for sample analysis. The bulk of the reaction stream was collected in a Parr pressure vessel, with the system pressurized by an inert gas (N_2) from a cylinder. A slow bleed vent was also incorporated to dilute the CO and to account for the liquid displacement. The samples from the fraction collector were diluted with acetone and analyzed by GC (Agilent HP 6890), with the results calibrated to the internal standard. The system was controlled through a Matlab (version 2010b) interface allowing automated control of reaction time and temperature and the collection of the reaction aliquot for analysis.

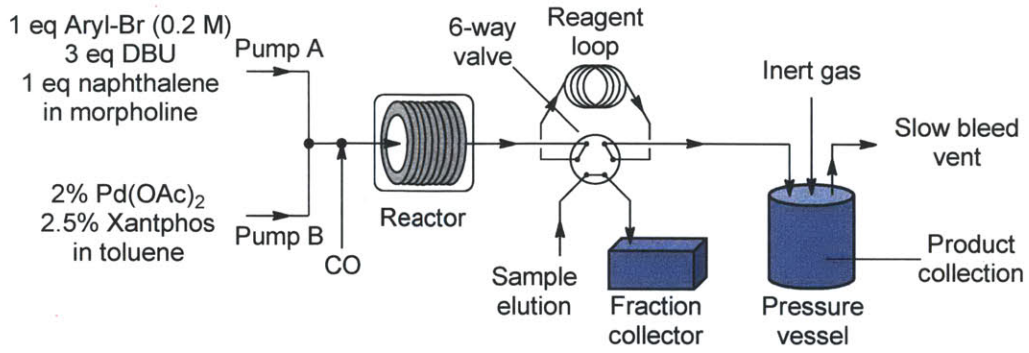

Scheme 4.2. System diagram.

Two reactor systems were used: a 230-μL silicon nitride spiral reactor[65, 66] and a stainless steel tube[92] (Waters HPLC column, 100 mm x 5 mm I.D.) filled with stainless steel spheres (60–125 μm) housed within an aluminum heating block, with a steel nut and approximately 3 cm of steel tubing leading to the entrance (Figure 4.1).

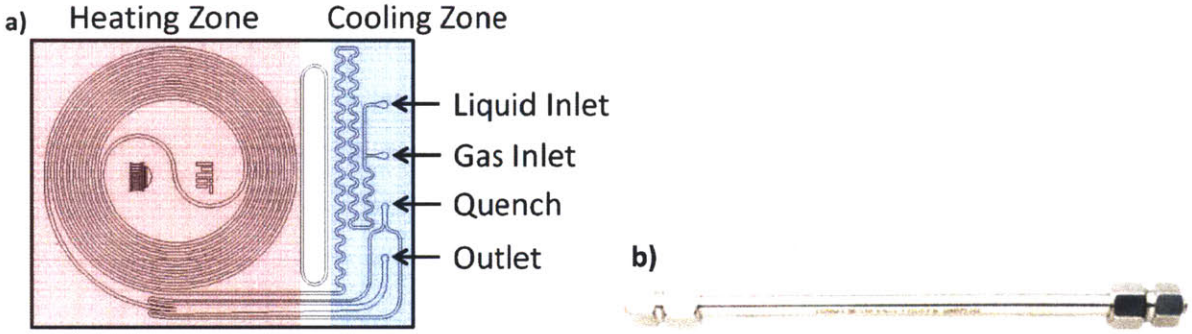

Figure 4.1. Schematics of (a) silicon microreactor and (b) tubular reactor.

4.2.2 ReactIR System

The overall reaction rate with respect to temperature was then further investigated with *in situ* monitoring *via* the ReactIR system from Mettler-Toledo. The Mettler Toledo ReactIR iC10 system consists of a 51-μL flow cell with a diamond window. Mid-range IR is then collected using an attenuated total reflectance (ATR) probe with a penetration depth of approximately 2 μm from several reflections. Advantageously, the system can be used in a biphasic liquid-gas system, due to the preferential wetting of the diamond window by the liquid phase. The first reaction using the ReactIR system revealed that there was no single peak that could be used to easily monitor the formation of the product and consumption of the starting material. In this example both the mono and double products possess characteristic amide stretches that overlap

and the starting material has very few stretches, which would complicate monitoring its disappearance.

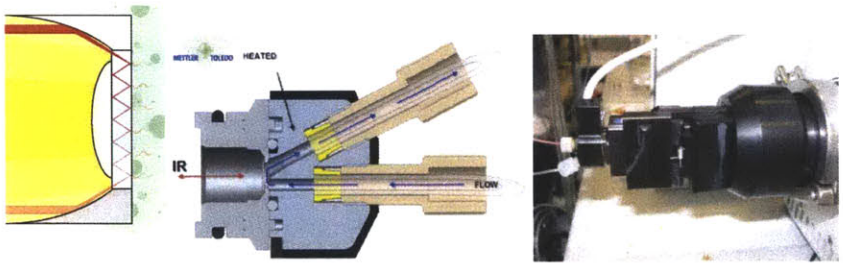

Figure 4.2. Mettler-Todedo ReactIR flow cell.[48]

To this end, the built-in software of the system was used to perform a principal-component least squares regression analysis, which required some initial calibrations to be performed. In this case the individual components (starting material (**1**), mono (**2**), double (**3**), DBU and naphalene) were dissolved in 1:1 v:v toluene:morpholine and measured in the flow cell at different concentrations (0.02, 0.04, 0.06, 0.08, and 0.1 M). The system took 167 scans every minute, averaged them as a time point, and stored the spectrum as an Excel file, which could be easily accessed continuously as the experiment was performed.

4.3 Results and Discussion

4.3.1 para-Bromobenzonitrile

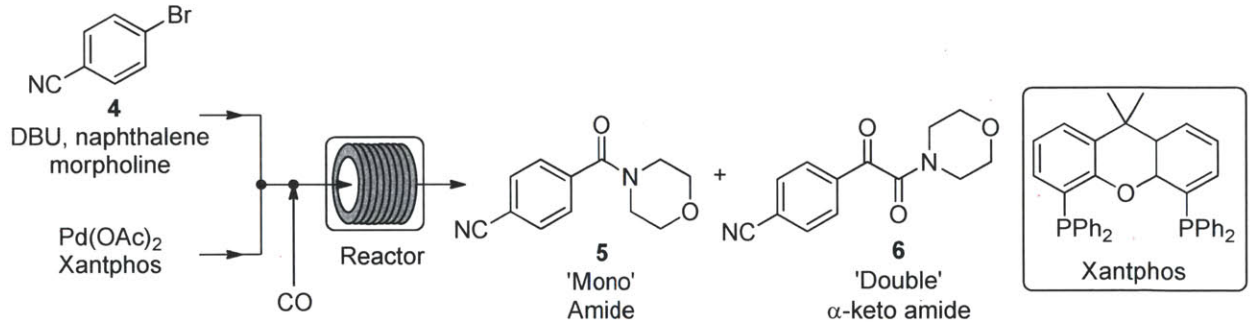

Scheme 4.3. Aminocarbonylation of *para*-bromobenzonitrile in the silicon microreactor.

While numerous single-phase automated screening studies are known, two-phase gas-liquid systems are more complex, and, as a result, there are significantly fewer examples of automated screenings across multiple reaction variables.[40, 93] In this study, the 230-μL silicon nitride spiral reactor and the activated aryl bromide, *para*-bromobenzonitrile were used (Scheme

4.3). A CO pressure of 120 psi, representing a CO gas phase concentration of 0.37 M, and a liquid phase *para*-bromobenzonitrile concentration of 0.1 M with a residence time of 3 minutes (resulting in a CO mass flow rate of 0.96 sccm) could be easily achieved using a mass flow controller. A series of experiments were programmed between 90-160 °C at 5 °C intervals with an equilibrium time of 3.5 residence volumes (3 min x 3.5 = 10.5 minutes) employed between collections to ensure no contamination between experiments (Figure 4.3). The temperature dependence of the product ratio, with the proportion of the double insertion product reduced substantially with respect to the mono product above 130 °C, agreed with prior carbonylation studies.[94-97]

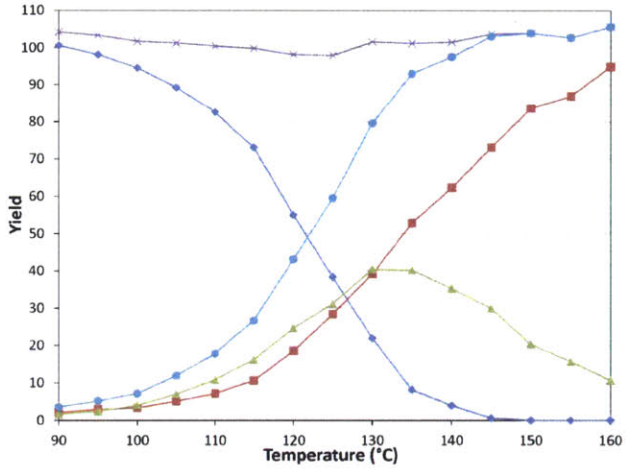

Figure 4.3. Silicon reactor, τ = 3 min, P_{CO} = 120 psi, using 4-bromobenzonitrile. Aryl bromide starting material (◆), mono product (■), double product (▲), total product (●), and mass balance (×).

These results prompted us to evaluate the pressure dependency of the reaction. Continuing with constant 1:1, v:v, l:g, the pressures of 40, 80, 120, and 180 psi were examined, where 40 psi was the lowest reliable flow rate of the mass flow meter and 180 psi was the pressure limit of the syringe pumps. The results (Figure 4.4) demonstrate the expected pattern where decreasing the pressure leads to a higher overall rate and increasing the pressure leads to a higher proportion of the double insertion product.

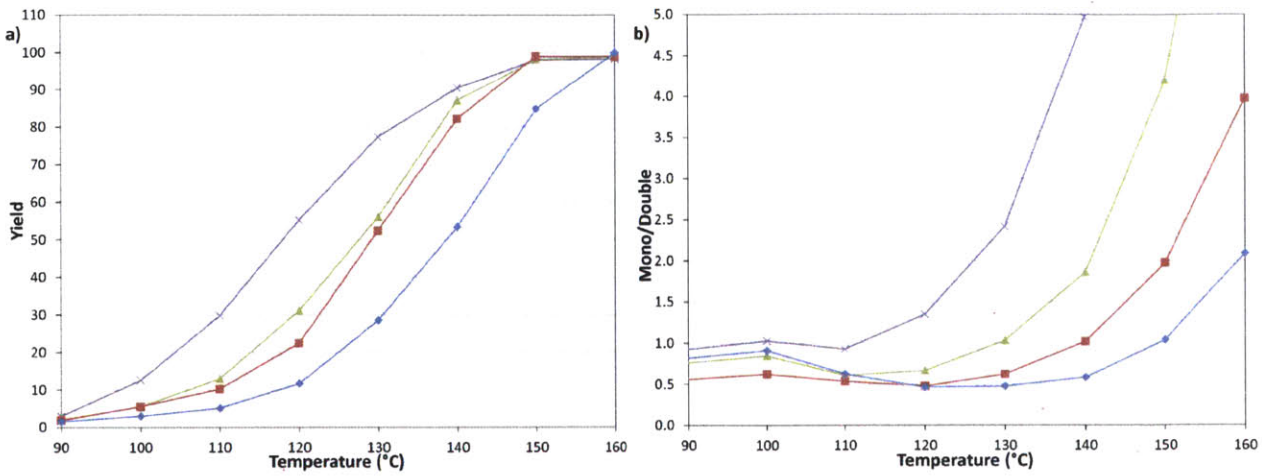

Figure 4.4. Temperature and pressure dependency of (a) yield and (b) selectivity.40 psi (×), 80 psi (▲), 120 psi (■), 180 psi (◆).

Given the fixed 1:1, v:v, l:g proportions throughout these studies, a concern whether mass transfer limitations might influence the observed trends was raised. To this end, reactions were repeated with varying liquid and gas slug lengths. No effect on the product distribution was observed, implying that the mass transfer rate was greater than the intrinsic kinetic reaction rate.

4.3.2 AMINOCARBONYLATIONS

Upon establishing the automated system, the scope of the reaction was examined by varying the electro- and nucleophilic species. The tubular reactor with a residence time of 8.3 minutes and a pressure of 120 psi was used. The six pairs of reactants were chosen to permit some comparison between the different species (Figure 4.5).

Table 4.1. Substrate scope performed in the tubular reactor.

I	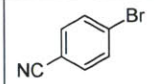	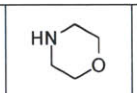	II	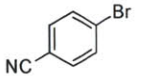	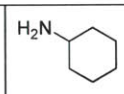	III	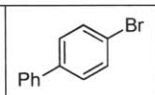	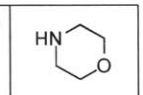
IV	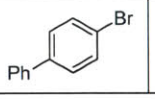	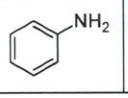	V	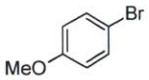	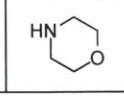	VI	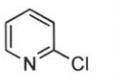	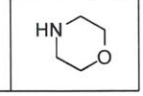

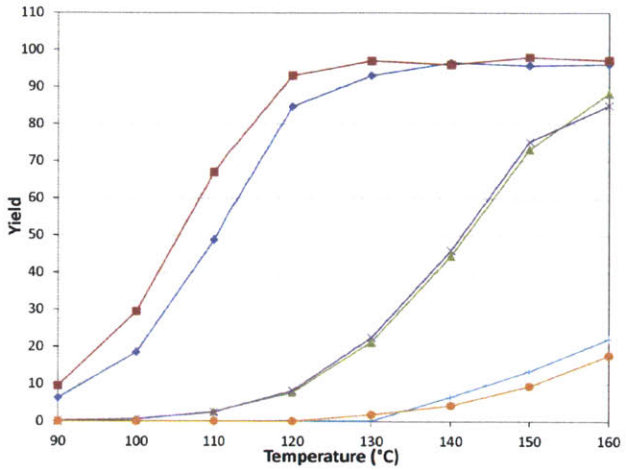

Figure 4.5. Substrate scope examination. Tubular reactor: τ = 8.3 min, P = 120 psi. In reference to the combinations in Table 4.1: I (◆), II (■), III (▲), IV (×), V (+), VI (●).

As expected, electron deficient aryl halides (I and II) proved to be more reactive due to the relative ease of oxidative addition. The change from morpholine to cyclohexylamine did not result in a significant difference of reactivity. The *para*-phenyl examples (III and IV) showed similar reactivity, and the reduced nucleophilicity of the aniline only afforded the mono product. The more deactivated substrates involving *para*-methoxy and 2-chloropyridine[98] (V and VI) proved unreactive until temperatures reached 150 °C.

4.3.3 Aryl Iodides

Expanding the scope of aryl halides, aryl iodides were examined. Both the silicon (τ = 3 min) and tubular reactors (τ = 8.3 min) were used (P_{CO} = 120 and 180 psi) and their results compared (Figure 4.6).

The reaction, as expected, proved to be rapid even at relatively moderate temperatures, resulting in full conversion above 90 °C but with ~2:1 ratio in favor of the α-keto amide double insertion product, compared to the roughly equal proportions of both products but lower conversion for the bromo analogue. As the temperature increased, the proportion of amide increased, dramatically so for the silicon microreactor, leading to nearly sole conversion at 170 °C. As seen earlier, the increase in pressure results in a higher proportion of the double insertion product but only at higher temperatures. The tubular reactor shows an apparent decrease in effect of temperature on selectivity.

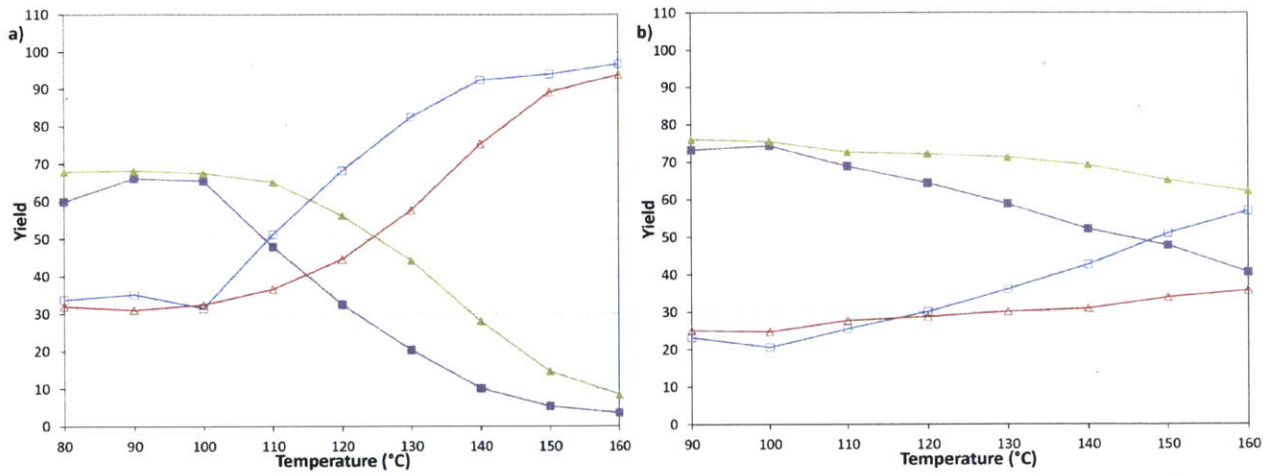

Figure 4.6. *Para*-iodobenzonitrile reaction in (a) silicon microreactor and (b) tubular reactor. Mono product at 120 psi (□), double product at 120 psi (■), mono product at 180 psi (△), double product at 180 psi (▲).

This temperature effect can be ascribed to the difference between the heating zone entrance length of the two reactors. The high thermal conductivity of the silicon microreactor in combination with the thermal isolation through-etch leads to a sharp transition between the actively cooled mixing zone and the heated reaction zone. When the tubular reactor was heated to 120 °C, the steel tubing leading into the reactor was measured to be ~60 °C. This relatively long transition time (on the order of seconds) resulted in a significant amount of premature reaction before the mixture reached the desired temperature and the observed anomalous results. These complications are only expected to be observed for rapid reactions.

4.3.4 Aryl Chlorides

Aryl chlorides are an attractive alternative to bromides and iodides due to their lower cost and wider availability, though prove to be a more difficult substrate, due to the high aryl-Cl bond dissociation energy. Using the analogous *para*-chlorobenzonitrile under the previously described conditions (tubular reactor, P = 120 psi, T ≤170 °C, and τ ≤20 min) only trace amounts (< 1% by GC) of the amide product were found with the starting material making up the remaining mass balance.

A number of other ligand systems have proven effective for the carbonylation of aryl chlorides.[75, 99-103] The Buchwald method to form phenolate esters using dcpp·2HBF$_4$ (1,3-bis(dicyclohexylphosphino) propane) was chosen due to its mild reaction conditions (Scheme

4.4).[104, 105] Although solids have been handled in continuous flow,[37, 106, 107] the technical requirements were beyond the scope of this work and substitutions for the insoluble inorganic base, molecular sieves, and the KCl by-product were explored.

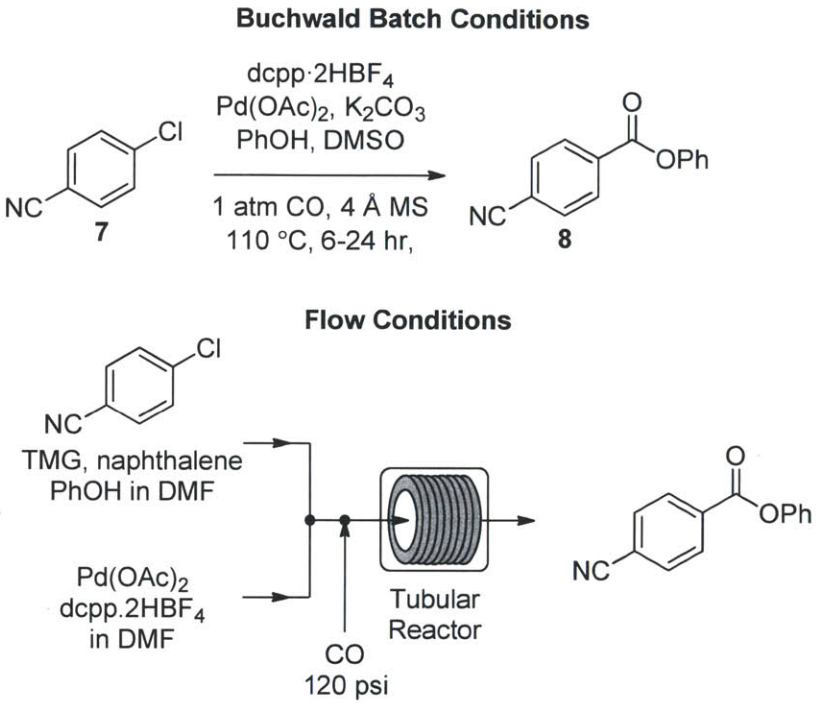

Scheme 4.4. Batch and flow carbonylation of aryl chloride using an organic base.

The transfer to a flow system necessitated the separation of catalyst and starting material solutions to ensure that the reaction took place in the larger tubular reactor (Scheme 4.4). The reaction was performed at 120 psi with residence times of 8.3 and 20 minutes (the upper limit of residence time). Nearly full conversion was observed at 170 °C and 20 minutes (Figure 4.7). As the reaction was performed at the upper limits of residence time and temperature for this system, further optimization was not undertaken, although it is expected that as pressure is decreased, the observed reaction rate will increase and could be a further line of enquiry.

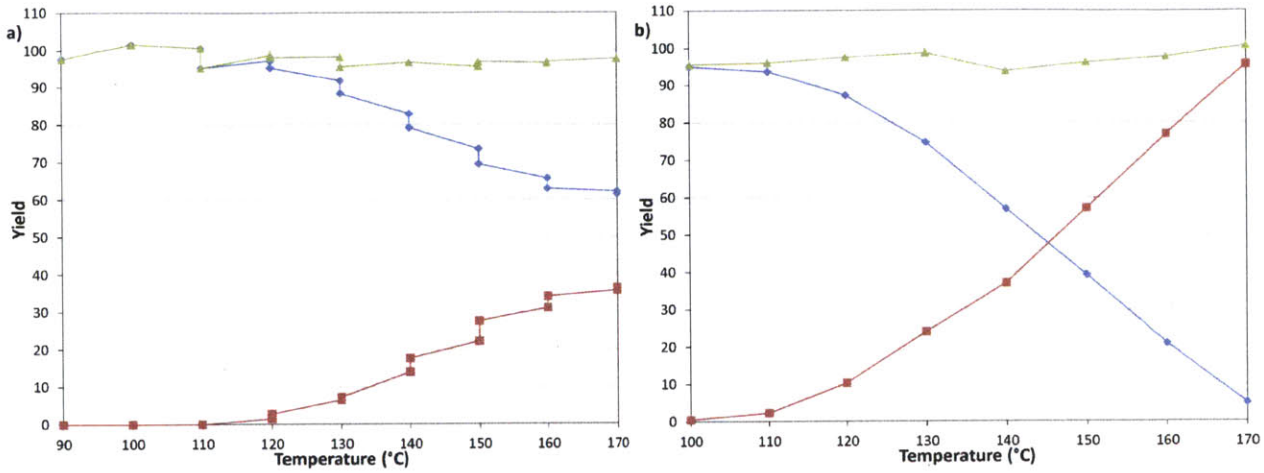

Figure 4.7. Aryl chloride, 120 psi for (a) 8.3 and (b) 20 min residence time. Starting material (◆), product (■), mass balance (▲).

4.3.5 Ester Formation

Carbon monoxide is also a versatile reagent in the synthesis of esters, and given the similarity in reaction schemes, the reaction space was examined using the system. Three different alcohols were used: methanol, ethanol, and benzyl alcohol. The methanol and ethanol examples resulted in full conversion by 120 °C in the tubular reactor at a residence time of 8.3 minutes and a pressure of 120 psi, whereas the benzyl alcohol example reached full conversion at 140 °C.

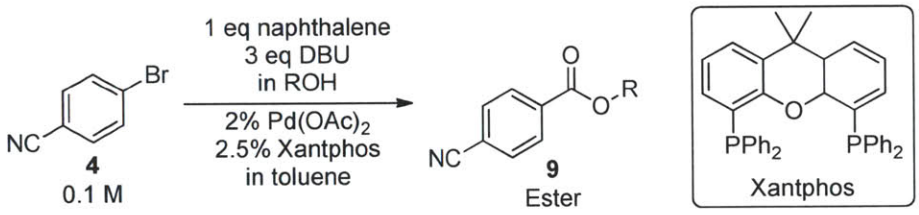

Scheme 4.5. Carbonylation using alcohols as the nucleophiles.

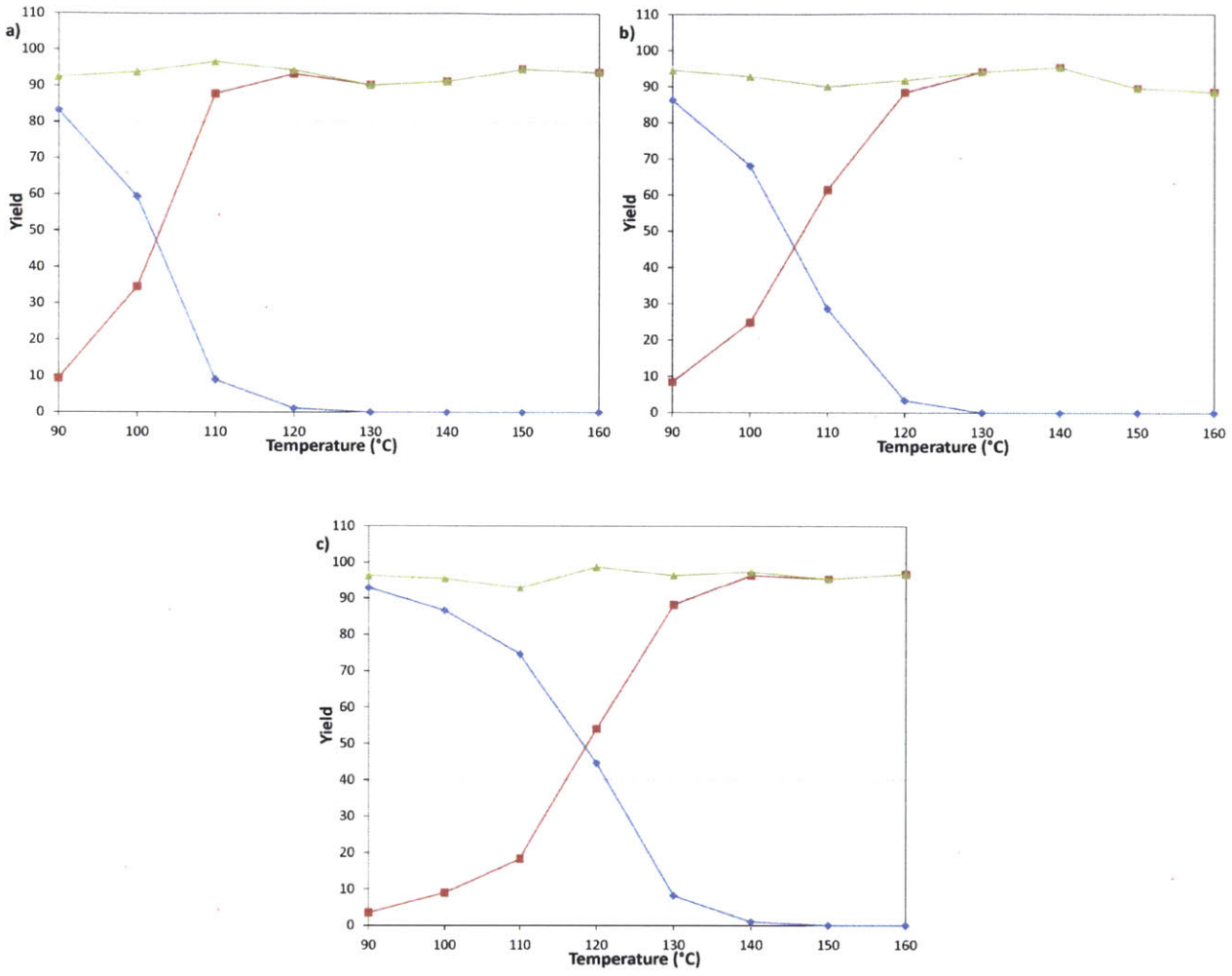

Figure 4.8. Ester formation using the tubular reactor 8.3 minutes and 120 psi: (a) EtOH, (b) MeOH, (c) BnOH.Starting material (◆), product (■), mass balance (▲).

4.3.6 KINETICS

There is significant interest in understanding the kinetics of this gas-liquid system, especially to determine the effect that dictates the product ratio. For aryl bromides, the oxidative addition of palladium is often assumed to be the rate-determining step[97] after which the reaction then bifurcates; thus, overall conversion should be able to be modeled without needing to account for product selectivity (Scheme 4.6). Furthermore, it was observed that as the pressure of carbon monoxide increased, the rate of the reaction decreased, implying that carbon monoxide was reversibly poisoning the palladium catalyst. Finally, after coordination of the first molecule of carbon monoxide the two products were formed.

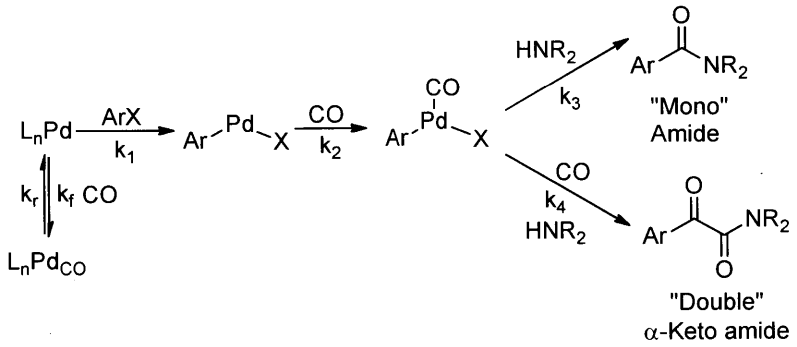

Scheme 4.6. Simplified model of the aminocarbonylation reaction.

Since oxidative addition is assumed to be the rate-determining step, the rate of loss of starting material (ArX) can be written as a first-order reaction in both aryl halide and palladium (Eq. 4.1). The next simplification in this process was to assume the steady state approximation for the active palladium catalyst, L_nPd. By using the steady-state approximation, an expression for concentration of active palladium, [Pd] (Eq. 4.2), is found and can be substituted in Eq. 4.1. This leads to Eq. 4.3, a pseudo first-order expression for the rate of reaction:

$$-\frac{d[ArX]}{dt} = k_1\ [Pd][L][ArX] \tag{4.1}$$

$$[Pd] = \frac{[Pd]_0}{1+K[CO]} \tag{4.2}$$

$$-\frac{d[ArX]}{dt} = k_{obs}\ [ArX] \tag{4.3}$$

$$k_{obs} = \frac{k_1[Pd]_0[L]}{1+K[CO]} \tag{4.4}$$

The result of this simplification finds that the observed rate, k_{obs}, is proportional to the initial concentration of the palladium used and inversely proportion to the concentration of the carbon monoxide in the liquid phase of the system. With varying pressures of carbon monoxide Henry's Law predicts that [CO] $\propto$ CO pressure; hence a higher pressure will adversely affect the rate of the reaction. The temperature dependence of the Henry's Law constant for the solvent system was modeled using Aspen Plus (see Figure C.1).

The reaction was run in the tubular reactor at 120 psi and with 8.3 minutes residence time. It was decided to take advantage of the *in situ* monitoring to continuously increase the reaction temperature at constant residence time, which would be analogous to a time profile found in batch studies. In this example, the temperature was increased by 1 °C every 2 minutes. The temperature was held at 104 °C for 4 minutes to assist in aligning temperature and concentration data. Additionally, the concentration profiles flatten at this point, showing that the system is never operating far from steady state. The pattern observed was the same as for the steady state analysis, where the ratio of mono/double remains constant until approximately 120 °C, above which the ratio of mono increases substantially. However, the IR analysis is less sensitive to lower concentrations, causing significant noise beyond approximately 95% conversion.

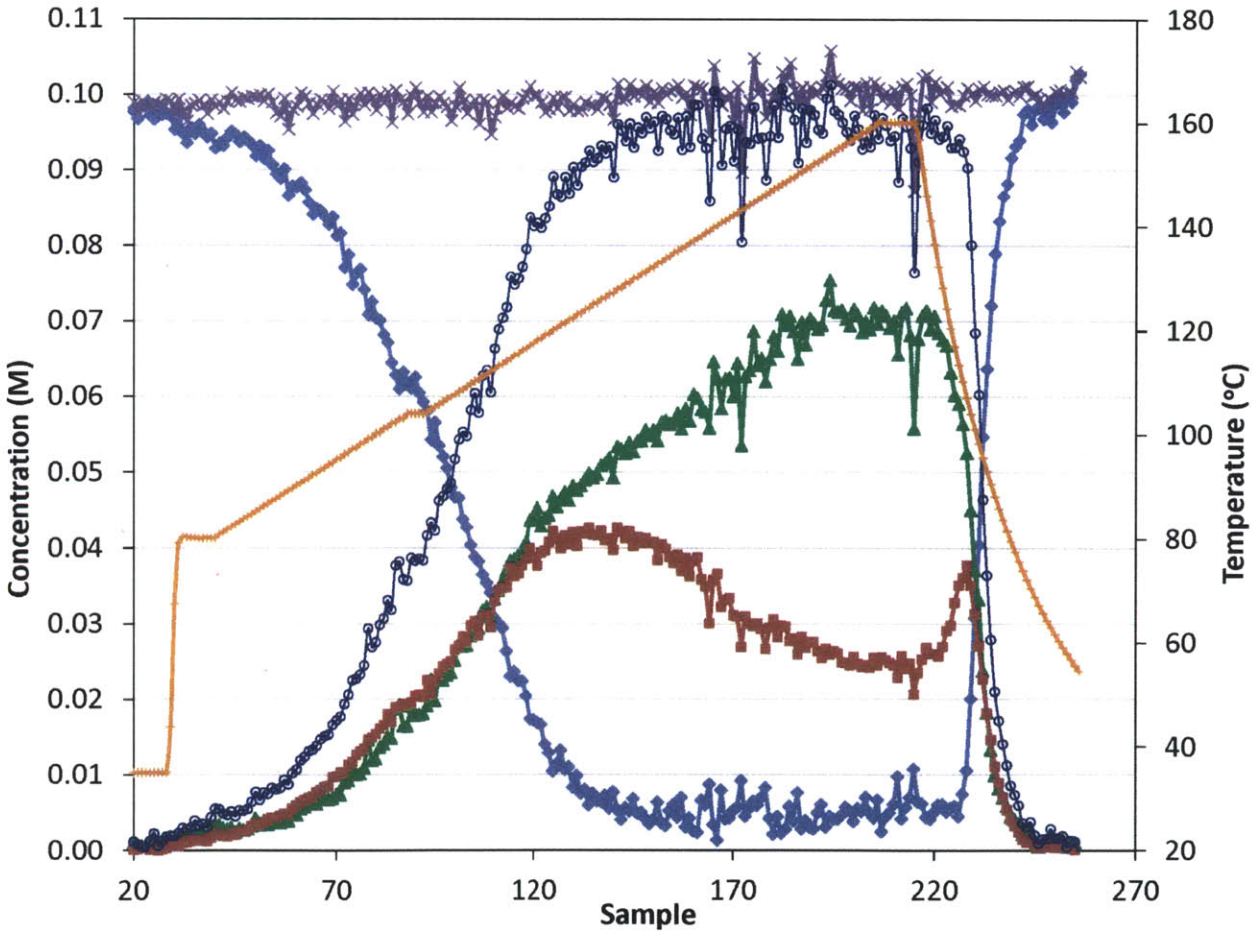

Figure 4.9. ReactIR with a temperature gradient 1 °C every 2 minutes (tubular reactor, 8.3 min residence time, 120 psi CO).Starting material (◆), mono product (▲), di product (■), mass balance (×), total product (O), and temperature (+).

From the data above it is possible to form an Arrhenius plot of $\ln(k_{obs})$ vs. 1/T to determine the activation energy from the slope (Figure 4.10). In principal, the pre-exponential factor can also be determined (the intercept of y-axis) but the substantial extrapolation required can present significant errors. The system demonstrates a steady slope from 80 °C to 120 °C, but beyond 120 °C a change in slope is observed, indicating that there appears to be a change in the rate-limiting step.

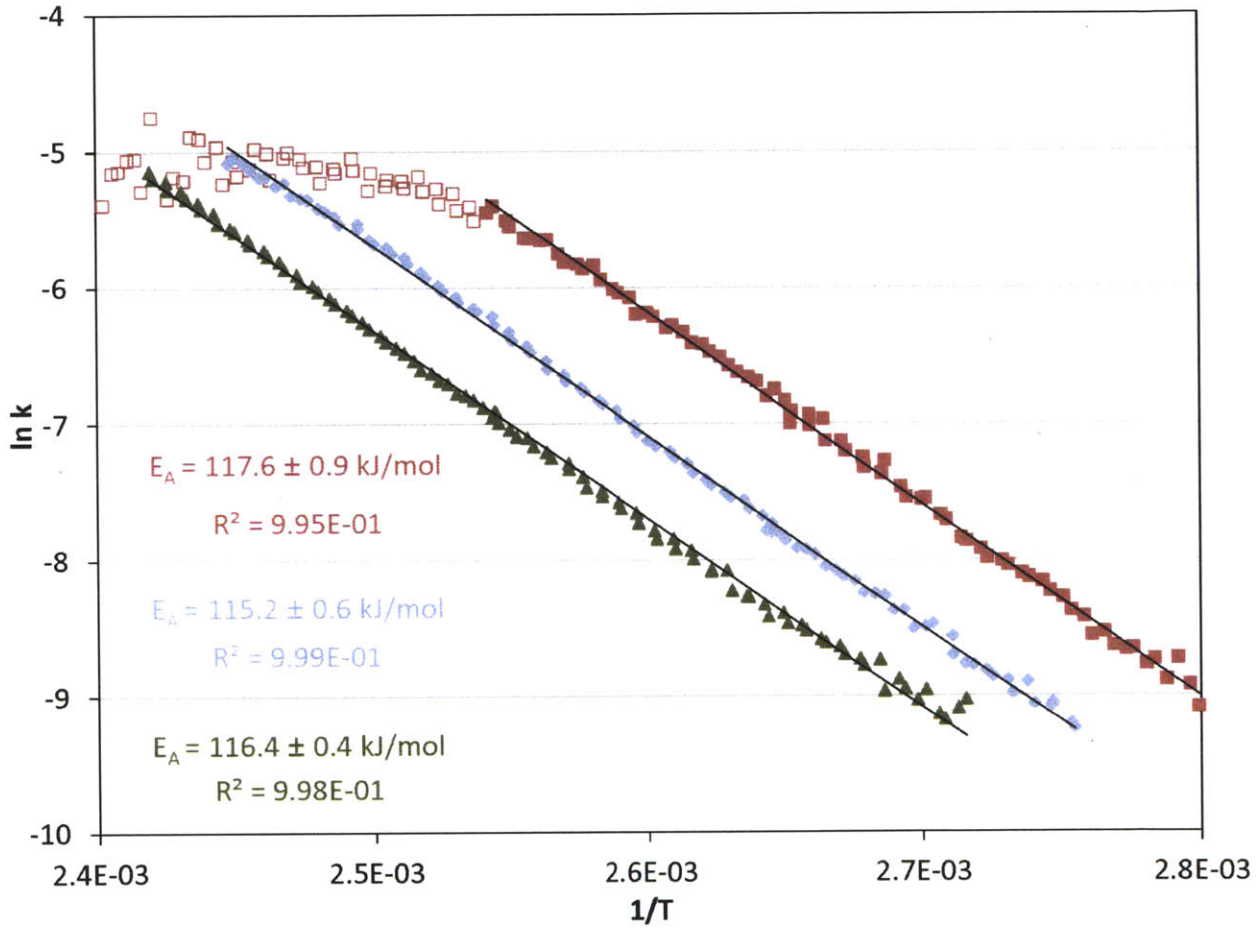

Figure 4.10. Arrenihus plot for the tubular reactor temperature ramp experiments: Exp. 1 (■) at 120 psi CO and 2 % Pd, Exp. 2 (▲) at 200 psi CO and 2 % Pd, and Exp. 3 (◆) at 120 psi CO and 1 % Pd. Upper temperature regime (□) results from Exp. 1.

When the conditions between 80-120 °C are plotted on an Arrhenius plot (filled shapes), a straight line is found, with a slope corresponding to the activation energy. The system was applied at three conditions as described in Table 4.2, resulting in similar activation energies.

Table 4.2. Summary of continuous temperature ramp experiments in the tubular reactor with 8.3 residence time. Errors given are the standard error of the line slope.

Exp	P_{CO} (psi)	mol% Pd	E_a (kJ/mol)
1	120	2	117.6 ± 0.9
2	200	2	115.2 ± 0.6
3	120	1	116.4 ± 0.4

4.3.7 Further Kinetic Analysis and Modeling

Similar Arrhenius analysis can be performed at steady state for reactions under different conditions in the microreactor and tubular reactor using offline GC analysis. As can be seen in Figure 4.11, at a given temperature, the conditions of the reaction cause a significant range in the reaction rate constant. However, the correlation with temperature holds across conditions. The same behavior observed in the IR experiments can be seen at high temperatures, where the apparent rate constant begins to decrease as the rate-limiting step begins to shift. As the reaction rate appeared to vary linearly with the inverse of the CO pressure, the rate constant equation was simplified to

$$k_{obs} = \frac{k_1[Pd]_0[L]}{1+K[CO]} \rightarrow k_{obs} = \frac{k_1[Pd]_0[L]}{K[CO]} \tag{4.5}$$

which assumes that under the conditions investigated, the *K[CO]* term is significantly greater than 1. The data from the IR experiments was analyzed to find values of the activation energy, E_a, for k_1/K, which can be found from the slope of the best-fit line of the lower temperature regime in the Arrhenius plot. The range given is for one standard error. The same analysis was performed for the microreactor and tubular reactor steady-state experiments using offline GC analysis. The results are summarized in Table 4.3, which shows that all three experiment types produced approximately the same activation energy. However, the continuous temperature ramp experiment with online IR analysis required significantly less reagent consumption and produced

the data more rapidly (9 h for IR tubular data vs. 21 h for GC tubular data, which does not include time required to prepare, run, and analyze ~75 GC samples). Due to the larger amount of data at each set of reaction conditions, there was sufficient data to calculate individual lines of best fit rather than combined as with the GC analysis, resulting in a significantly smaller confidence interval for the activation energy.

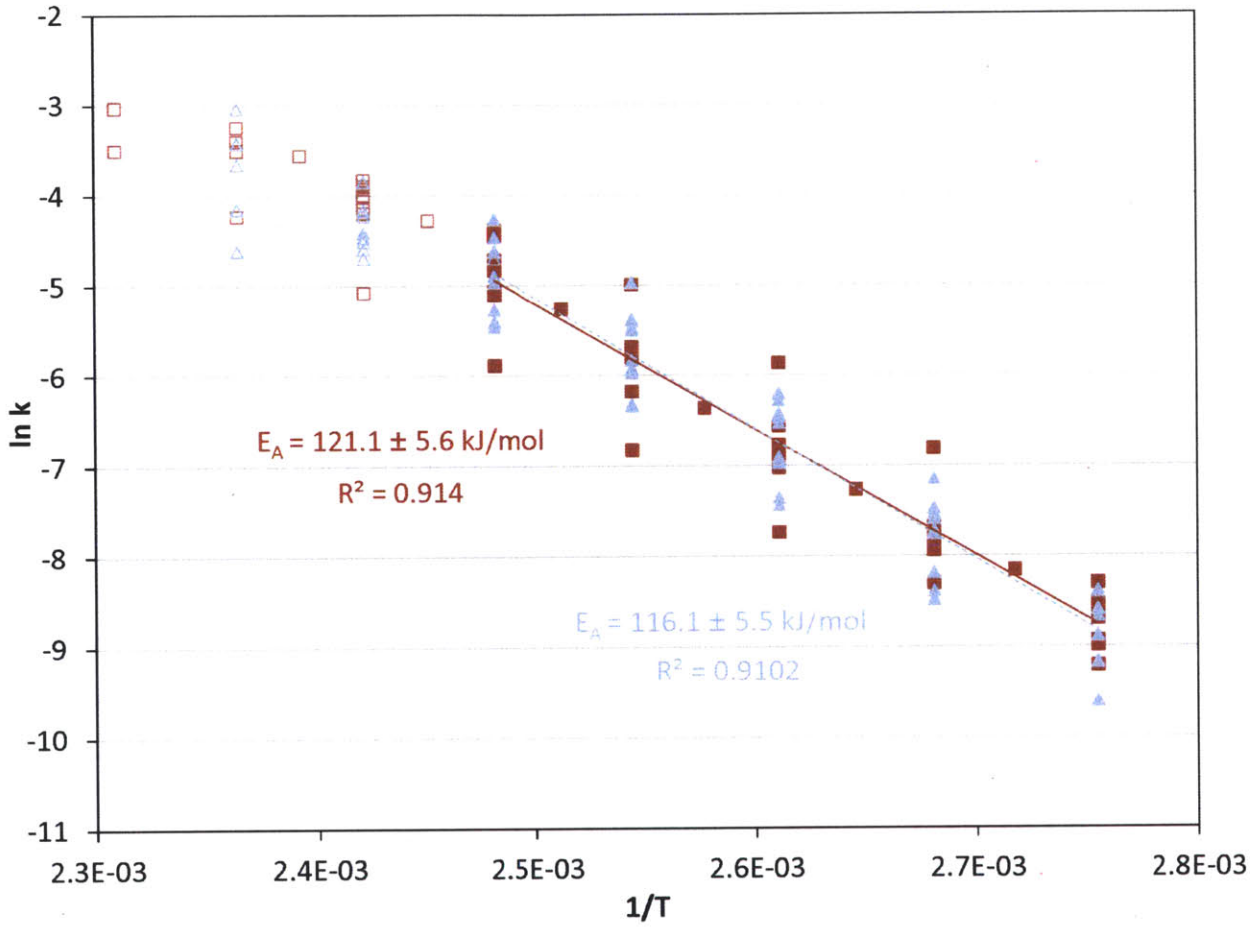

Figure 4.11. Arrhenius plot for reactions performed at a number of temperatures. Silicon microreactor (▲) at 2 minute residence time and 40, 80, 120, and 180 psi CO and at 3 minute residence time and 120 psi CO. Tubular reactor (■) at 2 minute residence time with 80, 120, and 180 psi CO, at 3 minute residence time with 120 and 180 psi CO, at 4 minute residence time with 120 psi CO, at 6 minute residence time with 120 psi CO, and at 8.3 min residence time with 50, 120, and 200 psi CO. All reactions were performed with 2 mol% Pd. Filled shapes are in the lower temperature regime and were used for the best-fit lines.

Table 4.3. Kinetic parameters determined from IR experiments performed in the silicon microreactor.

Experiment	E_a (kJ/mol)
Tubular Reactor Temperature Ramp with Online IR Analysis	116.4 ± 1.2
Microreactor Steady States with Offline GC Analysis	116.1 ± 5.5
Tubular Reactor Steady States with Offline GC Analysis	121.1 ± 5.6

However, as this simplified first-order analysis only holds below 120 °C, the full reaction scheme must be considered to completely model both reaction regimes. To this end, the selectivities were modeled using the Yamamoto mechanism.[95] The selectivity at the first reaction branch (Figure 4.12), S_1, was modeled as shown in Eq. 4.6. Likewise, the selectivity at the second branch point, S_2, was modeled as shown in Eq. 4.7. The simplification shown in the equations allows each selectivity to be modeled with two variables based upon the ratio of the pre-exponential factors and the difference in the activation energies of the two reactions involved. Matlab was used to fit the data for the microreactor at several sets of experimental conditions. The activation energies used were those found by Arrhenius analysis. The results for the model and experimental conversion for both the microreactor and tubular reactor are given in Figure 4.13, with model parameters in Table 4.4. The selectivity for the microreactor results are shown in Figure 4.14. The model trends for conversion and selectivity match the experimental data. Additionally, as the tubular reactor conversion data was not used to fit the model, these points serve as a validation set for the model. The change in trends around 120 °C can be explained by the combined effects of temperature on S_1 and the subsequent reactions. Thus, as temperature increases, this branch increasingly favors the upper pathway through the more entropically favored intermediate that leads solely to the mono product. However, the next step in the mechanism has a slower rate than the oxidative addition, causing this to become the rate-limiting step. Further model details are provided in Appendix C.

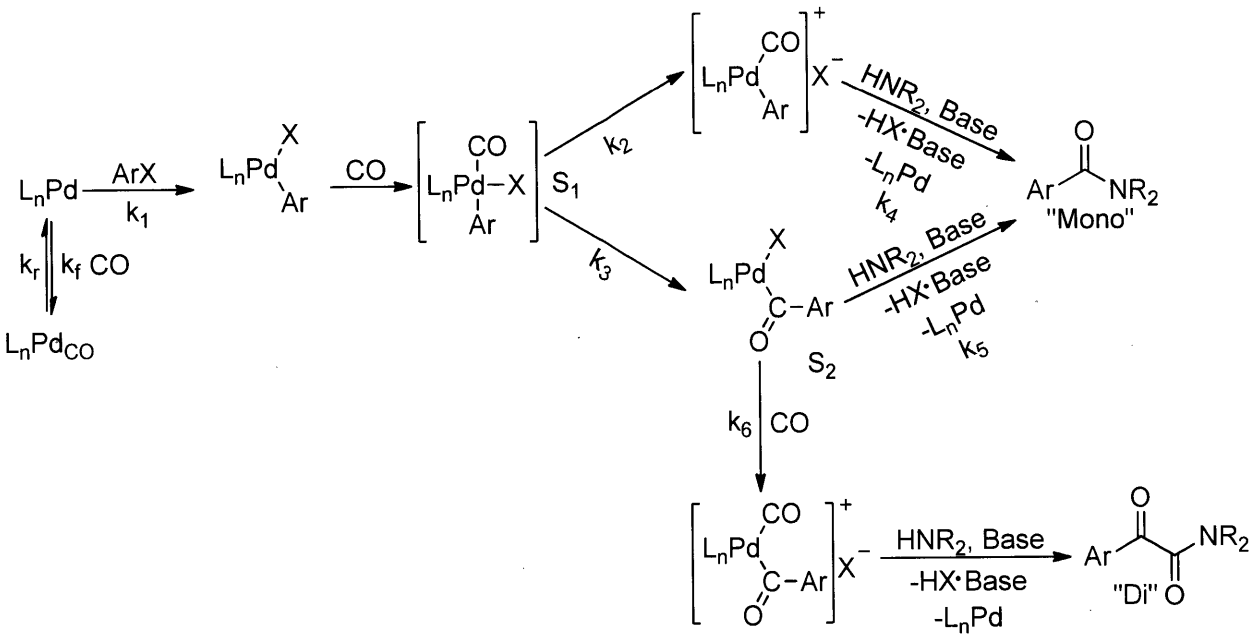

Figure 4.12. Model to which kinetic parameters were fit based upon the Yamamoto mechanism.[95]

$$S_1 = \frac{k_0^{[2]} e^{-E_A^{[2]}/RT}}{k_0^{[2]} e^{-E_A^{[2]}/RT} + k_0^{[3]} e^{-E_A^{[3]}/RT}} = \frac{1}{1 + \frac{k_0^{[3]}}{k_0^{[2]}} e^{\left(E_A^{[2]} - E_A^{[3]}\right)/RT}} \tag{4.6}$$

$$S_2 = \frac{k_0^{[5]} e^{-E_A^{[5]}/RT}}{k_0^{[5]} e^{-E_A^{[5]}/RT} + k_0^{[6]} e^{-E_A^{[6]}/RT} H_{CO} p_{CO}} = \frac{1}{1 + \frac{k_0^{[6]}}{k_0^{[5]}} e^{\left(E_A^{[5]} - E_A^{[6]}\right)/RT} H_{CO} p_{CO}} \tag{4.7}$$

Table 4.4. Best-fit model parameters.

$k_0^{[1]}$	1.33×10^{17} L/(mol·s)
$E_A^{[1]}$	116.4 kJ/mol
$k_0^{[4]}$	1.11×10^{6} s^{-1}
$E_A^{[4]}$	55.6 kJ/mol
$(E_A^{[2]} - E_A^{[3]})$	1.07×10^{2} kJ/mol
$k_0^{[3]}/k_0^{[2]}$	2.42×10^{-13}
$(E_A^{[5]} - E_A^{[6]})$	3.87×10^{1} kJ/mol
$k_0^{[6]}/k_0^{[5]}$	2.01×10^{-4}

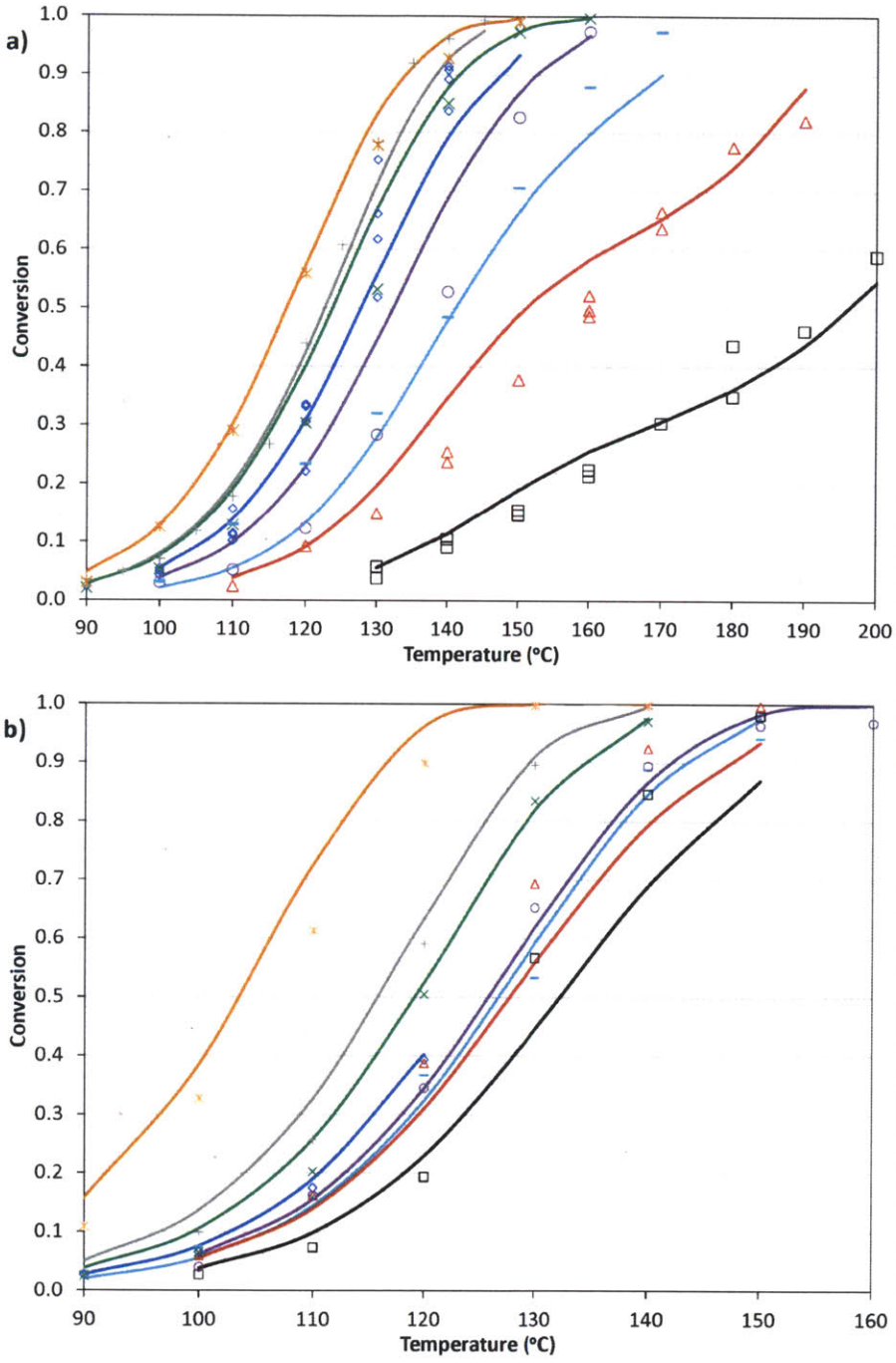

Figure 4.13. Summary of model and experimental conversion for a) microreactor at these conditions

Marker	[Pd] (%)	P_{CO} (psi)	τ (min)
*	2	40	2
+	2	120	3
×	2	80	2
◇	2	120	2
○	2	180	2
–	1	120	3
△	1	120	2
□	0.5	120	2

and b) tubular reactor at these conditions.

Marker	[Pd] (%)	P_{CO} (psi)	τ (min)
*	2	50	2
+	2	200	8.4
×	2	120	4
◇	2	80	2
○	1	120	4
–	2	180	3
△	2	120	2
□	2	180	2

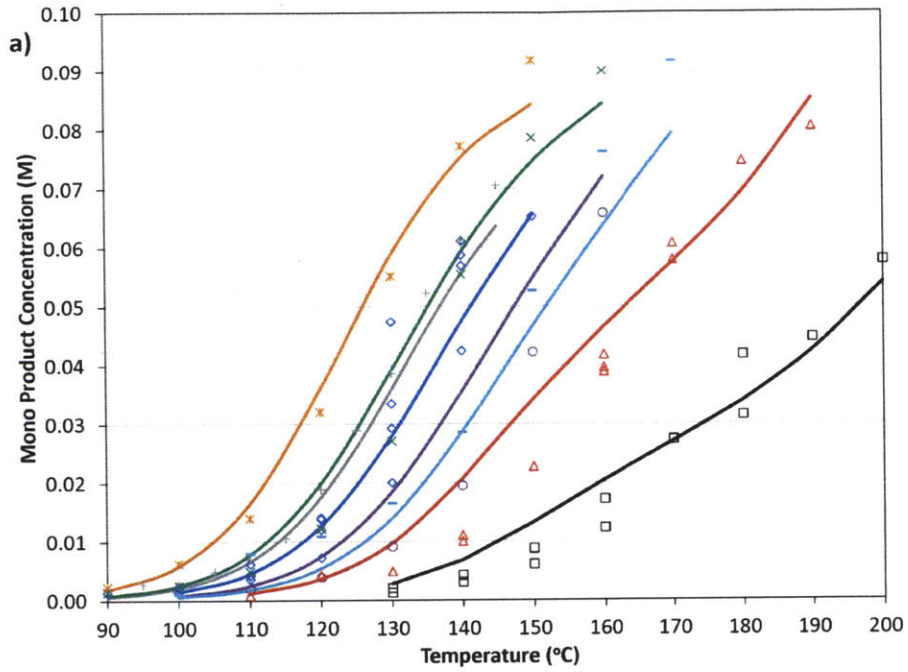

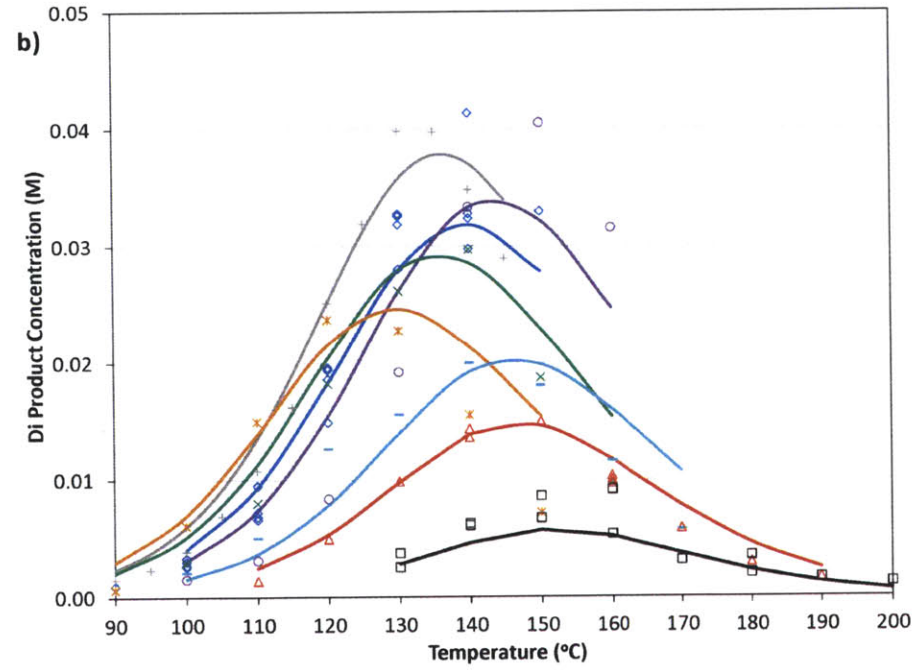

Figure 4.14. Summary of model and experimental selectivity in the microreactor for a) mono product and b) di product. Markers correspond to those given in Figure 4.13 (a).

4.4 CONCLUSIONS

An automated screening system suitable for continuous gas-liquid flow systems was successfully demonstrated. The applicability of the system was proven for the successful carbonylation of aryl iodides, bromides, and chlorides. The choice of reactor was observed to have a significant influence on the outcome of a reaction, as identified with aryl iodides. The effect of temperature, residence time, gas stoichiometry, and pressure can be easily controlled with minimum operator intervention beyond the initial start-up and shut-down processes. It is expected that the facile control of the reaction conditions and ease of data capture will have a significant impact on the study of reaction kinetics leading to more efficient catalytic processes.

Having successfully demonstrated an automated screening system for carbonylation of aryl iodides, bromides, and chlorides, the kinetics of the palladium-catalyzed aminocarbonylation of aryl bromide were further investigated. In agreement with previous results, the reaction was found to be divided into two temperature regimes. For the lower temperature regime, this study compared traditional, steady-state experiments paired with offline GC analysis to transient temperature ramp experiments paired with online IR analysis and found that, while both methods provided similar activation energies, the latter method was significantly more efficient in both time and reagents. Additionally, both the conversion and selectivity for both regimes were modeled in good agreement with experimental data. Below 120°C, the oxidative addition was found to be the rate-limiting step, with nearly equal selectivity for the two products. However, at higher temperatures, the selectivity shifted to a pathway that provides only the mono product from a slower intermediate step, reducing the overall reaction rate.

5 INVESTIGATION OF PETASIS AND UGI REACTIONS IN SERIES IN AN AUTOMATED MICROREACTOR SYSTEM

5.1 INTRODUCTION

5.1.1 CHARACTERISTICS AND RELEVANCE OF MULTICOMPONENT REACTIONS

Multicomponent reactions (MCRs) convert more than two reactants directly into their products.[108] The first MCRs were performed in the 19th century, but it was only in the past decade that they have come into significant research focus. As the number of possible products formed by a reaction increases exponentially with the number of reactants, MCRs offer the possibility to reach a much larger area of the chemical space than binary reactions.[109]

As complex molecules can be formed in a single step out of several reactants, multicomponent reactions offer some major advantages compared to the alternative of a multistep synthesis. Ideally, all reactants can be added simultaneously, which requires the particular steps of the mechanism to take place in a uniquely ordered manner.[109] In multistep reactions, it is often necessary to optimize each step to achieve reasonable overall yields, requiring the solvent or even the catalyst to be changed several times. Thus, more material and effort must be spent than for a one-pot MCR, where the particular steps take place under uniform conditions.

MCRs have been used to create large chemical libraries consisting of a variety of different compounds with a common core structure in the search for novel or improved drugs, and many examples of therapeutically active compounds have been formed by MCRs so far.[110] Furthermore, the simplicity of the experimental procedure and the one-pot character of MCRs make them suitable for automated synthesis.[109]

5.1.2 THE PETASIS REACTION

The Petasis reaction is a derivative of the Mannich reaction, employing organoboronic acids as nucleophiles.[111] The Petasis reaction involves a secondary amine, a β-hydroxy carbonyl, and the organoboronic acid to form a β-hydroxy amine and boric acid (Scheme 5.1).

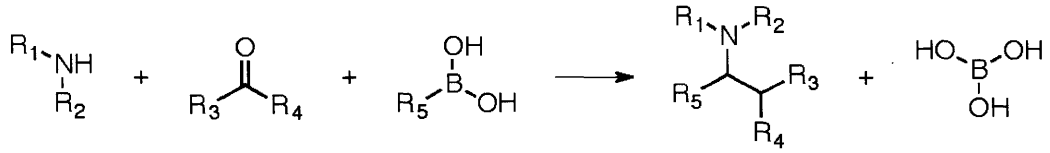

Scheme 5.1. General form of the Petasis reaction.[56, 111]

Although the details of the Petasis reaction mechanism are still disputed, a recent study using density functional theory (DFT) calculations suggested the pathway presented in Scheme 5.2 as the most likely.[112] The carbon-carbon bond formation is an irreversible reaction and proposed to be the rate-limiting step of the mechanism[113]. In theoretical calculations[112] as well as in experimental studies,[114] the Petasis reaction shows a high dependency on the employed solvent, with polar solvents stabilizing the ionic intermediates. The Petasis reaction is typically conducted in batch at temperatures from 20 to 80 °C for 12 to 24 h. The reactivity is reported to be highly dependent on the employed reagents. Using secondary amines, α-hydroxy aldehydes, and vinyl or aryl boronic acids increases the reaction rate significantly.[113]

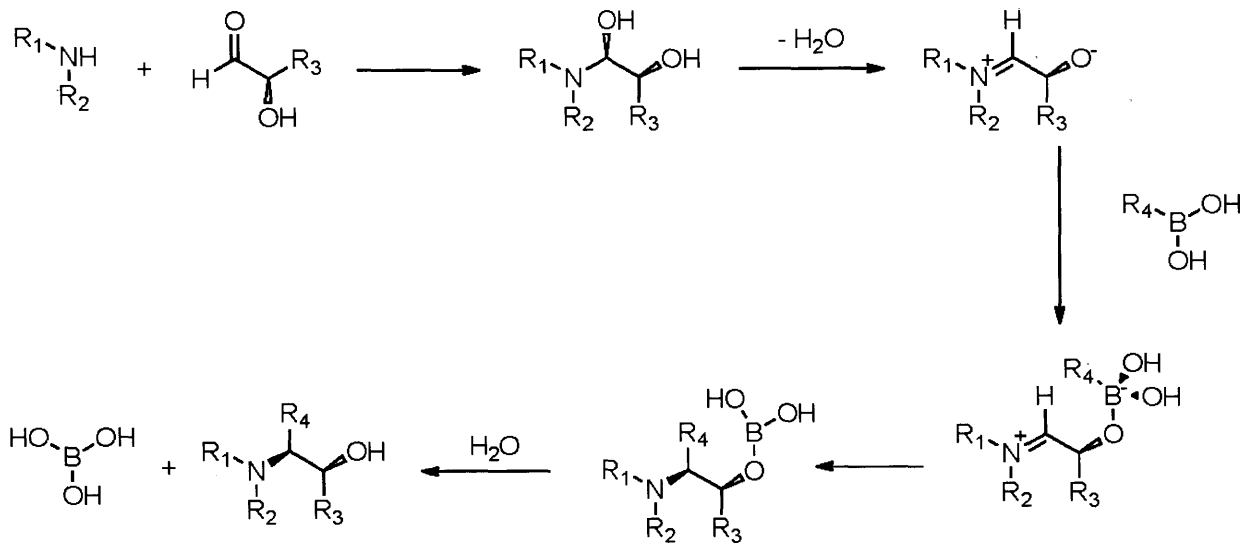

Scheme 5.2. Proposed mechanism of the Petasis reaction.[112]

The highly diastereoselective formation of the carbon-carbon bond makes the Petasis reaction especially interesting for the synthesis of optically pure drugs.[115] As the employed organoboronic acid reacts selectively with the intermediate imine, it is possible to employ reagents with a variety of functional groups without the risk of interference with the main reaction. This enables the generation of multifunctional molecules needed for complex bioactive

compounds. Examples include the use of glyoxylic acid to generate β-γ-unsaturated α-amino acids[113] and of aryl boronic acids to produce α-aryl glycines, which act on the glutamate receptors of the central nervous system.[116] In a recent study, the synthesis of clopidogrel (Plavix®), the world's second highest selling drug in 2005, has been accomplished using a Petasis reaction with a yield 13 % higher than in the patented Sanofi synthesis that is conventionally employed for production.[117]

5.1.3 THE UGI REACTION

The reaction of a ketone or an aldehyde, an amine, a carboxylic acid, and an isocyanide was first published by Ivar Ugi in 1959.[118] Over the last 50 years, the Ugi reaction (Scheme 5.3) became one of the most important multicomponent reactions in organic chemistry.[119]

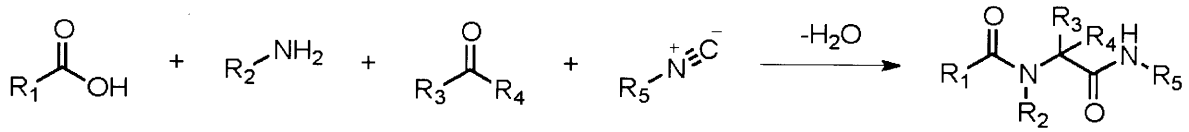

Scheme 5.3. General form of the Ugi reaction.[119]

The mechanism of the Ugi reaction involves the formation of an imine by reaction of the ketone or aldehyde with the amine as the initial step. Furthermore, the existence of an intermediate imidate has been proven, which reacts to the final product by an intramolecular rearrangement.[120] However, the details of the trimolecular reaction of the imine, the carboxylic acid, and the isocyanide to the imidate are still unknown.

Ugi-type reactions are part of the industrial production of various pharmaceuticals, such as the HIV protease inhibitor Crixivan®.[121] In research, the Ugi reaction is often used as a tool to generate chemical libraries with a large number of different compounds featuring the same backbone for drug screening experiments.[110] The Ugi reaction can be conducted in batch at room temperature within a few hours, achieving almost complete conversions.[122]

Because of the generally high conversion of Ugi reactions and the tolerance of the isocyanide to various functional groups,[109] Ugi reactions are well suited for combination with other chemical reactions. Scheme 5.4 shows combining the Ugi reaction with the Petasis reaction,[123] resulting in an effectively six-component reaction, enabling access to an enormous variety of compounds by a two-step process.

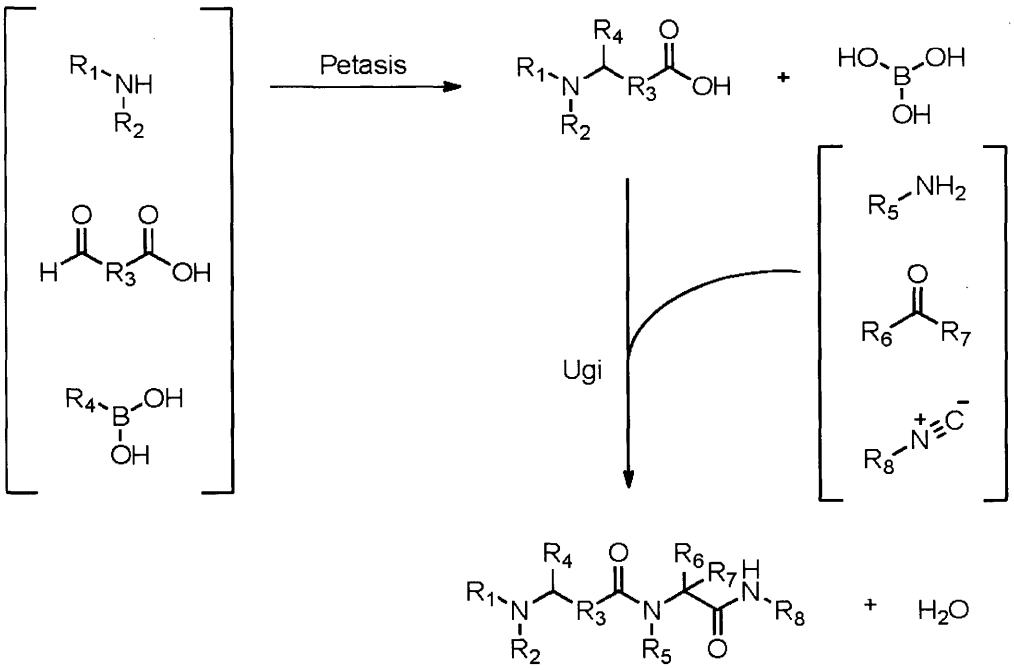

Scheme 5.4. Petasis-Ugi tandem reaction.[123]

5.2 EXPERIMENTAL SECTION

As no reports on the conduction of these reactions in a microfluidic system have been published thus far, every reaction was first tested in batch. To obtain specific information on both steps of the tandem reaction, the Petasis reaction was examined individually first. Then, the Ugi reaction was studied, successively employing acetic acid, the purified Petasis product, and finally the raw Petasis product.

As a first step, the reactions were conducted at several concentrations in a variety of different solvents. To avoid clogging the microreactors used in subsequent experiments, solvents were tested to keep all reagents, the desired product, and eventual side-products in solution. The pure reagents, as well as the resulting raw product solution, were analyzed by Ultra Performance Liquid Chromatography (UPLC) and Gas Chromatography-Mass Spectrometry (GC-MS) to identify a suitable method to monitor yield and conversion of the reactions. UPLC was found to be the superior technique to monitor the reagent and product concentrations. The experimental results presented were obtained using an Water Acquity UPLC with a Mercury Luna 3μ C18(2) column. The elution was carried out at a flow rate of 0.3 mL/min using a reverse phase gradient of acetonitrile and water containing 0.1 % formic acid. After steps of isolation and purification,

the pure product was analyzed by Nuclear Magnetic Resonance (NMR) spectroscopy to verify its structure.

5.2.1 *Layout of the microreactor system*

The reactions were conducted in a microreactor with a volume of 232 µL. The layout of the employed microreactor is illustrated in Figure 5.1. Besides two inlets and an outlet, an additional inlet channel joins the reaction channel near the outlet to quench the reaction.

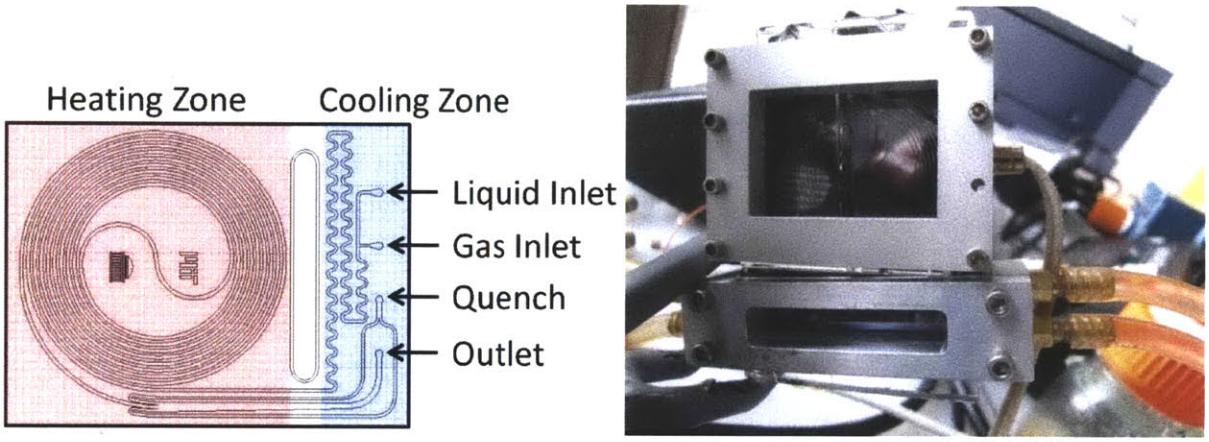

Figure 5.1. Schematic and photograph of the employed microreactor.[65, 66]

The microreactor was mounted in two separate stainless steel compression chucks. One chuck was placed on the area that is marked by a blue background in Figure 5.1 and equipped with ports for the inlets and outlet of the reactor as well as for cooling water. The second chuck was mounted on the area of the reactor that is marked red in Figure 5.1 and served to heat the reaction zone of the microreactor with an integrated Omega (CSS-01235/120V) heating cartridge.

To achieve a precisely controlled and uniform flow rate of the reagents, the prepared solutions were loaded in 8-mL Harvard Apparatus stainless steel syringes and infused by Harvard Apparatus PHD 2000 pumps.

A constant pressure during the reactions was accomplished by connecting a 100-psi backpressure regulator to the outlet of the microreactor. The temperature of the reactor was maintained by an Omega (CN9311) temperature controller. The cooling water was taken from a reservoir at room temperature by a recirculating pump.

The setpoint of the temperature controllers and syringe pumps were set by an automated Labview (version 8.5.1) program. Additionally, this platform controlled a Rheodyne six-way valve with a 2-μL sample loop after the reactor outlet to allow automated injection into the UPLC for analysis after steady state had been reached. In this way, several sets of reaction conditions were run and analyzed with minimal input required from the experimenter or downtime between reactions.

5.2.2 *Procedure employed to study the Petasis reaction*

At first, a simple example described in the literature[124] was chosen to investigate the Petasis reaction. This reaction (Scheme 5.5) involved morpholine, salicylaldehyde, and phenylboronic acid. Indeed, these reagents cannot be employed for the Petasis-Ugi tandem reaction as the Petasis product requires a carboxyl group to react with the Ugi reagents.

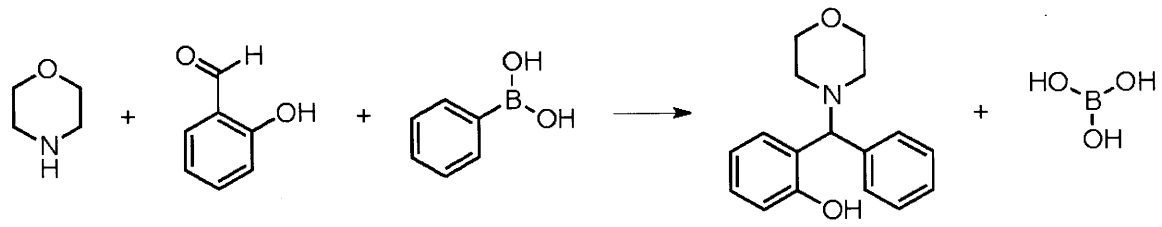

Scheme 5.5. Petasis reaction of morpholine, salicylaldehyde, and phenylboronic acid.

Next, the reagents were changed with the goal of obtaining a product suitable for the successive Ugi reaction. Glyoxylic acid is a suitable substance as it features the functionality of an aldehyde needed for the Petasis reaction, as well as a carboxyl group required for the successive Ugi reaction, as reported by Portlock *et al.*[123]

As shown in Scheme 5.6, glyoxylic acid was combined with phenylboronic acid and piperidine, replacing the morpholine used in the first reaction. The employment of piperidine simplified the validation of the product structure, as a published NMR spectrum of this product could be used as reference.

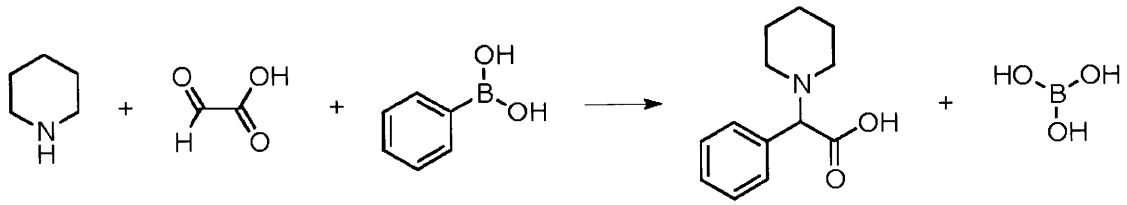

Scheme 5.6. Petasis reaction of piperidine, glyoxylic acid, and phenylboronic acid.

5.2.3 PRELIMINARY EXPERIMENTS IN BATCH

In order to identify suitable solvents and to isolate and purify the desired product, the two Petasis reactions were first conducted in batch reactors.

5.2.3.1 Morpholine, salicylaldehyde, and phenylboronic acid

871.2 mg (10 mmol) morpholine, 1221.2 mg (10mmol) salicylaldehyde, and 1219.3 mg (10mmol) phenylboronic acid were dissolved in 10 mL acetonitrile. The reaction was conducted in a stirred 20-mL vial at 90 °C for 16 h. During the reaction, the solution developed a dark yellow color and white solid particles formed. Successive solubility studies showed that the particles were boric acid. The isolation of the pure product was accomplished by an aqueous workup to remove the water-soluble boric acid. After evaporation of the acetonitrile, pure product remained as an orange solid.

5.2.3.2 Piperidine, glyoxylic acid, and phenylboronic acid

851.5 mg (10 mmol) piperidine, 920.5 mg (10 mmol) glyoxylic acid, and 1219.3 mg (10 mmol) phenylboronic acid were dissolved in 10 mL methanol. The equimolar reaction was conducted in a stirred 20-mL vial at 60 °C for 16 h. During the reaction, the solution assumed a dark yellow color. The isolation of the pure product was accomplished by flash chromatography using silica gel as the stationary phase. First, a 9:1 mixture of chloroform and methanol was used to elute unreacted phenylboronic acid from the crude product. In a second step, the eluent was changed to an 8:2:2 mixture of 2-butanol, acetic acid, and water to isolate the desired product. After removal of the solvent, a sticky, slightly yellow solid was obtained. For the final purification, this solid was dissolved in isopropanol. The pure product could be precipitated by addition of n-hexane. After filtration and drying, the pure product was obtained as a white powder.

5.2.4 SERIES OF MEASUREMENT IN MICROFLOW

The employed experimental flow setup for the Petasis reaction is illustrated in Figure 5.2. As the employed microreactor has only two inlets, two of the three reagents were mixed in one syringe. To avoid the preliminary reaction of the aldehyde and the amine to the imine, these two compounds were kept in separate syringes. In order to ease the dissolution of the solid phenylboronic acid, it was chosen to add the liquid amine. 1,2-Dimethoxybenzene was used as internal standard added to the aldehyde solution.

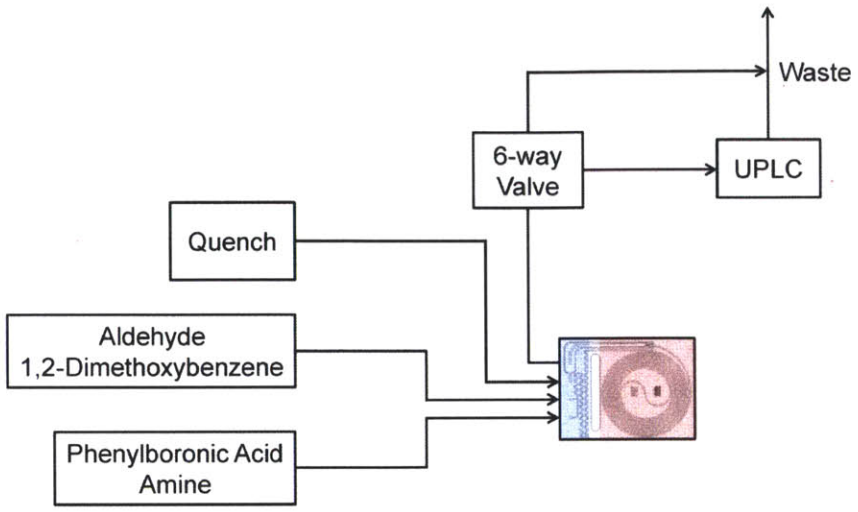

Figure 5.2. Setup of the microreactor system employed to study the Petasis reaction.

5.2.4.1 Morpholine, salicylaldehyde, and phenylboronic acid

One of the 8-mL Harvard Apparatus stainless steel syringes was filled with an equimolar 0.1 M solution of salicylaldehyde and 1,2-dimethoxybenzene (DMB); 122.12 mg salicylaldehyde and 138.16 mg DMB were dissolved in N,N-dimethylformamide (DMF) using a 10-mL volumetric flask. The other 8-mL syringe was filled with a solution of phenylboronic acid and 3 equivalents of morpholine; 121.93 mg phenylboronic acid and 261.36 mg morpholine were dissolved in DMF using a 10-mL volumetric flask. As quench, pure DMF was flowed from a 10-mL S.G.E. glass syringe. All three syringes were driven at equal flow rates.

5.2.4.2 Piperidine, glyoxylic acid, and phenylboronic acid

One of the 8-mL Harvard Apparatus stainless steel syringes was filled with a solution of 1.5 M glyoxylic acid and 0.2 M DMB, which served as an internal standard; 1380.75 mg glyoxylic acid and 276.32 mg DMB were dissolved in dimethylsulfoxide (DMSO) using a 10-mL volumetric flask.

The second 8-mL syringe was filled with a solution of 1 M phenylboronic acid and 1.5 M piperidine. First, 1219.3 mg phenylboronic acid were dissolved in 5 mL DMSO. The addition of 1277.25 mg piperidine caused the phenylboronic acid to precipitate, but the addition of 1 mL trifluoracetic acid (TFA) redissolved the solid. The 10-mL volumetric flask was then filled with DMSO.

5.2.5 *Examination of the Petasis-Ugi combination*

To begin the examination of the Petasis-Ugi tandem reaction, an individual Ugi reaction was conducted in a batch reactor. The established exemplary reaction involving acetic acid, n-butylamine, benzaldehyde, and ethylisocyanoacetate is shown in Scheme 5.7. This individual Ugi reaction was only conducted in batch and not in the microreactor setup.

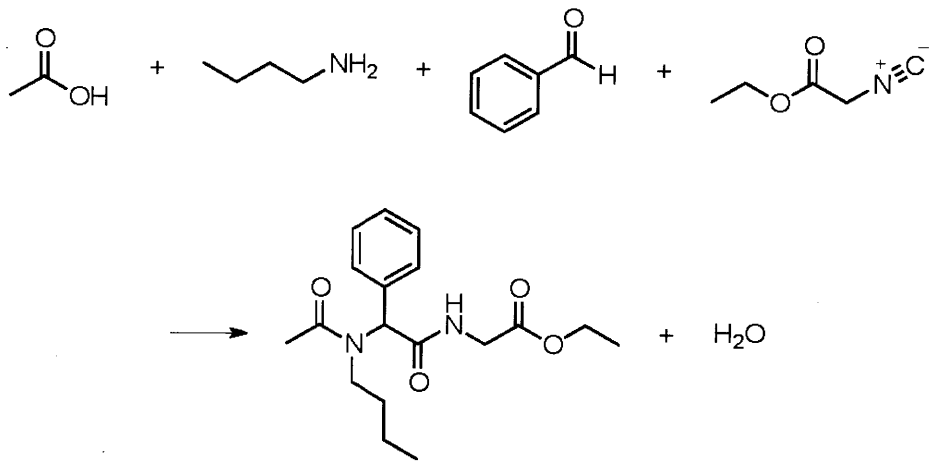

Scheme 5.7. Ugi reaction of acetic acid, n-butylamine, benzaldehyde and ethylisocyanoacetate.

5.2.6 *Ugi reaction in batch*

The Ugi reactions in batch were conducted following published experimental guidelines.[120] As recommended in the literature, benzaldehyde and n-butylamine were joined first for about 30 minutes in order to form the intermediate imine before the rest of the reagents were added.

5.2.6.1 Acetic acid, n-butylamine, benzaldehyde, and ethylisocyanoacetate

106.12 mg (1 mmol) benzaldehyde and 73.14 mg (1 mmol) n-butylamine were reacted in 1 mL methanol at room temperature. After 30 minutes, 60.05 mg (1 mmol) acetic acid and 113.11 mg (1 mmol) ethylisocyanoacetate were added and the solution left at room temperature for 18 hours.

In the next step, the Ugi reaction was conducted employing the isolated and purified aminoacid formed by the Petasis reaction, n-butylamine, benzaldehyde, and cyclohexylisocyanide. Employing the purified Petasis product, this reaction (Scheme 5.8) can be seen as an individual Ugi reaction.

5.2.6.2 Petasis product, n-butylamine, benzaldehyde, and cyclohexylisocyanide

146.28 mg (2 mmol) n-butylamine and 203.3 µL (2 mmol) benzaldehyde were brought to reaction in 2 mL methanol for 30 min at room temperature to form the intermediate imine. Then 249.2 µL (2 mmol) cyclohexylisocyanide and 219.8 mg (1 mmol) of the Petasis product were added. The reaction was conducted in a stirred 20-mL vial at room temperature for 16 h.

The isolation of the final product was accomplished by flash chromatography with silica gel as the stationary phase. A 3:1 mixture of n-hexane and ethylacetate with 1.5 % triethylamine was used as eluent. After removal of the solvent, a sticky white solid remained.

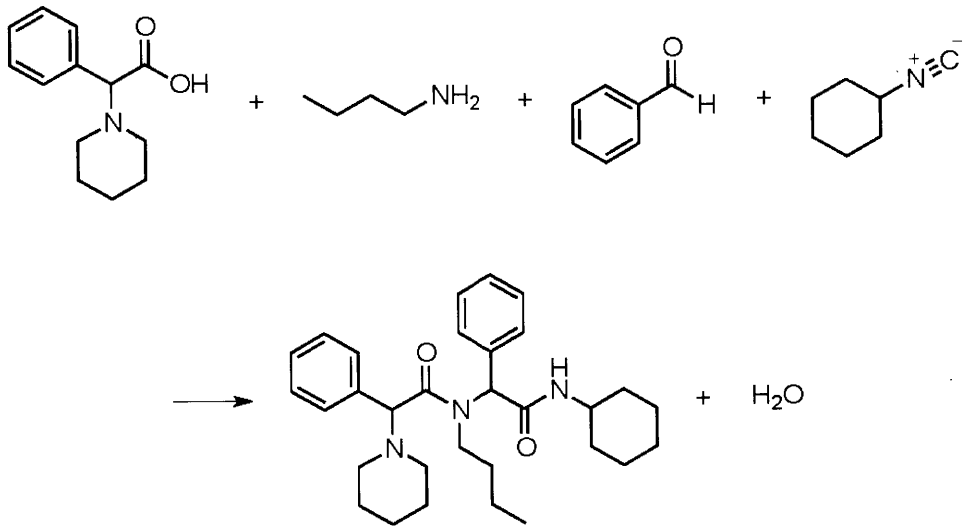

Scheme 5.8. Ugi reaction of the Petasis product, n-butylamine, benzaldehyde, and cyclohexylisocyanide.

5.2.7 PETASIS-UGI TANDEM REACTION IN FLOW

Finally, the combination of a Petasis reaction of glyoxylic acid, piperidine, and phenylboronic acid and a successive Ugi reaction by addition of n-butylamine, benzaldehyde, and cyclohexylisocyanide was examined (Scheme 5.9) in the microreactor system.

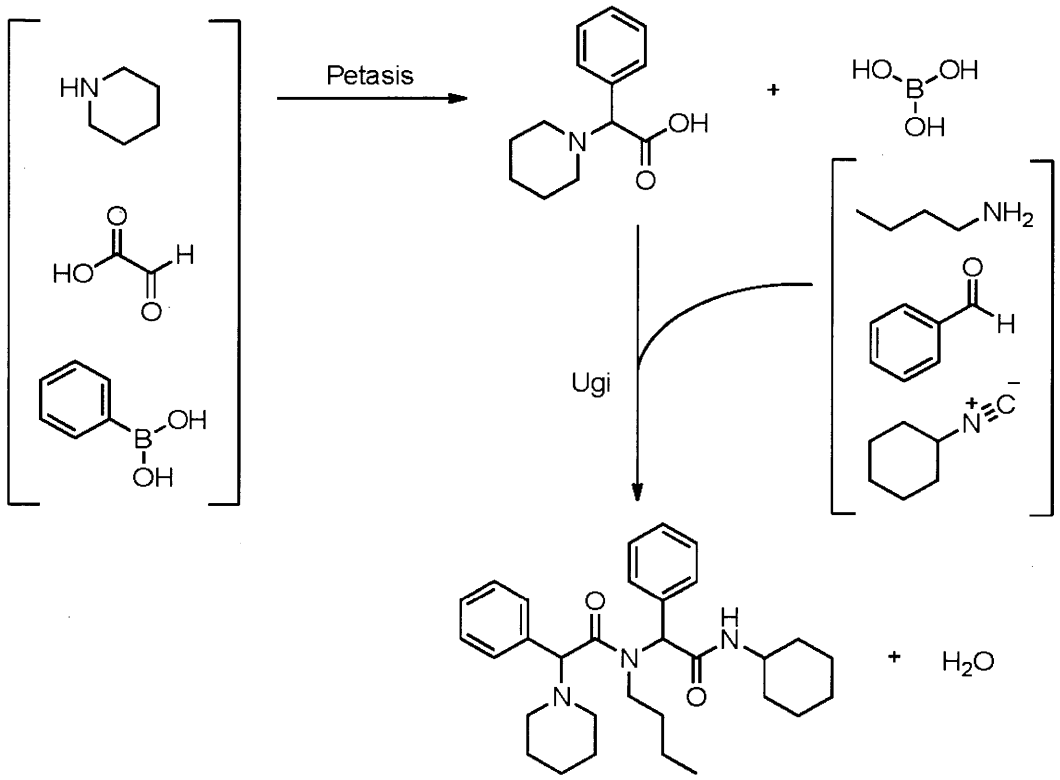

Scheme 5.9. Examined Petasis-Ugi tandem reaction.

The two reactions were conducted in two identical 232-μL silicon microreactors that were sequentially connected. The temperature was maintained independently for each reactor by two Omega temperature controllers, with their setpoints in turn controlled by the Labview program. The Petasis reaction was conducted as described, but instead of pure DMSO, the Ugi reactants were fed into the quench inlet of the first reactor. The outlet of the first reactor was connected to the second inlet of the second reactor. The first inlet of the second reactor was closed and pure DMSO fed into the quench inlet of the second reactor. This setup (Figure 5.3) was chosen to avoid dilution of the reactants by a DMSO quench of the first reactor and fluctuations of the product stream composition that would be caused by closing the quench inlet of the first reactor. The chromatogram in Figure 5.4 was recorded by UPLC and shows the peaks of the reagents, the desired product, and the two internal standards, 1,2-dimethoxybenzene and naphthalene.

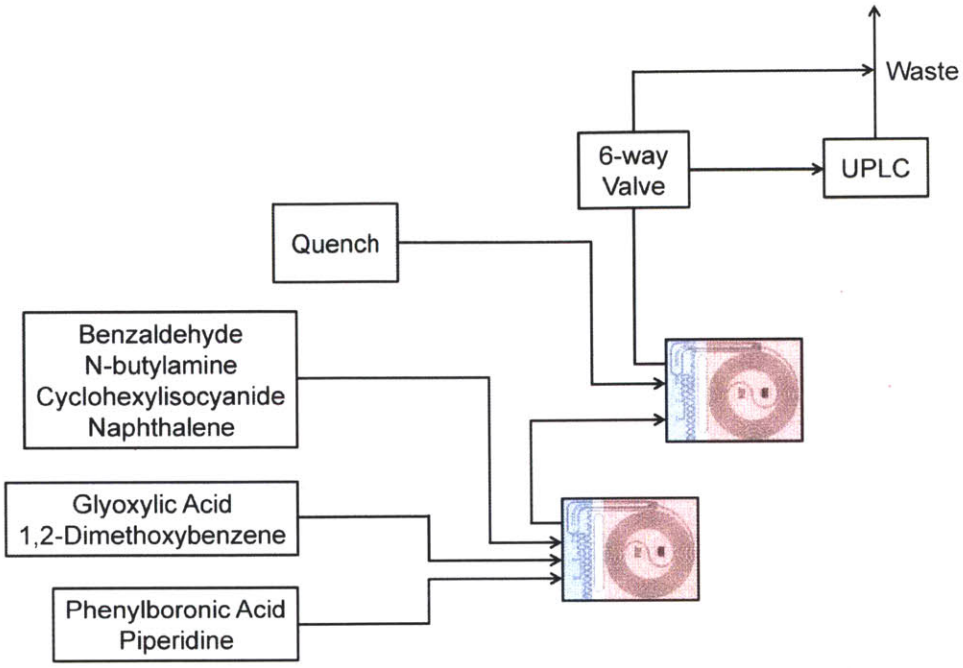

Figure 5.3. Setup of the microreactor system employed to study the Petasis-Ugi tandem reaction.

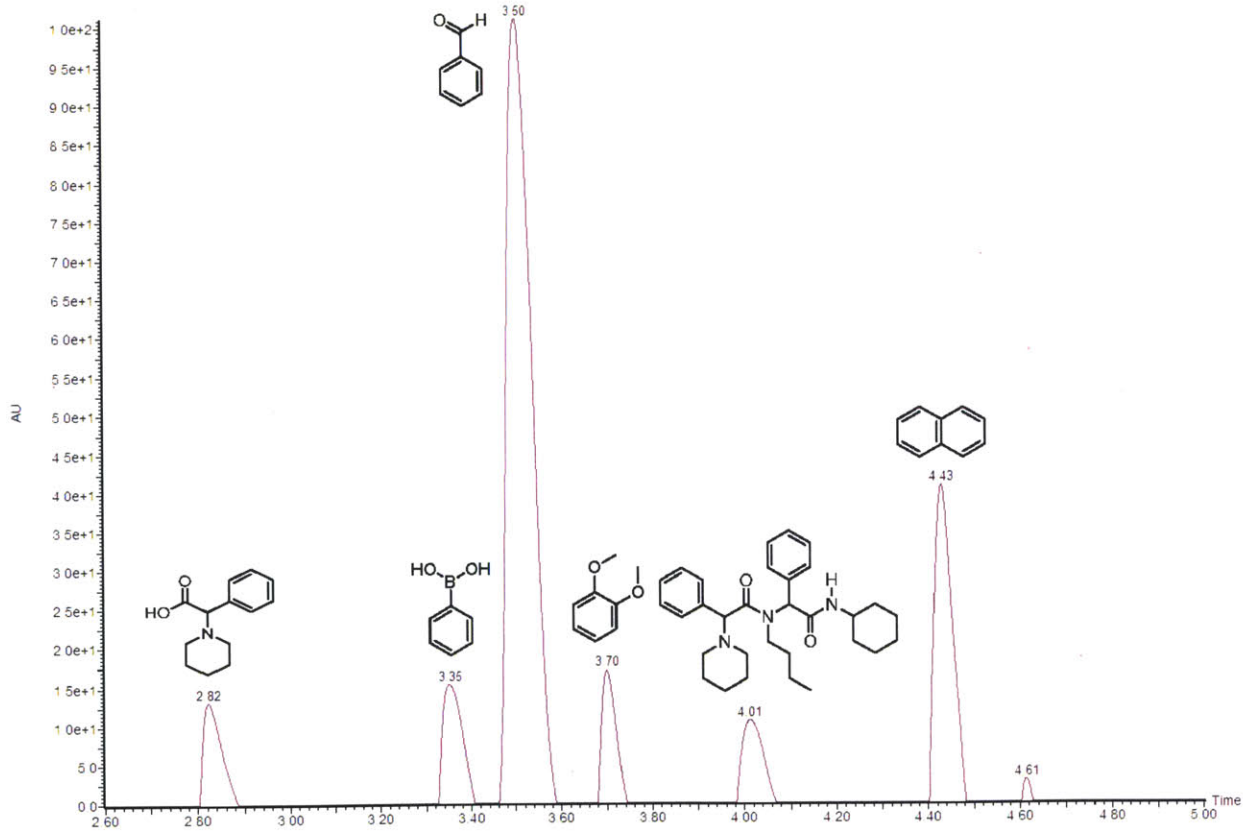

Figure 5.4. Example UPLC spectrum of the Petasis-Ugi tandem reaction.

5.3 RESULTS AND DISCUSSION

In order to explore the characteristics and the potential of a Petasis-Ugi tandem reaction conducted in continuous microflow, this study aimed at the optimization of the reaction conditions and the determination of the reaction kinetics. Besides gaining general knowledge about the reaction, this enabled the identification of rate-limiting steps in the process and the determination of activation energies.

5.3.1 OPTIMIZATION OF THE PETASIS REACTION

5.3.1.1 Morpholine, salicylaldehyde, and phenylboronic acid

The Petasis reaction of morpholine, salicylaldehyde, and phenylboronic acid shown in Scheme 5.5 was studied first. The results of these series of measurements are presented in Figure 5.5. The graphs show the yield of the desired product and formation of a side product at varying temperatures, T, and reaction times, τ. The graph of the yield forms a clear peak that is shifted to lower temperature at longer residence time. The maximum yield is about 10 % lower at a residence time of 5 min than at 10 min. The graph representing the side product formation steadily increases with temperature and is shifted to lower temperature at longer residence time. Figure 5.5 (b) shows a similar form, with a maximum in yield that is shifted to shorter residence times with increasing temperature.

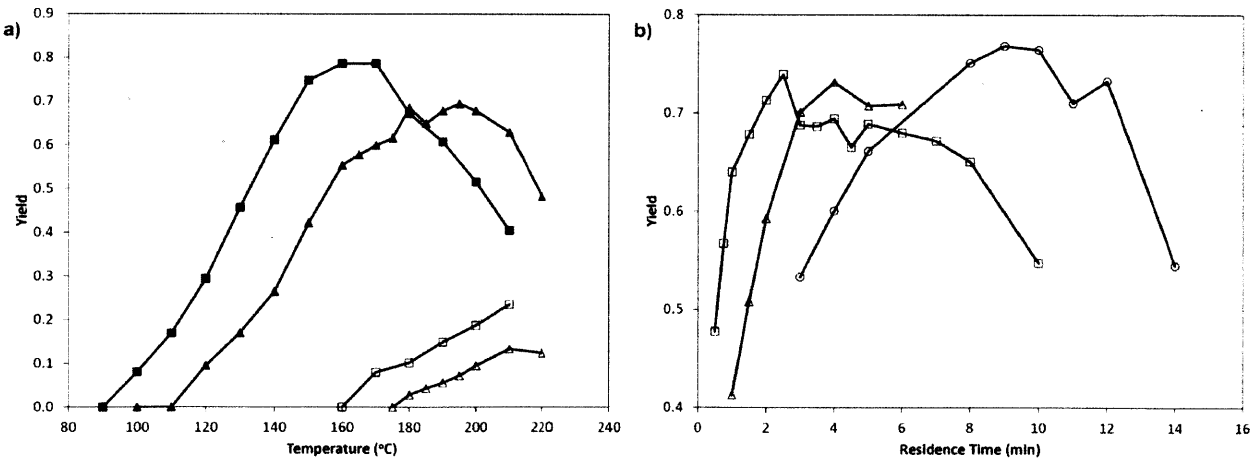

Figure 5.5. Petasis reaction of 0.3 M morpholine, 0.1 M salicylaldehyde, and 0.1 M phenylboronic acid in DMF.a) Yield desired product 10 min (■), yield desired product 5 min (▲), yield side product 10 min (□), yield side product 5 min (△). b) Yield of desired product at 200 °C (□), 180 °C (△), 160 °C (○).

5.3.1.2 Piperidine, glyoxylic acid, and phenylboronic acid

The Petasis reaction of piperidine, glyoxylic acid, and phenylboronic acid (Scheme 5.6) showed similar characteristics (Figure 5.6). The yield of the desired product forms a clear peak with varying temperature at a constant residence time. In analogy to the reaction of salicylaldehyde, morpholine, and phenylboronic acid, the formation of a side product was detected again. In addition to the yield of the desired product and the signal of the side product, Figure 5.6 shows the conversion of the reaction based on the concentration of phenylboronic acid. The curve representing the conversion forms a peak reaching a maximum at the same temperature as the yield.

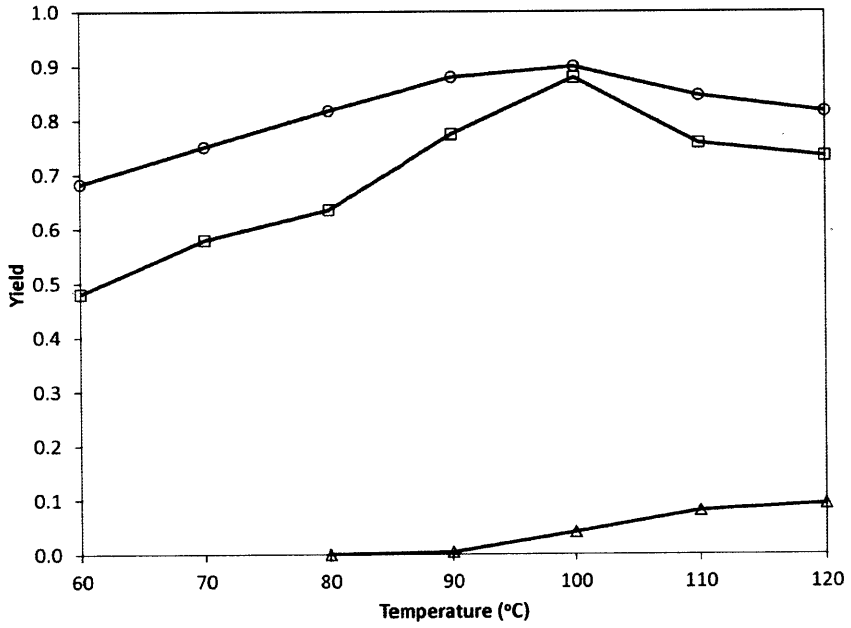

Figure 5.6. Petasis reaction of 1.2 M glyoxylic acid, 1.2 M piperidine, and 1.0 M phenylboronic acid in DMSO with 10 % TFA at a residence time of 3.5 min.Conversion (O), yield (□), side product (△).

Figure 5.7 shows the results of a series of measurements that was conducted at a lower temperature range, a longer residence time, and a slightly higher concentration of glyoxylic acid and piperidine than the one presented in Figure 5.6. Both curves representing the yield of the desired product and the conversion on the basis of phenylboronic acid show a steady increase with temperature. A maximum was not reached within the examined temperature range. Although the desired product was not formed at all below a temperature of about 45 °C, the

conversion was already at a constant value of nearly 60 % at this temperature. The conversion began rising at the temperature that corresponds to the start of formation of the desired product.

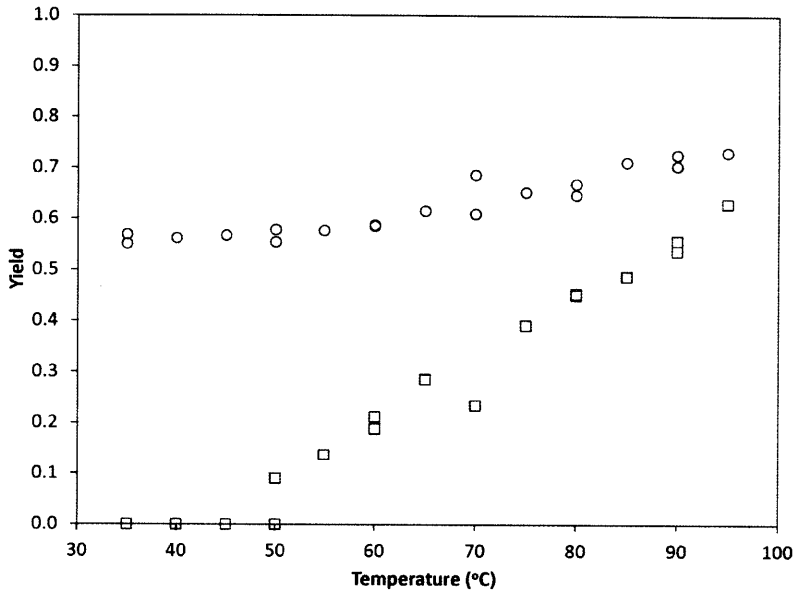

Figure 5.7. Petasis reaction of 1.5 M glyoxylic acid, 1.5 M piperidine, and 1.0 M phenylboronic acid in DMSO with 12 % TFA at a residence time of 10 min.Conversion (O), yield (□).

5.3.2 INTERPRETATION OF THE EXPERIMENTAL DATA

A common feature of both Petasis reactions is the peak in yield at varying temperature. As can be seen in Figure 5.5 (a) and Figure 5.6, the detected side product started to form approximately at the same temperature at which the yield began to decrease. It can be concluded that the side product is the result of a thermally induced decomposition reaction either of the desired product or of one of the reagents. As the plotted conversion in Figure 5.6 is determined on the basis of the concentration of phenylboronic acid, the conversion curve indicates that at temperatures higher than 100 °C, less phenylboronic acid is consumed by the reaction with increasing temperature. Thus, phenylboronic acid cannot be consumed in the side product formation.

From Figure 5.7, as the conversion is already at a high level of about 60 % at such low temperatures where the desired product was not formed at all, the phenylboronic acid must be consumed in a reversible process that takes place even at low temperatures. A possible explanation is that phenylboronic acid participates in a preliminary equilibrium reaction with one of the other reagents or with the intermediate imine.

The curves in Figure 5.5 (b) allow a conclusion on the overall mechanism of the Petasis reaction. After reaching a maximum, the yield continuously decreased with longer residence times, so the side product formation is an irreversible reaction. A thermal decomposition process would be a consistent explanation for the observed yield curves.

Comparing the series of measurements on the two different Petasis reactions, it can be stated that glyoxylic acid, piperidine, and phenylboronic acid react to the desired product at significantly lower temperatures than salicylaldehyde, morpholine, and phenylboronic acid. The similar curves exhibit a large temperature shift, especially considering that the second Petasis reaction was run at shorter residence time than the first. Furthermore, the maximum yield that could be accomplished was about 10 % higher in the reaction of glyoxylic acid, piperidine, and phenylboronic acid.

5.3.3 Optimization of the Petasis-Ugi tandem reaction

Figure 5.8 shows the results of the Petasis-Ugi tandem reaction. The formation of two different side-products could be detected. In this case, the conversion of the reaction was calculated on the basis of the concentration of the aminoacid that was formed by the Petasis reaction and acted as a reagent in the successive Ugi reaction. In this series of measurement, just the temperature of the Ugi reaction was varied, keeping the conditions in the Petasis reaction and the residence time in the Ugi reaction constant.

The curve of the the desired product in Figure 5.8 forms a peak with the maximum at about 115 °C. Similar to the Petasis reaction, a side product was formed, corresponding to the decreasing yield of the desired product at higher temperatures. At 140 °C, the formation of a second side product was detected, further reducing the yield of the desired product.

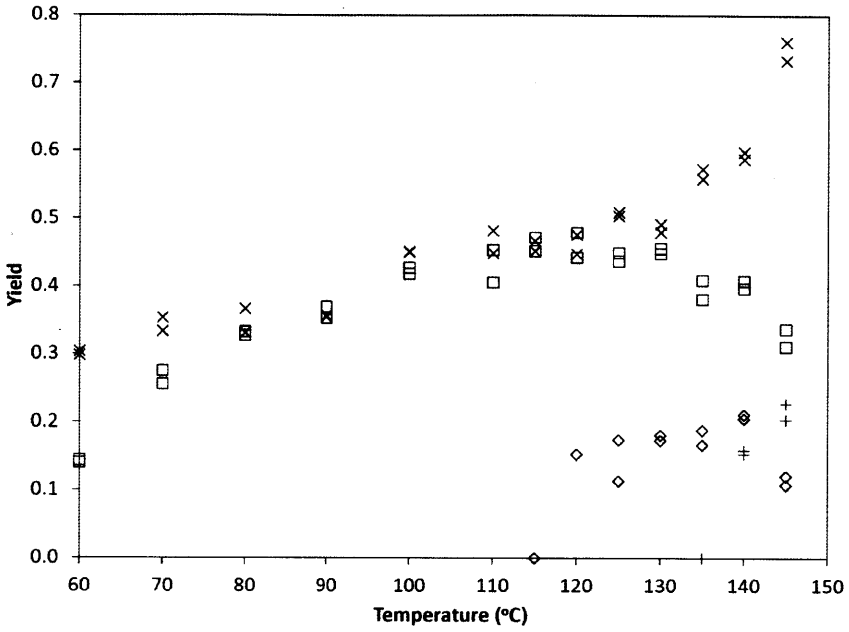

Figure 5.8. Petasis-Ugi tandem reaction of 1.2 M glyoxylic acid, 1.2 M piperidine, 1.0 M phenylboronic acid, and 1.2 M benzaldehyde, 1.2 M n-butyl amine, 1.0 M cyclohexylisocyanide in DMSO with $T_{Petasis}$ = 100 °C, $\tau_{Petasis}$ = 10 min, τ_{Ugi} = 6.66 min. Conversion (✕), yield (□), side product 1 (◇), side product 2 (+).

5.3.4 Kinetic Characterization of the Petasis Reaction

The proposed mechanism of the Petasis reaction involves a number of bimolecular reactions and the rearrangement of transition states. Although the basic steps of the mechanism cannot be directly observed, the gathered data of the overall reaction allowed a number of conclusions on the underlying elementary processes. As the rate of the overall reaction is limited by the slowest step in the mechanism, the comparison of the experimental data with several theory-based kinetic models enables the identification of the rate-limiting step. In the following, the fit of the data to three different kinetic models, given in Table 5.1, is evaluated based upon conversion, X, and the ratio of non-equimolar starting reagents, M.

Table 5.1. Rate laws depending upon rate-limiting step.

Rate-Limiting Step	Rate Law
1st-Order	$\ln(1-X)$
2nd-Order Non-Equimolar	$\ln\frac{M-X}{M(1-X)}$
2nd-Order Equimolar	$\frac{X}{1-X}$

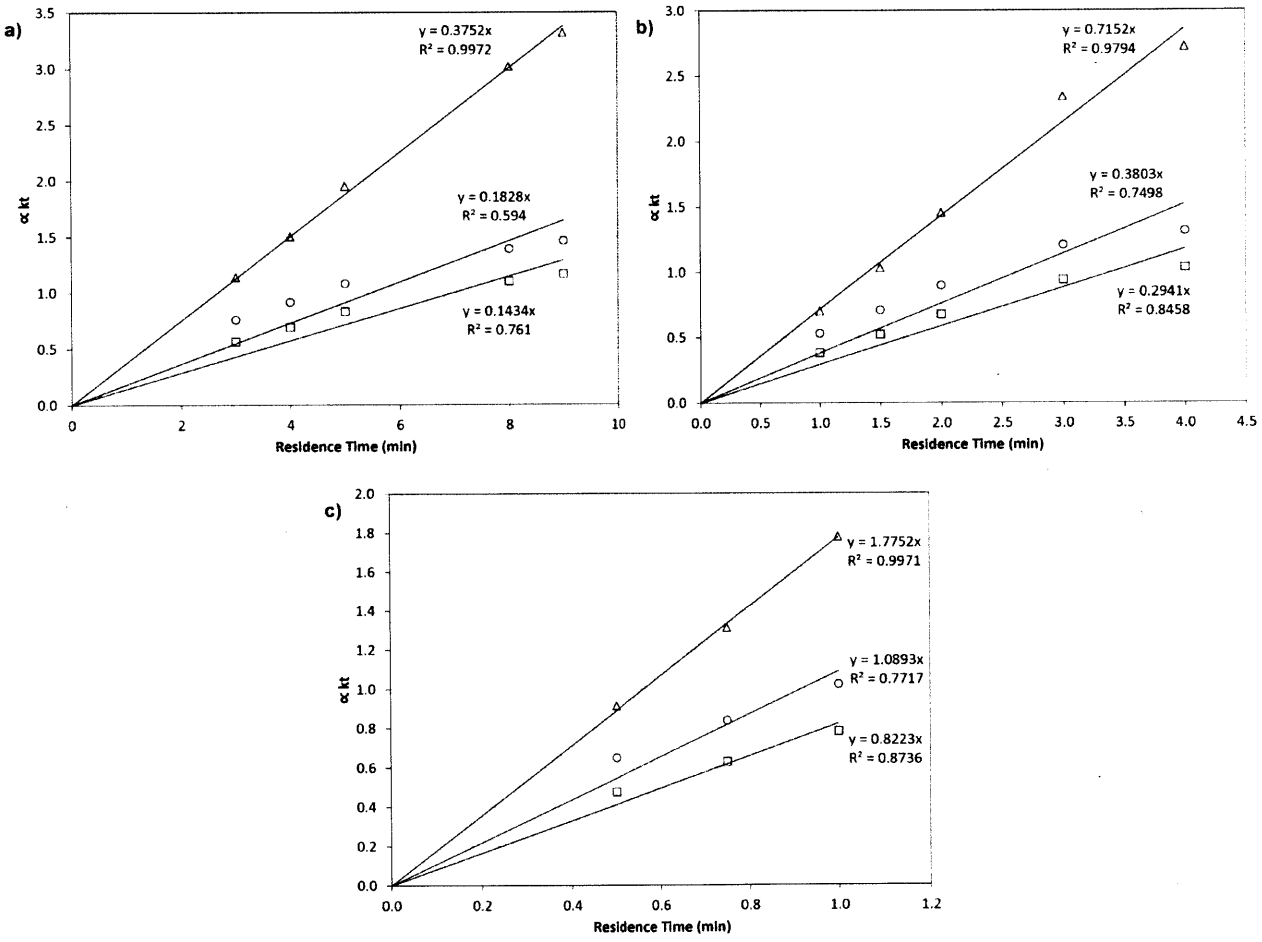

Figure 5.9. Application of different kinetic models to the experimental data of the Petasis reaction of salicylaldehyde at a) 160 °C, b) 180 °C, and c) 200 °C.First-order (O), second-order non-equimolar (□), second-order equimolar (△) rate-limiting step.

For the reaction of 0.1 M salicylaldehyde, 0.3 M morpholine and 0.1 M phenylboronic acid, Figure 5.9 indicates that the kinetic model of a 2nd-order equimolar has the highest coefficient of determination, R^2, and does not exhibit significant trend about the line of best fit for all three temperatures. Salicylaldehyde and morpholine, which react in the first step of the mechanism, were employed in concentrations differing by the factor 3. For this reason, it can be excluded that the rate-limiting step of the overall reaction is the reaction of the intermediate imine with the phenylboronic acid. This complies with the experimental observation that the combination of dissolved salicylaldehyde and morpholine caused significant heating of the solution, implying a fast exothermic reaction.

5.3.5 ACTIVATION ENERGIES

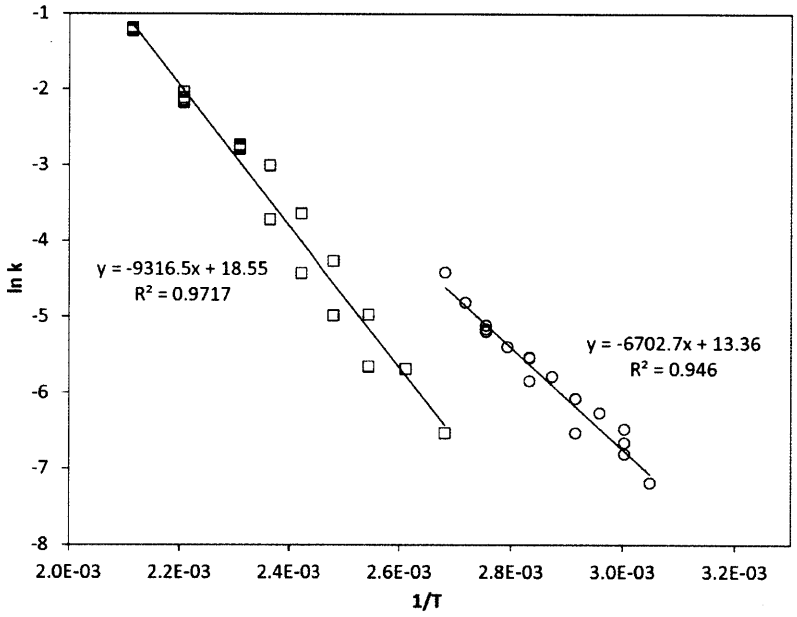

Figure 5.10. Arrhenius plot of ln k versus 1/T used to determine the activation energy of the Petasis reaction of salicylaldehyde (□) and the Petasis reaction of glyoxylic acid (○).

Figure 5.10 shows the Arrhenius plot for both Petasis reactions, which was used to determine the activation energies given in Table 5.2. The activation energy of the reaction of salicylaldehyde, morpholine, and phenylboronic acid is over 20 kJ/mol higher than the one of glyoxylic acid, piperidine, and phenylboronic acid. This agrees with the observation that reaction of salicylaldehyde required significantly higher temperatures than glyoxylic acid, which is consistent with the literature, which states that glyoxylic acid shows a higher reactivity in the Petasis reaction than salicylaldehyde.[114]

Table 5.2. Activation energies for the Petasis reactions.

Reaction	E_a (kJ/mol)
Salicylaldehyde	-77.5 ± 2.9
Glyoxylic Acid	-55.7 ± 3.3

Assuming that the initial step of the Ugi reaction to form the imine is the rate-limiting step, a similar kinetics analysis can performed, resulting in the Arrhenius plot in Figure 5.11, which yields an activation energy of 20.2 ± 1.6 kJ/mol.

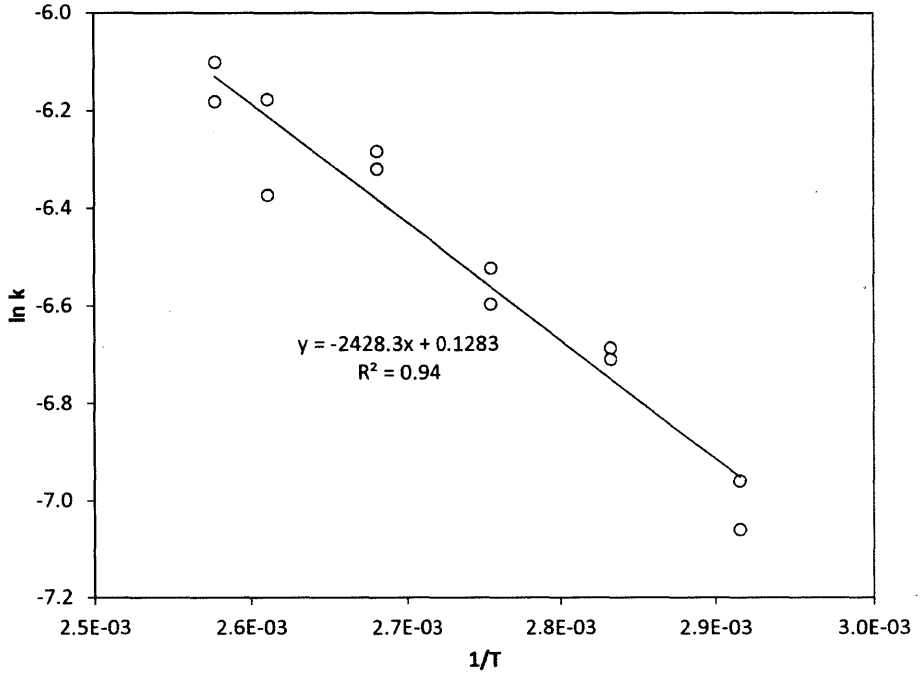

Figure 5.11. Arrhenius plot of the Ugi reaction of the Petasis product.

5.4 CONCLUSION

The serial combination of a Petasis and an Ugi multicomponent reaction was accomplished in a continuous flow microreactor setup. The employed small-scale equipment enabled the conduction of extensive chemical studies in a cost-effective and environmentally-friendly manner by significantly reducing the consumption of reagents and solvents. The Petasis-Ugi tandem reaction was examined by successively conducting experiments on the individual reactions in batch and microflow, followed by a series of measurements on the combined

reaction in serially connected microreactors. Characteristic properties of the Petasis reaction were identified by conducting similar experiments on two different examples. By variation of temperature and residence time and measurement of the resulting yields of the desired product, the optimal conditions for the conducted reactions were determined. Furthermore, the gathered data were kinetically interpreted in order to identify rate-limiting steps, determine activation energies, and evaluate the proposed mechanisms.

6 AUTOMATED MICROCALORIMETRY USING SILICON MICROREACTORS AND ONLINE IR ANALYSIS

6.1 INTRODUCTION

Silicon microreactors are being increasingly used for early process development, as they confer a number of advantages over larger scale flow and batch systems. The small reactor volume minimizes the consumption of starting materials7 and allows for the safer handling of more hazardous reactions.

[38] The small length scales allow fast radial mixing, rapidly reducing concentration gradients2,[13] and leading to low axial dispersion, except at very short residence times.[10] Furthermore, the small length scales combined with the high heat transfer of silicon allow internal temperature gradients to be significantly reduced and allow rapid changes between temperatures.[1, 3] In combination, these characteristics allow for a more intrinsic and complete understanding of a reaction being studied due to the high degree of control achievable.

Previous chapters utilized a continuous flow silicon microreactor system combined with automated setpoint control and inline monitoring for a number of applications. Incorporating intelligent, robust optimization algorithms and continuously assessing approach to steady state increased the efficiency of reaction optimizations in a design space with a complex objective function.[72] Time-course kinetic data, as typically results from batch reactions, were generated rapidly in flow by continuous residence time manipulation. Reaction conditions were quickly screened, and activation energy was determined by a continuous temperature ramp. In these ways and others, microreactors are most beneficial to discovery and early development of reactions.[125] However, once these initial studies have been completed, if the chemistry is desired to be scaled to significant production levels, more traditional flow reactors will often be necessary.[39] While these previous works have increased the ability to determine optimal conditions and generate kinetic models for scaling, a thermodynamic analysis is also necessary when moving away from the rapid heat transfer of silicon microreactors. To this end, the ability to perform calorimetry utilizing the previously introduced online control and monitoring techniques was investigated.

Existing reaction calorimetry is typically done in batch on the scale of several milliliters to a liter and examines reaction kinetics by fitting a model to a heat flow curve[126, 127], although use of *in situ* measurement techniques, such as FTIR, have been demonstrated.[128-130] Microliter-scale flow calorimeters also exist, but tend to require a significant amount of specialized fabrication.[131-135] For this work, it was desired to see if by simply modifying the current microreactor automation system it would be possible to perform flow microcalorimetry without the need for additional fabrication. Two well-known examples of exothermic reactions were investigated: the nitration of benzene (Scheme 6.1)[136, 137] and a Paal-Knorr reaction (Scheme 2.1).[60-62]

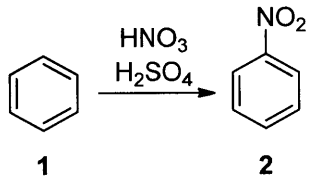

Scheme 6.1. Benzene nitration.

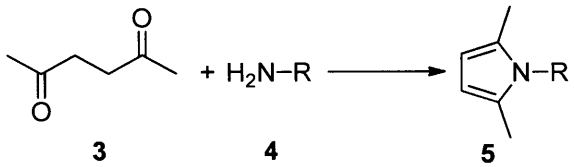

Scheme 6.2. Paal-Knorr reaction. 4a – R = -CH_2CH_2OH. 4b – R = Me.

6.2 EXPERIMENTAL SECTION

The microfluidic system used in this work is similar to the previous systems;[72] however, the hot reaction zone of the reactor is now sandwiched between two thermoelectric (TE) elements (Tellurex G1-44-0333) and two separately controlled aluminum heating blocks and the whole system insulated, as depicted in Figure 6.1. This figure also shows the location of thermocouples to continuously measure temperature, including on the schematic of the 140-μL silicon microreactor.[65, 66]

Three Harvard syringe pumps (PHD 2000) were used to control the residence time. The flow rates were updated *via* daisy-chained RS-232 communications to a Dell (Optiplex 960) computer. The inlet/outlet zone was cooled with a recirculating Thermo Scientific chiller (model AC 200) set to 0 °C, which allowed the reactant streams to mix fully before reaction occurred,

thermally quenched the reaction, and acted as a controlled heat sink. The temperature of the reaction zone was controlled with two Omega (CN9311) controllers and Omega (CSH-102135/120V) heating cartridges, one in each aluminum heating chuck. These controllers were connected through RS-232 cables to the computer to program the temperature setpoint, which was always the same for both controllers. A Mettler Toledo ReactIR iC 10 outfitted with a DiComp ATR 10-μL flow cell[48] was used for continuous inline monitoring of reaction conversion. Labview software (version 8.5.1) on the computer communicated with the syringe pumps and temperature controllers. Matlab scripts (version 2010b) within Labview controlled the reaction temperature setpoints and syringe pump flow rates.

The temperature difference between the two sides of the thermoelectric elements, one side in contact with the heating blocks and the other with the reactor, generates a voltage, which is measured continuously. When an exothermic reaction is occurring within the reactor channel, the temperature difference across the thermoelectric elements is reduced, resulting in a change in the measured voltage. Comparison of the stability in the measured temperature difference and the thermoelectric voltage is discussed below.

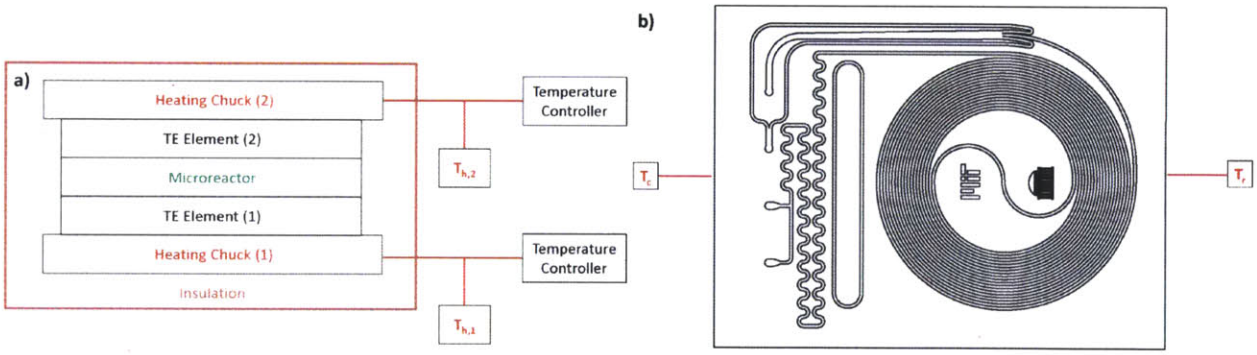

Figure 6.1. Schematic of microcalorimetry system showing points of temperature measurements on (a) heating chucks and (b) microreactor.

6.2.1 Benzene Nitration

Both heating block temperature controllers were set to 50 °C and the chiller was set to 0 °C. A syringe (NormJect, 5 mL) was filled with pure benzene (3.14 M) and placed on a syringe pump to be infused at 19.581 μL/min. Another syringe (SGE glass, 10 mL) was filled with a nitrating solution of 2 parts H_2SO_4 (from 98% solution) to 1 part HNO_3 (from 70% solution) to be infused at 50.419 μL/min, resulting in a 5% excess of nitric acid in the reactor[138] and a

residence time of 2 min. Chloroform, used to quench the reaction by diluting the organic phase to 2 M benzene/nitrobenzene, was flowed at 109.86 μL/min from a third syringe (SGE glass, 50 mL). A 5 psi backpressure regulator was connected to the outlet. Chloroform was chosen as the quench because it has been shown to be inert to nitrating solution.[139] After initial thermal equilibration, monitoring of the voltage across the thermoelectric elements was started 30 min prior to starting syringe pumps. Total reagent volumes were chosen to allow chloroform to continue flowing after the reaction had completed to generate a voltage baseline under flow conditions with no reaction. The baseline difference between only quench flow and reagent flow replacing the nitrating solution with water was found to be insignificant. IR monitoring was not possible due to the inability to measure only one phase. Thus, GC analysis was used to quantify conversion.

6.2.2 Paal-Knorr Reaction

An initial reaction (see Figure E.3) was performed with 2,5-hexanedione and ethanolamine (5.63 M both reagents); however, due to the formation of an aqueous phase at high conversion, inline IR monitoring proved problematic. Thus, a Paal-Knorr reaction was performed replacing the ethanolamine with methylamine (33 wt% in ethanol). Both heating block temperature controllers were set to 50 °C and the chiller was set to 0 °C. A syringe (Harvard Stainless, 8 mL) was filled with hexanedione to be infused at 35 μL/min. Another syringe (Harvard Stainless, 8 mL) was partially filled with 6 mL methylamine in ethanol (diluted to 8.52 M) to be infused at 35 μL/min, resulting in a reaction concentration of 4.26 M of both reagents and a residence time of 2 min. A third syringe (Harvard Stainless, 50 mL) was partially filled with 25 mL ethanol to flow at 79.181 μL/min to quench the reaction by dilution to 2 M total hexanedione and product. A 20 psi backpressure regulator was connected to the outlet. After initial thermal equilibration, monitoring of the voltage across the thermoelectric elements was started 30 min prior to starting syringe pumps. Total reagent volumes were chosen to allow ethanol and hexanedione to continue flowing after the reaction had completed to generate a voltage baseline under flow conditions with no reaction. The baseline difference between these conditions and flow at reaction flow rates replacing the methylamine solution with ethanol was found to be insignificant.

6.2.3 *Heat of Reaction Quantification*

The heat of reaction was calculated by performing an energy balance around the calorimeter both with and without reaction (Figure 6.2) and comparing the results. Assuming that the relationship between the temperature differences across the thermoelectric element is linearly related to the voltage produced within the range studied, the best-fit line will be of the form

$$V = a(T_h - T_r) + b \tag{6.1}$$

where V is the measured voltage, T_h is the hot side temperature averaged between the two thermoelectric elements, T_r is the measured reactor temperature, and a and b are the calculated fit parameters. For the baseline,

$$V_0 = a(T_h - T_r)\big|_{X=0} + b \tag{6.2}$$

where V_0 is the baseline voltage and the temperatures are those when conversion, X, is 0. Performing the energy balance then results in

$$\Delta q = \left(\frac{kA}{d}\right)_{TE} \frac{V - V_0}{a} \tag{6.3}$$

where Δq is the change in heat flow, k is the thermal conductivity of the thermoelectric element, A is the area (1600 mm^2 × 2 elements), and d is the thickness (3.2 mm). The thermal conductivity was taken from the literature to be 1.2 W/(m·K).[140] The heat of reaction, ΔH_r, can then be calculated by

$$\Delta H_r = \frac{\Delta q}{CXQ} \tag{6.4}$$

where C is the reaction concentration and Q is the flow rate. In the case of no reaction, the heating chucks provided all the heat required to maintain the reactor temperature. However, during reaction, the necessary heat input required was reduced as the reaction provided some of the energy necessary. Note that the flow rate affected the heat flow from the reactor to the cooling chuck, q_c. Thus, the baseline voltage was always found under flow conditions but without reaction.

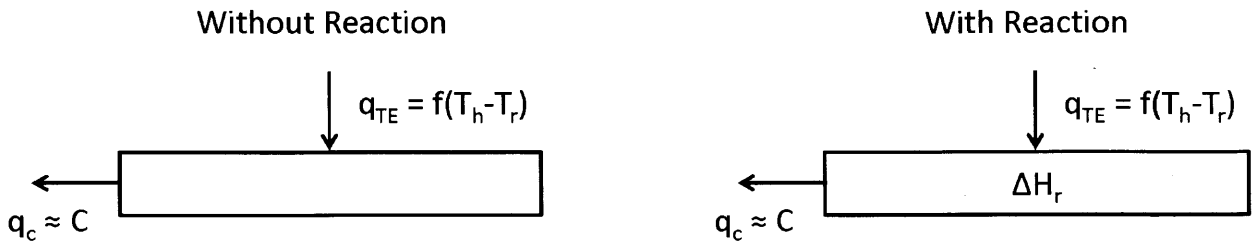

Figure 6.2. Microcalorimeter energy balance.

6.3 Results and Discussion

The nitration of benzene was used initially to test the capability of the system to measure changes in heat flux through the reactor. The thermoelectric output (Figure 6.3) significantly decreased at the start of reaction and remained near this level until one of the reagents were depleted, at which time the measured voltage returned to approximately the same level as before the reaction. The correlation between voltage and temperature difference was indeed shown to be largely linear as assumed (see Figure E.1 and Figure E.2). The resulting heat balance, calculated by Eq. 6.3, is summarized in Table 6.1. The heat of reaction was calculated to be -118.6 ± 2.4 kJ/mol (1 standard deviation) by averaging the voltage difference between the two thermoelectric output levels. This range includes the literature value for the heat of reaction of -117 kJ/mol.[141] Thus, the microcalorimeter could be used to accurately determine the heat of reaction.

However, the thermoelectric output of the benzene nitration showed significant noise due to short-term oscillations in liquid-liquid flow, as depicted in the inset of Figure 6.3. Additionally, the reaction conversion could not be measured online.

A Paal-Knorr reaction of 2,5-hexanedione and methylamine in ethanol was chosen in an effort to increase the signal-to-noise ratio and allow for online monitoring by IR analysis. The results for the thermoelectric output and the measured conversion are given in Figure 6.4 and Figure 6.5, respectively. The same heat balance analysis was performed (Table 6.2), producing a calculated heat of reaction of -50.2 ± 3.3 kJ/mol. As this analysis requires measuring the temperature on both sides of the thermoelectric elements, it could be argued why the thermoelectric element is necessary at all. However, as Figure 6.6 illustrates, there was significantly less noise in the thermoelectric output voltage than in the temperature measurement due to oscillations in the hot side temperatures caused by interaction of the two temperature

controllers. Averaging the output of the two thermoelectric elements in combination with the output voltage corresponding to the average temperature difference across the elements rather than at a single point also reduced the noise in voltage.

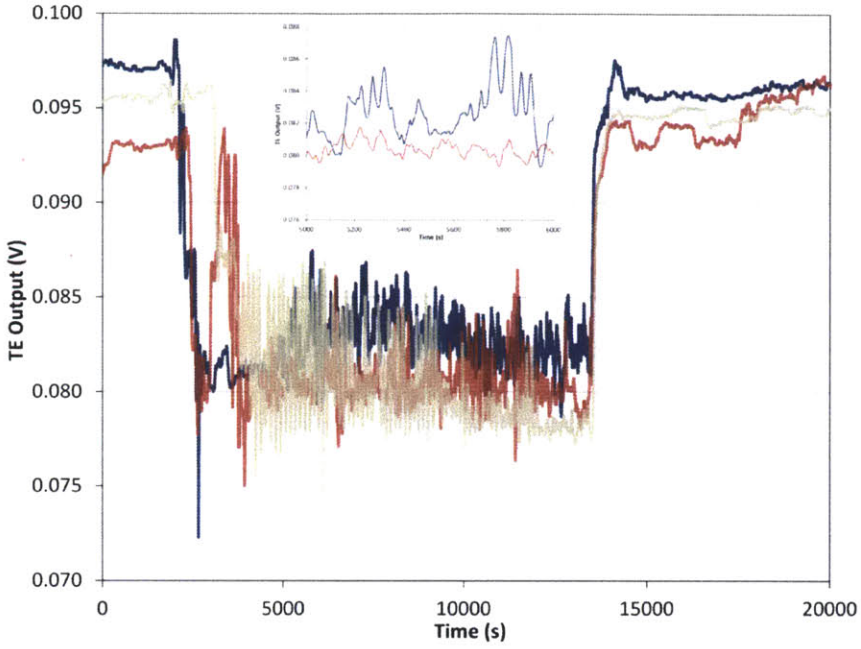

Figure 6.3. Benzene nitration thermoelectric output for repeat 1 (dark blue), 2 (red), and 3 (tan). Inset shows the level of oscillations due to slug flow oscillations.

Table 6.1. Summary of benzene nitration results.

Repeat	**1**	**2**	**3**	**Average**
Δq (W)	-0.311	-0.304	-0.281	-0.299
X	0.721	0.710	0.632	0.688
ΔH_r (kJ/mol)	-117.8	-116.7	-121.3	-118.6 ± 2.4

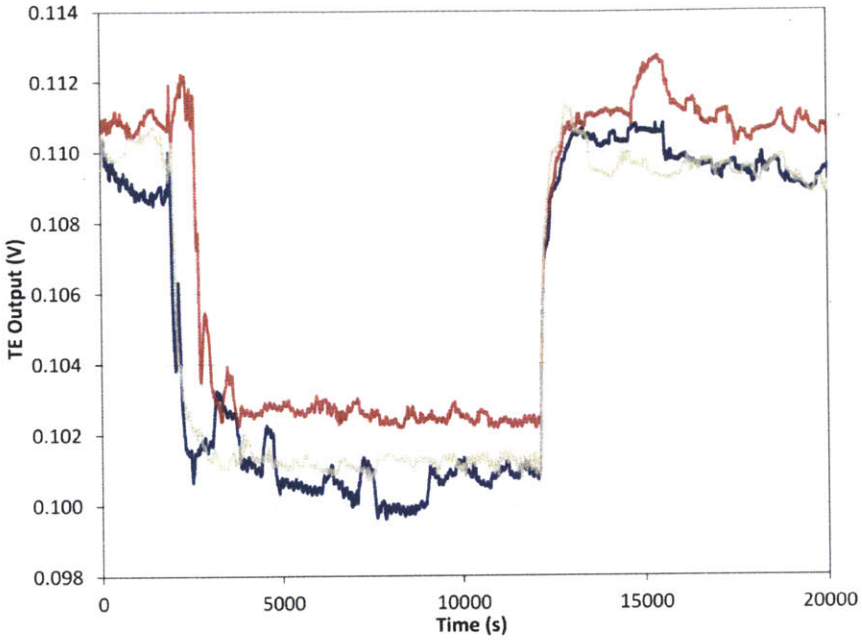

Figure 6.4. Paal-Knorr thermoelectric output for repeat 1 (dark blue), 2 (red), and 3 (tan).

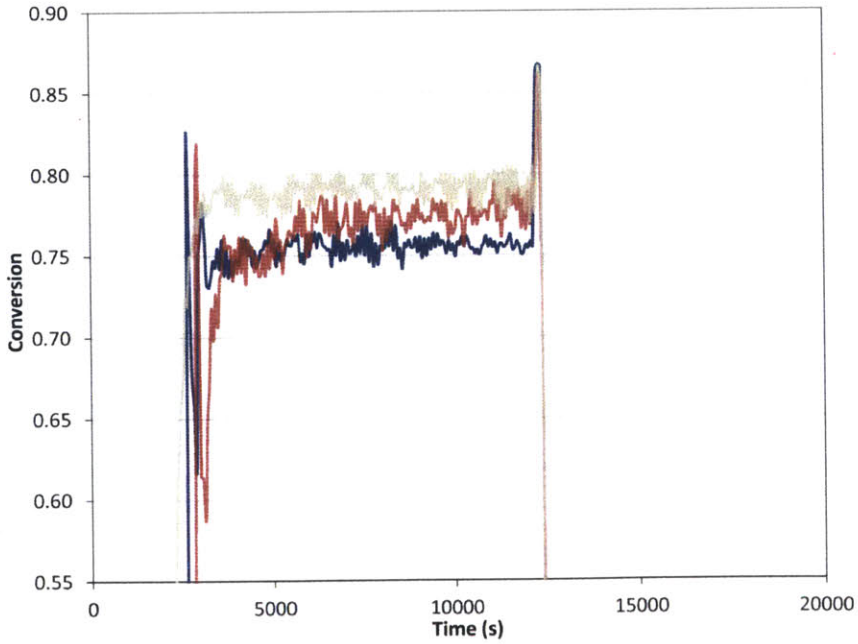

Figure 6.5. Paal-Knorr conversion for repeat 1 (dark blue), 2 (red), and 3 (tan).

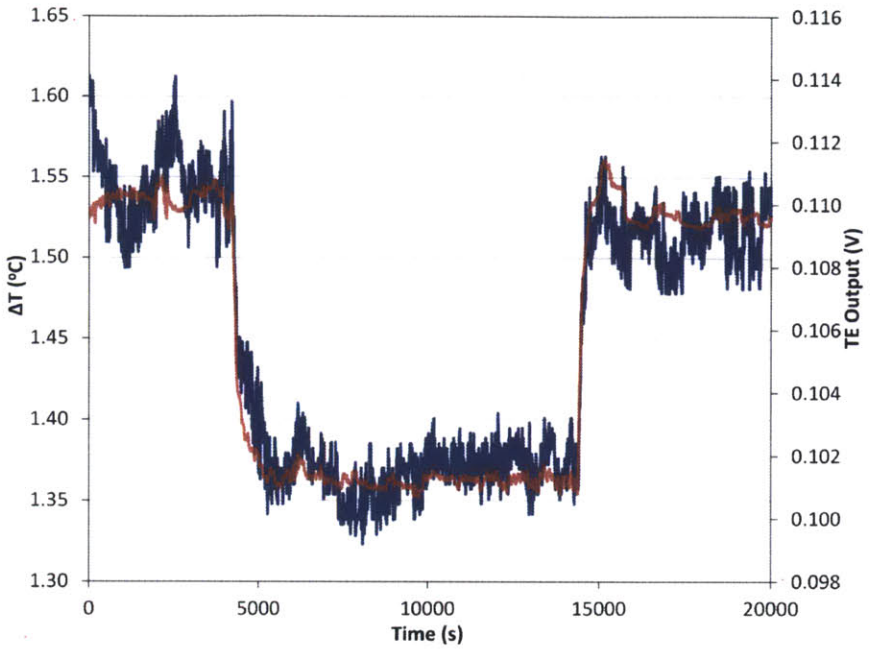

Figure 6.6. Paal-Knorr temperature difference across thermoelectric elements (dark blue) and thermoelectric output voltage (red) for repeat 3.

Table 6.2. Summary of Paal-Knorr results.

Repeat	1	2	3	Average
Δq (W)	-0.201	-0.179	-0.196	-0.299
X	0.755	0.768	0.790	0.771
ΔH_r (kJ/mol)	-53.5	-46.9	-50.1	-50.2 ± 3.3

To further test the capabilities of the microcalorimeter, a residence time ramp experiment was performed starting from an initial residence time of 0.5 min and gradually increasing the residence time, τ, by 0.05 minutes per minute of experiment time. This procedure was repeated three times during the experiment (Figure 6.7). As flow rate through the microcalorimeter affects the heat transfer, causing $(T_h\text{-}T_r)|_{X=0}$ to change with time, a baseline experiment was also run where the methylamine in ethanol solution was replaced with only ethanol. The resulting thermoelectric output is shown in Figure 6.8, which exemplefies the effect of flow rate on the baseline voltage. Conversion was measured continuously by inline IR and used to calculate the heat of reaction by Eq. 6.4 (Figure 6.9). The heat of reaction oscillates approximately 5 kJ/mol around 50 kJ/mol, in agreement with the previous results.

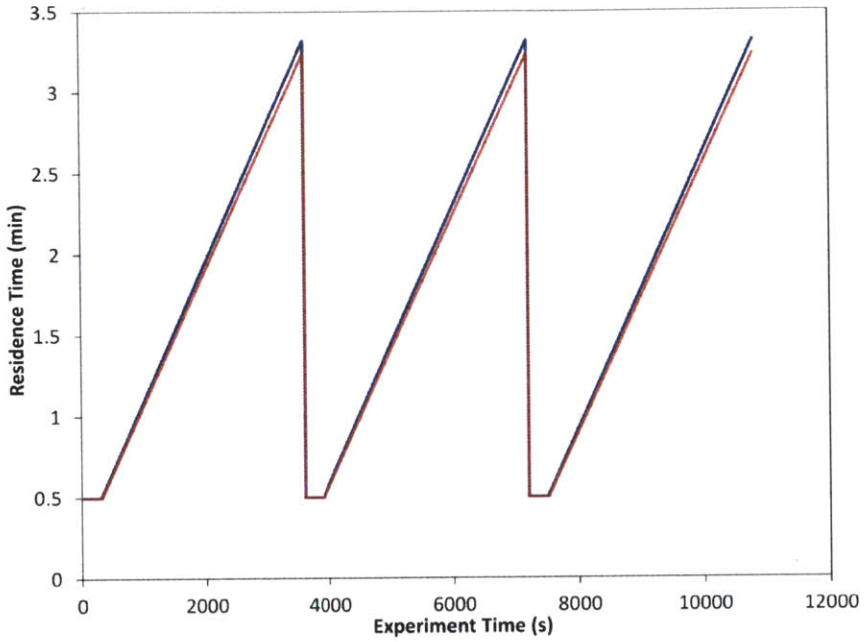

Figure 6.7. Residence time ramp: τ_{ins} (dark blue) and τ (red).

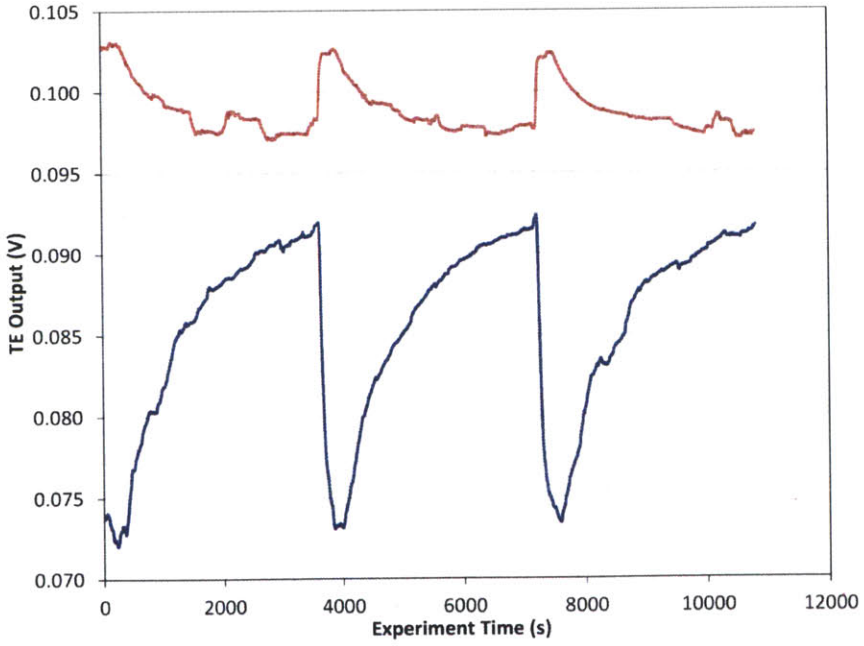

Figure 6.8. Residence time ramp thermoelectric output: reaction (dark blue) and baseline (red).

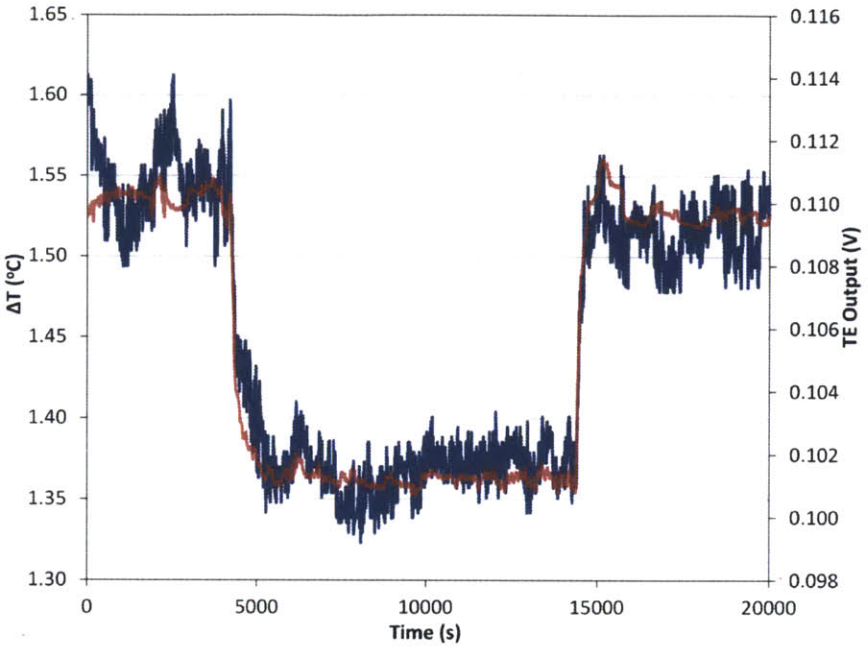

Figure 6.6. Paal-Knorr temperature difference across thermoelectric elements (dark blue) and thermoelectric output voltage (red) for repeat 3.

Table 6.2. Summary of Paal-Knorr results.

Repeat	1	2	3	Average
Δq (W)	-0.201	-0.179	-0.196	-0.299
X	0.755	0.768	0.790	0.771
ΔH_r (kJ/mol)	-53.5	-46.9	-50.1	-50.2 ± 3.3

To further test the capabilities of the microcalorimeter, a residence time ramp experiment was performed starting from an initial residence time of 0.5 min and gradually increasing the residence time, τ, by 0.05 minutes per minute of experiment time. This procedure was repeated three times during the experiment (Figure 6.7). As flow rate through the microcalorimeter affects the heat transfer, causing $(T_h\text{-}T_r)|_{X=0}$ to change with time, a baseline experiment was also run where the methylamine in ethanol solution was replaced with only ethanol. The resulting thermoelectric output is shown in Figure 6.8, which exemplefies the effect of flow rate on the baseline voltage. Conversion was measured continuously by inline IR and used to calculate the heat of reaction by Eq. 6.4 (Figure 6.9). The heat of reaction oscillates approximately 5 kJ/mol around 50 kJ/mol, in agreement with the previous results.

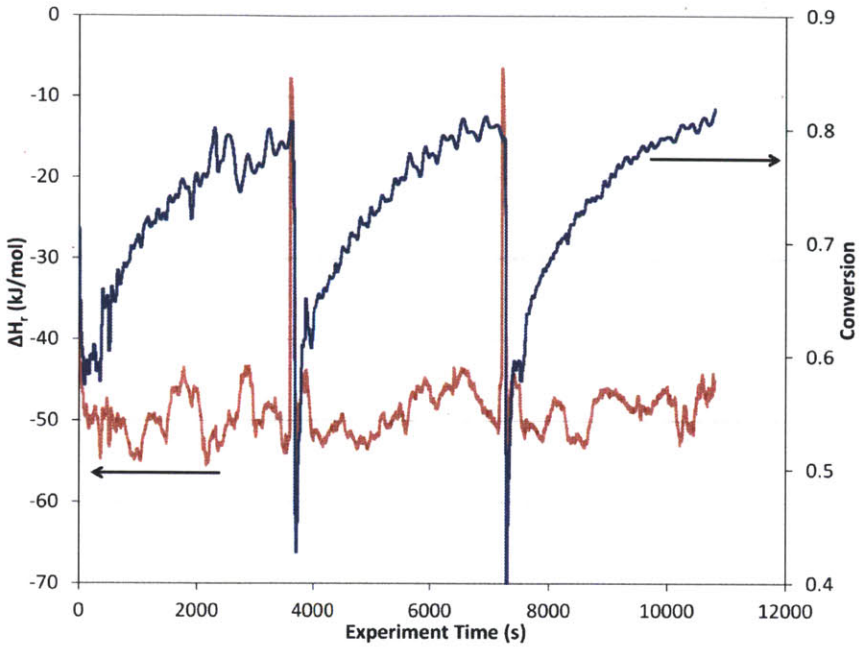

Figure 6.9. Residence time ramp: ΔH_r (red) and X (dark blue).

To investigate the lower bound of the microcalorimeter sensitivity, a concentration ramp Paal-Knorr experiment was then run. In this experiment, rather than changing the residence time of reaction at a constant concentration, the concentration of both reactants was gradually changed from 4 M to 0.25 M and back at a rate of 0.05 M/min at a constant residence time of 2 min (Figure 6.10). This ramp was accomplished by joining the reactant streams with a stream of ethanol from another syringe pump and controlling the flow rates such that the total was constant. The resulting thermoelectric output is given in Figure 6.10. While the noise level in measured thermoelectric output and conversion (see Figure E.4) was relatively constant over the concentration range, this noise is amplified when calculating the heat of reaction as concentration decreased below approximately 2 M (Figure 6.11), corresponding to a voltage difference of 5 mV from baseline and a heat flow difference of 0.1 W.

In an effort to reduce the noise in the thermoelectric output by dampening the noise generated by the on/off temperature controllers, a second heating chuck was designed with a much larger thermal mass (960 J/K vs. 74.5 J/K per side; see Figure 6.12).5 Another concentration ramp experiment was run, but, while the large thermal mass did reduce short-term oscillations in T_h and thermoelectric voltage (Figure 6.13), it also significantly increased the system time constant. This change caused the reactor temperature to vary due to the buildup of heat at maximum reaction concentration. Consequently, the reactor was no longer isothermal across its surface, causing the measured relationship between the temperature difference across the reactor and the thermoelectric voltage to poorly model experimental results. However, having previously characterized this relationship for the thermoelectric elements, the model generated with the smaller chuck could be used. While that relationship assumed a constant heat flow from the reactor to the cooling chuck, the reactor temperature fluctuations in time were two orders of magnitude smaller than this temperature difference, allowing this effect to be neglected. As illustrated in Figure 6.14, the heat of reaction was indeed significantly less noisy, and the lower limit of stable measurement was reduced to approximately 1 M, corresponding to a voltage difference of 2.5 mV from baseline and a heat flow difference of 0.05 W. Additionally, the calculated heat of reaction better centers around 50 kJ/mol, in agreement with the previous results.

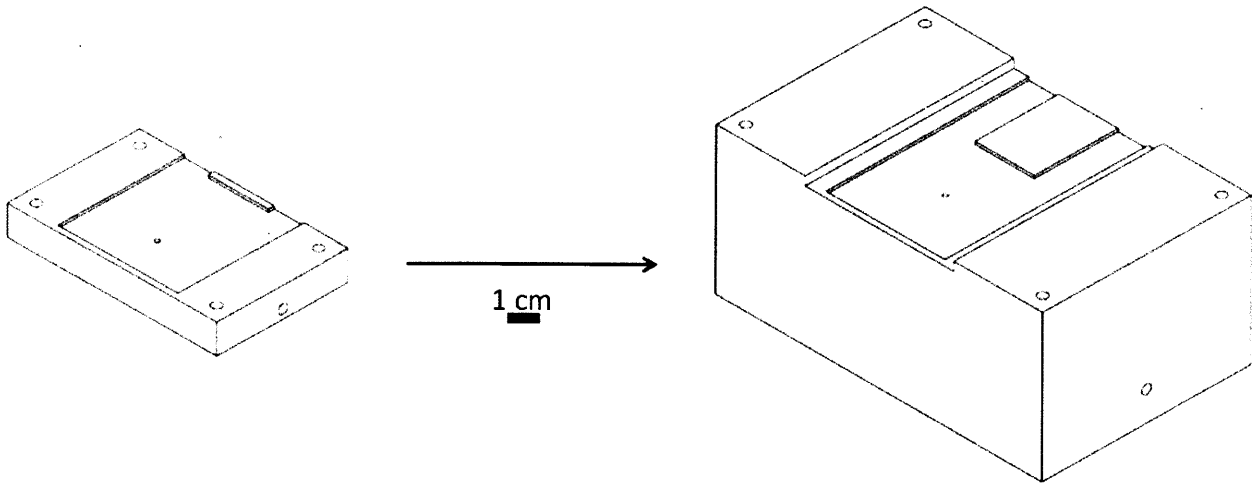

Figure 6.12. Microcalorimeter 1 (left) vs. 2 (right) schematic.

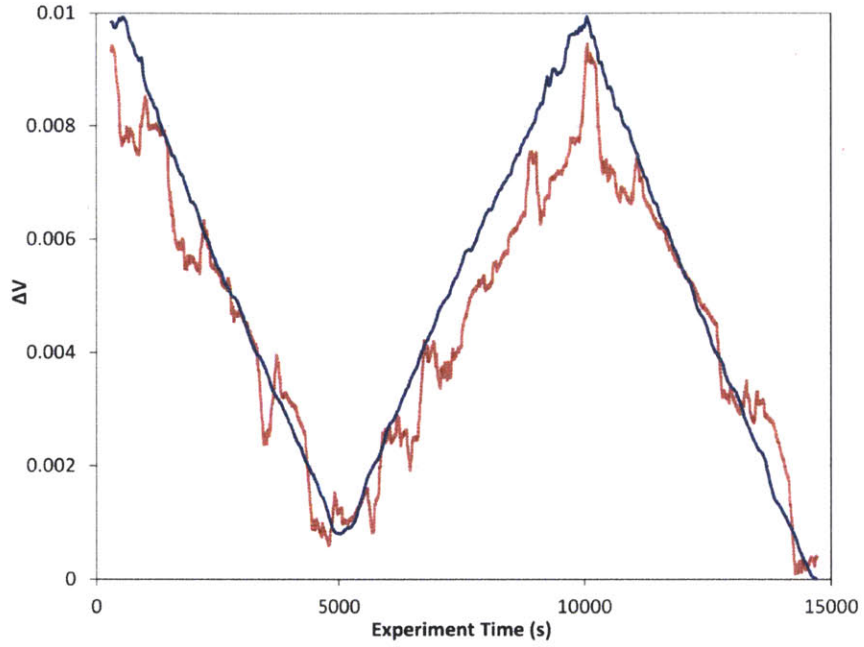

Figure 6.13. Thermoelectric voltage difference during reaction concentration ramp. Microcalorimeter 1 (red) vs. 2 (dark blue).

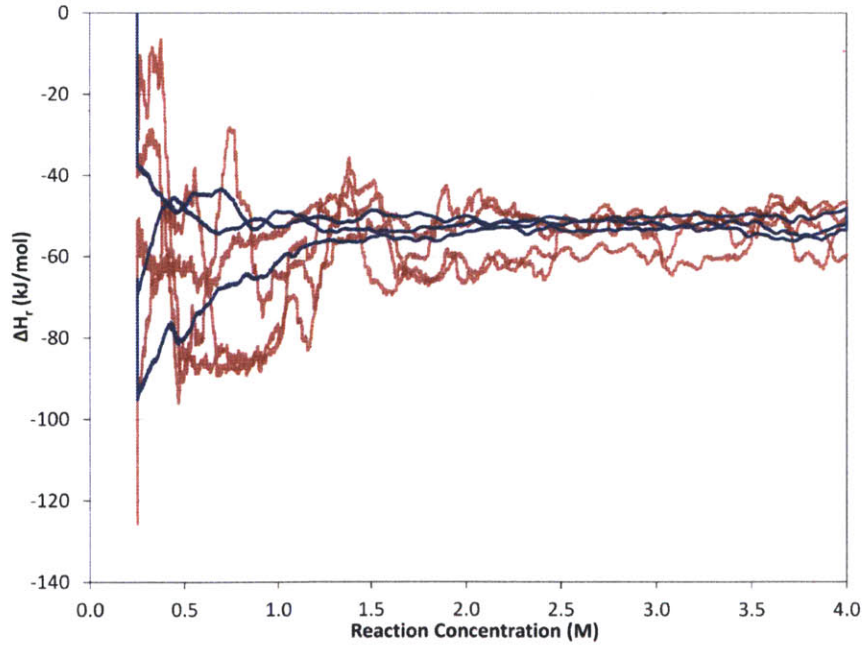

Figure 6.14. Heat of reaction during reaction concentration ramp. Microcalorimeter 1 (red) vs. 2 (dark blue).

6.4 CONCLUSIONS

Microcalorimetry was demonstrated in a flow system by coupling a standard microreactor with off-the-shelf thermoelectric elements, allowing estimation of heats of reaction without the typically necessary specialized fabrication techniques. The heat of reaction of the nitration of benzene was measured to be -118.6 ± 2.4 kJ/mol, in agreement with the literature value of -117 kJ/mol. A single-phase Paal-Knorr reaction was also investigated using steady-state, residence time ramp, and concentration ramp experiments, which all gave heats of reaction of approximately -50 kJ/mol. Lastly, a second-generation calorimeter was used to significantly reduce experimental noise and the lower limit of sensitivity.

7 CONCLUSIONS AND OUTLOOK

7.1 SUMMARY OF THESIS CONTRIBUTIONS

This thesis has centered on the theme of using automation and inline monitoring to increase the efficiency of using microreactor systems to gain new understanding of reactions. Microreactors were chosen as the central element due to their many benefits, including small volume, accurate and rapid temperature control, low dispersion, and increased safety. It is hoped that this work will be built upon to increase the efficiency and speed of development in chemical industry, especially in regard to pharmaceuticals.

In Chapter 2 of this thesis, an automated optimization system was introduced, which utilized online IR analysis of reaction conversion to realize multi-trajectory optimization. Several optimization algorithms were investigated, and a conjugate gradient method incorporating an Armijo-type line search was found to be most efficient. While the primary focus was on maximizing the production rate of a Paal-Knorr reaction, it would be possible to use this same technique for other reactions or other objective functions, as was also demonstrated.

In Chapter 3, the low-dispersion nature of microreactors was employed in combination with controlled flow manipulation to generate time-course "batch" data in flow. It was found that the conversion resulting from this method matched values found from steady-state flow experiments, but these data could be generated much more rapidly using this method. Adding the rapid and precise temperature control of microreactors allowed the generation of a kinetic model in only one automated experiment.

Chapter 4 then focused on the automated investigation of palladium-catalyzed carbonylation, with particular focus on the aminocarbonylation of aryl bromide. Temperature, residence time, gas stoichiometry, and pressure were investigated with minimal experimenter intervention. It was found that the reaction was divided into two temperature regimes. A continuous temperature ramp experiment was devised to rapidly determine the activation energy of rate-limiting step of the lower-temperature regime. These results were found to agree with steady-state GC data, but required significantly less time to acquire. Furthermore, conversion and

selectivity were modeled for both regimes and found to be in good agreement with experimental results.

In Chapter 5, the multicomponent Petasis and Ugi reactions were developed from batch experiments to be combined in microreactors in series. As the Petasis reaction involves three components, and the Ugi reaction involves three in addition to the Petasis product, it was possible to effectively accomplish a six-component reaction. Despite being discovered decades ago, the mechanisms of these reactions are still in dispute. Two examples of the Petasis reaction were investigated to find optimal conditions and to perform a kinetics analysis to identify the rate-limiting step of the proposed mechanism and to determine their activation energies, as well as the activation energy of the Ugi reaction using a Petasis product.

In Chapter 6, a simple microcalorimetry system was demonstrated, allowing heats of reaction to be estimated without the need for specialized fabrication techniques that are typically used. The nitration of benzene was initially investigated, and the heat of reaction was measured to be -118.6 ± 2.4 kJ/mol, in agreement with the literature value of -117 kJ/mol. To allow for online measurement with IR, a single-phase Paal-Knorr reaction was then used for experiments investigating conditions at steady state, in a residence time ramp, and in a concentration ramp. These three experiment types all produced heats of reaction of approximately -50 kJ/mol. Finally, the sensitivity of the microcalorimeter was improved by creating a second-generation with a larger thermal mass.

7.1 Future Outlook

The integration of inline analysis in this and other recent works highlights the increasing interest in generating fundamental process understanding. The dual *in silico* nature of combining automated microreactor systems with computer modeling should greatly increase the efficiency of chemical investigations from the earliest stages through production scale up. At present, there is still a significant barrier to entry into microreactor research due to the high cost of both the reactors and the necessary peripheral equipment. However, even during the course of this thesis, significant standardization and improvements were made in this area. In contrast to many previous works, a single microreactor design was the focus of this work and indeed has become the standard used by many researchers in this lab. Another example is the improvements in the

primary analytical technique used in this work. At the onset of this thesis, the IR microflow cell used was an early prototype retrofit to a base unit typically used for studying batch chemistry. As this research progressed, several improvements were seen in the available devices, significantly reducing both the volume of the flow cell and the size of the base unit, which eventually became dedicated to flow experiments. Continued advances in these areas should further their adoption in academic and industrial research and development.

The optimization algorithms investigated in Chapter 2 of this thesis performed well for continuous variables. However, reactions often involve integer variables, such as catalyst, ligand, or reactant species. Approaches to these combined mixed-integer optimizations are still a worthy area of investigation. Additionally, the techniques investigated here were based upon local search algorithms. While in a convex optimization space these algorithms will find the global optimum, no such guarantee can be made for non-convex spaces. Unfortunately, global search techniques, such as simulated annealing or a genetic algorithm, typically involve a large number of experiments, as well as requiring the tuning of adjustable parameters. Developing algorithms to efficiently design experiments and utilize the resulting data will be required to continue expanding the optimization toolbox.

Combining the techniques of Chapters 3 and 6 could allow for automated microreactor systems that can use reaction transients to rapidly determine reaction kinetics and thermodynamics for safe, efficient scale up. Furthermore, integrating continuous IR measurement into the entire flow path of a microreactor could vastly improve the efficiency of these investigations. Combination of a transmission IR array reactor with liquid handling capabilities could allow for following the full conversion curve, including reactive intermediates, of integer experiments. However, there are still significant challenges to these goals before they can be met by researchers.

8 REFERENCES

1 Andrew J. deMello. Control and detection of chemical reactions in microfluidic systems. *Nature*, 442: 394–402, 2006. doi: 10.1038/nature05062.

2 V. Hessel and H. Löwe. Organic synthesis with microstructured reactors. *Chem. Eng. Technol.*, 28: 267–284, 2005. doi: 10.1002/ceat.200407167.

3 Klaus Jähnisch, Volker Hessel, Holger Löwe, and Manfred Baerns. Chemistry in microstructured reactors. *Angew. Chem., Int. Ed.*, 43: 406–446, 2004. doi: 10.1002/anie.200300577.

4 Nadim Maluf. *An Introduction to Microelectromechanical Systems Engineering*. Artech House, 2000.

5 James Welty, Charles Wicks, Robert Wilson, and Gregory Rorrer. *Fundamentals of Momentum, Heat, and Mass Transfer*. John Wiley & Sons, Inc., 4th edition, 2001.

6 T. Schwalbe, A. Kursawe, and J. Sommer. Application report on operating cellular process chemistry plants in fine chemical and contract manufacturing industries. *Chem. Eng. Technol.*, 28: 408–419, 2005. doi: 10.1002/ceat.200500014.

7 Klavs F. Jensen. Silicon-based microchemical systems: Characteristics and applications. *MRS Bull.*, 2: 101–107, 2006. doi: 10.1557/mrs2006.23.

8 Axel Günther, Manish Jhunjhunwala, Martina Thalmann, Martin A. Schmidt, and Klavs F. Jensen. Micromixing of miscible liquids in segmented gas-liquid flow. *Langmuir*, 21 (4): 1547–1555, 2005. doi: 10.1021/la0482406. PMID: 15697306.

9 Brian K. H. Yen, Axel Günther, Martin A. Schmidt, Klavs F. Jensen, and Moungi G. Bawendi. A microfabricated gas-liquid segmented flow reactor for high-temperature synthesis: The case of cdse quantum dots. *Angew. Chem., Int. Ed.*, 44 (34): 5447–5451, 2005. ISSN 1521-3773. doi: 10.1002/anie.200500792.

10 Kevin D. Nagy, Bo Shen, Timothy F. Jamison, and Klavs F. Jensen. Mixing and dispersion in small-scale flow systems. *Org. Process Res. Dev.*, 16 (5): 976–981, 2012. doi: 10.1021/op200349f. 10.1021/op200349f.

11 Volker Hessel, Panagiota Angeli, Asterios Gavriilidis, and Holger Löwe. Gas-liquid and gas-liquid-solid microstructured reactors: Contacting principles and applications. *Ind. Eng. Chem. Res.*, 44 (25): 9750–9769, 2005. doi: 10.1021/ie0503139.

12 Helmut Pennemann, Paul Watts, Stephen J. Haswell, Volker Hessel, and Holger Löwe. Benchmarking of microreactor applications. *Org. Process Res. Dev.*, 8 (3): 422–439, 2004. doi: 10.1021/op0341770.

13 Klavs F. Jensen. Microreaction engineering – is small better? *Chem. Eng. Sci.*, 56 (2): 293–303, 2001. ISSN 0009-2509. doi: 10.1016/S0009-2509(00)00230-X.

14 Franz Trachsel, Cédric Hutter, and Philipp Rudolf von Rohr. Transparent silicon/glass microreactor for high-pressure and high-temperature reactions. *Chem. Eng. J.*, 135 (Supplement 1): 309–316, 2008. doi: 10.1016/j.cej.2007.07.049.

15 Gernot Müller, Theo Gaupp, Fabian Wahl, and Gregor Wille. Continuous chemistry in microreaction systems for practical use. *Chimia*, 60: 618–622, 2006. doi: 10.2533/chimia.2006.618.

16 Dana Kralisch and Guenter Kreisel. Assessment of the ecological potential of microreaction technology. *Chem. Eng. Sci.*, 62 (4): 1094–1100, 2007. doi: 10.1016/j.ces.2006.11.009.

17 *Guidance for Industry PAT*. Food and Drug Administration, September 2004. URL http://www.fda.gov/cder/guidance/6419fnl.pdf.

18 K. Plumb. Continuous processing in the pharmaceutical industry: Changing the mind set. *Chem. Eng. Res. Des.*, 83 (6): 730–738, 2005. ISSN 0263-8762. doi: 10.1205/cherd.04359.

19 Axel Günther, Saif A. Khan, Martina Thalmann, Franz Trachsel, and Klavs F. Jensen. Transport and reaction in microscale segmented gas–liquid flow. *Lab Chip*, 4: 278–286, 2004. doi: 10.1039/b403982c.

20 Hemantkumar Sahoo. *Design and Operation of Microchemical Systems for Multistep Chemical Syntheses*. PhD thesis, Massachusetts Institute of Technology, 2008.

21 Hemantkumar R. Sahoo, Jason G. Kralj, and Klavs F. Jensen. Multistep continuous-flow microchemical synthesis involving multiple reactions and separations. *Angew. Chem., Int. Ed.*, 46: 5704–5708, 2007. doi: 10.1002/anie.200701434.

22 Adelina Smirnova, Kazuma Mawatari, Akihide Hibara, Mikhail A. Proskurnin, and Takehiko Kitamori. Micro-multiphase laminar flows for the extraction and detection of carbaryl derivative. *Anal. Chim. Acta*, 558 (1-2): 69–74, 2006. ISSN 0003-2670. doi: 10.1016/j.aca.2005.10.073.

23 David E. Bergbreiter, Patrick N. Hamilton, and Nirmal M. Koshti. Self-separating homogeneous copper (i) catalysts. *J. Am. Chem. Soc.*, 129 (35): 10666–10667, 2007. doi: 10.1021/ja0741372.

24 K. F. Lam, E. Cao, E. Sorensen, and A. Gavriilidis. Development of multistage distillation in a microfluidic chip. *Lab Chip*, 11: 1311–1317, 2011. doi: 10.1039/C0LC00428F.

25 Ryan L. Hartman, Hemantkumar R. Sahoo, Bernard C. Yen, and Klavs F. Jensen. Distillation in microchemical systems using capillary forces and segmented flow. *Lab Chip*, 9: 1843–1849, 2009. doi: 10.1039/b901790a.

26 J. A. Nelder and R. Mead. A simplex method for function minimization. *Comput. J.*, 7 (4): 308–313, 1965. doi: 10.1093/comjnl/7.4.308.

27 Kenneth J. Beers. *Numerical Methods for Chemical Engineering*. Cambridge University Press, 2007.

28 M. T. Kuo, D. I. Rubin, and B. S. Wright. Optimization of complex chemical processes. comparison of variational and steepest descent methods. *Ind. Eng. Chem. Res.*, 5 (4): 404–408, 1966. doi: 10.1021/i260020a011.

29 Waltraud Huyer and Arnold Neumaier. Snobfit stable noisy optimization by branch and fit. *ACM Transactions on Mathematical Software*, 35 (2): 9:1–9:25, July 2008. doi: 10.1145/1377612.1377613.

30 Manuel Lozano, Francisco Herrera, Natalio Krasnogor, and Daniel Molina. Real-coded memetic algorithms with crossover hill-climbing. *Evolutionary Computation*, 12: 273–302, 2004. doi: 10.1162/1063656041774983.

31 S. Kirkpatrick, C. D. Gelatt, and M. P. Vecchi. Optimization by simulated annealing. *Science*, 220 (4598): 671–680, 1983. ISSN 00368075. doi: 10.2307/1690046.

32 D. Brynn Hibbert. A hybrid genetic algorithm for the estimation of kinetic parameters. *Chemom. Intell. Lab. Syst.*, 19: 319–329, 1993. doi: 10.1016/0169-7439(93)80031-C.

33 John R. Goodell, Jonathan P. McMullen, Nikolay Zaborenko, Jason R. Maloney, Chuan-Xing Ho, Klavs F. Jensen, John A. Porco, and Aaron B. Beeler. Development of an automated microfluidic reaction platform for multidimensional screening: Reaction discovery employing bicyclo[3.2.1]octanoid scaffolds. *J. Org. Chem.*, 74 (16): 6169–6180, 2009. doi: 10.1021/jo901073v. PMID: 20560568.

34 Jonathan P. McMullen and Klavs F. Jensen. An automated microfluidic system for online optimization in chemical synthesis. *Org. Process Res. Dev.*, 14: 1169–1176, 2010. doi: 10.1021/op100123e.

35 Jonathan P. McMullen and Klavs F. Jensen. Rapid determination of reaction kinetics with an automated microfluidic system. *Org. Process Res. Dev.*, 15 (2): 398–407, 2011. doi: 10.1021/op100300p.

36 Jonathan P. McMullen, Matthew T. Stone, Stephen L. Buchwald, and Klavs F. Jensen. An integrated microreactor system for self-optimization of a heck reaction. *Angew. Chem., Int. Ed.*, 49: 7076–7080, 2010. doi: 10.1002/anie.201002590.

37 T. Noel, J. R. Naber, R. L. Hartman, J. P. McMullen, K. F. Jensen, and S. L. Buchwald. Palladium-catalyzed amination reactions in flow: overcoming the challenges of clogging via acoustic irradiation. *Chem. Sci.*, 2: 287–290, 2011. doi: 10.1039/C0SC00524J.

38 Karolin Geyer, Tomas Gustafsson, and Peter H. Seeberger. Developing continuous-flow microreactors as tools for synthetic chemists. *Synlett*, 15: 2382–2391, 2009. doi: 10.1055/s-0029-1217828.

39 Ryan L. Hartman and Klavs F. Jensen. Microchemical systems for continuous-flow synthesis. *Lab Chip*, 9: 2495–2507, 2009. doi: 10.1039/B906343A.

40 Jonathan P. McMullen and Klavs F. Jensen. Integrated microreactors for reaction automation: New approaches to reaction development. *Annu. Rev. Anal. Chem.*, 3: 19–42, 2010. doi: 10.1146/annurev.anchem.111808.073718.

41 Ryan L. Hartman, Jonathan P. McMullen, and Klavs F. Jensen. Deciding whether to go with the flow: Evaluating the merits of flow reactors for synthesis. *Angew. Chem., Int. Ed.*, 50: 7502–7519, 2011. doi: 10.1002/anie.201004637.

42 Volker Hessel and Patrick Löb. *Micro Process Engineering*, volume 1. Wiley-VCH, 2009.

43 Samuel Marre, Andrea Adamo, Soubir Basak, Cyril Aymonier, and Klavs F. Jensen. Design and packaging of microreactors for high pressure and high temperature applications. *Ind. Eng. Chem. Res.*, 49 (22): 11310–11320, 2010. doi: 10.1021/ie101346u.

44 Helmut Pennemann, Volker Hessel, and Holger Löwe. Chemical microprocess technology–from laboratory-scale to production. *Chem. Eng. Sci.*, 59 (22-23): 4789–4794, 2004. doi: 10.1016/j.ces.2004.07.049.

45 Paul Watts. The application of microreactors in combinatorial chemistry. *QSAR Comb. Sci.*, 24: 701–711, 2005. doi: 10.1002/qsar.200540004.

46 Charlotte Wiles and Paul Watts. High-throughput organic synthesis in microreactors. *Adv. Chem. Eng.*, 38: J. C. Schouten, 2010. doi: 10.1016/S0065-2377(10)38003-3.

47 S. Krishnadasan, R. J. C. Brown, A. J. deMello, and J. C. deMello. Intelligent routes to the controlled synthesis of nanoparticles. *Lab Chip*, 7: 1434–1441, 2007. doi: 10.1039/B711412E.

48 Ds series sampling technology. mettler toledo, llc. URL http://us.mt.com/us/en/home/-products/L1_AutochemProducts/L2_in-situSpectrocopy/AgX-FiberConduit-Sampling-Technology-DS-Series.html. Accessed Nov. 7, 2010.

49 Catherine F. Carter, Heiko Lange, Steven V. Ley, Ian R. Baxendale, Brian Wittkamp, Jon G. Goode, and Nigel L. Gaunt. Reactir flow cell: A new analytical tool for continuous flow chemical processing. *Org. Process Res. Dev.*, 14 (2): 393–404, 2010. doi: 10.1021/op900305v.

50 Tobias Brodmann, Peter Koos, Albrecht Metzger, Paul Knochel, and Steven V. Ley. Continuous preparation of arylmagnesium reagents in flow with inline ir monitoring. *Org. Process Res. Dev.*, 16 (5): 1102–1113, 2012. doi: 10.1021/op200275d. 10.1021/op200275d.

51 Benjamin J. Littler, Adam R. Looker, and Todd A. Blythe. Optimization of a hydrogenation process using real-time mid-ir, heat flow and gas uptake measurements. *Org. Process Res. Dev.*, 14: 1512–1517, 2010. doi: 10.1021/op100169j.

52 Venkataraman Amarnath, Douglas C. Anthony, Kalyani Amarnath, William M. Valentine, Lawrence A. Wetterau, and Doyle G. Graham. Intermediates in the paal-knorr synthesis of pyrroles. *J. Org. Chem.*, 56: 6924–6931, 1991. doi: 10.1021/jo00024a040.

53 Belquis Mothana and Russell J. Boyd. A density functional theory study of the mechanism of the paal-knorr pyrrole synthesis. *J. Mol. Struct.*, 811 (1-3): 97–107, 2007. doi: 10.1016/j.theochem.2006.11.034.

54 Surya De. Ruthenium (iii) chloride as a novel and efficient catalyst for the synthesis of substituted pyrroles under solvent-free conditions. *Catal. Lett.*, 124: 174–177, 2008. doi: 10.1007/s10562-008-9461-1. 10.1007/s10562-008-9461-1.

55 Chang-Shun Li, Ya-Hsuan Tsai, Wei-Chen Lee, and Wen-Jang Kuo. Synthesis and photophysical properties of pyrrole/polycyclic aromatic units hybrid fluorophores. *J. Org. Chem.*, 75 (12): 4004–4013, 2010. doi: 10.1021/jo100158a.

56 Jie-Jack Li and E. J. Corey, editors. *Name Reactions in Heterocyclic Chemistry*. John Wiley & Sons, Inc., Hoboken, N. J., 2005.

57 G. Balme. Pyrrole syntheses by multicomponent coupling reactions. *Angew. Chem., Int. Ed.*, 43: 6238–6241, 2004. doi: 10.1002/anie.200461073.

58 Ivana Bianchi, Roberto Forlani, Giacomo Minetto, Ilaria Peretto, Nickolas Regalia, Maurizio Taddei, and Luca F. Raveglia. Solution phase synthesis of a library of tetrasubstituted pyrrole amides. *J. Comb. Chem.*, 8 (4): 491–499, 2006. doi: 10.1021/cc060008q.

59 Pieter J. Nieuwland, Ruth Segers, Kaspar Koch, Jan C. M. van Hest, and Floris P. J. T. Rutjes. Fast scale-up using microreactors: Pyrrole synthesis from micro to production scale. *Org. Process Res. Dev.*, 15 (4): 783–787, 2011. doi: 10.1021/op100338z.

60 Ludwig Knorr. Einwirkung des diacetbernsteinsäureesters auf ammoniak und primäre aminbasen. *Ber. Dtsch. Chem. Ges.*, 18: 299–311, 1885. doi: 10.1002/cber.18850180154.

61 C. Paal. Synthese von thiophen- und pyrrolderivaten. *Ber. Dtsch. Chem. Ges.*, 18: 367–371, 1885. doi: 10.1002/cber.18850180175.

62 Venkataraman Amarnath, Kalyani Amarnath, William M. Valentine, Michael A. Eng, and Doyle G. Graham. Intermediates in the paal-knorr synthesis of pyrroles. 4-oxoaldehydes. *Chem. Res. Toxicol.*, 8 (2): 234–238, 1995. doi: 10.1021/tx00044a008.

63 Schaefer Mechtilde, Stach Eduard, and Foitzik Andreas. Computer controlled chemical micro-reactor. *J. Phys. Conf. Ser.*, 28 (1): 115, 2006. URL http://stacks.iop.org/1742-6596/28/i=1/a=024.

64 K. L. Andrew Chan, X. Niu, A. J. deMello, and S. G. Kazarian. Generation of chemical movies: Ft-ir spectroscopic imaging of segmented flows. *Anal. Chem.*, 83 (9): 3606–3609, 2011. doi: 10.1021/ac200497a.

65 Matthew W. Bedore, Nikolay Zaborenko, Klavs F. Jensen, and Timothy F. Jamison. Aminolysis of epoxides in a microreactor system: A continuous flow approach to beta-amino alcohols. *Org. Process Res. Dev.*, 14 (2): 432–440, 2010. doi: 10.1021/op9003136.

66 Nikolay Zaborenko, Matthew W. Bedore, Timothy F. Jamison, and Klavs F. Jensen. Kinetic and scale-up investigations of epoxide aminolysis in microreactors at high temperatures and pressures. *Org. Process Res. Dev.*, 15 (1): 131–139, 2011. doi: 10.1021/op100252m.

67 Panos Papalambros and Douglass Wilde. *Principles of Optimal Design*. Cambridge University Press, 2000.

68 Wenyu Sun and Ya-Xiang Yuan. *Optimization Theory and Methods*. Springer Science, 2006. URL http://mit.worldcat.org/title/optimization-theory-and-methods-nonlinear-programming/oclc/262687419.

69 Octave Levenspiel. *Chemical Reaction Engineering*. John Wiley & Sons, 3rd edition, 1999.

70 Fernando E. Valera, Michela Quaranta, Antonio Moran, John Blacker, Alan Armstrong, João T. Cabral, and Donna G. Blackmond. The flow's the thing...or is it? assessing the merits of homogeneous reactions in flask and flow. *Angew. Chem., Int. Ed.*, 49: 2478–2485, 2010. doi: 10.1002/anie.200906095.

71 Sergey Mozharov, Alison Nordon, David Littlejohn, Charlotte Wiles, Paul Watts, Paul Dallin, and John M. Girkin. Improved method for kinetic studies in microreactors using flow manipulation and noninvasive raman spectrometry. *J. Am. Chem. Soc.*, 133 (10): 3601–3608, 2011. doi: 10.1021/ja1102234.

72 Jason S. Moore and Klavs F. Jensen. Automated multitrajectory method for reaction optimization in a microfluidic system using online ir analysis. *Org. Process Res. Dev.*, 16 (8): 1409–1415, 2012. doi: 10.1021/op300099x.

73 C. L. Allen and J. M. J Williams. Metal-catalyzed approaches to amide bond formation. *Chem. Soc. Rev.*, 40: 3405–3415, 2011. doi: 10.1039/C0CS00196A.

74 A. Brennführer, H. Neumann, and M. Beller. Palladium-catalyzed carbonylation reactions of aryl halides and related compounds. *Angew. Chem., Int. Ed.*, 48: 4114–4133, 2009. doi: 10.1002/anie.200900013.

75 C. F. J. Barnard. Palladium-catalyzed carbonylation — a reaction come of age. *Organometallics*, 27: 5402–5422, 2008. doi: 10.1021/om800549q.

76 C. F. J. Barnard. Carbonylation of aryl halides: Extending the scope of the reaction. *Org. Process Res. Dev.*, 12: 566–574, 2008. doi: 10.1021/op800069w.

77 M. Beller and M. Eckert. Aminocarbonylation - an efficient route to amino acid derivatives. *Angew. Chem., Int. Ed.*, 39: 1010–1027, 2000. doi: 10.1002/(SICI)1521-3773(20000317)39:6<1010::AID-ANIE1010>3.0.CO;2-P.

78 Y. Q. Wan, M. Alterman, M. Larhed, and A. Hallberg. Dimethylformamide as a carbon monoxide source in fast palladium-catalyzed aminocarbonylations of aryl bromides. *J. Org. Chem.*, 67: 6232–6235, 2002. doi: 10.1021/jo025965a.

79 Y. Wan, M. Alterman, M. Larhed, and A. Hallberg. Formamide as a combined ammonia synthon and carbon monoxide source in fast palladium-catalyzed aminocarbonylations of aryl halides. *J. Comb. Chem.*, 5: 82–84, 2003. doi: 10.1021/cc0200843.

80 J. Ruan and J. Xiao. From arylation of olefins to acylation with aldehydes: A journey in regiocontrol of the heck reaction. *Accounts Chem. Res.*, 44: 614–626, 2011. doi: 10.1021/ar200053d.

81 P. Appukkuttan, L. Axelsson, E. Van der Eycken, and M. Larhed. Microwave-assisted, mo(co)(6)-mediated, palladium-catalyzed amino-carbonylation of aryl halides using allylamine: from exploration to scale-up. *Tet. Lett.*, 49: 5625–5628, 2008. doi: 10.1016/j.tetlet.2008.07.053.

82 W. Ren and M. Yamane. Mo(co)6-mediated carbamoylation of aryl halides. *J. Org. Chem.*, 75: 8410–8415, 2010. doi: 10.1021/jo101611g.

83 B. Desai and C. O. Kappe. Heterogeneous hydrogenation reactions using a continuous flow high pressure device. *J. Comb. Chem.*, 7: 641–643, 2005. doi: 10.1021/cc050076x.

84 S. Saaby, K. R. Knudsen, M. Ladlow, and S. V. Ley. The use of a continuous flow-reactor employing a mixed hydrogen-liquid flow stream for the efficient reduction of imines to amines. *Chem. Comm.*, 23: 2909–2911, 2005. doi: 10.1039/B504854K.

85 Csaba Csajági, Bernadett Borcsek, Krisztián Niesz, Ildikó Kovács, Zsolt Székelyhidi, Zoltán Bajkó, László Ürge, and Ferenc Darvas. High-efficiency aminocarbonylation by introducing co to a pressurized continuous flow reactor. *Org. Lett.*, 10: 1589–1592, 2008. doi: 10.1021/ol7030894.

86 P. Koos, U. Gross, A. Polyzos, M. O'Brien, I. Baxendale, and S. V. Ley. Teflon af-2400 mediated gas-liquid contact in continuous flow methoxycarbonylations and in-line ftir measurement of co concentration. *Org. Biomol. Chem.*, 9: 6903–6908, 2011. doi: 10.1039/C1OB06017A.

87 M. O'Brien, N. Taylor, A. Polyzos, I. R. Baxendale, and S. V. Ley. Hydrogenation in flow: Homogeneous and heterogeneous catalysis using teflon af-2400 to effect gas-liquid contact at elevated pressure. *Chem. Sci.*, 2: 1250–1257, 2011. doi: 10.1039/C1SC00055A.

88 P. W. Miller, N. J. Long, A. J. de Mello, R. Vilar, H. Audrain, D. Bender, J. Passchier, and A. Gee. Rapid multiphase carbonylation reactions by using a microtube reactor: Applications in positron emission tomography 11c-radiolabeling. *Angew. Chem.*, 119: 2933–2936, 2007. doi: 10.1002/ange.200604541.

89 W. M. Philip, E. J. Lucy, J. D. Andrew, D. G. Antony, J. L. Nicholas, and V. Ramon. A microfluidic approach to the rapid screening of palladium-catalysed aminocarbonylation reactions. *Adv. Synth. Catal.*, 351: 3260–3268, 2009. doi: 10.1002/adsc.200900563.

90 J. Balogh, Á. Kuik, L. Ürge, F. Darvas, J. Bakos, and R. Skoda-Földes. Double carbonylation of iodobenzene in a microfluidics-based high throughput flow reactor. *J. Mol. Catal. A-Chem.*, 302: 76–79, 2009. doi: 10.1016/j.molcata.2008.11.035.

91 The actual residence time of the gas/liquid reaction is complicated by the expansion of the gas at elevated temperature and the consumption of CO as the reaction proceeds.

92 J. R. Naber and S. L. Buchwald. Packed-bed reactors for continuous-flow c-n cross-coupling. *Angew. Chem., Int. Ed.*, 49: 9469–9474, 2010. doi: 10.1002/anie.201004425.

93 E. R. Murphy, J. R. Martinelli, N. Zaborenko, S. L. Buchwald, and K. F. Jensen. Accelerating reactions with microreactors at elevated temperatures and pressures: Profiling aminocarbonylation reactions. *Angew. Chem., Int. Ed.*, 46: 1734–1737, 2007. doi: 10.1002/anie.200604175.

94 F. Ozawa, T. Sugimoto, Y. Yuasa, M. Santra, T. Yamamoto, and A. Yamamoto. Palladium-promoted double-carbonylation reactions. reactions of organopalladium compounds with carbon monoxide and amines to give alpha-keto amides. *Organometallics*, 3: 683–692, 1984. doi: 10.1021/om00083a007.

95 Yong-Shou Lin and Akio Yamamoto. Studies relevant to palladium-catalyzed carbonylation processes. *Organometallics*, 17: 3466–3478, 1998. doi: 10.1021/om980234f.

96 F. Ozawa, N. Kawasaki, H. Okamoto, T. Yamamoto, and A. Yamamoto. Mechanisms of double and single carbonylation reactions of aryl iodides catalyzed by palladium complexes to give.alpha.-keto esters and esters. *Organometallics*, 6: 1640–1651, 1987. doi: 10.1021/om00151a008.

97 Fumiyuki Ozawa, Hidehiko Soyama, Hisayoshi Yanagihara, Issei Aoyama, Hiroaki Takino, Kunisuke Izawa, Takakazu Yamamoto, and Akio Yamamoto. Palladium-catalyzed double carbonylation of aryl halides to give alpha-keto amides. *J. Am. Chem. Soc.*, 107 (11): 3235–3245, 1985. doi: 10.1021/ja00297a033.

98 M. Beller, W. Mägerlein, A. F. Indolese, and C. Fischer. Efficient palladium-catalyzed alkoxycarbonylation of n-heteroaryl chlorides - a practical synthesis of building blocks for pharmaceuticals and herbicides. *Synthesis*, 2001: 1098–1109, 2001. doi: 10.1055/s-2001-14576.

99 R. J. Perry and B. D. Wilson. Palladium-catalyzed carbonylation and coupling reactions of aryl chlorides and amines. *J. Org. Chem.*, 61: 7482–7485, 1996. doi: 10.1021/jo960861j.

100 Y. Ben-David, M. Portnoy, and D. Milstein. Chelate-assisted, palladium-catalyzed efficient carbonylation of aryl chlorides. *J. Am. Chem. Soc*, 111: 8742–8744, 1989. doi: 10.1021/ja00205a039.

101 W. Mägerlein, A. F. Indolese, and M. Beller. A more efficient catalyst for the carbonylation of chloroarenes. *Angew. Chem., Int. Ed.*, 40: 2856–2859, 2001. doi: 10.1002/1521-3773(20010803)40:15<2856::AID-ANIE2856>3.0.CO;2-1.

102 C. Jimenez-Rodriguez, G. R. Eastham, and D. J. Cole-Hamilton. The methoxycarbonylation of aryl chlorides catalysed by palladium complexes of bis(di-tert-butylphosphinomethyl)benzene. *Dalton Trans.*, 10: 1826–1830, 2005. doi: 10.1039/B501868D.

103 V. Dufaud, J. Thivolle-Cazat, and J.-M. Basset. Palladium catalysed carbonylation of aryl chlorides to the corresponding methyl esters. *J. Chem. Soc. Chem. Comm.*, 1990: 426–427, 1990. doi: 10.1039/C39900000426.

104 D. A. Watson, X. Fan, and S. L. Buchwald. Carbonylation of aryl chlorides with oxygen nucleophiles at atmospheric pressure. preparation of phenyl esters as acyl transfer agents and the direct preparation of alkyl esters and carboxylic acids. *J. Org. Chem.*, 73: 7096–7101, 2008. doi: 10.1021/jo800907e.

105 J. R. Martinelli, T. P. Clark, D. A. Watson, R. H. Munday, and S. L. Buchwald. Palladium-catalyzed aminocarbonylation of aryl chlorides at atmospheric pressure: The dual role of sodium phenoxide. *Angew. Chem., Int. Ed.*, 46: 8460–8463, 2007. doi: 10.1002/anie.200702943.

106 J. R. Sedelmeier, S. V. Ley, I. R. Baxendale, and M. Baumann. Kmno4-mediated oxidation as a continuous flow process. *Org. Lett.*, 12: 3618–3621, 2010. doi: 10.1021/ol101345z.

107 R. L. Hartman, J. R. Naber, N. Zaborenko, S. L. Buchwald, and K. F. Jensen. Overcoming the challenges of solid bridging and constriction during pd-catalyzed c-n bond formation in microreactors. *Org. Process Res. Dev.*, 14: 1347–1357, 2010. doi: 10.1021/op100154d.

108 Ivar Ugi. Recent progress in the chemistry of multicomponent reactions. *Pure Appl. Chem.*, 73 (1): 187–191, 2001. doi: 10.1351/pac200173010187.

109 Alexander Dömling. Recent developments in isocyanide based multicomponent reactions in applied chemistry. *Chem. Rev.*, 106 (1): 17–89, 2006. doi: 10.1021/cr0505728.

110 Sang Woong Kim, Shawn M. Bauer, and Robert W. Armstrong. Construction of combinatorial chemical libraries using a rapid and efficient solid phase synthesis based on a multicomponent condensation reaction. *Tetrahedron Lett.*, 39 (39): 6993 – 6996, 1998. ISSN 0040-4039. doi: 10.1016/S0040-4039(98)01547-0.

111 Nicos A. Petasis and Irini Akritopoulou. The boronic acid mannich reaction: A new method for the synthesis of geometrically pure allylamines. *Tetrahedron Lett.*, 34 (4): 583 – 586, 1993. ISSN 0040-4039. doi: 10.1016/S0040-4039(00)61625-8.

112 Jingcong Tao and Shuhua Li. Theoretical study on the mechanism of the petasis-type boronic mannich reaction of organoboronic acids, amines, and α-hydroxy aldehydes. *Chin. J. Chem.*, 28: 41–49, 2010. doi: 10.1002/cjoc.201090033.

113 Nuno R. Candeias, Francesco Montalbano, Pedro M. S. D. Cal, and Pedro M. P. Gois. Boronic acids and esters in the petasis-borono mannich multicomponent reaction. *Chem. Rev.*, 110 (10): 6169–6193, 2010. doi: 10.1021/cr100108k.

114 Nuno R. Candeias, Pedro M.S.D. Cal, Vania André, M. Teresa Duarte, Luis F. Veiros, and Pedro M.P. Gois. Water as the reaction medium for multicomponent reactions based on boronic acids. *Tetrahedron*, 66 (14): 2736 – 2745, 2010. ISSN 0040-4020. doi: 10.1016/j.tet.2010.01.084.

115 Nicos A. Petasis and Ilia A. Zavialov. Highly stereocontrolled one-step synthesis of *anti*-β-amino alcohols from organoboronic acids, amines, and α-hydroxy aldehydes. *J. Am. Chem. Soc.*, 120 (45): 11798–11799, 1998. doi: 10.1021/ja981075u.

116 J.C. Watkins and G.L. Collingridge. Phenylglycine derivatives as antagonists of metabotropic glutamate receptors. *Trends Pharmacol. Sci.*, 15 (9): 333 – 342, 1994. ISSN 0165-6147. doi: 10.1016/0165-6147(94)90028-0.

117 Cédric Kalinski, Hugues Lemoine, Jürgen Schmidt, Christoph Burdack, Jürgen Kolb, Michael Umkehrer, and Günther Ross. Multicomponent reactions as a powerful tool for generic drug synthesis. *Synthesis*, 24: 4007–4011, 2008. doi: 10.1055/s-0028-1083239.

118 I. Ugi, R. Meyr, U. Fetzer, and C. Steinbrückner. Versuche mit isonitrilen. *Angew. Chem.*, 71: 373–388, 1959. doi: 10.1002/ange.19590711110.

119 Ana Cukalovic, Jean-Christophe Monbaliu, and Christian Stevens. *Microreactor technology as an efficient tool for multicomponent reactions*. Synthesis of Heterocycles via Multicomponent Reactions. Springer, 2010.

120 Cristina Faggi, Maria Garcia-Valverde, Stefano Marcaccini, and Gloria Menchi. Isolation of ugi four-component condensation primary adducts: A straightforward route to isocoumarins. *Org. Lett.*, 12 (4): 788–791, 2010. doi: 10.1021/ol9028622. PMID: 20104888.

121 K. Rossen, P.J. Pye, L.M. DiMichele, R.P. Volante, and P.J. Reider. An efficient asymmetric hydrogenation approach to the synthesis of the crixivan® piperazine intermediate. *Tetrahedron Lett.*, 39 (38): 6823 – 6826, 1998. ISSN 0040-4039. doi: 10.1016/S0040-4039(98)01484-1.

122 Alexander Dömling and Ivar Ugi. Multicomponent reactions with isocyanides. *Angew. Chem., Int. Ed.*, 39 (18): 3168–3210, 2000. ISSN 1521-3773. doi: 10.1002/1521-3773(20000915)39:18<3168::AID-ANIE3168>3.0.CO;2-U.

123 David E. Portlock, Ryszard Ostaszewski, Dinabandhu Naskar, and Laura West. A tandem petasis-ugi multi component condensation reaction: solution phase synthesis of six dimensional libraries. *Tetrahedron Lett.*, 44 (3): 603 – 605, 2003. ISSN 0040-4039. doi: 10.1016/S0040-4039(02)02619-9.

124 Nicos A. Petasis and Sougato Boral. One-step three-component reaction among organoboronic acids, amines and salicylaldehydes. *Tetrahedron Lett.*, 42: 539 – 542, 2001. doi: 10.1016/S0040-4039(00)02014-1.

125 Klavs F. Jensen. Microchemical systems for discovery and development. *Ernst Schering Found. Symp. Proc.*, 3: 57–76, 2007. doi: 10.1007/2789_2007_028.

126 Wilfried Hoffmann, Ying Kang, John C. Mitchell, and Martin J. Snowden. Kinetic data by nonisothermal reaction calorimetry: A model-assisted calorimetric evaluation. *Org. Process Res. Dev.*, 11 (1): 25–29, 2007. doi: 10.1021/op060144j.

127 Gilles Richner, Yorck-Michael Neuhold, and Konrad Hungerbuehler. Nonisothermal calorimetry for fast thermokinetic reaction analysis: Solvent-free esterification of n-butanol by acetic anhydride. *Org. Process Res. Dev.*, 14 (3): 524–536, 2010. doi: 10.1021/op900298x.

128 Jörg Pastré, Andreas Zogg, Ulrich Fischer, and Konrad Hungerbühler. Determination of reaction parameters using a small calorimeter with an integrated ft-ir probe and parameter fitting. *Organic Process Research & Development*, 5 (2): 158–166, 2001. doi: 10.1021/op000072a.

129 Andreas Zogg, Ulrich Fischer, and Konrad Hungerbühler. A new small-scale reaction calorimeter that combines the principles of power compensation and heat balance. *Ind. Eng. Chem. Res.*, 42 (4): 767–776, 2003. doi: 10.1021/ie0201258.

130 Fabio Visentin, Stefano I. Gianoli, Andreas Zogg, Oemer M. Kut, and Konrad Hungerbühler. A pressure-resistant small-scale reaction calorimeter that combines the principles of power compensation and heat balance (crc.v4). *Org. Process Res. Dev.*, 8 (5): 725–737, 2004. doi: 10.1021/op049900g.

131 J. M. Köhler and M. Zieren. Micro flow calorimeter for thermoelectrical detection of heat of reaction in small volumes. *Fresenius J. Anal. Chem.*, 358: 683–686, 1997.

132 J Lerchner, A Wolf, R Hüttl, and G Wolf. Direct monitoring of biochemical processes using micro-structured heat power detectors. *Chem. Eng. J.*, 101 (1–3): 187 – 194, 2004. ISSN 1385-8947. doi: 10.1016/j.cej.2003.11.006.

133 V. Baier, R. Födisch, A. Ihring, E. Kessler, J. Lerchner, G. Wolf, J.M. Köhler, M. Nietzsch, and M. Krügel. Highly sensitive thermopile heat power sensor for micro-fluid calorimetry of biochemical processes. *Sensor. Actuat. A-Phys.*, 123–124 (0): 354 – 359, 2005. ISSN 0924-4247. doi: 10.1016/j.sna.2005.05.018.

134 Juergen Antes, Martin Gegenheimer, Stefan Löbbecke, and Horst Krause. Reaction calorimetry in microreactors: Fast reaction screening and process design. *International*

Conference on Miniaturized Systems for Chemistry and Life Sciences, 12: 1260–1262, 2008.

135 Richard Cavicchi, Gregory Poirier, John Suehle, Michael Gaitan, and Nim Tea. Micron-scale differential scanning calorimeter on a chip, 2000. URL http://patapsco.nist.gov/TS/-220/sharedpatent/pdf/6079873.pdf.

136 R. D. Biggs and R. R. White. Rate of nitration of benzene with mixed acid. *AIChE Journal*, 2 (1): 26–33, 1956. ISSN 1547-5905. doi: 10.1002/aic.690020106.

137 Paulo A. Quadros, Nuno M.C. Oliveira, and Cristina M.S.G. Baptista. Continuous adiabatic industrial benzene nitration with mixed acid at a pilot plant scale. *Chemical Engineering Journal*, 108 (1–2): 1 – 11, 2005. ISSN 1385-8947. doi: 10.1016/j.cej.2004.12.022.

138 Tadeusz Urbanski. *Chemistry and Technology of Explosives*. Pergamon Press, 1964.

139 Kenneth Schofield. *Aromatic Nitration*. Cambridge University Press, 1981.

140 Makoto Takiishi, Saburo Tanaka, Koji Miyazaki, and Hiroshi Tsukamoto. Thermal conductivity measurements of bismuth telluride thin films by using the 3 omega method. *Japan Symposium on Thermophysical Properties*, 27: 24–26, 2006. URL http://-sciencelinks.jp/j-east/article/200707/000020070707A0043210.php.

141 Gerald Booth. *Nitro Compounds, Aromatic*, pages 301–349. Wiley-VCH, 2000. ISBN 9783527306732. doi: 10.1002/14356007.a17_411.

Appendix A: Chapter 2 Supporting Information

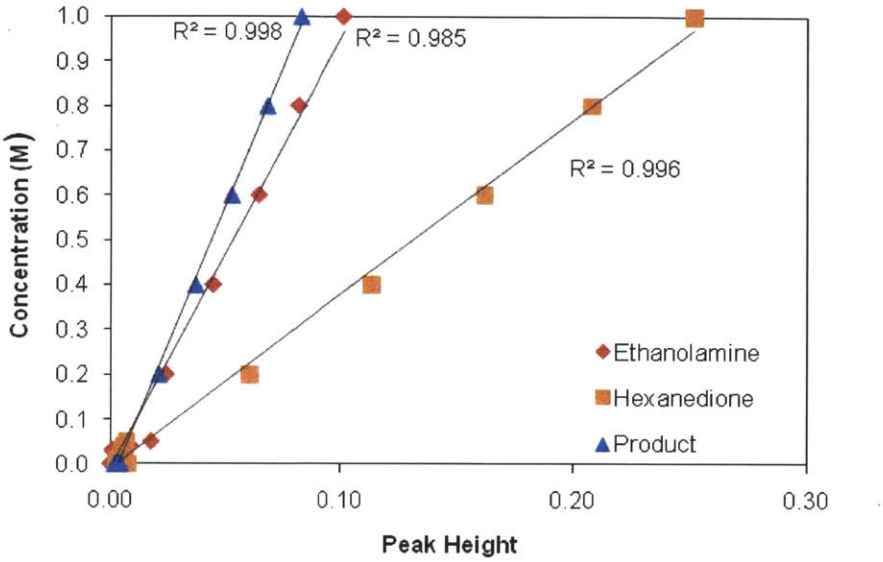

Figure A.1. Calibration of IR peaks for the reactants and products.

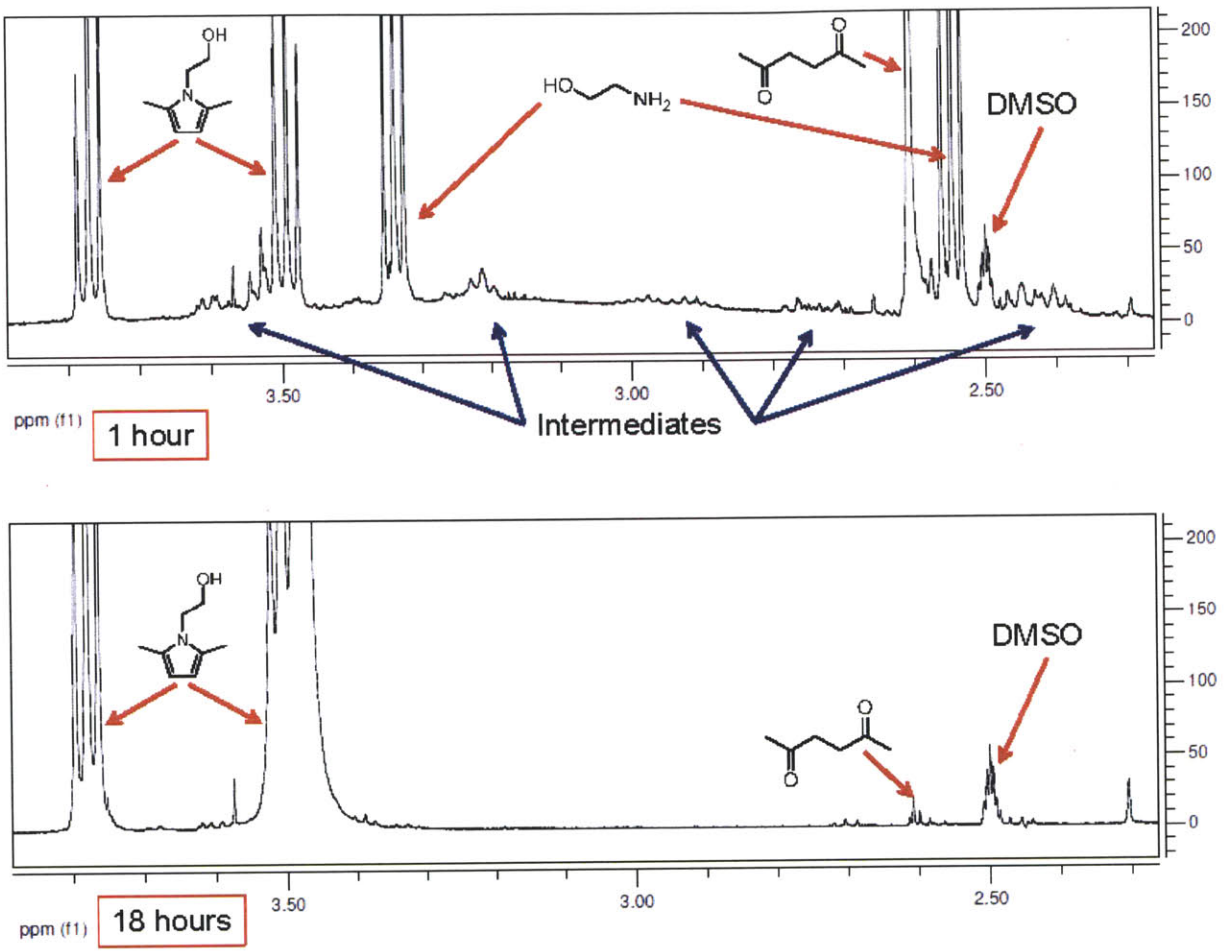

Figure A.2. NMR spectra of the reaction solution.

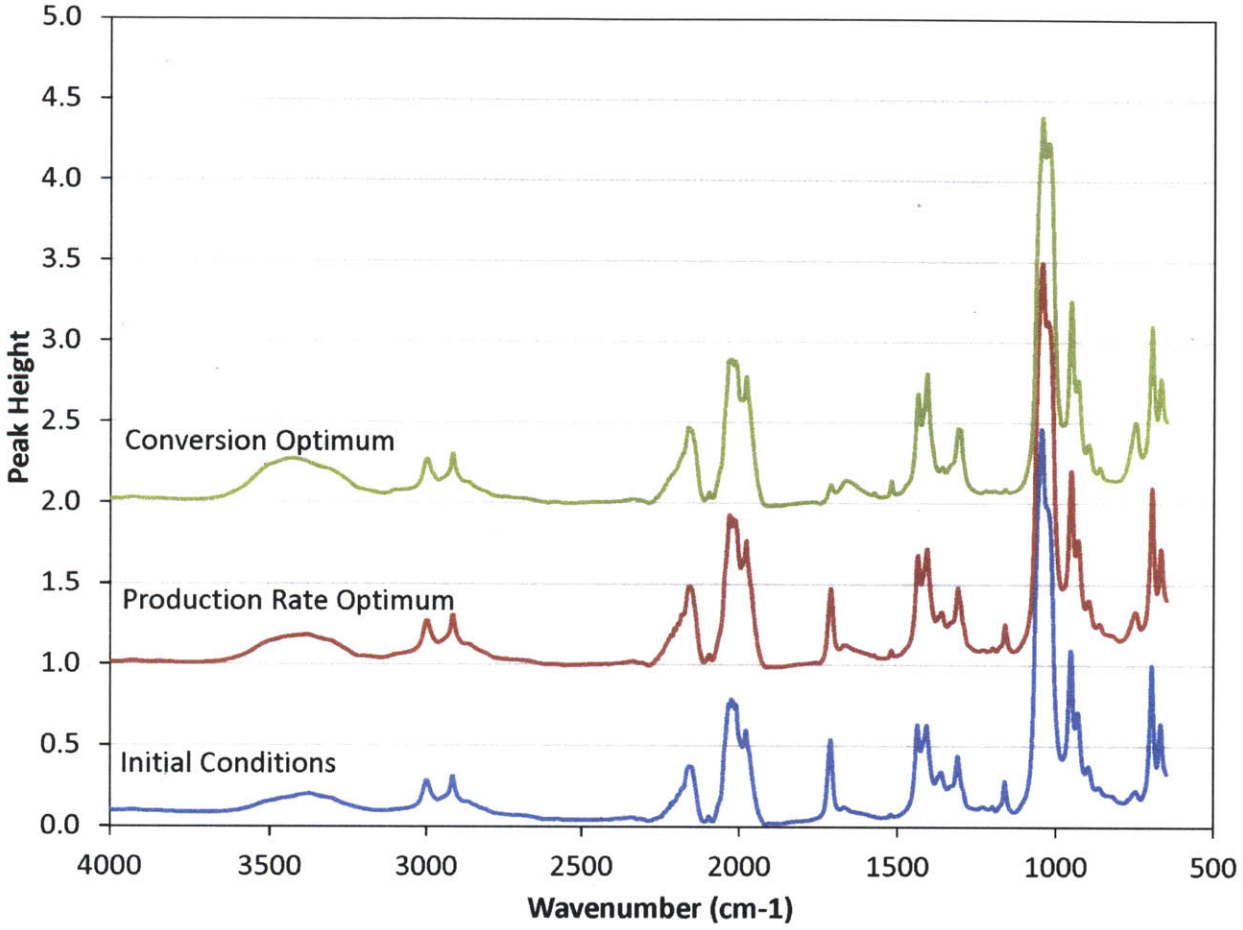

Figure A.3. ATR-FTIR spectra of the reaction solution at different conversions.

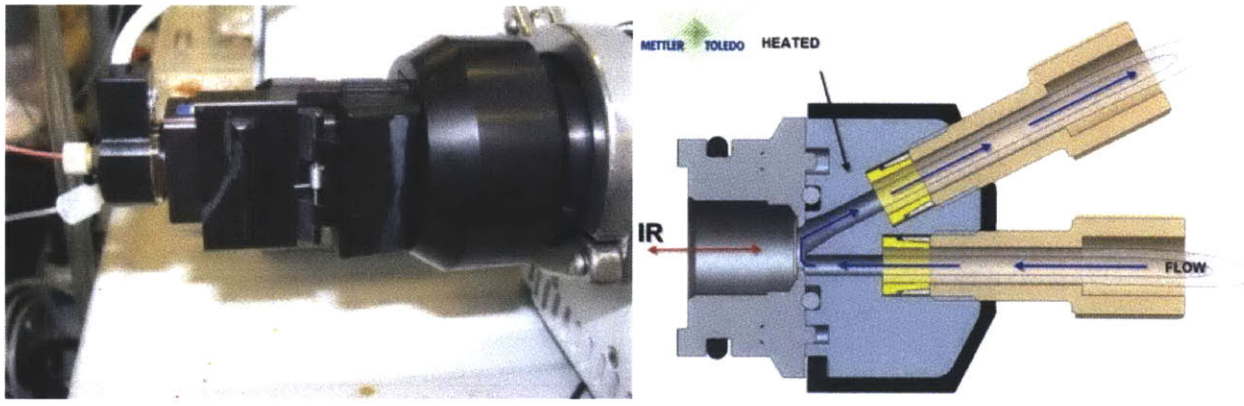

Figure A.4. Mettler-Toledo ReactIR micro flow cell, which has a 51-uL flow cell equipped with a multi-pass diamond window to allow for continuous monitoring of the mid-IR range.[48]

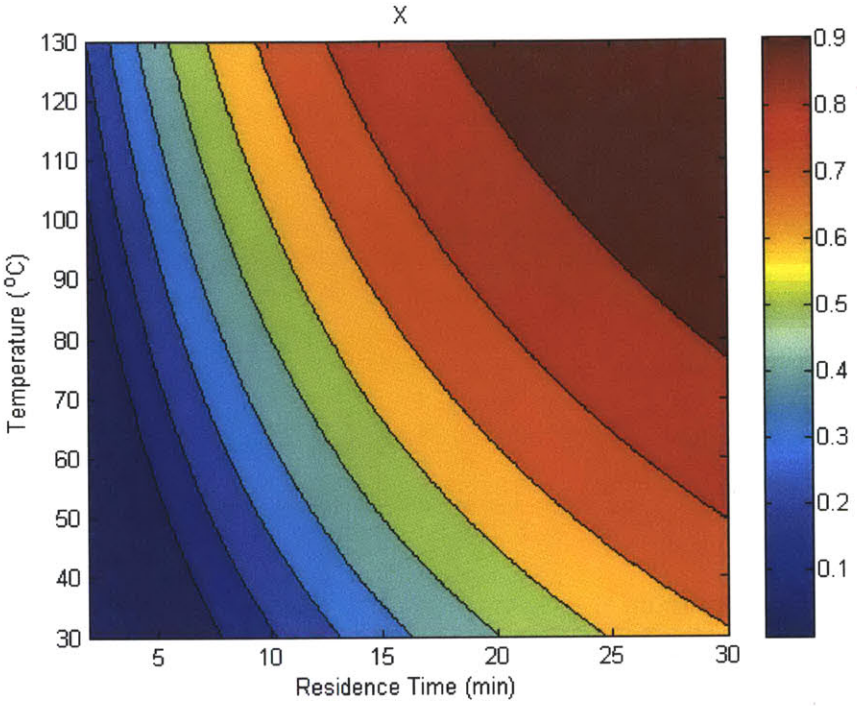

Figure A.5. Reaction conversion model based upon first-order kinetics with a time delay by $X = 1 - 1.50e^{-2.75e^{-1226/T}(\tau+2.75)}$ where X is the conversion fraction, T is the temperature in K, and τ is the residence time in minutes.

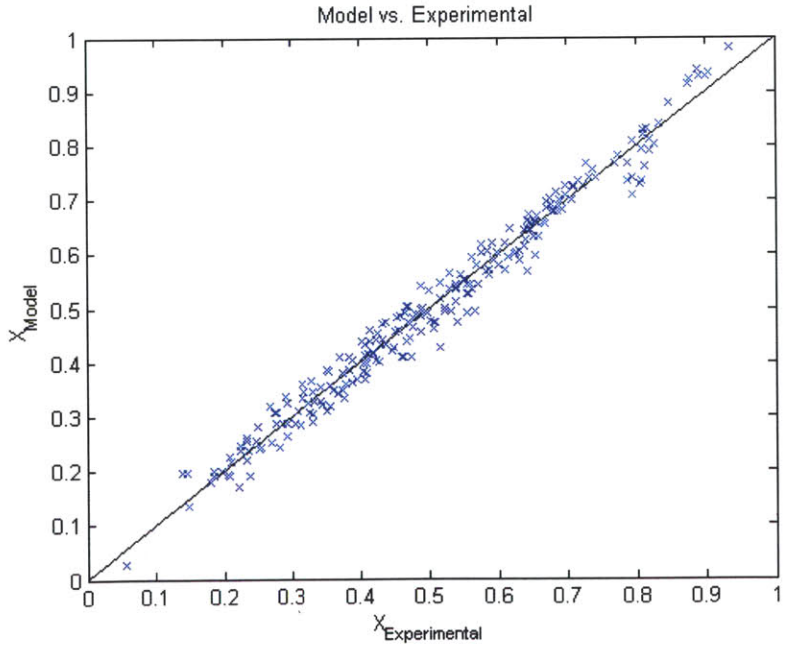

Figure A.6. Comparison of model predictions of conversion (X_{Model}) versus experimental data ($X_{Experimental}$).

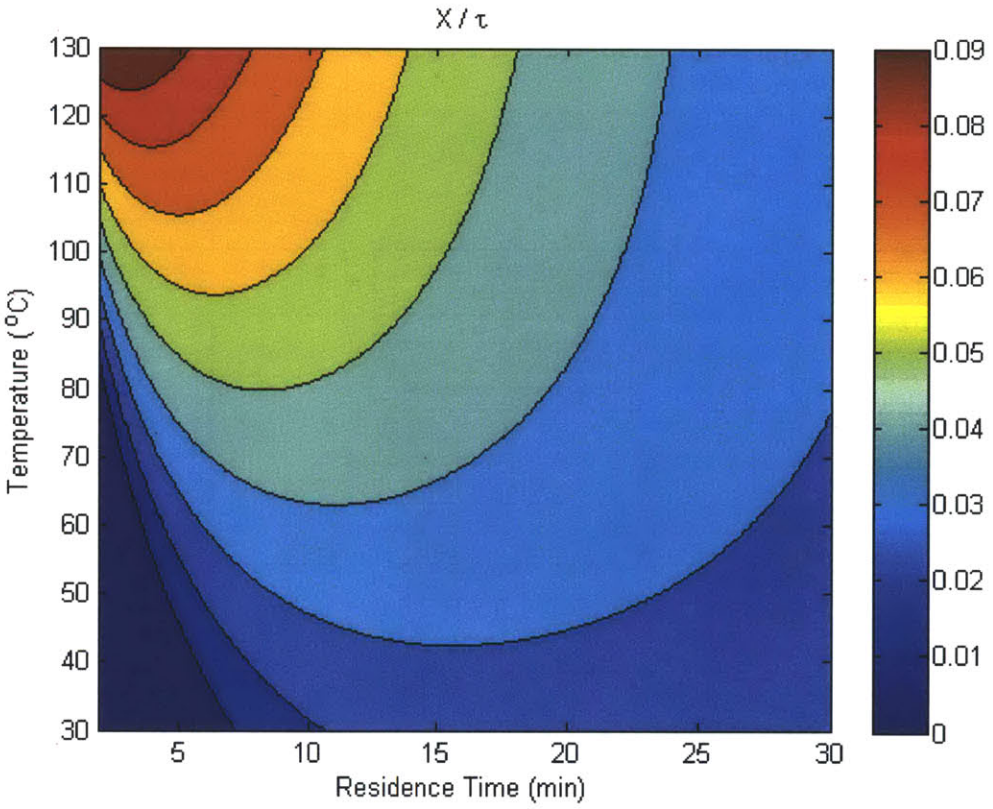

Figure A.7. Objective function based on the above model.

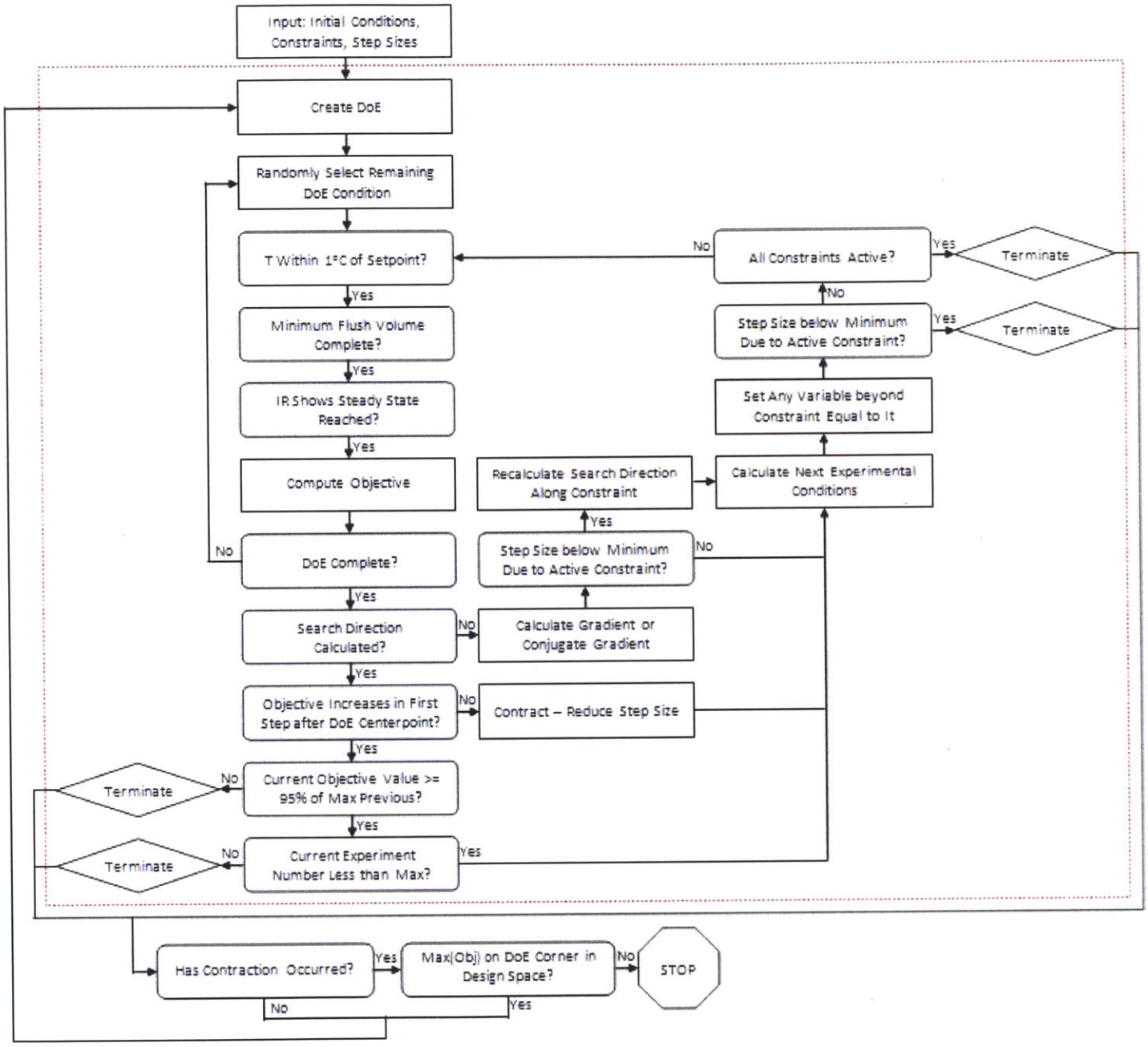

Figure A.8. Optimization decision tree.

Table A.1. Paal-Knorr optimization experimental data. Control variables at the corners of each DoE are bolded and the optimum is highlighted.

Results from Steepest Descent Optimization

Temperature (°C)	Residence Time (min)	Conversion	Conversion/Residence Time
38	**11.000**	0.250	0.0228
38	**9.000**	0.186	0.0207
42	**9.000**	0.207	0.0230
42	**11.000**	0.274	0.0249
40	10.000	0.234	0.0234
41	12.614	0.316	0.0250
43	15.228	0.416	0.0273
44	17.842	0.489	0.0274
46	20.457	0.576	0.0282
47	23.071	0.682	0.0296
49	25.685	0.716	0.0279
49	**22.071**	0.656	0.0297
45	**22.071**	0.642	0.0291
45	**24.071**	0.669	0.0278
49	**24.071**	0.698	0.0290
47	23.071	0.680	0.0295
48	20.334	0.641	0.0315
49	17.597	0.583	0.0332
51	14.860	0.523	0.0352
52	12.123	0.413	0.0341
53	9.386	0.310	0.0330
49	**15.860**	0.515	0.0325
53	**13.860**	0.478	0.0345
53	**15.860**	0.538	0.0340
49	**13.860**	0.451	0.0325

51	14.860	0.491	0.0330
54	13.902	0.486	0.0350
57	12.944	0.470	0.0363
60	11.986	0.456	0.0381
62	11.028	0.432	0.0391
65	10.070	0.409	0.0407
68	9.112	0.384	0.0422
71	8.154	0.358	0.0439
74	7.196	0.325	0.0451
77	6.238	0.286	0.0458
79	5.280	0.236	0.0447
82	4.322	0.186	0.0430
75	**5.238**	0.210	0.0400
79	**5.238**	0.223	0.0426
75	**7.238**	0.317	0.0437
79	**7.238**	0.344	0.0475
77	6.238	0.278	0.0446
78	9.050	0.424	0.0469
79	11.862	0.545	0.0460
80	14.674	0.642	0.0437
76	**10.050**	0.471	0.0469
76	**8.050**	0.375	0.0466
80	**8.050**	0.390	0.0484
80	**10.050**	0.488	0.0485
78	9.050	0.433	0.0478
81	9.757	0.482	0.0494
84	10.464	0.529	0.0506
87	11.171	0.568	0.0508
90	11.878	0.611	0.0514
93	12.585	0.648	0.0515

95	13.292	0.678	0.0510
98	13.999	0.710	0.0507
101	14.706	0.737	0.0501
104	15.413	0.773	0.0501
107	16.120	0.795	0.0493
110	16.827	0.816	0.0485
95	**11.585**	0.658	0.0568
91	**11.585**	0.638	0.0551
91	**13.585**	0.694	0.0511
95	**13.585**	0.706	0.0520
93	12.585	0.666	0.0529
93	9.619	0.559	0.0581
94	6.652	0.411	0.0617
94	3.686	0.196	0.0533
92	**7.652**	0.472	0.0617
96	**5.652**	0.361	0.0638
96	**7.652**	0.476	0.0623
92	**5.652**	0.335	0.0592
94	6.652	0.405	0.0609
97	7.647	0.473	0.0619
100	8.642	0.539	0.0623
102	9.637	0.594	0.0616
105	10.632	0.648	0.0609
108	11.627	0.686	0.0590
102	**9.642**	0.632	0.0656
98	**9.642**	0.610	0.0633
102	**7.642**	0.532	0.0696
98	**7.642**	0.509	0.0666
100	8.642	0.563	0.0652
101	5.826	0.406	0.0697

102	3.010	0.181	0.0600
99	**6.826**	0.409	0.0599
99	**4.826**	0.277	0.0574
103	**4.826**	0.293	0.0608
103	**6.826**	0.426	0.0624
101	5.826	0.356	0.0611
103	8.279	0.501	0.0606
102	6.644	0.414	0.0623
102	7.461	0.455	0.0610
100	**7.644**	0.459	0.0600
104	**5.644**	0.354	0.0627
100	**5.644**	0.330	0.0584
104	**7.644**	0.469	0.0614
102	6.644	0.404	0.0608
105	6.964	0.434	0.0623
108	7.284	0.468	0.0643
111	7.604	0.499	0.0657
114	7.925	0.531	0.0670
117	8.245	0.563	0.0683
120	8.565	0.591	0.0689
123	8.885	0.617	0.0695
126	9.205	0.645	0.0701
129	9.526	0.670	0.0703
130	9.846	0.685	0.0696
130	10.166	0.698	0.0687
131	**10.526**	0.732	0.0695
127	**10.526**	0.709	0.0674
127	**8.526**	0.643	0.0754
131	**8.526**	0.653	0.0766
129	9.526	0.690	0.0725

129	6.544	0.551	0.0843
130	3.563	0.319	0.0896
130	2.000	0.145	0.0727
128	**2.563**	0.224	0.0873
132	**2.563**	0.233	0.0910
128	**4.563**	0.419	0.0918
132	**4.563**	0.439	0.0962
130	3.563	0.333	0.0934
130	6.334	0.556	0.0878
130	4.486	0.420	0.0935
130	5.410	0.489	0.0904

Results from Conjugate Gradient Optimization

Temperature (°C)	Residence Time (min)	Conversion	Conversion/Residence Time
38	**11.000**	0.250	0.023
38	**9.000**	0.186	0.021
42	**9.000**	0.207	0.023
42	**11.000**	0.274	0.025
40	10.000	0.234	0.023
41	12.614	0.316	0.025
43	15.228	0.416	0.027
44	17.842	0.489	0.027
46	20.457	0.576	0.028
47	23.071	0.682	0.03
49	25.685	0.716	0.028
49	**22.071**	0.656	0.03
45	**22.071**	0.642	0.029
45	**24.071**	0.669	0.028
49	**24.071**	0.698	0.029

47	23.071	0.687	0.03
49	21.283	0.668	0.031
52	19.494	0.652	0.033
54	17.706	0.623	0.035
57	15.918	0.588	0.037
59	14.130	0.557	0.039
61	12.342	0.503	0.041
64	10.553	0.450	0.043
66	8.765	0.381	0.043
69	6.977	0.304	0.044
71	5.189	0.209	0.04
71	**7.977**	0.376	0.047
67	**7.977**	0.343	0.043
67	**5.977**	0.233	0.039
71	**5.977**	0.252	0.042
69	6.977	0.292	0.042
72	5.945	0.253	0.043
75	4.912	0.206	0.042
77	3.879	0.148	0.038
70	**4.944**	0.221	0.045
74	**4.944**	0.238	0.048
70	**6.944**	0.333	0.048
74	**6.944**	0.353	0.051
72	5.944	0.282	0.047
75	6.015	0.294	0.049
78	6.086	0.313	0.051
81	6.157	0.332	0.054
84	6.228	0.347	0.056
87	6.299	0.370	0.059

90	6.370	0.389	0.061
93	6.440	0.410	0.064
96	6.511	0.428	0.066
99	6.582	0.448	0.068
102	6.653	0.467	0.07
105	6.724	0.488	0.073
108	6.795	0.506	0.075
111	6.866	0.523	0.076
114	6.936	0.538	0.078
117	7.007	0.555	0.079
120	7.078	0.571	0.081
123	7.149	0.588	0.082
126	7.220	0.602	0.083
129	7.291	0.616	0.085
130	7.362	0.627	0.085
130	7.432	0.631	0.085
128	**6.362**	0.539	0.085
132	**6.362**	0.554	0.087
128	**8.362**	0.639	0.076
132	**8.362**	0.655	0.078
130	7.362	0.599	0.081
130	4.362	0.385	0.088
130	2.000	0.138	0.069
132	**5.362**	0.466	0.087
132	**3.362**	0.291	0.086
128	**3.362**	0.268	0.08
128	**5.362**	0.438	0.082
130	4.362	0.372	0.085
130	7.362	0.575	0.078

130	5.362	0.453	0.085
130	6.362	0.517	0.081

Results from Armijo Conjugate Gradient Optimization

Temperature (°C)	Residence Time (min)	Conversion	Conversion/Residence Time
38	**11.000**	0.250	0.023
38	**9.000**	0.186	0.021
42	**9.000**	0.207	0.023
42	**11.000**	0.274	0.025
40	10.000	0.206	0.021
48	23.942	0.574	0.024
56	30.000	0.676	0.023
52	30.000	0.683	0.023
50	27.428	0.656	0.024
49	25.685	0.673	0.026
47	**26.685**	0.663	0.025
51	**26.685**	0.678	0.025
51	**24.685**	0.671	0.027
47	**24.685**	0.662	0.027
49	25.685	0.657	0.026
62	15.792	0.545	0.035
74	5.900	0.225	0.038
87	2.000	0.047	0.023
68	10.846	0.422	0.039
71	8.373	0.340	0.041
69	**7.373**	0.327	0.044
73	**7.373**	0.334	0.045
73	**9.373**	0.515	0.055
69	**9.373**	0.424	0.045

71	8.373	0.397	0.047
87	9.135	0.498	0.055
103	9.897	0.585	0.059
119	10.660	0.675	0.063
130	11.422	0.770	0.067
132	**12.422**	0.826	0.066
132	**10.422**	0.741	0.071
128	**10.422**	0.724	0.069
128	**12.422**	0.819	0.066
130	11.422	0.728	0.064
130	2.000	0.140	0.070
130	6.711	0.642	0.096
130	4.355	0.474	0.109
130	5.533	0.567	0.103

Results from Quadratic Penalty Armijo Conjugate Gradient Optimization

Temperature (°C)	**Residence Time (min)**	**Conversion**	**Penalized Objective Function**
128	**3.355**	0.357	0.586
132	**3.355**	0.379	0.613
128	**5.355**	0.541	0.728
132	**5.355**	0.556	0.740
130	4.355	0.463	0.679
130	20.355	0.890	0.766
130	30.000	0.935	0.754
128	**21.355**	0.905	0.765
128	**19.355**	0.875	0.768
132	**19.355**	0.878	0.768
132	**21.355**	0.888	0.764
130	20.355	0.901	0.767

130	4.355	0.460	0.676
130	12.355	0.807	0.786
130	16.355	0.847	0.774
130	14.355	0.834	0.780
130	13.355	0.810	0.782

Results from Quadratic Penalty Armijo Conjugate Gradient Optimization above 130 °C

Temperature (°C)	**Residence Time (min)**	**Conversion**	**Penalized Objective Function**
132	**13.355**	0.797	0.779
128	**13.355**	0.778	0.776
132	**11.355**	0.753	0.780
128	**11.355**	0.735	0.774
130	12.355	0.763	0.777
145	16.640	0.853	0.774
138	14.497	0.799	0.775
134	13.426	0.784	0.777
132	12.891	0.772	0.776
132	**12.426**	0.772	0.779
136	**12.426**	0.780	0.780
132	**14.426**	0.798	0.775
136	**14.426**	0.811	0.777
134	13.426	0.741	0.766
149	8.163	0.669	0.772
164	2.899	0.418	0.680
141	10.794	0.716	0.771
145	9.479	0.688	0.769
147	8.821	0.679	0.770
148	8.492	0.668	0.768
147	**9.163**	0.690	0.772

147	**7.163**	0.626	0.760
151	**7.163**	0.640	0.768
151	**9.163**	0.705	0.778
149	8.163	0.673	0.773
165	5.377	0.610	0.778
181	2.591	0.453	0.739
196	2.000	0.425	0.755
212	2.000	0.480	0.826
228	2.000	0.246	0.481
204	2.000	0.449	0.786
208	2.000	0.462	0.802
210	2.000	0.466	0.808
210	**3.000**	0.515	0.782
210	**1.000**	0.220	0.545
214	**1.000**	0.228	0.563
214	**3.000**	0.511	0.778
212	2.000	0.451	0.788
212	17.998	0.910	0.773
212	10.000	0.847	0.807
212	6.000	0.741	0.834
212	8.000	0.809	0.822
212	7.000	0.778	0.828
210	**7.000**	0.768	0.825
210	**5.000**	0.690	0.835
214	**5.000**	0.572	0.760
214	**7.000**	0.460	0.636
212	6.000	0.764	0.843

Appendix B: Chapter 3 Supporting Information

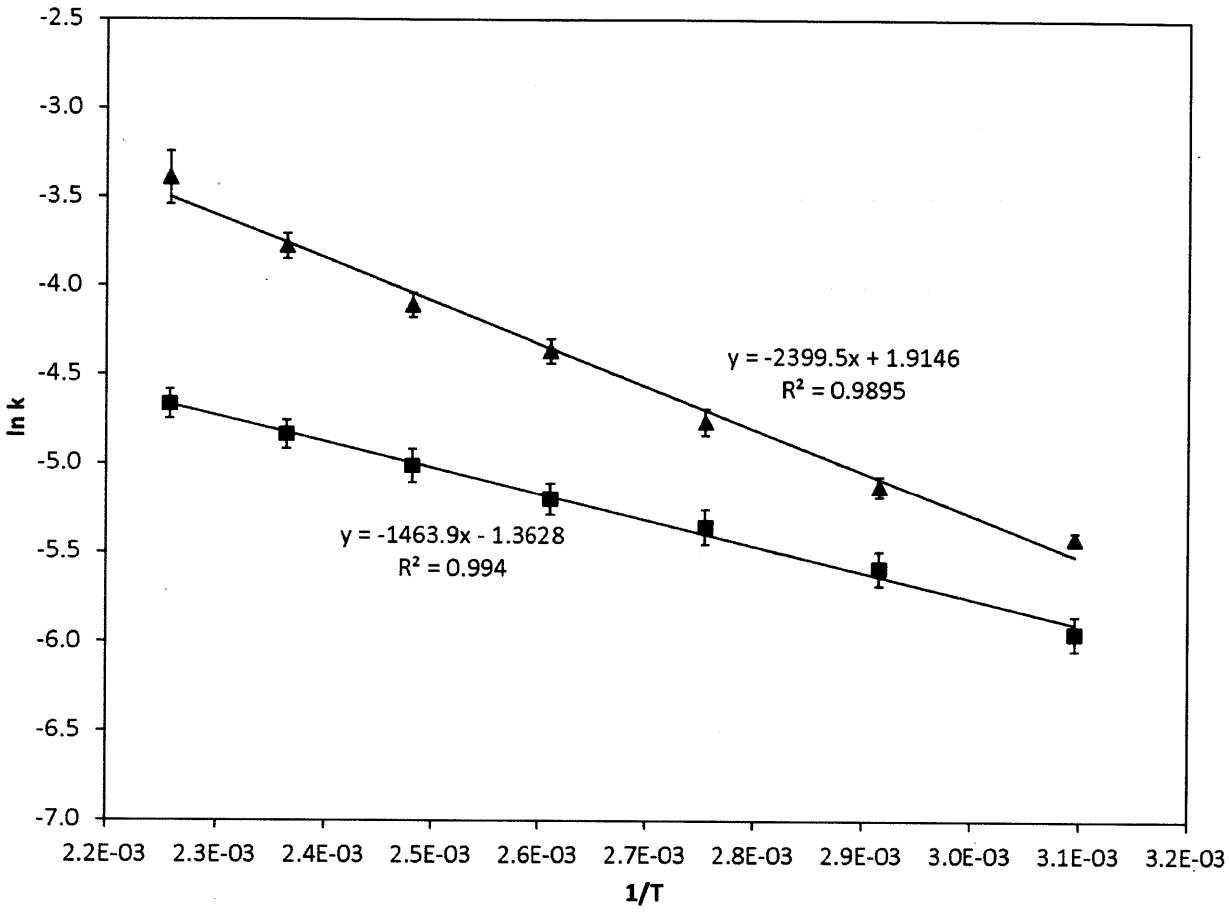

Figure B.1. Arrhenius plot with ln k_1 (■) and ln k_2 (▲).

Residence Time Calculation

Calculation of τ

$$\tau_{ins} = \tau_0 + \alpha t$$

$$\tau = \tau_0 + St$$

$$Q(t) = \frac{V_r}{\tau_{ins}} = \frac{V_r}{\tau_0 + \alpha t}$$

$$V_r = \int_{t_i}^{t_f} Q(t)\,dt = \int_{t_i}^{t_f} \frac{V_r}{\tau_0 + \alpha t}\,dt$$

$$1 = \frac{1}{\alpha}\ln(\tau_0 + \alpha t)\Big|_{t_i}^{t_f}$$

$$\alpha = \ln\left(\frac{\tau_0 + \alpha t_f}{\tau_0 + \alpha t_i}\right)$$

$$e^{\alpha}(\tau_0 + \alpha t_i) = \tau_0 + \alpha t_f$$

$$t_f = e^{\alpha} t_i + (e^{\alpha} - 1)\frac{\tau_0}{\alpha}$$

$$t_i = e^{-\alpha} t_f - (1 - e^{-\alpha})\frac{\tau_0}{\alpha}$$

Substitution for τ

$$\tau = t_f - t_i$$

$$\tau = t_f - \left(e^{-\alpha} t_f - (1 - e^{-\alpha})\frac{\tau_0}{\alpha}\right)$$

$$\tau = (1 - e^{-\alpha})\left(t_f + \frac{\tau_0}{\alpha}\right)$$

$$S = slope\{\tau, t_f\} = (1 - e^{-\alpha})$$

$$t_f = \frac{e^{\alpha}}{e^{\alpha} - 1}\tau - \frac{\tau_0}{\alpha}$$

Relation to τ_{ins}

$$t_f = \frac{\tau_{ins} - \tau_0}{\alpha}$$

$$\tau = \left(1 - e^{-\alpha}\right)\left(\frac{\tau_{ins} - \tau_0}{\alpha} + \frac{\tau_0}{\alpha}\right)$$

$$\tau = \left(1 - e^{-\alpha}\right)\frac{\tau_{ins}}{\alpha} = \frac{S}{\alpha}\tau_{ins}$$

Corrected τ

$$V_d = \int_{t_f}^{t_m} \frac{V_r}{\tau_0 + \alpha t} dt$$

$$\frac{V_d}{V_r}\alpha = \ln\left(\frac{\tau_0 + \alpha t_m}{\tau_0 + \alpha t_f}\right)$$

$$e^{\frac{V_d}{V_r}\alpha}\left(\tau_0 + t_f\right) = \tau_0 + \alpha t_m$$

$$t_m = e^{\frac{V_d}{V_r}\alpha} t_f + \left(e^{\frac{V_d}{V_r}\alpha} - 1\right)\frac{\tau_0}{\alpha}$$

$$t_f = e^{-\frac{V_d}{V_r}\alpha} t_m - \left(1 - e^{-\frac{V_d}{V_r}\alpha}\right)\frac{\tau_0}{\alpha}$$

$$\frac{e^{\alpha}}{e^{\alpha} - 1}\tau - \frac{\tau_0}{\alpha} = e^{-\frac{V_d}{V_r}\alpha} t_m - \left(1 - e^{-\frac{V_d}{V_r}\alpha}\right)\frac{\tau_0}{\alpha}$$

$$\tau = \left(1 - e^{-\alpha}\right)e^{-\frac{V_d}{V_r}\alpha}\left(t_m + \frac{\tau_0}{\alpha}\right)$$

If $t_i < 0$ and $t_f \geq 0$

$$V_r = \int_{t_i}^{0} \frac{V_r}{\tau_0} dt + \int_{0}^{t_f} \frac{V_r}{\tau_0 + \alpha t} dt$$

$$1 = \frac{-t_i}{\tau_0} + \frac{1}{\alpha} \ln\left(\frac{\tau_0 + \alpha t_f}{\tau_0}\right)$$

$$t_i = \tau_0 \left(\frac{1}{\alpha} \ln\left(\frac{\tau_0 + \alpha t_f}{\tau_0}\right) - 1\right)$$

$$\tau = t_f - \tau_0 \left(\frac{1}{\alpha} \ln\left(\frac{\tau_0 + \alpha t_f}{\tau_0}\right) - 1\right)$$

Appendix C: Chapter 4 Supporting Information

Table C.1. Molar concentration of a gas at different pressures.

Pressure (psi)	Pressure (bar)	Concentration CO (M)
14.5/atmosphere	1.0	0.04
40	2.8	0.12
80	5.5	0.25
120	8.3	0.37
180	12.4	0.55

Pseudo First-Order Approximation

$$-\frac{d[ArX]}{dt} = k_1[Pd][L][ArX] \quad (1)$$

$$-\frac{d[ArX]}{dt} = k_1\frac{[Pd]_0[L]}{1+K[CO]}[ArX]$$

$$-\frac{d[ArX]}{dt} = k_{obs}[ArX] \quad (3)$$

$$k_{obs} = \frac{k_1[Pd]_0[L]}{1+K[CO]}$$

Steady-State Approximation

$$[Pd] = [Pd]_0 - [Pd_{CO}]$$

$$k_f[Pd][CO] = k_r[Pd_{CO}]$$

$$[Pd_{CO}] = \frac{k_f[Pd][CO]}{k_r}$$

$$[Pd] = [Pd]_0 - \frac{k_f[Pd][CO]}{k_r}$$

$$[Pd] = \frac{[Pd]_0}{1+K[CO]} \quad (2)$$

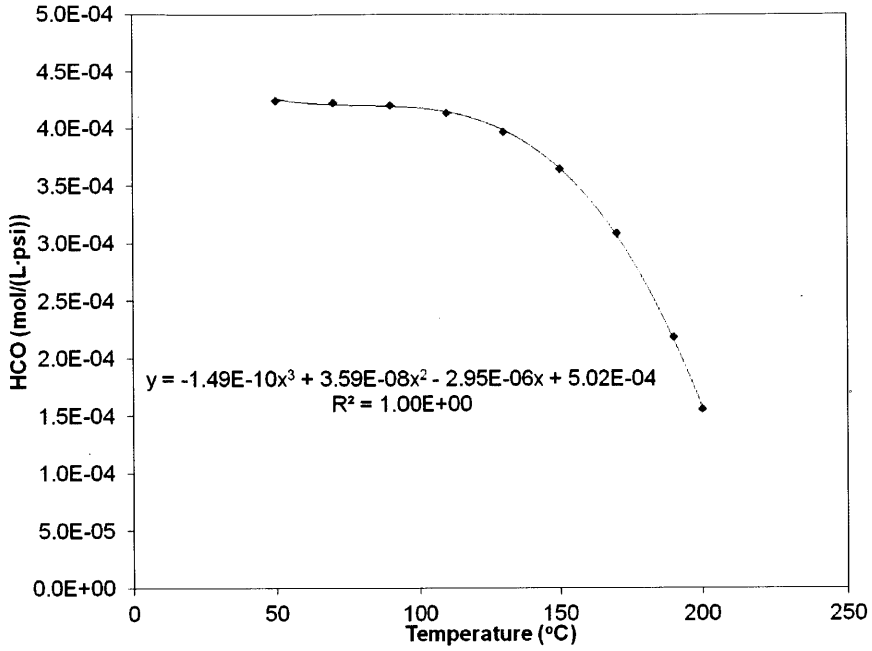

Figure C.1. Carbon monoxide Henry's Law constant as a function of temperature. Polynomial was fit to data generated with Aspen Plus.

Model Details

Beginning with the full reaction scheme, several simplifications can be made based upon the pseudo-steady state assumption (PSSA). Firstly, as is discussed in the text, the reversible palladium poisoning by carbon monoxide can be lumped into an observed rate constant, k_{obs}. Additionally, as the oxidative addition is significantly slower than the carbon monoxide association, PSSA can be assumed to eliminate this intermediate step from the rate laws. For simplicity in writing the rate expressions, all intermediates have been numbered 1 through 5.

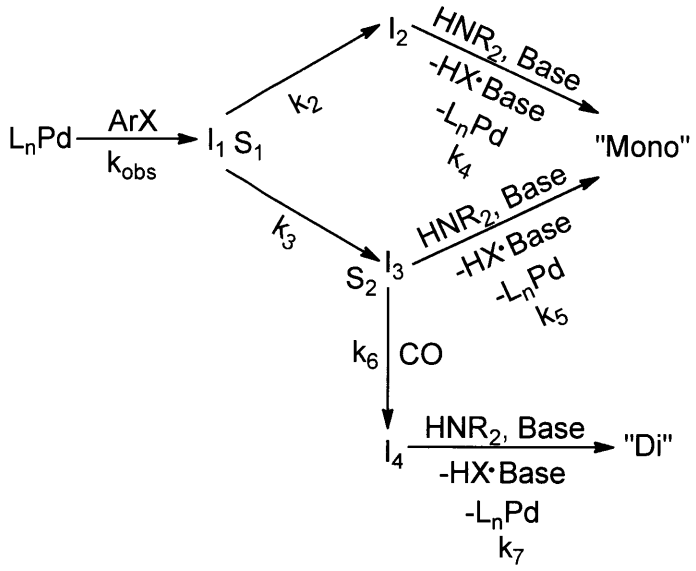

This produces the reaction rates:

$$\frac{d[ArX]}{dt} = -k_{obs}[ArX]$$

$$\frac{d[I_1]}{dt} = k_{obs}[ArX] - k_2[I_1] - k_3[I_1]$$

$$\frac{d[I_2]}{dt} = k_2[I_1] - k_4[I_2]$$

$$\frac{d[I_3]}{dt} = k_3[I_1] - k_5[I_3] - k_6[I_3]$$

$$\frac{d[I_4]}{dt} = k_6[I_3] - k_7[I_4]$$

$$\frac{d[Mono]}{dt} = k_4[I_2] + k_5[I_3]$$

$$\frac{d[Di]}{dt} = k_7[I_4]$$

Now, lumping the reaction rates at each bifurcation and using the selectivity terms modifies the equations to become:

$$\frac{d[ArX]}{dt} = -k_{obs}[ArX]$$
$$\frac{d[I_1]}{dt} = k_{obs}[ArX] - k_{S_1}[I_1]$$
$$\frac{d[I_2]}{dt} = k_{S_1}S_1[I_1] - k_4[I_2]$$
$$\frac{d[I_3]}{dt} = k_{S_1}(1-S_1)[I_1] - k_{S_2}[I_3]$$
$$\frac{d[I_4]}{dt} = k_{S_2}(1-S_2)[I_3] - k_7[I_4]$$
$$\frac{d[Mono]}{dt} = k_4[I_2] + k_{S_2}S_2[I_3]$$
$$\frac{d[Di]}{dt} = k_7[I_4]$$

Further applying PSSA to intermediates 1, 3, and 4 produces the following equalities:

$$k_{obs}[ArX] \approx k_{S_1}[I_1]$$
$$k_{S_1}(1-S_1)[I_1] \approx k_{S_2}[I_3]$$
$$k_{S_2}(1-S_2)[I_3] \approx k_7[I_4]$$

The remaining equations then become:

$$\frac{d[ArX]}{dt} = -k_{obs}[ArX]$$
$$\frac{d[I_2]}{dt} = k_{obs}S_1[ArX] - k_4[I_2]$$
$$\frac{d[Mono]}{dt} = k_4[I_2] + k_{obs}S_2(1-S_1)[ArX]$$
$$\frac{d[Di]}{dt} = k_{obs}(1-S_1)(1-S_2)[ArX]$$

Additionally, the Pd balance is given by:

$$\frac{d[Pd]}{dt} = -\frac{d[ArX]}{dt} + \frac{d[Mono]}{dt} + \frac{d[Di]}{dt}$$

$$\frac{d[Pd]}{dt} = -k_{obs}[ArX] + k_4[I_2] + k_{obs}S_2(1-S_1)[ArX] + k_{obs}(1-S_1)(1-S_2)[ArX]$$

$$\frac{d[Pd]}{dt} = k_4[I_2] - k_{obs}S_1[ArX]$$

This set of equations was modeled in Matlab using the following differential code and fitted parameters:

```
k = ([1.3334, 1.1147, 1.0712, 2.4226, 3.8659, 2.0095]);
k = [k(1)*1E17,116.4,k(2)*1E6,55.6,k(3)*1E2,k(4)*1E-13,k(5)*1E1,k(6)*1E-4];

% [(k0,[1]), (EA,[1]), (k0,[4]), (EA,[4]), (EA,[2]-EA,[3]), (k0,[3]/k0,[2]),
(EA,[5]-EA,[6]), (k0,[6]/k0,[5])]

function der = ODEFun(~,C,T,pCO,Pd0,k)
% C = [ArX, I2, M, D, Pd]

HCO = -1.49E-10*T^3+3.59E-8*T^2-2.95E-6*T+5.02E-4;

k1 = k(1)*exp(-k(2)*1E3/(8.314*(273+T)));
k4 = k(3)*exp(-k(4)*1E3/(8.314*(273+T)));

kobs = k1*(C(5)*Pd0/(HCO*pCO));
S1 = 1/(1+k(6)*exp(k(5)*1E3/(8.314*(273+T))));
S2 = 1/(1+k(8)*exp(k(7)*1E3/(8.314*(273+T)))*HCO*pCO);

der(1,1) = -kobs*C(1); %d[ArX]/dt
der(2,1) = S1*kobs*C(1)-k4*C(2); %d[I2]/dt
der(3,1) = k4*C(2)+(1-S1)*kobs*C(1)*S2; %d[M]/dt
der(4,1) = (1-S1)*kobs*C(1)*(1-S2); %d[D]/dt
der(5,1) = k4*C(2)-S1*kobs*C(1); %d[Pd]/dt
```

Appendix D: Chapter 5 Supporting Information

Table D.1. Salicylaldehyde Petasis yield vs. temperature.

Temperature (°C)	Residence Time (min)	Yield	Side Product
90	10	0.000	0
100	10	0.081	0
110	10	0.169	0
120	10	0.294	0
130	10	0.458	0
140	10	0.612	0
150	10	0.748	0
160	10	0.787	0
170	10	0.787	0.08
180	10	0.672	0.102
190	10	0.607	0.149
200	10	0.516	0.187
210	10	0.405	0.235
100	5	0.000	0
110	5	0.000	0
120	5	0.095	0
130	5	0.171	0
140	5	0.264	0
150	5	0.422	0
160	5	0.554	0
165	5	0.578	0
170	5	0.599	0
175	5	0.616	0
180	5	0.685	0.028
185	5	0.649	0.043

190	5	0.678	0.056
195	5	0.694	0.072
200	5	0.678	0.095
210	5	0.629	0.133
220	5	0.483	0.124

Table D.2. Salicylaldehyde Petasis yield vs. residence time.

Temperature (°C)	Residence Time (min)	Yield
160	3	0.533
160	4	0.600
160	5	0.661
160	8	0.751
160	9	0.768
160	10	0.764
160	11	0.710
160	12	0.733
160	14	0.545
180	1	0.413
180	1.5	0.508
180	2	0.592
180	3	0.701
180	4	0.731
180	5	0.707
180	6	0.709
200	0.5	0.477
200	0.75	0.567
200	1	0.640
200	1.5	0.678
200	2	0.713
200	2.5	0.739
200	3	0.688
200	3.5	0.686
200	4	0.694
200	4.5	0.665
200	5	0.689

200	6	0.680
200	7	0.672
200	8	0.651
200	10	0.547

Table D.3. 1.2 M glyoxylic acid Petasis.

Temperature (°C)	Residence Time (min)	Yield	Conversion	Side Product
60	10	0.480	0.683	0.000
70	10	0.579	0.751	0.000
80	10	0.635	0.818	0.000
90	10	0.774	0.879	0.004
100	10	0.879	0.899	0.041
110	10	0.758	0.846	0.080
120	10	0.734	0.816	0.093

Table D.4. 1.5 M glyoxylic acid Petasis.

Temperature (°C)	Residence Time (min)	Yield	Conversion
35	3.5	0.000	0.550
35	3.5	0.000	0.569
40	3.5	0.000	0.561
45	3.5	0.000	0.567
50	3.5	0.090	0.554
50	3.5	0.000	0.578
55	3.5	0.137	0.577
60	3.5	0.189	0.586
60	3.5	0.212	0.588
65	3.5	0.286	0.616
70	3.5	0.235	0.610
70	3.5	0.235	0.687
75	3.5	0.392	0.653
80	3.5	0.451	0.669
80	3.5	0.454	0.647
85	3.5	0.488	0.712

90	3.5	0.558	0.705
90	3.5	0.538	0.727
95	3.5	0.631	0.732

Table D.5. Petasis-Ugi tandem reaction.

Petasis Temperature (°C)	Petasis Residence Time (min)	Ugi Temperature (°C)	Ugi Residence Time (min)	Yield	Conversion	Side Product 1	Side Product 2
100	10	60	6.66	0.140	0.298	0.000	0.000
100	10	60	6.66	0.144	0.303	0.000	0.000
100	10	70	6.66	0.256	0.353	0.000	0.000
100	10	70	6.66	0.275	0.333	0.000	0.000
100	10	80	6.66	0.333	0.331	0.000	0.000
100	10	80	6.66	0.327	0.367	0.000	0.000
100	10	90	6.66	0.353	0.357	0.000	0.000
100	10	90	6.66	0.370	0.355	0.000	0.000
100	10	100	6.66	0.418	0.450	0.000	0.000
100	10	100	6.66	0.427	0.451	0.000	0.000
100	10	110	6.66	0.405	0.482	0.000	0.000
100	10	110	6.66	0.453	0.449	0.000	0.000
100	10	115	6.66	0.472	0.452	0.000	0.000
100	10	115	6.66	0.452	0.467	0.000	0.000
100	10	120	6.66	0.480	0.448	0.153	0.000
100	10	125	6.66	0.450	0.504	0.174	0.000
100	10	125	6.66	0.438	0.510	0.113	0.000
100	10	130	6.66	0.457	0.480	0.181	0.000
100	10	130	6.66	0.449	0.492	0.173	0.000
100	10	135	6.66	0.410	0.559	0.188	0.000
100	10	135	6.66	0.382	0.574	0.167	0.000
100	10	140	6.66	0.409	0.588	0.211	0.159
100	10	140	6.66	0.397	0.599	0.205	0.153
100	10	145	6.66	0.337	0.733	0.121	0.228
100	10	145	6.66	0.312	0.761	0.108	0.204

Appendix E: Chapter 6 Supporting Information

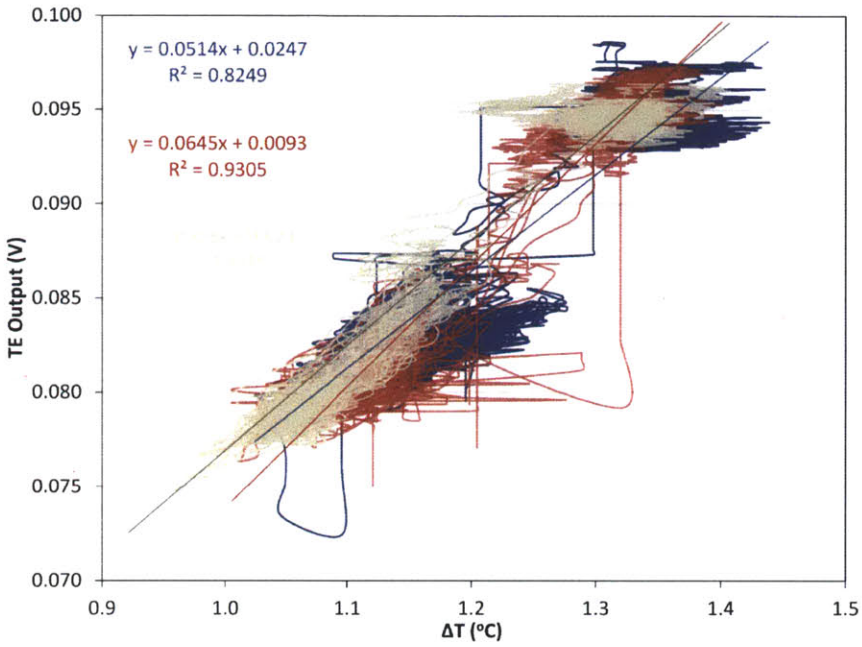

Figure E.1. Benzene nitration correlation between thermoelectric output and temperature difference across thermoelectric elements for repeat 1 (dark blue), 2 (red), and 3 (tan).

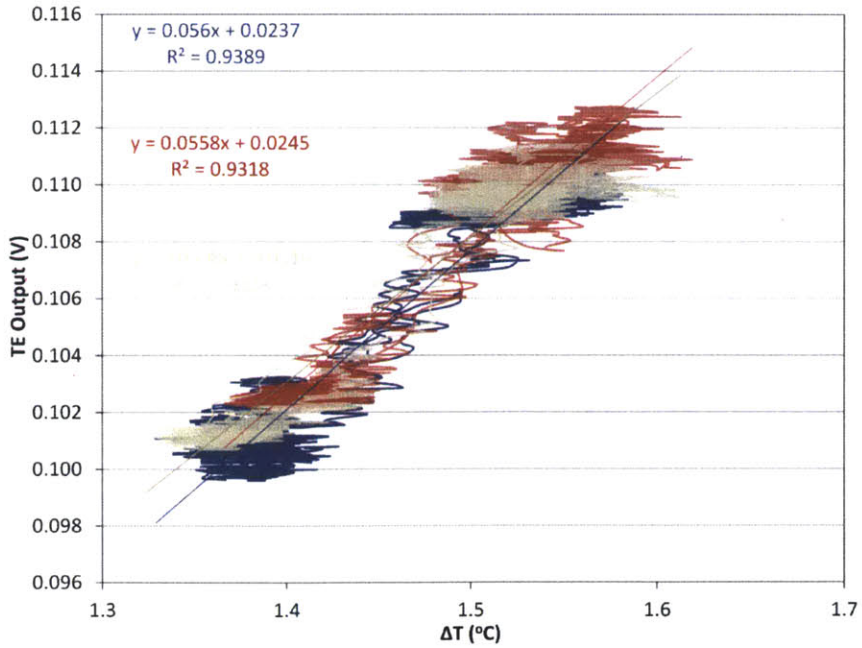

Figure E.2. Paal-Knorr correlation between thermoelectric output and temperature difference across thermoelectric elements for repeat 1 (dark blue), 2 (red), and 3 (tan).

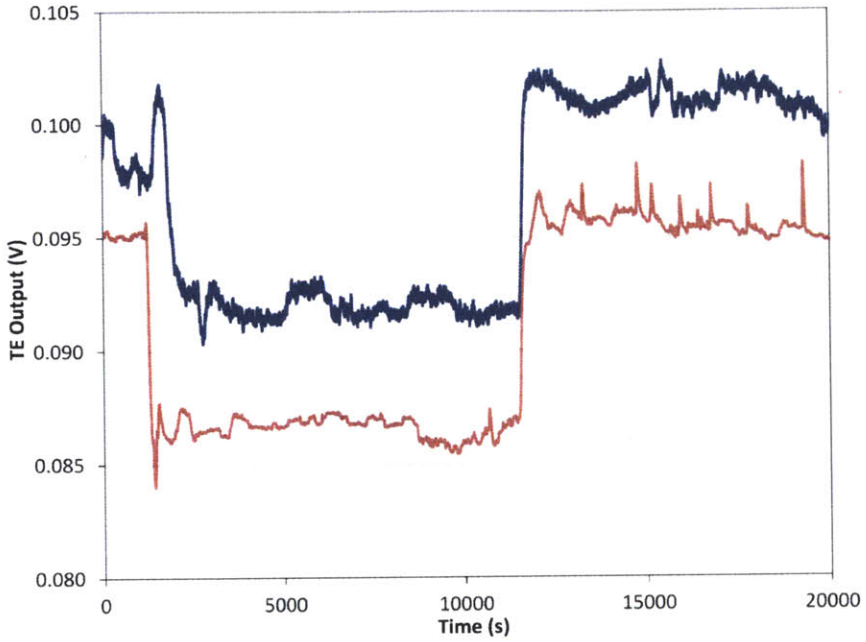

Figure E.3. Neat Paal-Knorr thermoelectric output for repeat 1 (dark blue) and 2 (red).

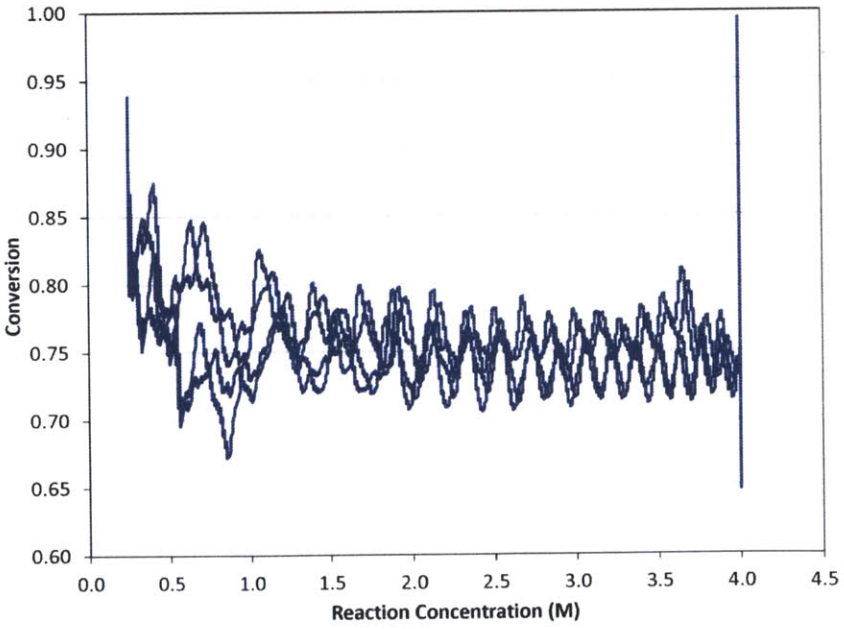

Figure E.4. Paal-Knorr reaction concentration ramp conversion.

Appendix F: pH Microflow Cell

A pH microflow cell was developed to measure pH online. Typical pH flow cells are multiple milliliters in volume, and dye-based systems designed for microsystems do not cover the full pH range. The flow cell itself and a schematic are shown in Figure F.1.

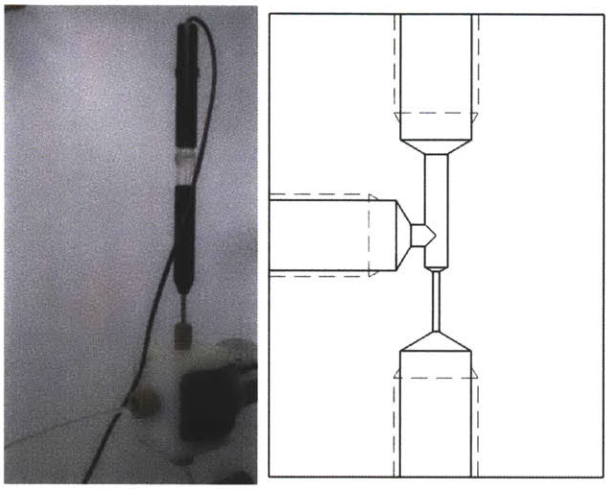

Figure F.1. Inline pH probe.

This relatively simple flow cell with an internal volume of approximately 20 μL has proven effective at online measurement and rapidly responding to changes in pH, as demonstrated in Figure F.2.

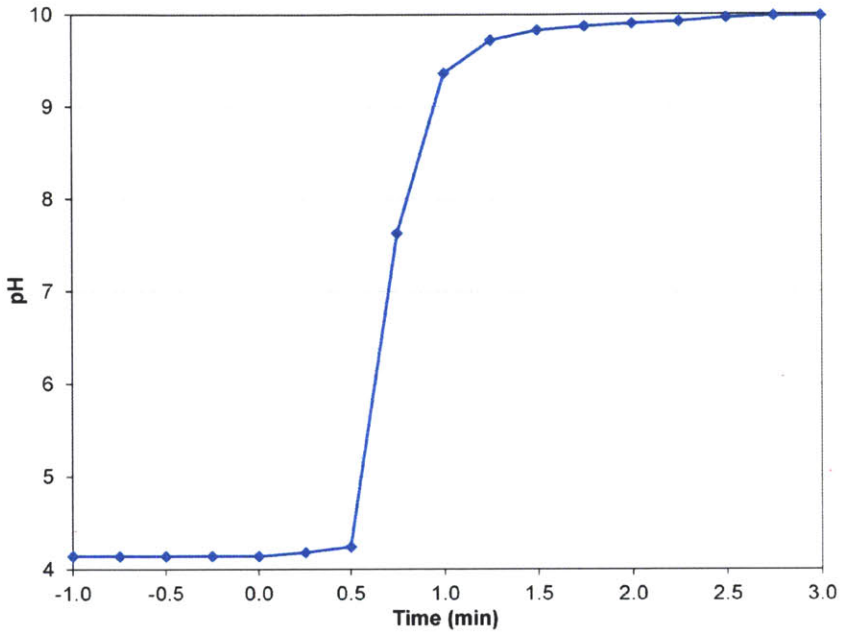

Figure F.2. Switching from pH 4 buffer to pH 10 buffer, while flowing at 10 μL/min.

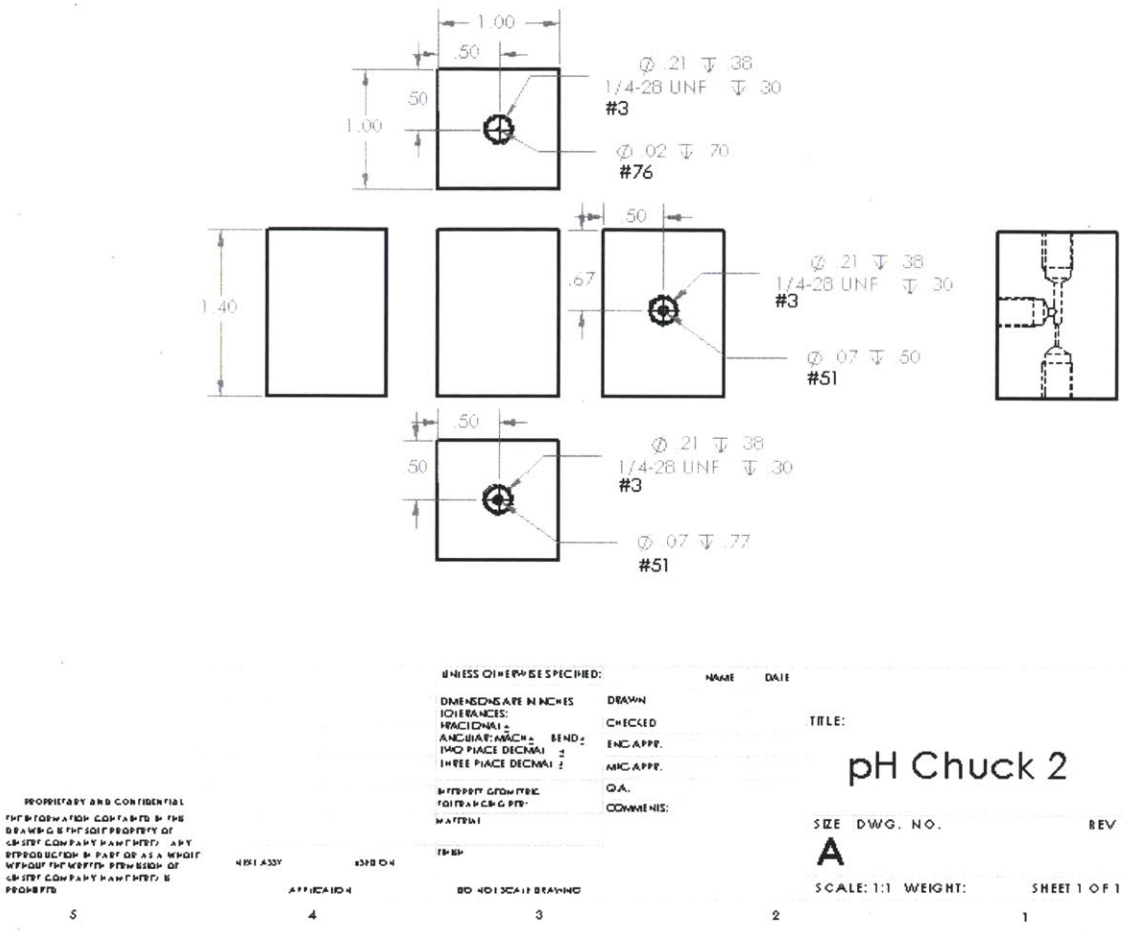

Figure F.3. SolidWorks drawing of pH microflow cell.Dimensions are in inches. Scale 1:1.

Appendix G: MICROREACTOR CHUCKS

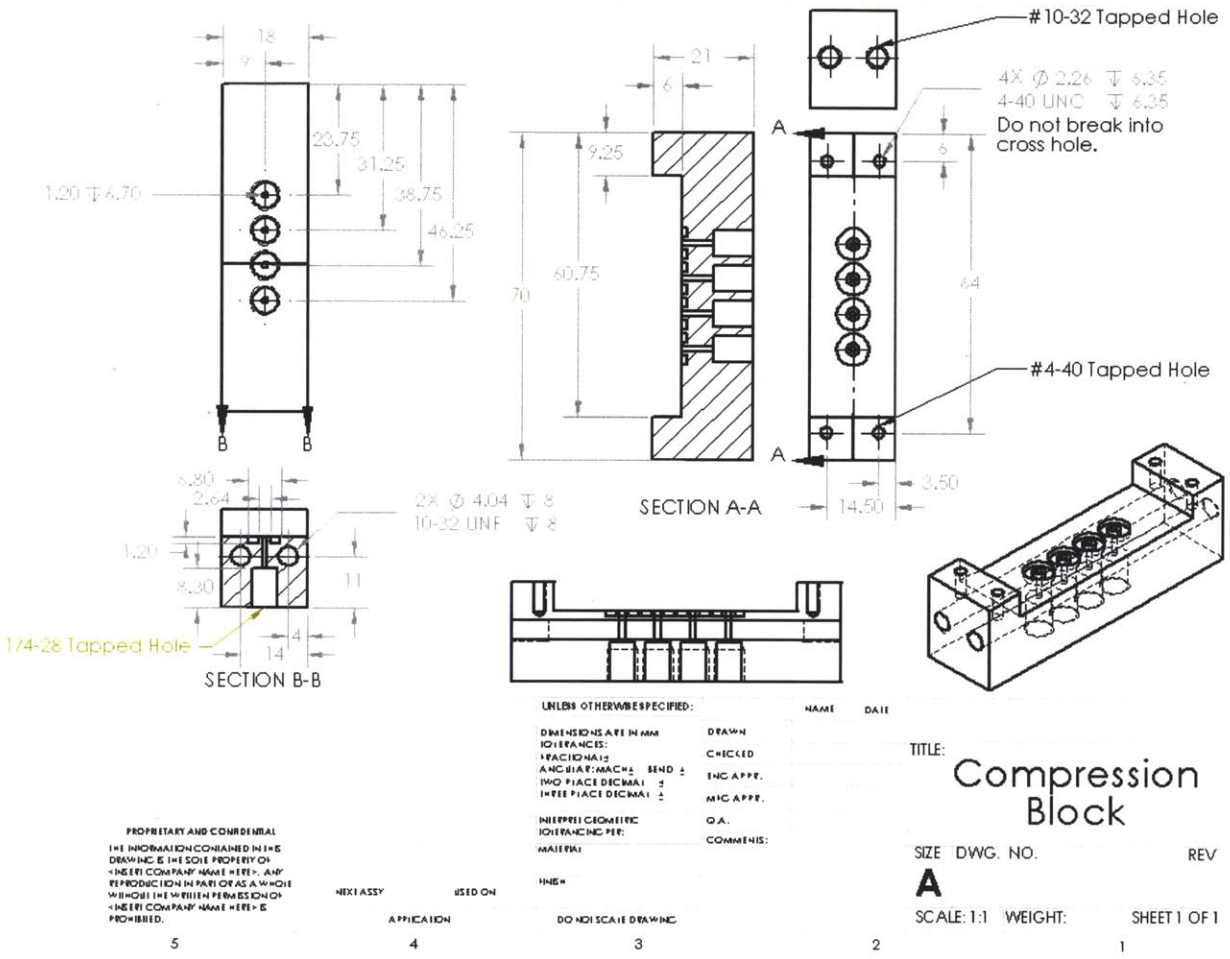

Figure G.1. SolidWorks drawing of microreactor cold-side compression block.Dimensions are in mm. Scale 1:1.

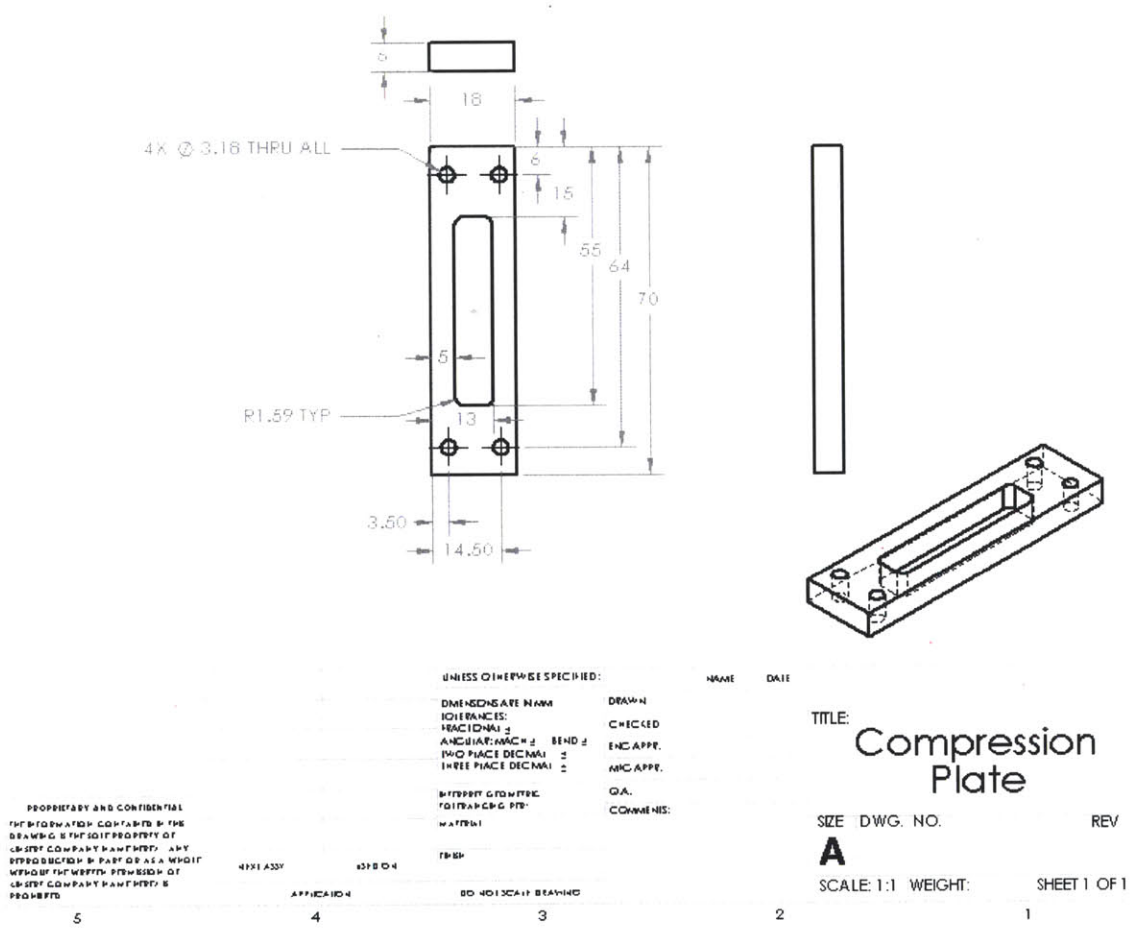

Figure G.2. SolidWorks drawing of microreactor cold-side compression plate.Dimensions are in mm. Scale 1:1.

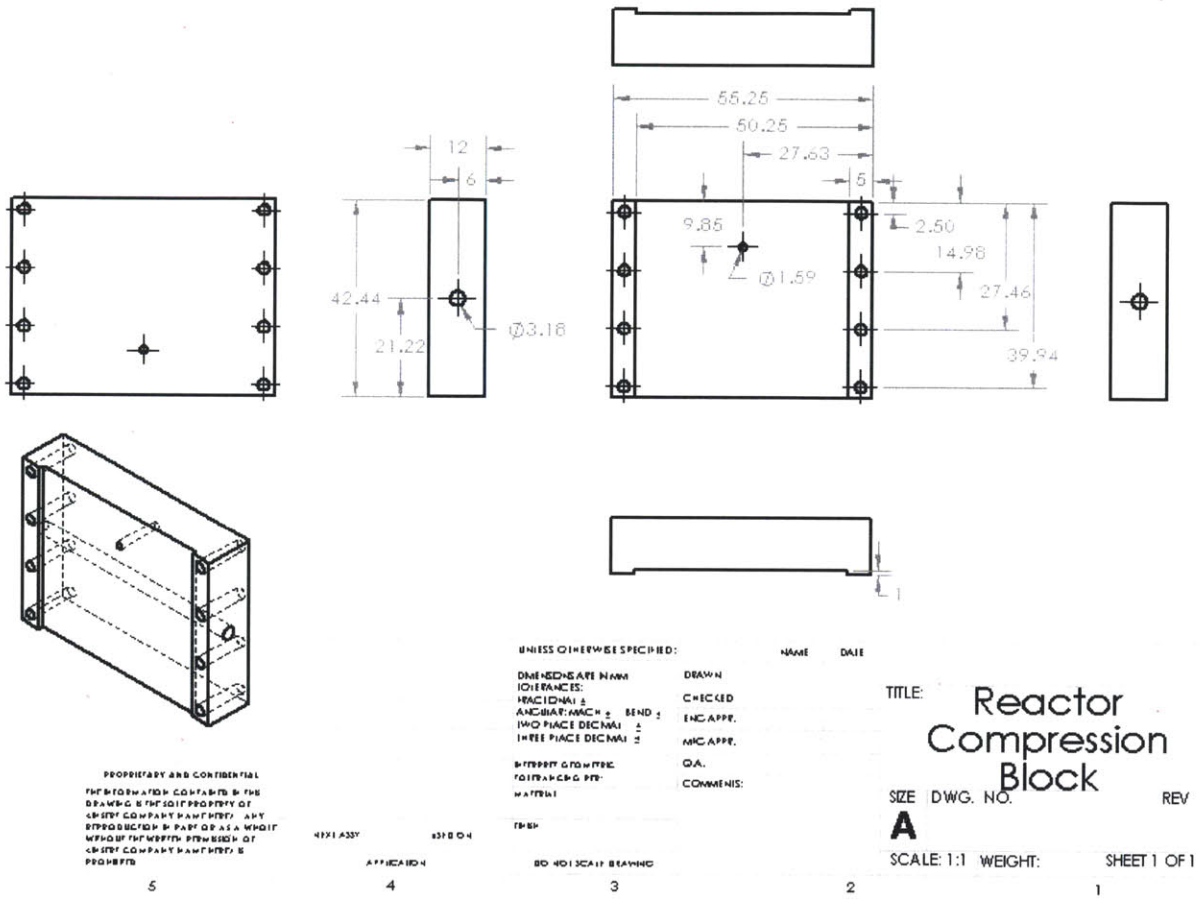

Figure G.3. SolidWorks drawing of microreactor hot-side compression block.Dimensions are in mm. Scale 1:1.

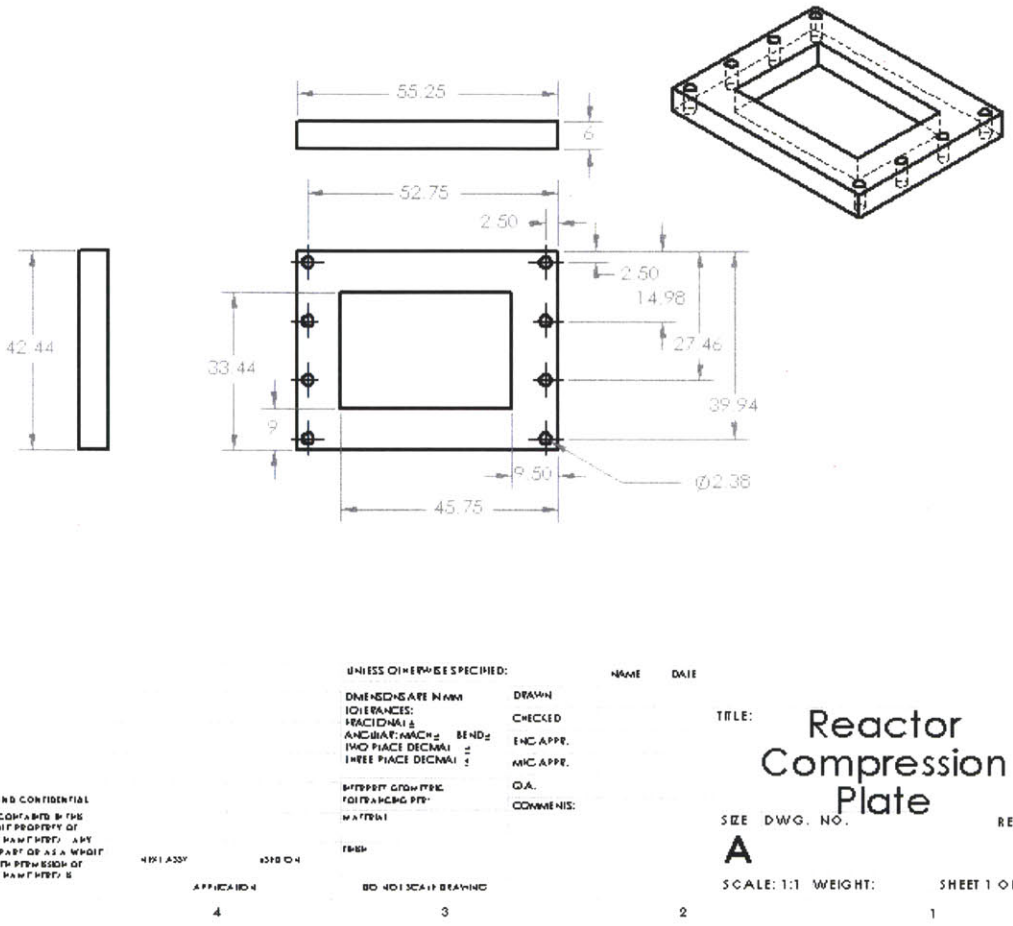

Figure G.4. SolidWorks drawing of microreactor hot-side compression plate.Dimensions are in mm. Scale 1:1.

Appendix H: MICROCALORIMETER CHUCKS

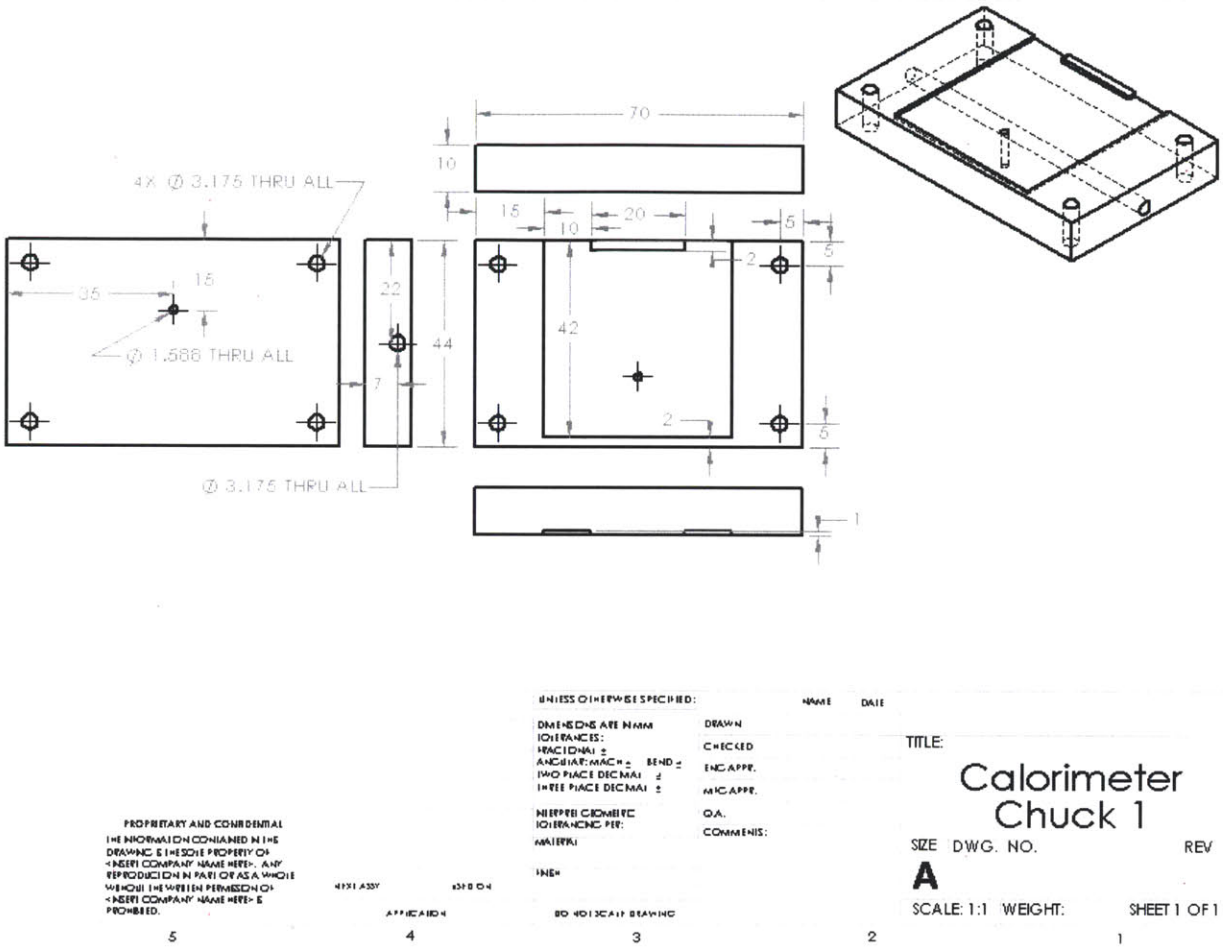

Figure H.1. SolidWorks drawing of microcalorimeter 1 chuck. Dimensions are in mm. Scale 1:1.

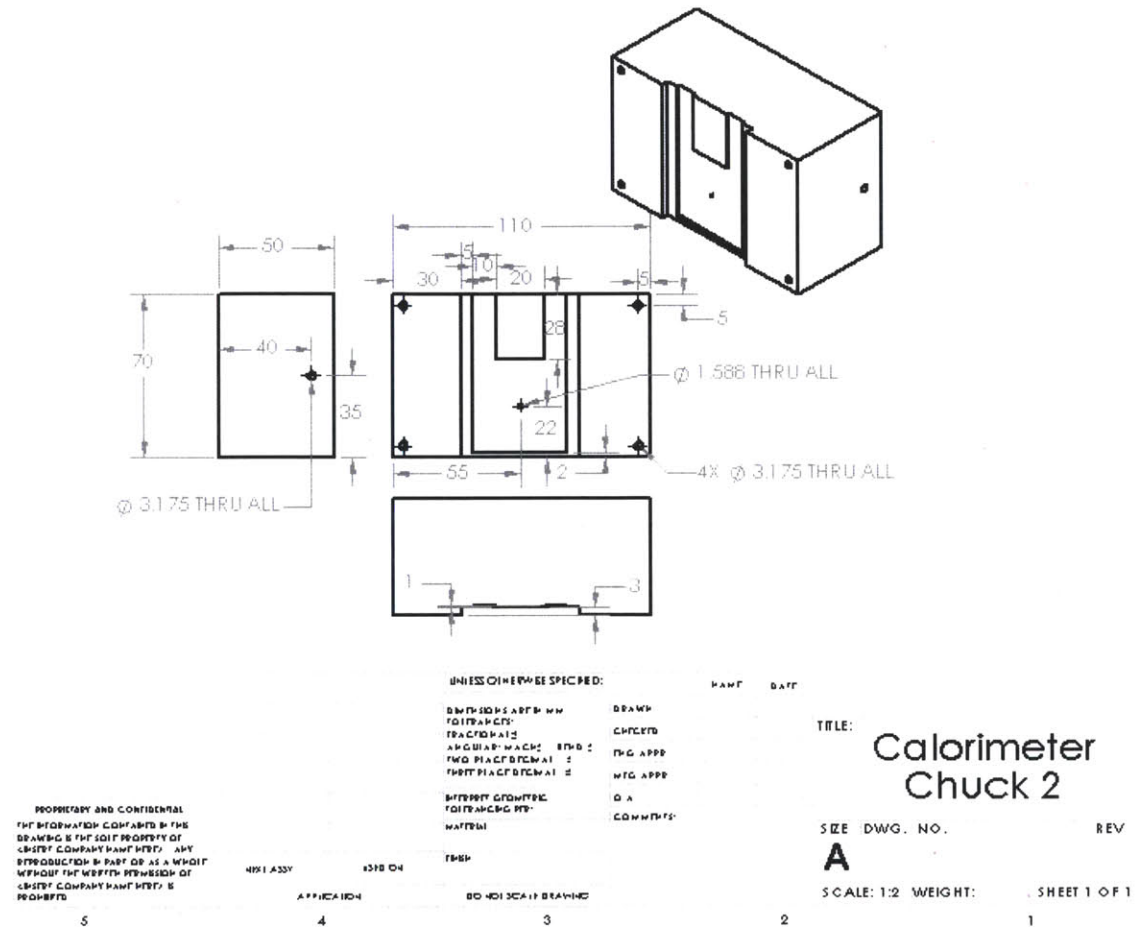

Figure H.2. SolidWorks drawing of microcalorimeter 2 chuck. Dimensions are in mm. Scale 1:2.

Appendix I: LabVIEW Programs

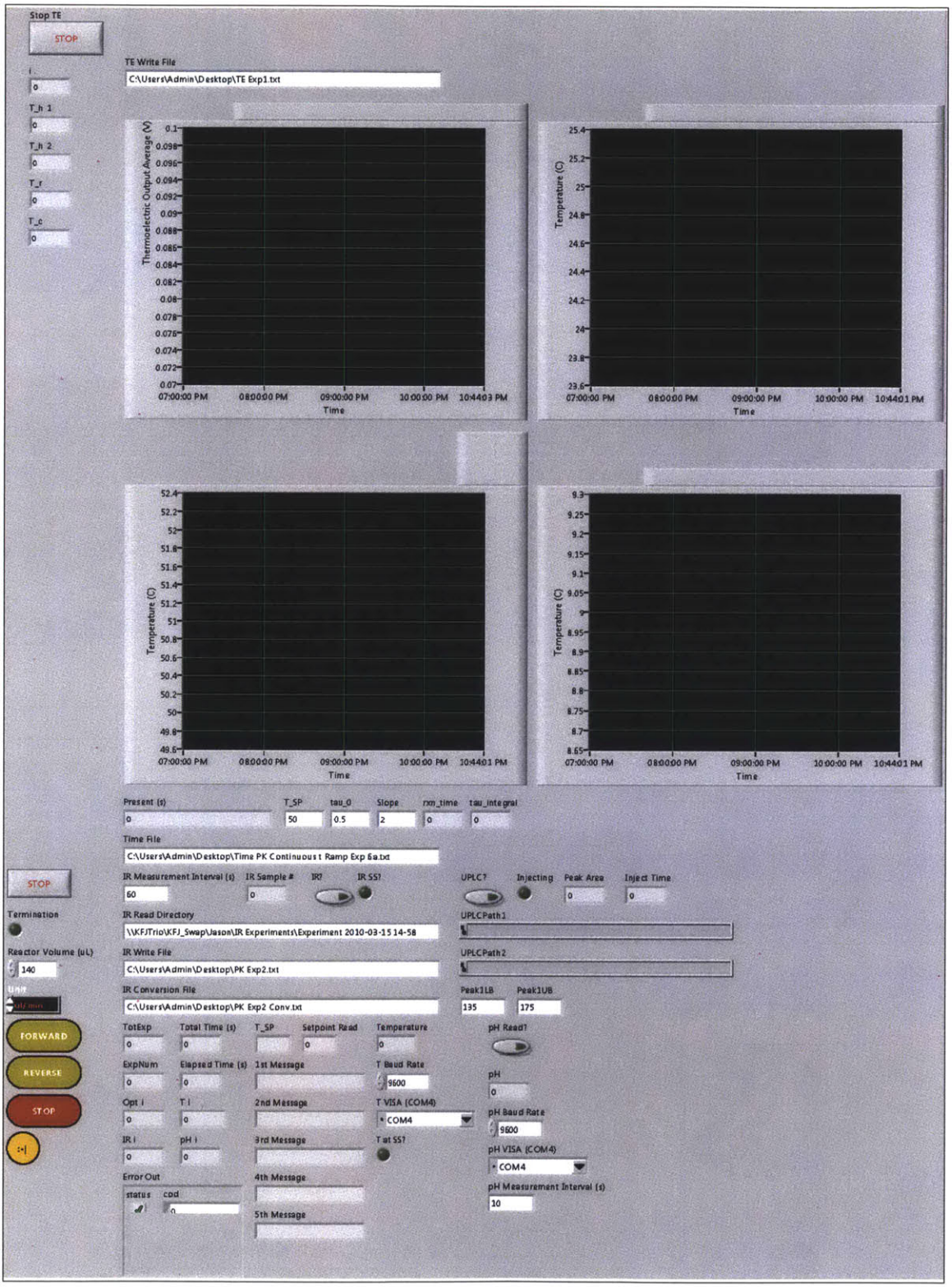

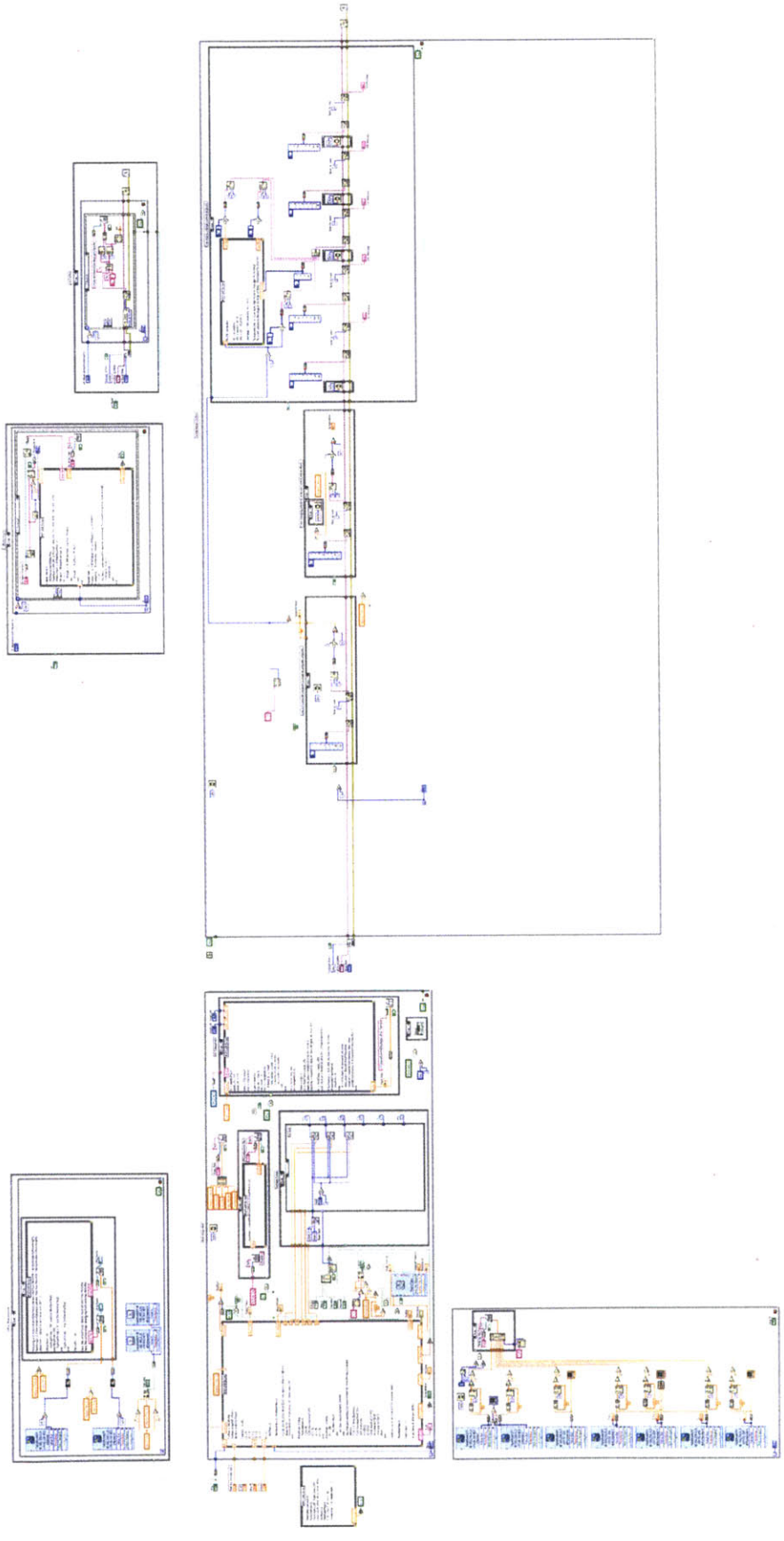

Appendix J: LabVIEW MATLAB Code

Setpoint Control

```
Creactor = 1;
C1 = 2;
C2 = 2;
C3 = 2;
C4 = 2;
C5 = 2;
Flush_Volume =6*Vr;%%%%Fix 3*Vr (uL)

if UPLC == 1
    Analysis_time = 0.5;
else
    Analysis_time = 0.1;
end

if i<=1
    ExpNum=1;

    NextExpFlag=0; FlowRateFlag=0;

    v1=10; v2=10; v3=0; v4=0; T0=50; Q=1; rxn_time=1; Max=0; ratio=1;
    cond=[v1 v2 v3 v4 Q T0 rxn_time ratio];
    Data=[0; 0];
    Termination=0; Flush_time=1E7; Total_time=1E7;
end

FlowRateFlag=0;
%Data(ExpNum)=Max;

if NextExpFlag~=ExpNum
    if ExpNum>TotExp
        Termination=1;
        T_SP=1;
        T_SP_Str=num2str(T_SP);
        v1 = 0.1;
        v2 = 0.1;
        v3 = 0.1;
    end
    if ExpNum<=TotExp
        pt_history(ExpNum,:) = [pt(ExpNum,:), Data(ExpNum)];
        rxn_time=pt(ExpNum,2);
        ratio=pt(ExpNum,3);
        T_SP=pt(ExpNum,4);
        T_SP_Str=num2str(T_SP);
        Q=Vr/rxn_time;
        v1=Creactor*Q/C1;
        v2=Creactor*Q/C2;
        v3=Creactor*Q/C3;
        v4=Creactor*Q/C4;
        v5=Creactor*Q/C5;
```

```
        v6=0;
    end

    cond=[v1 v2 v3 v4 v5 v6 Q T_SP rxn_time ratio];

    NextExpFlag=ExpNum;
    FlowRateFlag=1;
end

if UPLC == 1
    Inject_time=max(Flush_Volume/Q*60,20*60);
else
    Inject_time=Flush_Volume/Q*60;
end

Flush_time=Inject_time+Analysis_time*60; %Need time values in s

Total_time=Flush_time+15;
```

Steepest Descent Optimization

```
if i == 0
    Creactor = 1;
    C1 = 2;
    C2 = 2;
    Flush_Volume =4*Vr;%%%%Fix 4*Vr (uL)
    MaxExp = 50;
    GradStep = 0;
    Contract = 0;
    TConstraint = 0;
    tauConstraint = 0;

    TSpan = [30,130,2,5]; % [Tmin,Tmax,dT,TInt] (C)
    tauSpan = [2,30,1,1]; % [taumin,taumax,dtau,tauInt] (min)
    InitT = 130; % Initial DoE T center (C)
    Inittau = 4.9923; % Initial DoE tau center (min)

    DoEExpNum = 4;
    DoET = [InitT-TSpan(3),InitT-TSpan(3),InitT+TSpan(3),InitT+TSpan(3)];
    DoEtau = [Inittau-tauSpan(3),Inittau+tauSpan(3),Inittau-
tauSpan(3),Inittau+tauSpan(3)];
    DoEratio = [1,1,1,1];
    [YRand,IRand] = sort(rand(1,DoEExpNum));
    pt = [[1:1:DoEExpNum]',DoEtau(IRand)',DoEratio(IRand)',DoET(IRand)'];

    if UPLC == 1
        Analysis_time = 5;%%%%Fix 5 (min)
    else
        Analysis_time = 0.1;%%%%Fix 5 (min)
    end

    % DoE Skip
```

```
%     pt = [1,3,1,128;2,3,1,132;3,1,1,128;4,1,1,132];
%     pt_history = pt;
%     Conv = [0.0745;0.0809;0.0380;0.0424];
%     ExpNum=5;
%     NextExpFlag=4;
    %%%%
    ExpNum=1;
    NextExpFlag=0;

    FlowRateFlag=0;
    v1=10; v2=10; v3=10; v4=10; T0=50; Q=1; rxn_time=10; ratio=1;
    cond=[v1 v2 v3 v4 Q T0 rxn_time ratio];
    Termination=0; Flush_time=1E7; Total_time=1E7;
end

FlowRateFlag=0;

if NextExpFlag ~= ExpNum && length(Conv) == NextExpFlag
    % Check for termination
    if ExpNum > DoEExpNum+3
        if ExpNum > MaxExp || (Conv(end) <= 0.95*max(Conv(5:end)) && Contract
== 0) || (Contract == 1 && ExpNum == 9) || (TConstraint == 1 && tauConstraint
== 1)
            Termination=1;
            T_SP = 1;
            T_SP_Str = num2str(T_SP);
            v1 = 0.1;
            v2 = 0.1;
        end
    end

    if ExpNum <= MaxExp && Termination == 0

        % Centerpoint after DoE Run
        if ExpNum == (DoEExpNum+1)
            GradT = (sum(Conv.*(pt(1:DoEExpNum,4)>InitT))-
sum(Conv.*(pt(1:DoEExpNum,4)<InitT)))/((DoEExpNum/2)*2*TSpan(3));
            Gradtau = (sum(Conv.*(pt(1:DoEExpNum,2)>Inittau))-
sum(Conv.*(pt(1:DoEExpNum,2)<Inittau)))/((DoEExpNum/2)*2*tauSpan(3));
            pt = [pt; ExpNum,Inittau,1,InitT];

            % Move along gradient after DoE
        elseif ExpNum == (DoEExpNum+2)
            StepSize = 3/sqrt(GradT^2+Gradtau^2);
            Flush_Volume = 2*Vr; % Reduce minimum flush volume during
gradient search (uL)
            GradStep = GradStep+1;
            if  Inittau+GradStep*Gradtau*StepSize < tauSpan(1) % Check tau
constraints
                taunew = tauSpan(1);
                tauConstraint = 1;
            elseif Inittau+GradStep*Gradtau*StepSize < tauSpan(2)
                taunew = Inittau+GradStep*Gradtau*StepSize;
            else
                taunew = tauSpan(2);
                tauConstraint = 1;
```

```
            end
            if InitT+GradStep*GradT*StepSize < TSpan(1) % Check T constraints
                Tnew = TSpan(1);
                TConstraint = 1;
            elseif InitT+GradStep*GradT*StepSize < TSpan(2)
                Tnew = round(InitT+GradStep*GradT*StepSize);
            else
                Tnew = TSpan(2);
                TConstraint = 1;
            end
            pt = [pt; ExpNum,taunew,1,Tnew];

            % If first step along gradient decreases, contract step size
        elseif ExpNum == (DoEExpNum+3) && Conv(end)<max(Conv(5:end))
            StepSize = 1/sqrt(GradT^2+Gradtau^2);
            GradStep = 1;
            Contract = 1;
            if  Inittau+GradStep*Gradtau*StepSize < tauSpan(1) % Check tau
constraints
                taunew = tauSpan(1);
                tauConstraint = 1;
            elseif Inittau+GradStep*Gradtau*StepSize < tauSpan(2)
                taunew = Inittau+GradStep*Gradtau*StepSize;
            else
                taunew = tauSpan(2);
                tauConstraint = 1;
            end
            if InitT+GradStep*GradT*StepSize < TSpan(1) % Check T constraints
                Tnew = TSpan(1);
                TConstraint = 1;
            elseif InitT+GradStep*GradT*StepSize < TSpan(2)
                Tnew = round(InitT+GradStep*GradT*StepSize);
            else
                Tnew = TSpan(2);
                TConstraint = 1;
            end
            pt = [pt; ExpNum,taunew,1,Tnew];

            % If conversion is increasing along gradient, continue
        elseif ExpNum > DoEExpNum+2
            GradStep = GradStep+1;
            if  Inittau+GradStep*Gradtau*StepSize < tauSpan(1) % Check tau
constraints
                taunew = tauSpan(1);
                tauConstraint = 1;
            elseif Inittau+GradStep*Gradtau*StepSize < tauSpan(2)
                taunew = Inittau+GradStep*Gradtau*StepSize;
            else
                taunew = tauSpan(2);
                tauConstraint = 1;
            end
            if InitT+GradStep*GradT*StepSize < TSpan(1) % Check T constraints
                Tnew = TSpan(1);
                TConstraint = 1;
            elseif InitT+GradStep*GradT*StepSize < TSpan(2)
                Tnew = round(InitT+GradStep*GradT*StepSize);
```

```
            else
                Tnew = TSpan(2);
                TConstraint = 1;
            end
            pt = [pt; ExpNum,taunew,1,Tnew];
        end

        pt_history(ExpNum,:) = pt(ExpNum,:);
        rxn_time=pt(ExpNum,2);
        ratio=pt(ExpNum,3);
        T_SP=pt(ExpNum,4);
        T_SP_Str=num2str(T_SP);
        Q=Vr/rxn_time;
        v1=Creactor*Q/C1;
        v2=Creactor*Q/C2;
        v3=0;
        v4=0;
        v5=0;
        v6=0;
    end

    cond=[v1 v2 v3 v4 v5 v6 Q T_SP rxn_time ratio];

    NextExpFlag=ExpNum;
    FlowRateFlag=1;
end

Inject_time=Flush_Volume/Q*60; % (s)
Flush_time=Inject_time+Analysis_time*60; % (s)

Total_time=Flush_time+15;%%%%Fix
```

Conjugate Gradient Optimization

```
if i == 0
    Creactor = 1;
    C1 = 2;
    C2 = 2;
    Flush_Volume =4*Vr;%%%%Fix 4*Vr (uL)
    MaxExp = 50;
    MinStep = 1;
    GradStep = 0;
    Contract = 0;
    TConstraint = 0;
    tauConstraint = 0;

    TSpan = [30,130,2,5]; % [Tmin,Tmax,dT,TInt] (C)
    tauSpan = [2,30,1,1]; % [taumin,taumax,dtau,tauInt] (min)
    InitT = 130; % Initial DoE T center (C)
    Inittau = 4.362; % Initial DoE tau center (min)
    GradOld = [5.5028E-4; -4.2905E-3];
    cg = [3.0214E-2; -3.5897E-3];
```

```
    DoEExpNum = 4;
    DoET = [InitT-TSpan(3),InitT-TSpan(3),InitT+TSpan(3),InitT+TSpan(3)];
    DoEtau = [Inittau-tauSpan(3),Inittau+tauSpan(3),Inittau-
tauSpan(3),Inittau+tauSpan(3)];
    DoEratio = [1,1,1,1];
    [YRand,IRand] = sort(rand(1,DoEExpNum));
    pt = [[1:1:DoEExpNum]',DoEtau(IRand)',DoEratio(IRand)',DoET(IRand)'];

    if UPLC == 1
        Analysis_time = 5;%%%%Fix 5 (min)
    else
        Analysis_time = 0.1;%%%%Fix 5 (min)
    end

    % DoE Skip
    %     pt = [1,6.9445,1,70;2,4.9445,1,70;3,4.9445,1,74;4,6.9445,1,74];
    %     pt_history = pt;
    %     Conv = [0.0437;0.0378;0.0403;0.0448];
    %     ExpNum=5;
    %     NextExpFlag=4;
    %%%%
    ExpNum=1;
    NextExpFlag=0;

    v1=10; v2=10; v3=10; v4=10; T0=50; Q=1; rxn_time=10; ratio=1;
    cond=[v1 v2 v3 v4 Q T0 rxn_time ratio];
    Termination=0; Flush_time=1E7; Total_time=1E7;
end

FlowRateFlag=0;

if NextExpFlag~=ExpNum && length(Conv) == NextExpFlag
    % Check for termination
    if ExpNum > DoEExpNum+3
        if ExpNum > MaxExp || (Conv(end) <= 0.95*max(Conv(5:end)) && Contract
== 0) || (Contract == 1 && ExpNum == 9) || ((TConstraint == 1 ||
abs(cg(1)*StepSize) < MinStep) && (tauConstraint == 1 || abs(cg(2)*StepSize)
< MinStep))
            Termination=1;
            T_SP = 1;
            T_SP_Str = num2str(T_SP);
            v1 = 0.1;
            v2 = 0.1;
        end
    end

    if ExpNum<=MaxExp && Termination == 0

        % Centerpoint after DoE Run
        if ExpNum == (DoEExpNum+1)
            GradT=(sum(Conv.*(pt(1:DoEExpNum,4)>InitT))-
sum(Conv.*(pt(1:DoEExpNum,4)<InitT)))/((DoEExpNum/2)*2*TSpan(3));
            Gradtau=(sum(Conv.*(pt(1:DoEExpNum,2)>Inittau))-
sum(Conv.*(pt(1:DoEExpNum,2)<Inittau)))/((DoEExpNum/2)*2*tauSpan(3));
            Grad = [GradT;Gradtau];
```

```
            beta = norm(Grad)^2/norm(GradOld)^2; % Fletcher-Reeves
            % beta = dot(Grad,(Grad-GradOld))/norm(GradOld)^2; % Polak-
Ribiere
            cg = Grad+beta*cg;
            pt = [pt; ExpNum,Inittau,1,InitT];

            % Move along gradient after DoE
        elseif ExpNum == (DoEExpNum+2)
            StepSize = 3/sqrt(cg(1)^2+cg(2)^2);
            if TSpan(1) == InitT || TSpan(2) == InitT % Check if InitT is on
constraint
                StepSize = 3/sqrt(cg(2)^2);
            elseif tauSpan(1) == Inittau || tauSpan(2) == Inittau % Check if
Inittau is on constraint
                StepSize = 3/sqrt(cg(1)^2);
            end
            Flush_Volume =2*Vr; % Reduce minimum flush volume during gradient
search (uL)
            GradStep = GradStep+1;
            if  Inittau+GradStep*cg(2)*StepSize < tauSpan(1) % Check tau
constraints
                taunew = tauSpan(1);
                tauConstraint = 1;
            elseif Inittau+GradStep*cg(2)*StepSize > tauSpan(2)
                taunew = tauSpan(2);
                tauConstraint = 1;
            else
                taunew = Inittau+GradStep*cg(2)*StepSize;
            end
            if InitT+GradStep*cg(1)*StepSize < TSpan(1) % Check T constraints
                Tnew = TSpan(1);
                TConstraint = 1;
            elseif InitT+GradStep*cg(1)*StepSize > TSpan(2)
                Tnew = TSpan(2);
                TConstraint = 1;
            else
                Tnew = round(InitT+GradStep*cg(1)*StepSize);
            end
            pt = [pt; ExpNum,taunew,1,Tnew];

            % If first step along gradient decreases, contract step size
        elseif ExpNum == (DoEExpNum+3) && Conv(end)<max(Conv(5:end))
            StepSize = 1/sqrt(cg(1)^2+cg(2)^2);
            if TSpan(1) == InitT || TSpan(2) == InitT % Check if InitT is on
constraint
                StepSize = 1/sqrt(cg(2)^2);
            elseif tauSpan(1) == Inittau || tauSpan(2) == Inittau % Check if
Inittau is on constraint
                StepSize = 1/sqrt(cg(1)^2);
            end
            GradStep = 1;
            Contract = 1;
            if  Inittau+GradStep*cg(2)*StepSize < tauSpan(1) % Check tau
constraints
                taunew = tauSpan(1);
                tauConstraint = 1;
```

```
            elseif Inittau+GradStep*cg(2)*StepSize > tauSpan(2)
                taunew = tauSpan(2);
                tauConstraint = 1;
            else
                taunew = Inittau+GradStep*cg(2)*StepSize;
            end
            if InitT+GradStep*cg(1)*StepSize < TSpan(1) % Check T constraints
                Tnew = TSpan(1);
                TConstraint = 1;
            elseif InitT+GradStep*cg(1)*StepSize > TSpan(2)
                Tnew = TSpan(2);
                TConstraint = 1;
            else
                Tnew = round(InitT+GradStep*cg(1)*StepSize);
            end
            pt = [pt; ExpNum,taunew,1,Tnew];

            % If conversion is increasing along gradient, continue
        elseif ExpNum > DoEExpNum+2
            GradStep = GradStep+1;
            if  Inittau+GradStep*cg(2)*StepSize < tauSpan(1) % Check tau
constraints
                taunew = tauSpan(1);
                tauConstraint = 1;
            elseif Inittau+GradStep*cg(2)*StepSize > tauSpan(2)
                taunew = tauSpan(2);
                tauConstraint = 1;
            else
                taunew = Inittau+GradStep*cg(2)*StepSize;
            end
            if InitT+GradStep*cg(1)*StepSize < TSpan(1) % Check T constraints
                Tnew = TSpan(1);
                TConstraint = 1;
            elseif InitT+GradStep*cg(1)*StepSize > TSpan(2)
                Tnew = TSpan(2);
                TConstraint = 1;
            else
                Tnew = round(InitT+GradStep*cg(1)*StepSize);
            end
            pt = [pt; ExpNum,taunew,1,Tnew];
        end
        pt_history(ExpNum,:) = pt(ExpNum,:);
        rxn_time=pt(ExpNum,2);
        ratio=pt(ExpNum,3);
        T_SP=pt(ExpNum,4);
        T_SP_Str=num2str(T_SP);
        Q=Vr/rxn_time;
        v1=Creactor*Q/C1;
        v2=Creactor*Q/C2;
        v3=0;
        v4=0;
        v5=0;
        v6=0;
    end

    cond=[v1 v2 v3 v4 v5 v6 Q T_SP rxn_time ratio];
```

```
    NextExpFlag=ExpNum;
    FlowRateFlag=1;
end

Inject_time=Flush_Volume/Q*60; % (s)
Flush_time=Inject_time+Analysis_time*60; % (s)

Total_time=Flush_time+15;%%%%Fix
```

Armijo Conjugate Gradient Optimization

```
if i == 0
    Creactor = 1;
    C1 = 2;
    C2 = 2;
    Flush_Volume =4*Vr;%%%%Fix 4*Vr (uL)
    MaxExp = 50;
    MinStep = 1;
    Step = 16;
    GradStep = 0;
    Contract = 0;
    ContractAccept = 0;
    ArmijoContract = 0;
    ArmijoAccept = 0;
    ArmijoStep = 1/2;
    TConstraint = 0;
    tauConstraint = 0;

    TSpan = [30,250,2,5]; % [Tmin,Tmax,dT,TInt] (C)
    tauSpan = [2,30,1,1]; % [taumin,taumax,dtau,tauInt] (min)
    InitT = 130; % Initial DoE T center (C)
    Inittau = 11.4218; % Initial DoE tau center (min)
    GradOld = [9.2088E-4; 1.6086E-3];
    cg = [2.7962E-3; 1.3335E-4];

    DoEExpNum = 4;
    DoET = [InitT-TSpan(3),InitT-TSpan(3),InitT+TSpan(3),InitT+TSpan(3)];
    DoEtau = [Inittau-tauSpan(3),Inittau+tauSpan(3),Inittau-
tauSpan(3),Inittau+tauSpan(3)];
    DoEratio = [1,1,1,1];
    [YRand,IRand] = sort(rand(1,DoEExpNum));
    pt = [[1:1:DoEExpNum]',DoEtau(IRand)',DoEratio(IRand)',DoET(IRand)'];

    if UPLC == 1
        Analysis_time = 5;%%%%Fix 5 (min)
    else
        Analysis_time = 0.1;%%%%Fix 5 (min)
    end

    % DoE Skip
    % pt = [1,6.9445,1,70;2,4.9445,1,70;3,4.9445,1,74;4,6.9445,1,74];
    % pt_history = pt;
```

```
    % Conv = [0.0437;0.0378;0.0403;0.0448];
    % ExpNum=5;
    % NextExpFlag=4;
    %%%%
    ExpNum=1;
    NextExpFlag=0;

    v1=10; v2=10; v3=10; v4=10; T0=50; Q=1; rxn_time=10; ratio=1;
    cond=[v1 v2 v3 v4 Q T0 rxn_time ratio];
    Termination=0; Flush_time=1E7; Total_time=1E7;
end

FlowRateFlag=0;

if NextExpFlag~=ExpNum && length(Conv) == NextExpFlag
    % Check for termination
    if ExpNum > DoEExpNum+3
        % Check for Armijo Contraction
        if Conv(end) <= 0.95*max(Conv(5:end)) && Contract == 0 &&
ArmijoContract == 0
            ArmijoContract = 1;
            GradStep = 0;
            MaxIndex = length(Conv)-1;
            if Conv(end) < Conv(end-2)
                Step = -Step;
            end
        end

        % Check for accepting Armijo step
        if ArmijoContract == 1
            % step size < minimum
            if Conv(end) > Conv(MaxIndex)
                ArmijoAccept = 1;
            elseif ((Tnew == TSpan(1) || Tnew == TSpan(2)) && (taunew ==
tauSpan(1) || taunew == tauSpan(2))) || ...
                    ((Tnew == TSpan(1) || Tnew == TSpan(2)) &&
abs(cg(2)*StepSize*ArmijoStep^(GradStep+1)) < MinStep) || ...
                    ((taunew == tauSpan(1) || taunew == tauSpan(2)) &&
abs(cg(1)*StepSize*ArmijoStep^(GradStep+1)) < MinStep) || ...
                    (abs(Step)*ArmijoStep^(GradStep+1) < MinStep)
                ArmijoAccept = 1
            end

        end

        % Check for accepting contraction Bisection step
        if Contract == 1
            % step size < minimum
%             if Conv(end) > Conv(5)
%                 ContractAccept = 1;
%             else
            if (TConstraint == 1 &&
abs(cg(2)*StepSize*ArmijoStep^(GradStep+1)) < MinStep) || ...
                (tauConstraint == 1 &&
abs(cg(1)*StepSize*ArmijoStep^(GradStep+1)) < MinStep) || ...
                (abs(Step)*ArmijoStep^(GradStep+1) < MinStep)
```

```
                ContractAccept = 1;
            end
        end

        % Termination criteria
        if ExpNum > MaxExp || ...
                (Conv(end) <= 0.95*max(Conv(5:end)) && Contract == 0  &&
ArmijoContract == 0) || ...
                (Contract == 1 && ContractAccept == 1) || ...
                ((TConstraint == 1 || abs(cg(1)*StepSize) < MinStep) &&
(tauConstraint == 1 || abs(cg(2)*StepSize) < MinStep) && Contract == 0 &&
ArmijoContract == 0) || ...
                (ArmijoContract == 1 && ArmijoAccept == 1)
            Termination=1;
            T_SP = 1;
            T_SP_Str = num2str(T_SP);
            v1 = 0.1;
            v2 = 0.1;
        end
    end

    if ExpNum<=MaxExp && Termination == 0

        % Centerpoint after DoE Run
        if ExpNum == (DoEExpNum+1)
            %GradT=(sum(Conv.*(pt(1:DoEExpNum,4)>InitT))-
sum(Conv.*(pt(1:DoEExpNum,4)<InitT)))/((DoEExpNum/2)*2*TSpan(3));
            %Gradtau=(sum(Conv.*(pt(1:DoEExpNum,2)>Inittau))-
sum(Conv.*(pt(1:DoEExpNum,2)<Inittau)))/((DoEExpNum/2)*2*tauSpan(3));
            %Grad = [GradT;Gradtau];
            %beta = norm(Grad)^2/norm(GradOld)^2; % Fletcher-Reeves
            % beta = dot(Grad,(Grad-GradOld))/norm(GradOld)^2; % Polak-
Ribiere
            %cg = Grad+beta*cg;
cg = [1.7606E-3; -2.0264E-3];
            pt = [pt; ExpNum,Inittau,1,InitT];

            % Move along gradient after DoE
        elseif ExpNum == (DoEExpNum+2)
            StepSize = Step/sqrt(cg(1)^2+cg(2)^2);
            if TSpan(1) == InitT || TSpan(2) == InitT % Check if InitT is on
constraint
                StepSize = Step/sqrt(cg(2)^2);
            elseif tauSpan(1) == Inittau || tauSpan(2) == Inittau % Check if
Inittau is on constraint
                StepSize = Step/sqrt(cg(1)^2);
            end
            Flush_Volume =2*Vr; % Reduce minimum flush volume during gradient
search (uL)
            GradStep = GradStep+1;
            if  Inittau+GradStep*cg(2)*StepSize < tauSpan(1) % Check tau
constraints
                taunew = tauSpan(1);
                tauConstraint = 1;
            elseif Inittau+GradStep*cg(2)*StepSize > tauSpan(2)
                taunew = tauSpan(2);
```

```
            tauConstraint = 1;
        else
            taunew = Inittau+GradStep*cg(2)*StepSize;
        end
        if InitT+GradStep*cg(1)*StepSize < TSpan(1) % Check T constraints
            Tnew = TSpan(1);
            TConstraint = 1;
        elseif InitT+GradStep*cg(1)*StepSize > TSpan(2)
            Tnew = TSpan(2);
            TConstraint = 1;
        else
            Tnew = round(InitT+GradStep*cg(1)*StepSize);
        end
        pt = [pt; ExpNum,taunew,1,Tnew];

        % If first step along gradient decreases, contract step size
    elseif (ExpNum == (DoEExpNum+3) && Conv(end)<max(Conv(5:end))) ||
Contract == 1 ...
            || (Contract == 0 && tauConstraint == 1 && TConstraint == 1)
        if Contract == 0
            GradStep = 0;
            Index = [5,6];
        end
        if length(Conv) > 6
            [~,minIndex] = min(Conv([Index,end]));
            Index(minIndex) = length(Conv);
        end
        Contract = 1;
        GradStep = GradStep+1;

        taunew = mean([pt(Index(1),2),pt(Index(2),2)]);
        Tnew = round(mean([pt(Index(1),4),pt(Index(2),4)]));
        pt = [pt; ExpNum,taunew,1,Tnew];

        % If second to last step along gradient is max, contract step
size
    elseif ArmijoContract == 1
        GradStep = GradStep+1;
        StepSize = Step/sqrt(cg(1)^2+cg(2)^2);
        if TSpan(1) == InitT || TSpan(2) == InitT % Check if InitT is on
constraint
            StepSize = Step/sqrt(cg(2)^2);
        elseif tauSpan(1) == Inittau || tauSpan(2) == Inittau % Check if
Inittau is on constraint
            StepSize = Step/sqrt(cg(1)^2);
        end
        if  pt(MaxIndex,2)+ArmijoStep^GradStep*cg(2)*StepSize <
tauSpan(1) % Check tau constraints
            taunew = tauSpan(1);
            tauConstraint = 1;
        elseif pt(MaxIndex,2)+ArmijoStep^GradStep*cg(2)*StepSize >
tauSpan(2)
            taunew = tauSpan(2);
            tauConstraint = 1;
        else
            taunew = pt(MaxIndex,2)+ArmijoStep^GradStep*cg(2)*StepSize;
```

```
            end
            if pt(MaxIndex,4)+ArmijoStep^GradStep*cg(1)*StepSize < TSpan(1) %
Check T constraints
                Tnew = TSpan(1);
                TConstraint = 1;
            elseif pt(MaxIndex,4)+ArmijoStep^GradStep*cg(1)*StepSize >
TSpan(2)
                Tnew = TSpan(2);
                TConstraint = 1;
            else
                Tnew =
round(pt(MaxIndex,4)+ArmijoStep^GradStep*cg(1)*StepSize);
            end
            pt = [pt; ExpNum,taunew,1,Tnew];

            % If conversion is increasing along gradient, continue
        elseif ExpNum > DoEExpNum+2
            GradStep = GradStep+1;
            if  Inittau+GradStep*cg(2)*StepSize < tauSpan(1) % Check tau
constraints
                taunew = tauSpan(1);
                tauConstraint = 1;
            elseif Inittau+GradStep*cg(2)*StepSize > tauSpan(2)
                taunew = tauSpan(2);
                tauConstraint = 1;
            else
                taunew = Inittau+GradStep*cg(2)*StepSize;
            end
            if InitT+GradStep*cg(1)*StepSize < TSpan(1) % Check T constraints
                Tnew = TSpan(1);
                TConstraint = 1;
            elseif InitT+GradStep*cg(1)*StepSize > TSpan(2)
                Tnew = TSpan(2);
                TConstraint = 1;
            else
                Tnew = round(InitT+GradStep*cg(1)*StepSize);
            end
            pt = [pt; ExpNum,taunew,1,Tnew];
        end
        pt_history(ExpNum,:) = pt(ExpNum,:);
        rxn_time=pt(ExpNum,2);
        ratio=pt(ExpNum,3);
        T_SP=pt(ExpNum,4);
        T_SP_Str=num2str(T_SP);
        Q=Vr/rxn_time;
        v1=Creactor*Q/C1;
        v2=Creactor*Q/C2;
        v3=0;
        v4=0;
        v5=0;
        v6=0;
    end

    cond=[v1 v2 v3 v4 v5 v6 Q T_SP rxn_time ratio];

    NextExpFlag=ExpNum;
```

```
    FlowRateFlag=1;
end

Inject_time=Flush_Volume/Q*60; % (s)
Flush_time=Inject_time+Analysis_time*60; % (s)

Total_time=Flush_time+15;%%%%Fix
```

Residence Time Ramp

```
T_SPvec = [50,50,50];
TotExp=length(T_SPvec);
alpha = log(1/(1-Slope));

Creactor = 4.262;
C1 = 4;
C2 = 4;
C3 = 2;
C4 = 2;
C5 = 2;

if i<=1
    ExpNum=1;

    NextExpFlag=0; FlowRateFlag=0;

    v1=10; v2=10; v3=0; v4=0; Q=1; rxn_time=1; Max=0; ratio=1;
    Data=[0; 0];
    Termination=0; Flush_time=1E7; Total_time=1E7;
end

if ExpNum>TotExp
    Termination=1;
    T_SP=50;
    T_SP_Str=num2str(T_SP);
    v1 = 70;
    v2 = 70;
    v3 = 70;
end
if ExpNum<=TotExp
    if t < 300
        rxn_time=tau_0;
    else
        rxn_time=tau_0+alpha*(t-300)/60;
    end
    tau_integral=max(tau_0,(1-exp(-alpha))*((t-300)/60+tau_0/alpha));
    ratio=1;
    T_SP = T_SPvec(ExpNum);
    T_SP_Str=num2str(T_SP);
    Q=Vr/rxn_time;
    v1=Q/C1;
    v2=Q/C2;
    v3=(Creactor/C3-1)*Q;
    v4=Creactor*Q/C4;
```

```
    v5=Creactor*Q/C5;
    v6=0;
end

cond=[v1 v2 v3 v4 v5 v6 Q T_SP rxn_time ratio];

FlowRateFlag=1;

Inject_time = 1;

Total_time=(2.5/Slope+10)*60;
```

Concentration Ramp

```
Cmax = 4;
Cmin = 0.25;
slope = 0.05; % M/min
trun = 2*((Cmax-Cmin)/slope+5)*60;
tmax = 2*trun;
TotExp=1;

Creactor = 1;
C1 = 2;
C2 = 2;
C3 = 2;
C4 = 2;
C5 = 2;

if i<=1
    ExpNum=1;

    NextExpFlag=0; FlowRateFlag=0;

    v1=10; v2=10; v3=0; v4=0; Q=1; rxn_time=1; Max=0; ratio=1;
    Data=[0; 0];
    Termination=0; Flush_time=1E7; Total_time=1E7;
end

if ExpNum>TotExp
    Termination=1;
    ratio = 2;
    T_SP=50;
    T_SP_Str=num2str(T_SP);
    v1 = Creactor*Q/2*ratio/4.262;
    v2 = Creactor*Q/2*ratio/4.262;
    v3 = Creactor*Q/2*(1-ratio/4.262);
end
if ExpNum<=TotExp
    time = mod(t,tmax/2);
    if time <= 5*60
        ratio = Cmax;
    elseif time <= trun/2
```

```
        ratio = (trun/2-time)/(trun/2-300)*(Cmax-Cmin)+Cmin;
    elseif time <= trun/2+5*60
        ratio = Cmin;
    else
        ratio = (time-trun/2-300)/(trun/2-300)*(Cmax-Cmin)+Cmin;
    end
    T_SP = 50;
    T_SP_Str=num2str(T_SP);
    rxn_time = 2;
    Q=Vr/rxn_time;
    v1=Creactor*Q/2*ratio/4.262;
    v2=Creactor*Q/4*ratio/4.262;
    v3=Creactor*Q/2*(1-ratio/4.262);
    v4=Creactor*Q/C4;
    v5=Creactor*Q/C5;
    v6=0;
end

cond=[v1 v2 v3 v4 v5 v6 Q T_SP rxn_time ratio];

FlowRateFlag=1;

Inject_time = 1;

Total_time=tmax;
```

Appendix K: MATLAB CODE TO GENERATE OPTIMIZATION PLOTS

```
function OptPlot(T,t,X)

% Production
cmap = colormap;
Font = 25;
Xc = ceil(size(cmap,1)*(X-.4)/(.9-.4));
a = axes('FontSize',Font);
axis(a,[0,30,120,240])
hold on

% line([2,30],[120,120],'Color','r','LineStyle',':','LineWidth',5)
line([30,30],[120,240],'Color','r','LineStyle',':','LineWidth',5)
% line([2,30],[240,240],'Color','r','LineStyle',':','LineWidth',5)
line([2,2],[120,240],'Color','r','LineStyle',':','LineWidth',5)

for i = 1:length(X)

plot(t(i),T(i),'o','MarkerSize',12,'MarkerFaceColor',cmap(Xc(i),:),'MarkerEdg
eColor',cmap(Xc(i),:),'LineWidth',2)
%     if i < length(X)
%         text(t(i),T(i),[' ',num2str(X(i)-
rem(X(i),0.01))],'HorizontalAlignment','left','VerticalAlignment','top','Font
Size',Font,'FontWeight','normal')
%         text(t(i),T(i),[num2str(i),'
'],'HorizontalAlignment','right','VerticalAlignment','middle','FontSize',Font
)
%     else
%         text(t(i),T(i),[' ',num2str(X(i)-
rem(X(i),0.01))],'HorizontalAlignment','left','VerticalAlignment','top','Font
Size',Font)
%         text(t(i),T(i),[num2str(i),'
'],'HorizontalAlignment','right','VerticalAlignment','middle','FontSize',Font
)
% %         text(t(i),T(i),['
,',num2str(X(i))],'HorizontalAlignment','left')
%     end
end

h=colorbar;
set(h,'YTickLabel',linspace(0.4,0.9,6),'FontSize',Font);
set(h,'YTick',linspace(1.5,64.5,6));
xlabel('Residence Time (min)','FontSize',Font)
ylabel('Temperature ( ^oC)','FontSize',Font)

% % Conversion
% cmap = colormap;
% Font = 25;
% Xc = ceil(size(cmap,1)*(X-0.55)/0.25);
%
```

```
% a = axes('FontSize',Font);
% axis(a,[0,30,35,135])
%
% line([2,30],[30,30],'Color','r','LineStyle',':','LineWidth',5)
% line([30,30],[30,130],'Color','r','LineStyle',':','LineWidth',5)
% line([2,30],[130,130],'Color','r','LineStyle',':','LineWidth',5)
% line([2,2],[30,130],'Color','r','LineStyle',':','LineWidth',5)
% hold on
%
% for i = 1:length(X)
%
plot(t(i),T(i),'o','MarkerSize',12,'MarkerFaceColor',cmap(Xc(i),:),'MarkerEdg
eColor',cmap(Xc(i),:),'LineWidth',2)
% %     if i < length(X)
% %         text(t(i),T(i),['
',num2str(X(i))],'HorizontalAlignment','left','VerticalAlignment','middle','F
ontSize',Font,'FontWeight','normal')
% %         text(t(i),T(i),[num2str(i),'
'],'HorizontalAlignment','right','VerticalAlignment','middle','FontSize',Font
,'FontWeight','normal')
% %     else
% %         text(t(i),T(i),['
',num2str(X(i))],'HorizontalAlignment','left','VerticalAlignment','bottom','F
ontSize',Font,'FontWeight','normal')
% %         text(t(i),T(i),[num2str(i),'
'],'HorizontalAlignment','right','VerticalAlignment','bottom','FontSize',Font
,'FontWeight','normal')
% %     end
% end
%
% h=colorbar;
% set(h,'YTickLabel',linspace(0.55,0.8,6),'FontSize',Font);
% set(h,'YTick',linspace(1.5,64.5,6));
% xlabel('Residence Time (min)','FontSize',Font)
% ylabel('Temperature ( ^oC)','FontSize',Font)
```

Appendix L: MATLAB CODE TO COMPILE IR AUTO-EXPORT DATA

```
function PKConv(N) % N = number of output files

Exp = 'Experiment 2012-05-24 17-18'; % Experiment name

if length(N) == 1
    N = [1,N];
end

tic
twrite = fopen([Exp,'.txt'],'wt');
for fnum = N(1):N(2)
    fnum
    if fnum < 10
        fid = fopen(['\\Kfjserver\KFJ_Swap\Jason\IR % Location of folder
Experiments\',Exp,'\',Exp,'_000',num2str(fnum),'_Spectrum.csv']);
    elseif fnum < 100
        fid = fopen(['\\Kfjserver\KFJ_Swap\Jason\IR
Experiments\',Exp,'\',Exp,'_00',num2str(fnum),'_Spectrum.csv']);
    elseif fnum < 1000
        fid = fopen(['\\Kfjserver\KFJ_Swap\Jason\IR
Experiments\',Exp,'\',Exp,'_0',num2str(fnum),'_Spectrum.csv']);
    else
        fid = fopen(['\\Kfjserver\KFJ_Swap\Jason\IR
Experiments\',Exp,'\',Exp,'_',num2str(fnum),'_Spectrum.csv']);
    end
    A = textscan(fid,'%s','delimiter',',');
    fclose(fid);
    B = A{1};
    for i = 1:(length(B)/2)
        C = B{2*i-1};
        D = B{2*i};
        IRWaveNum(1,i) = str2num(C(2:end-1));
        IRIntensity(1,i) = str2num(D(2:end-1));
    end
    if fnum == 1
        fprintf(twrite,'%f\t',IRWaveNum);
        fprintf(twrite,'\n');
        fprintf(twrite,'%f\t',IRIntensity);
        fprintf(twrite,'\n');
    else
        fprintf(twrite,'%f\t',IRIntensity);
        fprintf(twrite,'\n');
    end
end
fclose(twrite);
toc
```